Investigation and modelling of rubber friction

Gabriel, Philip

For additional information about this publication click this link.
https://qmro.qmul.ac.uk/jspui/handle/123456789/471

Investigation and modelling of rubber friction

Dipl.-Ing. (FH) Philip Gabriel
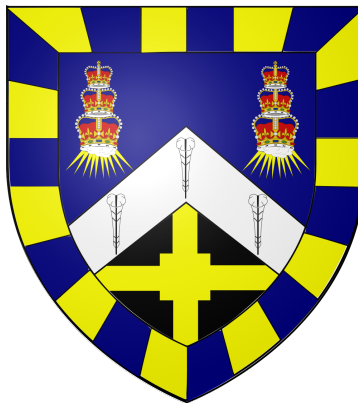
A thesis submitted to the University of London for the award of the degree of
Doctor of Philosophy

Queen Mary
University of London

School of Engineering and Materials Science

Mile End Road, London E1 4NS

June 2010

Abstract

The friction between a rubber surface in contact with a rigid surface is still not fully understood. Unlike other materials, friction behaviour in rubber is significantly dependent upon a variety of parameters due to its viscoelastic nature. The aim of this work is to understand frictional phenomena occurring on different length scales of intrest.

In the first part of this work the influence of an entirely geometric factor on friction is confirmed by FEA and is validated by experiments for the first time. Under certain conditions, it can increase the frictional force significantly above that expected from a consideration of the interfacial coefficient of friction alone. This term is thought likely to make a considerable contribution to frictional sliding applications such as a tyre on a road surface.

In the second part of this work an instability, observed at the rubber surface during sliding, is investigated. Despite experimental research in the past, virtually no information has been published on the modelling of the so-called Schallamach waves using FEA techniques. This work models successive Schallamach waves, giving the opportunity to investigate the transition of individual waves throughout the area of contact, for the first time. The use of FEA allows for a detailed stress and strain analysis at the interface and thus gives new insights into the onset of buckling instabilities.

So far, Schallamach waves have only been observed experimentally for optically smooth rubber surfaces, however, during this work, surface waves have been also noticed for rough rubber surfaces. Furthermore, the examination of the frequency dependence of Schallamach waves allows for the consideration of a relationship to stick-slip behaviour.

The third part of this work investigates the influence of the rubber surface topography as well as the rigid slider geometry on rubber friction under a wide range of experimental conditions. It was noted that subtle changes of surface finish significantly change the resulting frictional force. The knowledge gained from this can help in the design and understanding of more complex frictional interfaces.

Declaration

I hereby declare that the work carried out and presented in this thesis submitted for the degree of Doctor of Philosophy is original and my own. Any literature or figures not emerged from this original piece of work are referenced as such.

Philip Gabriel

Examination committee:

Professor Jacques W.M. Noordermeer

Elastomer Technology and Engineering Department
University of Twente, The Netherlands

Professor Julia C. Shelton

School of Engineering and Materials Science
Queen Mary, University of London, United Kingdom

Acknowledgements

Many people have contributed throughout this work to whom I am greatly in debt. I would like to express my most sincere gratitude to my supervisor, Dr. James Busfield, for offering me the opportunity to do a fully funded doctorate degree in his international research group and for his continual guidance and encouragement in this project. Furthermore, I am grateful to my second supervisor Professor Alan Thomas for valuable discussions and advice and his continuous visits to QMUL. I am also indebted to Professor Yoshihide Fukahori for his interest in my research and helpful advice and uninterrupted support by flying over to the UK from Japan three times a year. Furthermore, I would like to thank the other members of the Rubber Research Group, to mention, Dr. Mac, Dr. Vineet, Dr. Han and Dr. Praveen as well as Dr.'s to be Rob, David, Kartpan and Thomas for their experimental advice, support and a good time in and around the PhD office in Eng-235. It was a pleasure being part of such a great and multinational research group. In addition, I would like to express my gratitude to all staff of the Department of Materials for helpful support. Special mention must be made of Bill Godwin and Dr. Monisha Phillips.

Furthermore, I am deeply grateful for the financial support by: the Engineering and Physical Sciences Research Council (EPSRC), who funded my student fees for four years; James, who liberally offered me a studentship, which was also partly funded through collaborations with RedBull Racing and RML Mallock and the generous financial support from my family.

I am grateful to my family, my parents Angela & Inno as well as Roger & Carmen and my brother Alex, who supported me unconditionally through all years of research, by constantly asking how my research goes and how life is in London.

My deepest and greatest debt is to Jenny, who showed her absolute love by following me to London. Without her unceasing love, motivational encouragement and never ending support I would not have been in the place and situation I am in now.

5

To my parents and Jenny

Table of contents

List of figures

Chapter 3

Chapter 4

Chapter 5

Chapter 6

Chapter 7

Chapter 8

List of tables

Abbreviations

1D	One-dimensional
2D	Two-dimensional
3D	Three-dimensional
ABR	Acrylonitrile butadiene rubber
BPN	British pendulum number
BPT	British pendulum tester
BR	Polybutadiene rubber
DMA	Dynamic mechanical analysis
DOF	Degree of freedom
DPG	Diphenyl guanidine
DSC	Differential scanning calorimetry
FEA	Finite element analysis
IR	Polyisoprene rubber
IIR	Butyl rubber
IRHD	International rubber hardness degree
JKR	Johnson, Kendall and Roberts (1971)
LVDT	Linear variable differential transformer
MDR	Moving die rheometer
NR	Natural rubber
ODR	Oscillating die rheometer
phr	Parts by mass per hundred rubber
SBR	Styrene-butadiene rubber
SEF	Strain (or stored) energy function
SEM	Scanning electron microscope
TARRC	Tun Abdul Razak Research Centre
TPE	Thermoplastic elastomer
WLF	Williams, Landel and Ferry (1955)

Symbols

α_i	°	Geometrical angle
β	°	Angle of contact
β_P	°	Angle of peeling
γ	mJ/m^2	Surface energy (peel energy)
δ_t	mm	Thickness of excitated rubber layer
ε	-	Strain
ζ	nm	Characteristic length scale
ε_B	-	Strain at brake
η	Ns/m^2	Viscosity
η_c	-	Viscosity damping coefficient in tension
θ	°	Cone angle
θ_c	°	Angle between maximum σ_c and middle of contact
θ_{max}	°	Angle between point of contact and middle of contact
κ	-	Temperature dependent parameter
λ	-	Extension ratio
$\lambda_1, \lambda_2, \lambda_3$	-	Principal extension ratios
λ_w	nm	Wavelength
μ	-	Coefficient of friction
μ_I	-	Input coefficient of friction
μ_K	-	Kinetic coefficient of friction
μ_R	-	Output coefficient of friction
μ_S	-	Static coefficient of friction
ξ_{II}	nm	Horizontal cut off length
$\xi_\perp$	nm	Vertical cut off length
ξ_{min}	nm	Minimum coupling length
ρ	-	Poisson's ratio
σ	MPa	Engineering stress
σ_τ	MPa	Shear stress
σ_c	MPa	Compressive stress
σ_t	MPa	Tensile stress
σ_B	MPa	Stress at brake

σ_S	-	Standard deviation to describe the heights
$\sigma_{T1}, \sigma_{T2}, \sigma_{T3}$	MPa	True stresses for three-dimensional system
σ_*	MPa	Reduced stress
τ	MPa	Shear strength
Γ	J	Dissipated energy
φ	-	Friction ratio
ω	mm/s	Average wave progression velocity
ω_M	mm/s	Wave speed of a material
ω_{max}	Hz	Maximum mechanical excitation frequency
ω_{min}	Hz	Minimum mechanical excitation frequency
ψ	μm	Length scale of Schallamach waves

$[\mathbf{K}]$	-	Stiffness matrix
$\{F\}$	-	Force vector
$\{U\}$	-	Displacement vector
a	mm	Radius of contact
a_f	-	Coefficient of thermal expansion of f_v above T_g
a_T	-	Shift factor in the WLF equation
A	mm²	Real area of contact
A_0	mm²	Nominal area of contact
c	-	Damping coefficient
c_u	-	Material specific constant
c_v	-	Material specific constant f(v)
C, C_A, C_B	-	Constants
C_1, C_2, C_3	-	(Strain energy function) Elastic constants
C_{W1}, C_{W2}	-	Polymer dependent constants in the WLF equation
d	mm	Depth of deformation, depth of indentation
d_i	mm	Mean gap distance between two surfaces
D_i	mm	Diameter of sphere
D_{com}	MPa^{-1}	Bulk compliance
e	-	Equibiaxial strain
E	MPa	Young's modulus
E_B	MPa	Bulk modulus
E^*	MPa	Complex modulus
E'	MPa	Storage modulus
E''	MPa	Loss modulus
f	-	Number of waves traversing the interface in unit time
f_g	-	Fractional free volume
f_{max}	Hz	Frequency at maximum loss modulus
f_v	-	Fractional free volume at T_g
F	N	Force
$F_{ADHESION}$	-	Adhesional contribution to rubber friction
$F_{COHESION}$	-	Contribution to rubber friction through wear
F_C	N	Force applied to a crack of length L

F_F	N	Frictional force
$F_{HYSTERESIS}$	-	Deformation / hysteresis contribution to rubber friction
$F_{KINETIC}$	N	Kinetic frictional force
F_N	N	Normal force
F_{STATIC}	N	Static frictional force
$F_{VISCOUS}$	-	Contribution to rubber friction through lubrication
g	m/s^2	Gravity
G	MPa	Shear modulus
G'	MPa	Shear storage modulus
G''	MPa	Shear loss modulus
h	mm	Amplitude
H	mm	Instantaneous length of tensile test sample
H_0	mm	Initial length of tensile test sample
I_1, I_2, I_3	-	Strain variants
k	J/K	Boltzmann constant
k	N/mm	Measured stiffness of spring
K	-	Description of elastic constants in JKR equation
l_m	-	Length of jointed links in network chain
L	mm	Length
m	-	Slope
m_a	-	Friction specific constant (slope)
m_b	-	Friction specific constant (ordinate at origin)
M	Kg	Mass
M_L	Nm	Minimum torque
M_{HF}	Nm	Maximum torque when curve plateaus
M_{HR}	Nm	Maximum torque of a reverting curve
M_H	Nm	Highest torque during test with no plateau or maximum
n	-	Number of Schallamach waves
N	-	Number of chains in network
p	N/mm²	Pressure
r	nm	End to end chain length
R	mm	Radius
R_a	μm	Roughness average

R_D	μm	Fractal dimension
R_h	μm	Variance of height distribution
RF_F	N	Horizontal (frictional) reaction force
RF_N	N	Vertical (normal) reaction force
R_{max}	μm	Maximum peak to valley height
S	-	Complex parameter to describe surface topography
t	s	Time
t_{ex}	s	Excitation time
t_{relax}	s	Relaxation time
t_X	min	Minutes to x% of MH
T	°C	Temperature
T_{DEG}	°C	Degradation temperature
T_e	°C	DSC analysis: extrapolated end set temperature
T_f	°C	DSC analysis: extrapolated onset temperature
T_g	°C	Glass transition temperature
T_i	°C	DSC analysis: the inflection temperature
T_m	°C	DSC analysis: midpoint temperature
T_s	°C	Reference temperature
U	J	Energy
v	mm/s	Velocity
v_{max}	mm/s	Velocity at maximum friction
V	-	Total volume of system
V_f	-	Free volume available to system
w	J/K	Entropy of network
W	J/V	Elastically stored energy per unit volume
x	mm	Deformation

1 Introduction

Friction, being a restraint of relative motion between two contacting bodies, plays a vital role in many engineering applications in terms of ensuring stability, enhancing safety and reducing costs. Rubber friction represents a particularly interesting field of research, as it depends upon many parameters, such as contact area, sliding velocity or temperature, due to the viscoelastic nature exhibited by the rubber. While a high friction is crucial for some products, for example braking systems, others might require very low friction for instance in shaft seals or windscreen wipers. Consequently, engineering applications involving rubber friction have to be well designed and the friction mechanics well understood.

According to Amontons' friction law, the arising horizontal force at a sliding interface is proportional to the vertical force induced on the interface and their ratio can be expressed as the coefficient of friction μ. Despite the debate on the applicability of this law to rubber friction, when compared to rigid materials, which exhibit friction values in the range of $\mu=0.1$ up to 1.0, rubber friction can exhibit values up to 5.0 or higher. This high deviation in exhibited friction compared to other materials is mainly due to the ability of rubber to deform to large strains, which results in visco-elastic energy dissipation, as well as surface adhesion effects. Due to the induced shear forces at the rubber friction interface while sliding, large deformations of the rubber surface can also produce different forms of instabilities. These can manifest for example as waves of detachment or stick-slip motion. However, the origins and significance of the different parameters affecting rubber friction are still a subject of debate and not fully understood (Baumberger and Caroli 2006, Rand and Crosby 2007). Many approaches exist trying to describe the complexity of rubber friction by using a vast amount of parameters (Klüppel and Heinrich 2008, Persson 2001c). In these theories the sum of several parameters describe the expected frictional behaviour, however, the determination of 20 descriptors or more is elaborate and might be of little benefit to everyday friction testing. Complicating matters further, these parameters were proven to be correlated to

each other (Roberts 1986) and, therefore, make a general description of the coefficient of friction very difficult as the increase of only one parameter for example temperature does alter the influence of other parameters significantly. In this work it is investigated in how far a more general and simplistic approach to rubber friction can describe the experienced frictional behaviour.

The fundamental aim of this work is to investigate the interface geometry between a rigid body and a rubber at different length scales. By investigating the effect of macro and microasperities of the interface, different contributions to the total frictional force are investigated and surface effects, such as surface instabilities, arising under specific interface geometries are visualised and investigated using experimental techniques as well as computational modelling for the first time.

It was previously suggested that, beside adhesion and hysteresis, the macroscopic interface geometry (Schallamach 1969) might have an additional contributing (wrapping) effect to rubber friction and this is investigated here both experimentally and computationally by FEA. When the length scale of interest is increased, it is shown that the microscopic surface roughness of two bodies in contact is of paramount importance to the frictional behaviour (Grosch 1963, Barquins and Roberts 1986, Persson 2001, Klüppel and Heinrich 2008) so that this topic of debate is also considered here in Chapter 7.

Furthermore, the topography of microasperities as well as the (macro) geometry of the interface alters the displacement mechanisms between the contacting bodies, so that under certain conditions the relative displacement can occur by different forms of instabilities, for example stick-slip or Schallamach waves. The significance of the surface finish of the rubber in terms of micro-roughness on these displacement mechanisms is investigated in this work.

The use of finite element analysis can help to resolve problems by a detailed analysis of the stresses and strains developed at the friction interface, which can not be addressed experimentally. The structure of this thesis is given next.

Chapter 2 reviews the literature on rubber friction in detail and gives an overview on rubber behaviour.

In **Chapter 3** the rubber materials that were chosen to represent the materials found in industrial applications requiring high sliding friction, are characterised to derive their mechanical, thermal and chemical properties. The different test methods for this characterisation as well as the development of a friction tester, designed as part of this research, are described in this chapter.

Chapter 4 describes a novel and entirely geometric contribution to rubber friction resulting from the deformation of the rubber surface due to a macro asperity. This effect, which was investigated using finite element analysis (FEA) and validated experimentally, contributes to rubber friction under certain geometrical circumstances and provides insight into the general friction behaviour. The concept outlined in this chapter is based on the publication by Gabriel et al. (2010a).

Despite extensive experimental data sets published in the literature on surface instabilites arising from the contact between an optically smooth rubber and a smooth rigid body, virtually no information is available on the modelling of these so-called Schallamach waves. **Chapter 5** investigates computationally this phenomenon for the first time using FEA. By using an entirely elastic FEA approach a progressing surface instability could be modelled satisfactorily. This chapter is based on the paper accepted for publication by Gabriel et al. (2010b).

The investigation of Schallamach waves is continued experimentally in **Chapter 6**. Recently, a transition zone between Schallamach waves and stick-slip motion was mentioned in literature (Wu-Bavouzet et al. 2007) and this chapter investigates these parallels between Schallamach waves and stick-slip motion in terms of wave frequency and wave progression velocity further. In addition, a novel form of surface instability waves for rough rubber surfaces is presented here and compared to the behaviour of Schallamach waves. This chapter contains results contributed to the paper submitted for publication by Fukahori et al. (2010).

Chapter 7 investigates the effect of surface topography under considerations of the microasperities and the slider geometry on rubber friction. The change in frictional behaviour between mirror-like smooth surfaces and rough surfaces is shown in several experiments. In addition a detailed study on the influence of the geometry of a rigid slider on the frictional force is examined and it is explained why both smooth and rough surfaces exhibit high friction.

A summary of the significant results obtained in this work is given in **Chapter 8** along with suggestions for future work.

2 Literature survey

This chapter reviews findings and fundamental concepts of rubber research given in literature, which are used in this work to examine rubber and its frictional behaviour. In the first part (Sections 2.1 to 2.4) a general introduction to elastomers and their typical properties is given, while the second part (from Section 2.5) reviews the current literature of rubber friction and raises unresolved questions on topics which are still of debate. In general, rubber friction is dependent on many parameters for example sliding velocity, temperature, contact pressure, material properties and surface geometry. Particularly the surface geometry and the macro and microscopic topography of the two bodies in contact are of paramount importance in rubber friction and are investigated in this thesis on different length-scales of interest.

2.1 History of elastomers

Already in 1600 BC latex was used by the ancient Mesoamerican Mayas to manufacture bouncing rubber balls, human figurines and rubber bands to fix stone axe heads to their handles (Hosler et al. 1999). The latex was mixed with other vegetable products, for example fruit juices, to enhance durability and elasticity. Natural rubber (NR) was first introduced to the western world in the 18th century. Joseph Priestly (1733-1804) found out in 1770, that latex has the ability to rub out lead pencil marks when dried (Morton 1987). It is believed that he introduced the eponym for the product, which is today known worldwide as rubber. In the 19th century several pioneering discoveries were made. About 1821 Thomas Hancock (1786-1865) developed a machine, the 'masticator', allowing solid natural rubber to be softened, mixed and shaped. Hancock's Scottish colleague Charles Macintosh (1766-1843) rediscovered the process of dissolving rubber in a solvent so it could be applied to cloth to make it impermeable (Brydson 1978). Unfortunately the behaviour of rubber was still influenced by environmental conditions; it turned sticky in hot weather and got stiff and brittle in cold.

In 1826, Michael Faraday (1791-1867) found out that natural rubber was a hydrocarbon of the empirical equation $(C_5H_8)_n$ (Brydson 1988).

A significant milestone for the industrial utilisation was when Charles Goodyear (1800-1860) discovered the process of vulcanisation (termed by Brockeden from "Vulcan", the God of Fire) in 1839. He accidentally found out that by heating a mixture of NR and sulphur the rubber loses its dependence on environmental conditions and becomes a tough, elastic material (Ohm 1990). The next significant milestone occurred, when John Dunlop (1840-1921) patented the pneumatic tyre in 1888 (White and De 2001). Soon the needs for NR could not be met by Brazilian plantations alone and 70,000 tree seeds were exported illegally by Henry Wickham (1846-1928) to Asia where the largest amount of natural rubber is still produced. The very useful properties of rubber have resulted in a significant amount of exploitation of workers and the large displacement of indigenous people. It is estimated that throughout history on average one death has resulted from every 130kg of raw rubber produced. This broadly translates into 15,000,000 deaths due to exploitation and adverse working conditions. In the beginning of the 20th century the demand for a synthetically produced rubber increased during the first and second world wars. Scientists like Wallace Carothers (1896-1937) made great progress in developing synthetic polymers such as Neoprene$^{®}$ or Styrene-Butadiene rubber (SBR). With the increasing amount of cars produced in the early 20th century the need for tyre research increased and it remains a large topic of scientific interest today. Approximately 70% of natural and synthetic rubber is used to manufacture tyres, which results in the rubber industry being classified as either a tyre or a non-tyre industry. One of the most fundamental aspects of (tyre) research, rubber friction, is the subject of this work.

2.2   *General introduction on elastomer materials*

Polymers which have a high elasticity and recover to their original shape after a large deformation are diversified into two classes, *thermosets* (chemically bonded) and *thermoplastics (*physically aggregated). Beside their difference in the cohesion of their molecules, the main difference is that thermosets can not be reprocessed by heat without destruction, while thermoplastics soften upon heating. Furthermore the former swell,

but do not dissolve in contact with a suitable solvent, while the latter can be dissolved in a suitable solvent. In the tyre industry, which is the major end use for rubbers, only thermosets are used, because of their superior properties in comparison to thermoplastic elastomers (TPE). For this reason TPEs are not investigated in this thesis. The terms elastomer and rubber are used from now on exclusively to describe thermosets in this work. According to the British Standard 3558-1, "an elastomer is a macromolecular material, which, after substantial deformation by a weak stress and following release of the stress, returns rapidly to its approximate initial dimensions and shape. Whereas the term rubber is defined as an elastomer, which can be, or already is, modified to a state in which it is essentially insoluble in a suitable solvent. The modified elastomer is termed a rubber and cannot be easily remoulded to a permanent shape by the application of heat and moderate pressure". The forces between the molecules have to be weak, like in a liquid, and the compound must not be highly crystalline.

Rubbers are made up of long-chained molecules. These flexible chains consist of short molecular units, called monomers, which are linked together in a process called polymerisation. In contrast to thermoplastic polymers, the flexible chains of elastomers are crosslinked with each other. This linkage is due to the vulcanisation (see also Section 3.1), where freely rotating, long-chain molecules are chemically linked with each other along their length. The three-dimensional network present in rubber prevents the molecular chains from flowing easily over each other when stressed, and help return the network to their random configuration when the stress is released. This type of elasticity is described using an entropy spring model. A typical structure of a rubber with two further magnification steps is shown in Figure 2.1, where a) shows coiled polymer chains which are cross linked at several points (Figure 2.1 b)) to build up a network when vulcanised. The molecule chains are connected to each other via a cross linking agent, shown in Figure 2.1 c) as a chain of "x", which identifies single atoms in the crosslink, for example sulphur atoms. The number of atoms in the chain can vary, changing the physical properties of the crosslink.
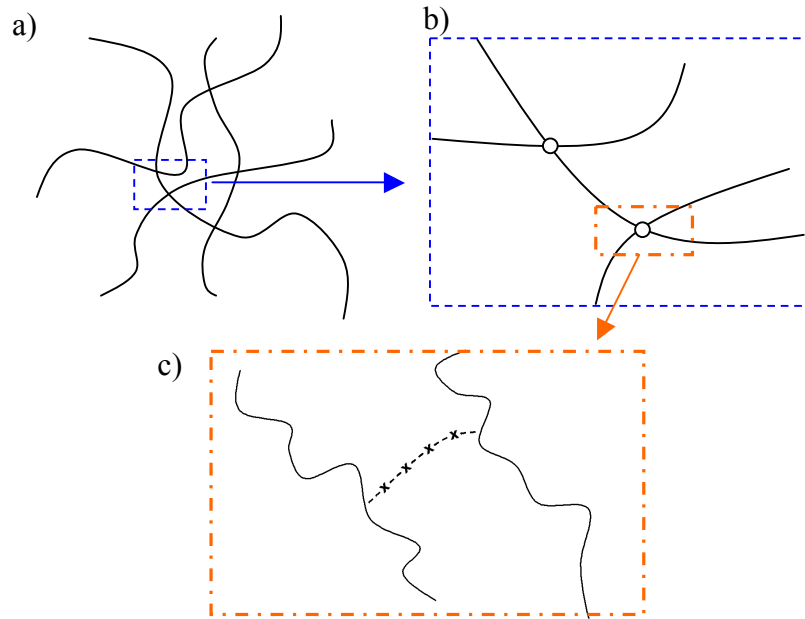
Figure 2.1: Several magnifications of a typical rubber structure. The schematic in a) shows random polymer molecules, while b) shows a magnification of the crosslink between two molecules and "o" identifies a crosslink. In c) a further magnification of this crosslink is shown, where "x" identifies an individual atom in the crosslink. Redrawn from Busfield (2010).

The increase of crosslink density increases the modulus of the rubber. However, the strength of the compound does not increase indefinitely with crosslinking. The number of crosslinks must be high enough to prevent failure by viscous flow, but low enough to avoid brittle failure (Busfield 2010). At low temperatures the amorphous polymer network is restricted in mobility and the elastomer is hard and brittle. The transition temperature, in which the elastomer changes its properties from glass-like behaviour through a leather-like state to rubbery behaviour, is denoted as the glass transition temperature, T_g. Above T_g the extension ratio can be up to 5 to 10 times larger than the original length. According to Treloar (1975) this large extensibility, exhibited under the action of comparatively small stresses, is the most important physical characteristic of an elastomer. A stress versus extension ratio curve for rubber, which is typically non-linear in shape, is shown in Figure 2.2.
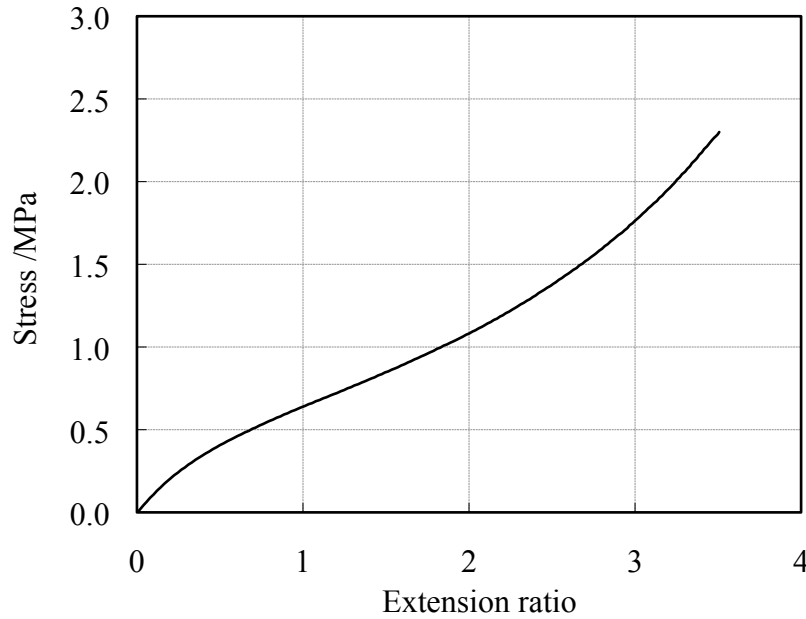
Figure 2.2: Typical, nonlinear force versus extension ratio curve for a vulcanized rubber.

A typical value for the Young's Modulus for a vulcanized rubber is around 1MPa. This modulus is very low when compared to the Young's Modulus of other solid materials for example steel, which is around $2x10^5$MPa (Treloar 1975). Due to the non-linear behaviour as shown above, Hooke's law does not apply except in a narrow region at small strains (<10%). Several approaches are available to predict the stress/strain behaviour of rubbers, some of which are explained in more detail in Section 2.3.

The most common elastomers for industrial usage are Natural Rubber (NR) and Styrene-Butadiene Rubber (SBR). Therefore, these are the materials studied in this work.

Natural Rubber (NR) and Polyisoprene (IR)

Natural rubber is an elastomer, which is extracted from latex of rubber trees (*Hevea brasiliensis*) (Hosler et al. 1999). It shares monomer chemistry with synthetically produced cis-polyisoprene (IR). Small differences in their chemical configuration (the amount of cis-configurations) gives NR a slightly lower glass transition temperature at about -75°C, whereas for IR it is around -70°C (Dick 2001). The chemical structure of NR is given in Figure 2.3.

$$CH_3$$
$$\left[CH_2\text{-}\overset{|}{C}\text{=}CH\text{-}CH_2 \right]_n$$
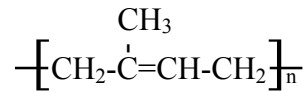
Figure 2.3: Chemical formula of isoprene (IR) and natural rubber (NR) (Hoffmann 1996).

Styrene-Butadiene Rubber (SBR)

SBR is made from the copolymerisation of styrene (usually 23%) and butadiene (usually 77%), as shown in Figure 2.4. A typical SBR has a glass transition temperature around -55°C (Gent 2001). It has a high chemical resistance against acids and bases as well as a wide range of operating temperatures (from -40°C to 70°C), making it a good material for use in car tyres. Its chemical structure is given in Figure 2.4

Butadiene unit   *Styrene unit*
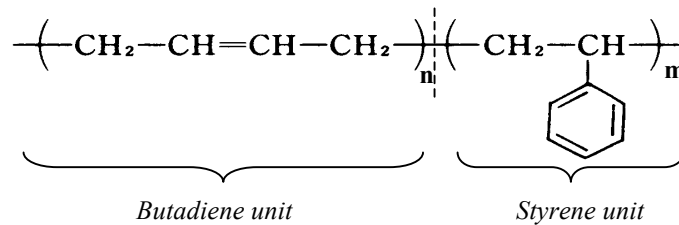
Figure 2.4: Chemical formula of Styrene-Butadiene rubber (Hoffmann 1996).

2.3 Elasticity

Two approaches to predict the mechanical behaviour of rubber are available, firstly the statistical or kinetic theory and secondly the phenomenological theory of rubber elasticity (Treloar 1975; Busfield 2000; Gent 2001). Both approaches result in the derivation of a strain (also referred to stored) energy function (SEF), which is a measure of the amount of energy stored elastically in a unit volume of rubber subjected to a specific state of strain (Busfield 2000). SEFs describe the stress/strain behaviour of a material and are used in this work as a material model in finite element analysis. The origins and derivation of the different SEFs used is explained next.

2.3.1 *Statistical theory of rubber elasticity*

Originally developed by Kuhn, this theory derives the elastic behaviour by considering the relationship between the elastic modulus and the molecular chain weight of elastomers (Kuhn 1936). A comprehensive review of the statistical theory, also known as the Neo-Hookean network theory, has been given by Treloar (1975), in which a polymer network is considered to consist of N chains per unit volume, each containing n freely jointed links of a length l_m, shown in Figure 2.5, while a chain is defined as a molecular segment between successive cross-links.
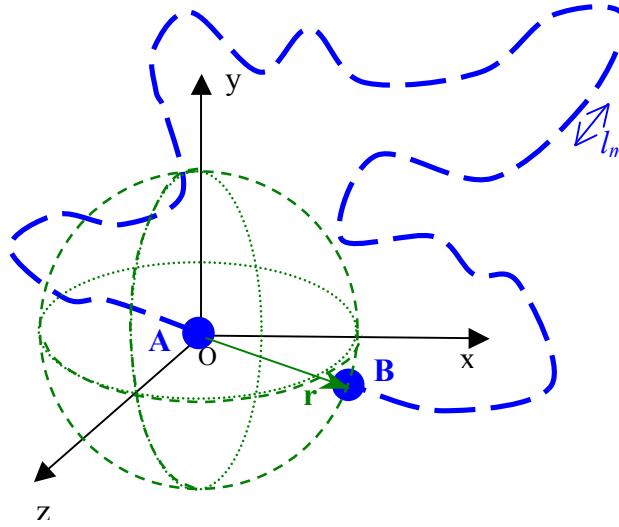
Figure 2.5: Schematic of a statistical linked polymer chain, containing *n* freely jointed links *l$_m$*. The sphere shows the statistically possible end-to-end length *r* from A to B in a Cartesian coordinate system. This modified schematic is based on Treloar (1975).

The likelihood of finding the end B of a molecular chain within a spherical distance r (shown in Figure 2.5) from its start A (at origin O of the Cartesian coordinate system), follows a Gaussian distribution and is calculated by the probability density P(r), if the number of flexible links n in the chain is sufficiently large.

$$P(r) = \left(\frac{b^3}{\pi^{\frac{3}{2}}} \right) \exp\left(-b^2 r^2 \right),$$

(2.1)

where b is considered to be a characteristic of a particular molecule. The root mean square of the end-to-end length r is given by

$$\left(\bar{r}^2 \right)^{\frac{1}{2}} = n^{\frac{1}{2}} l_m,$$

(2.2)

where n is the number of links of length l_m in the chain and

$$b^2 = \frac{3}{2nl^2}.$$

(2.3)

It is implicit that this expression is only an approximation, as it is assumed that the end-to-end length of the chain r is much less than the fully extended length ($r \ll nl_m$) (Treloar 1975). If an elastomer is subject to tensile deformation, the possible molecular conformations decrease with an increase in deformation. This results in an decrease in configurational entropy w of the network, while the internal energy is assumed to remain constant. The configurational entropy of a single chain, as shown in Figure 2.5, is defined as:

$$w = -\mathbf{k}T\ln P = \mathbf{k}Tb^2r^2,$$

(2.4)

where $\mathbf{k}$ is the Boltzmann constant and T the absolute temperature. The force F required to deform the chain in terms of end-to-end length r to a distance $r+\mathrm{d}r$ is expressed as

$$F = \frac{\partial w}{dr} = \frac{3\mathbf{k}Tr}{nl^2}.$$

(2.5)

In this statistical model a single elastomer molecule of the chain can be regarded as a spring with a stiffness being proportional to the absolute temperature and inversely proportional to the number of links in the molecule. A polymer chain network, as shown in Figure 2.1 (a) and (b), can be considered to be similar in principle to a single chain molecule so that the entropy of the whole network chains can be calculated for a given deformation. By the derivation of the free energy or the work of deformation, the stress for a given strain can be calculated. The elastically stored energy per unit volume of the rubber is derived as a strain energy function:

$$W = \frac{N\mathbf{k}T}{2}\left(\lambda_1^2 + \lambda_2^2 + \lambda_3^2 - 3\right),$$

(2.6)

where W is the elastically stored energy per unit volume, N describes the elastically active chains per unit volume and λ_1, λ_2, λ_3 are the principal extension ratios (the ratio of stretched to the unstretched length) (Treloar 1975). It is convenient to assume that for rubber incompressibility applies, so that the term $N\mathbf{k}T$ can be expressed in terms of only one physical parameter, the shear modulus G and Equation (2.6) reduces to the so-called Neo-Hookean SEF

$$W = \frac{G}{2}\left(\lambda_1^2 + \lambda_2^2 + \lambda_3^2 - 3\right).$$

(2.7)

By assuming a constant volume ($\lambda_1\lambda_2\lambda_3=1$) is maintained under strain, Equation (2.7) can be rewritten as

$$W = \frac{G}{2}\left(\lambda_1^2 + \lambda_2^2 + \left[\lambda_1\lambda_2\right]^{-2} - 3\right),$$

(2.8)

where W is a function of just two independent variables.

The above SEF fits experimental data reasonably well at an extension ratio λ between 1 and 1.3; however, at extension ratios larger than 1.3 it fails to predict the behaviour. Furthermore, the application of this theoretically derived model is not applicable to filled elastomers. Therefore, other approaches have been developed, based on either mathematical reasoning or from curve fitting of experimental observations.

2.3.2   *Phenomenological theory of rubber elasticity*

Mooney and later Rivlin (Mooney 1940; Rivlin 1948) developed the phenomenological approach of rubber elasticity to obtain strain energy functions, which reflect the experimentally observed stress/strain data of rubber. Under the assumption of an isotropic and elastic material behaviour the measures of strain can be given using strain invariants I_1, I_2 and I_3 (Mooney 1940) as

$$W = W\left(I_1, I_2, I_3\right),$$

(2.9)

where

$$I_1 = \lambda_1^2 + \lambda_2^2 + \lambda_3^2,$$

(2.10)

$$I_2 = \lambda_1^2\lambda_2^2 + \lambda_2^2\lambda_3^2 + \lambda_3^2\lambda_1^2,$$

(2.11)

$$I_3 = \lambda_1^2\lambda_2^2\lambda_3^2.$$

(2.12)

For an incompressible material I_3=1 allowing Equation (2.11) to be expressed as

$$I_2 = \frac{1}{\lambda_1^2} + \frac{1}{\lambda_2^2} + \frac{1}{\lambda_3^2}.$$

(2.13)

Mooney derived a SEF for incompressible materials given by:

$$W = C_1\left(\lambda_1^2 + \lambda_2^2 + \lambda_3^2 - 3\right) + C_2\left(\frac{1}{\lambda_1^2} + \frac{1}{\lambda_2^2} + \frac{1}{\lambda_3^2} - 3\right),$$

(2.14)

where C_1 and C_2 are elastic constants. Equation (2.14) can be rewritten in terms of the two strain invariants defined in Equations (2.10) and (2.11), so that

$$W = C_1\left(I_1 - 3\right) + C_2\left(I_2 - 3\right).$$

(2.15)

The derived function can be simplified to the Neo-Hookean SEF, shown in Equation (2.6) when C_1=G/2 and C_2=0 and this is expressed in terms of strain invariants as

$$W = C_1(I_1 - 3) \text{ or } W = \frac{G}{2}(I_1 - 3). \tag{2.16}$$

Rivlin (1956) later derived a more general SEF for incompressible materials (I_3=1) using a power series

$$W = \sum_{ij=0}^{\infty} C_{ij}(I_1 - 3)^i (I_2 - 3)^j. \tag{2.17}$$

However, Busfield (2000) showed that the derivation of coefficients for the Rivlin SEF, Equation (2.17) is complicated, as the stress terms have to be measured in two orthogonal axes independently. Depending on the strain application range the user has to decide carefully which SEF represents the expected strains most reliably.

For a pure homogenous strain, a set of relationships exist between the principal extension ratios λ_1, λ_2 and λ_3 and the true principal stresses, referred to the deformed dimensions σ_{T1}, σ_{T2} and σ_{T2} and the partial derivatives of W. The left hand side of Equation (2.18) is defined as the reduced stress (Rivlin 1956)

$$\frac{\sigma_{T1} - \sigma_{T2}}{\lambda_1^2 - \lambda_2^2} = 2\left(\frac{\partial W}{\partial I_1} + \lambda_3^2 \frac{\partial W}{\partial I_2}\right),$$

$$\frac{\sigma_{T1} - \sigma_{T3}}{\lambda_1^2 - \lambda_3^2} = 2\left(\frac{\partial W}{\partial I_1} + \lambda_2^2 \frac{\partial W}{\partial I_2}\right), \tag{2.18}$$

$$\frac{\sigma_{T2} - \sigma_{T3}}{\lambda_2^2 - \lambda_3^2} = 2\left(\frac{\partial W}{\partial I_1} + \lambda_1^2 \frac{\partial W}{\partial I_2}\right).$$

The relationship between engineering stress σ_1, relating to the undeformed state, and the true stress σ_{T1}, is given by

$$\sigma_{T1} = \frac{\sigma_1}{\lambda_2 \lambda_3}. \tag{2.19}$$

For incompressible elastomer materials, Equation (2.19) can also be expressed in terms of the engineering stress σ_i

$$\sigma_i = \frac{\sigma_{Ti}}{\lambda_i}. \tag{2.20}$$

The above relationships can be used to calculate the reduced stress σ^* for several homogenous deformation modes as shown in Figure 2.6. For an uniaxial deformation, as shown in Figure 2.6 (a), $\lambda_1 = \lambda$, $\lambda_2 = \lambda_3 = \lambda^{-1/2}$ the reduced stress term is given by:

$$\sigma^* = \frac{\sigma}{(\lambda - \lambda^{-2})} = 2\left[\left(\frac{\partial W}{\partial I_1}\right) + \frac{1}{\lambda}\left(\frac{\partial W}{\partial I_2}\right)\right], \tag{2.21}$$

for a pure shear deformation, as shown in Figure 2.6 (c), $\lambda_1=\lambda$, $\lambda_2=\lambda^{-1}$ and $\lambda_3=1$, so that the reduced stress term is expressed as:

$$\sigma^* = \frac{\sigma}{\left(\lambda - \lambda^{-3}\right)} = 2\left[\left(\frac{\partial W}{\partial I_1}\right) + \left(\frac{\partial W}{\partial I_2}\right)\right].$$

(2.22)

In simple shear deformation, shown in Figure 2.6 (b), Rivlin (1956) showed that the reduced stress, σ^* was the shear stress divided by the shear strain, thus:

$$\sigma^* = \frac{shear\ stress}{shear\ strain} = 2\left(\frac{\partial W}{\partial I_1} + \frac{\partial W}{\partial I_2}\right).$$

(2.23)

In simple shear the shear strain is related to the strain invariants I_1 and I_2 thus:

$$(shear\ strain)^2 = \left(I_1 - 3\right) = \left(I_2 - 3\right).$$

(2.24)
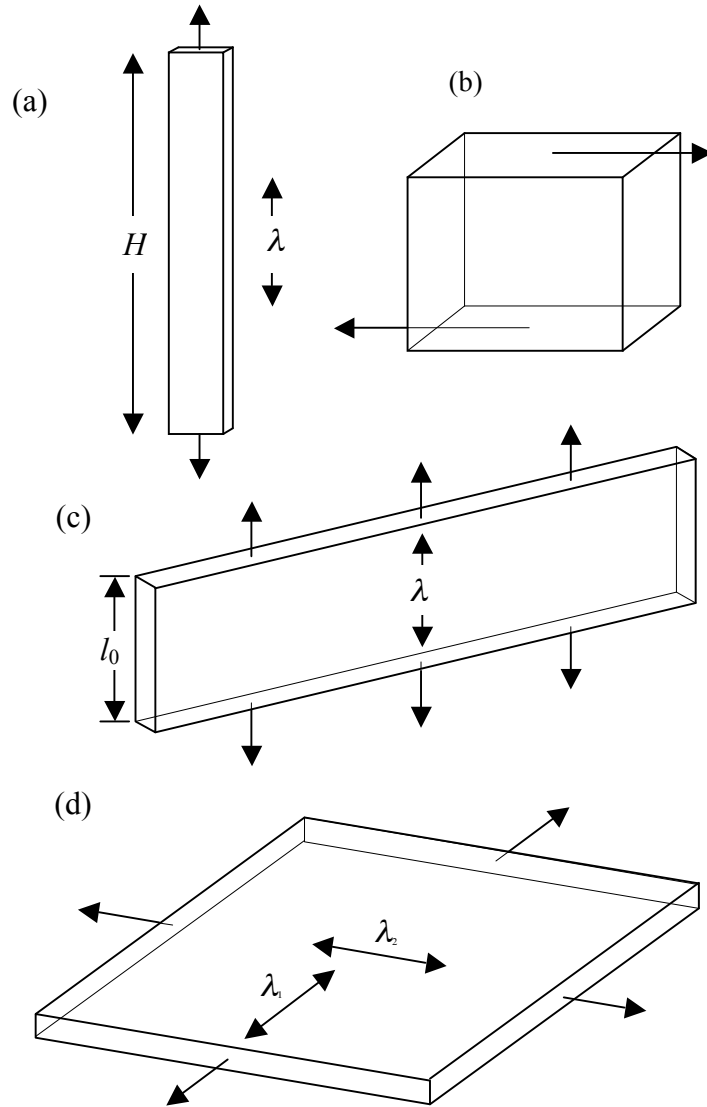
Figure 2.6: Four homogenous deformation modes, typically used for elastomer characterisation. (a) uniaxial tension, (b) simple shear, (c) pure shear and (d) biaxial tension (Ratsimba 2000).

2.4   Viscoelasticity

The previous Section 2.3 described the elastic behaviour of elastomers under the assumption of full reversibility of stress and strain and no energy dissipation. However, if an elastomer is subjected to a specific stress, its mechanical response is a combination of both characteristics, elastic solid and viscous fluid. For an ideal elastic solid, stress is proportional to strain (Hooke's law), while for an ideal fluid, stress is proportional to the rate of change in strain with time (Newton's viscosity law) (Arfken et al. 1989). Mathematically the elastic component is represented as an ideal spring with a force F

$$F = kx, \tag{2.25}$$

where k is the stiffness of the spring and x displacement (Hutchings 1992). Alternatively, Equation (2.25) may be expressed as:

$$\sigma = E\varepsilon, \tag{2.26}$$

where σ is the tensile stress, ε the tensile strain and E the elastic modulus. Fluids obeying Newton's viscosity law may be idealised as a dashpot and described as:

$$F = c\left(\frac{\partial x}{\partial t}\right), \tag{2.27}$$

where c is a viscous damping coefficient (Aklonis and MacKnight 1983). In terms of the tensile stress, Equation (2.27) can be rearranged as:

$$\sigma = \eta_c\left(\frac{\partial \varepsilon}{\partial t}\right), \tag{2.28}$$

where η_c is the viscous damping coefficient in tension. The viscoelastic behaviour of elastomers are often described as an array of springs and dashpots, either in series or in parallel, known as Maxwell or Voigt elements, shown in Figure 2.7 (Gent 2001).
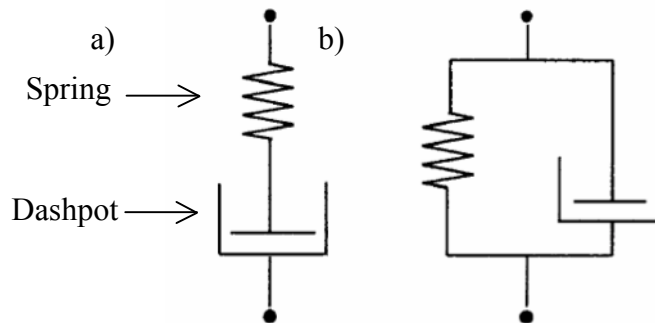
Figure 2.7: Spring and dashpot models of viscoelastic materials as a) Maxwell model in series and b) Voigt model in parallel (Gent 2001).

Both, Maxwell and Voigt models, can be characterised by a relaxation time

$$t = \frac{\eta_c}{E},$$

    (2.29)

while the former is usually used to describe stress relaxation experiments the latter describes creep experiments more satisfactorily. The strain can be calculated using a Maxwell model as

$$\varepsilon = \varepsilon_0 + \frac{\sigma\, t}{\eta_c},$$

    (2.30)

and for the Voigt model as

$$\varepsilon = \frac{\sigma_0}{E}\left[1 - \exp\left(\frac{-t}{t_0}\right)\right].$$

    (2.31)

Further examples of time dependent behaviour are stress relaxation and creep: When an elastomer is held at a fixed displacement, the amount of stress decreases with time (stress relaxation) and if it is subjected to a fixed load, the length increases over time (creep). The behaviour is further complicated when an elastomer is periodically deformed at a fixed amplitude, as cyclic stress softening occurs, due to the breaking of weak chains, crosslinks or filler-rubber network (Mullins effect) (Mullins 1969; Machado et al. 2009). The impact of hysteresis in rubber friction is discussed further in Section 2.5.4.

2.4.1 *Hysteresis*

When an ideal elastic material is subject to a deformation it fully recovers to its undeformed state as soon as the force is removed, while all energy in the system is regained. Rubber materials, however, dissipate energy due to internal viscoelastic energy dissipation mechanisms when deformed, which is one of the major sources of rubber friction. A typical loading and unloading curve for a carbon black filled rubber, emphasizing the non-linearity of an elastomer, is shown in Figure 2.8.
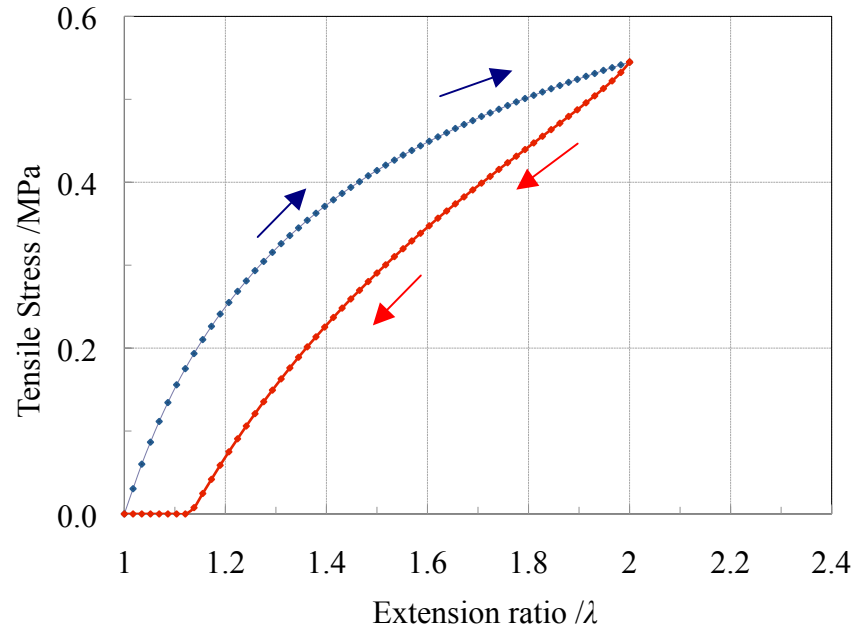
Figure 2.8: Loading and unloading curve for a carbon black filled SBR dumbbell specimen. The specimen, with a length of 25mm, was strained up to 100% at 1mm/s strain rate. The area between the blue loading curve and the red unloading curve is a measure of dissipated energy.

While the area under the loading curve and x-axis is proportional to the energy input, the area under the unloading curve relates to the recovered energy. The area between both curves is the dissipated energy or hysteresis loss, which is the main heat source for the temperature rise in a tyre (Lin and Hwang 2004). This dissipated energy has a major contribution to rubber friction and is further described in Section 2.5.4. According to Figure 2.8 hysteresis is, therefore, defined as the ratio of lost energy and the total (input) energy:

$$\text{Hysteresis} = \frac{\text{Lost energy}}{\text{Initial energy}}.$$

(2.32)

2.4.2   Dynamic mechanical properties of elastomers

While the elastic modulus E or the shear modulus G refer to quasistatic measurements, it is convenient to introduce the dynamic mechanical modulus when cyclic motions of stress and strain occur. For cyclically loaded elastomers, the strain lags somewhat behind the stress due to the materials viscosity. The response to dynamic loading can be represented by the complex modulus E^*, consisting of the storage modulus E' and the

loss modulus E''. While E' is a measure of elastically stored energy during deformation, E'' is a measure of the energy converted to heat (Sperling 2001). Representing the immediate response to an applied force, the storage modulus is an in-phase component, whereas the loss modulus represents the response with a time lag ($\pi/2$), being an out-of-phase component. The magnitude of the complex modulus can be derived from Figure 2.9 as

$$E* = \sqrt{(E')^2 + (E'')^2} \, ,$$

(2.33)

so that the loss angle tan δ can be derived as

$$\tan\delta(f,T) = \frac{E''}{E'} \, .$$

(2.34)
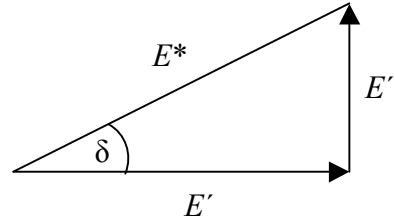
Figure 2.9: The relationship between $E*$, E' and E''.

An example of a typical graph showing E', E'' and tan δ is given in Section 3.2.3. tan δ is of great importance to rubber friction as it gives a measure of the internal friction or damping, relating the dynamic properties of for example a tyre compound to its friction or rolling resistance performance. However, a full analysis of the performance of rubber compounds is not easy to measure at extreme temperatures or at very high frequencies in laboratories. Thus a relationship between temperature and excitation frequency was proposed by Williams, Landel and Ferry (WLF) (1955), in which the introduction of the free volume and chain mobility concepts emphasised the ability of a polymer matrix to rearrange within a shorter period of time when temperature increases (Le Gal et al. 2005). This relationship is used here to predict rubber friction behaviour using test results made under easier test conditions. The WLF time-temperature superposition principle relates a change in temperature to a shift in either the time or the frequency scale. It can be applied to general measurements of time or temperature dependence as well as, for example to rubber friction (Grosch 1963). It is, therefore, possible to determine a material behaviour at a small frequency range over a large temperature

range, by shifting single curves along the time scale into one master curve. The temperature dependent shift factor a_T can be expressed as:

$$\log_{10} a_T = \frac{-C_{W1}(T - T_s)}{C_{W2} + T - T_s},$$

(2.35)

where T is the test temperature and T_s is a reference temperature. Initially, C_{W1} and C_{W2} were thought to be universal constants with the reference temperature defined as

$$T_s = T_g + 50\,°C.$$

(2.36)

However, studies have shown that C_{W1} and C_{W2} are polymer dependent constants with values for example for natural rubber 8.86 and 101.5 respectively (Ferry 1961; Tanner 2000). The WLF time-temperature superposition is reported to be applicable to most amorphous polymers in the range of their glass transition T_g up to T_g + 100°C. Examples for WLF time-temperature superposition can be found in Section 2.5.5. The WLF equation is based on the semiemperical Doolittle equation for the viscosity η of a liquid, which has been found to express the viscosity of simple liquids with a high degree of accuracy and is given as

$$\ln \eta = \ln C_A + C_B \left(\frac{V - V_f}{V_f} \right) \quad ,$$

(2.37)

where C_A and C_B are constants, V is the total volume of the system and V_f is the free volume available to the system (Shaw and MacKnight 2005). It is interpreted that the viscosity is intimately connected with mobility, which is closely related to the free volume. When the free volume increases, the viscosity decreases. Equation (2.37) can be rearranged as

$$\ln \eta = \ln C_A + C_B \left(\frac{1}{f_V} - 1 \right) \quad ,$$

(2.38)

where f_v is the fractional free volume V_f/V at a temperature T. When the region above T_g is considered, it can be assumed that the fractional free f_V volume increases linearly with temperature, so that

$$f_V = f_g + a_f(T - T_g),$$

(2.39)

where f_g is the fractional free volume at T_g and α_f is the coefficient of thermal expansion of f_V above T_g. In terms of Equation (2.39) the Doolittle Equation (2.38) becomes

$$\ln \eta(T) = \ln C_A + C_B \left(\frac{1}{f_g + a_f(T - T_g)} - 1 \right) \quad , \text{ at } T > T_g$$

(2.40)

and

$$\ln \eta(T_g) = \ln C_A + C_B \left(\frac{1}{f_g} - 1 \right) \quad , \text{ at } T_g.$$

(2.41)

Subtraction of Equation (2.41) from (2.40) yields to

$$\ln \frac{\eta(T)}{\eta(T_g)} = C_B \left(\frac{1}{f_g + a_f(T - T_g)} - \frac{1}{f_g} \right) ,$$

(2.42)

which simplifies to

$$\ln \frac{\eta(T)}{\eta(T_g)} = \log a_T = -\frac{C_B}{2.303 f_g} \left(\frac{T - T_g}{(f_g / a_f) + T - T_g} \right) ,$$

(2.43)

which is identical to the WLF Equation (2.35) when C_{W1} is defined as $C_B/2.303f_g$ and C_{W2} is defined as f_g/a_f.

2.5 Friction

Friction is a restraint of relative motion between two contacting bodies. The phenomenon of friction, whether desired or not, is present in most engineering applications. For example roller bearings are intended to reduce friction, while the friction in a breaking system should be as large as possible when the brake is operated. The following sections give an overview on general friction and a detailed analysis of state of the art of rubber friction.

2.5.1 Introduction and history of tribology

Moving large stones was only possible by reducing friction with roller bearings and lubricants, in ancient times (~2400 BC). Leonardo da Vinci (1452-1519) is thought to be the first person to describe the phenomenon of friction scientifically, by experiments on objects being moved over a surface, as shown in Figure 2.10.
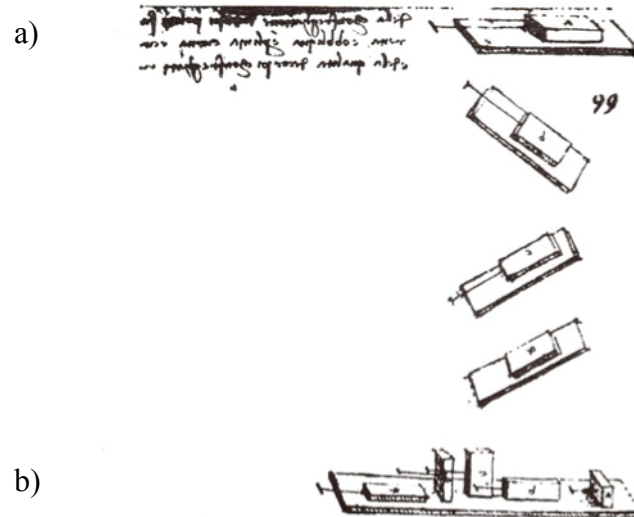
Figure 2.10: Experimental setup for Leonardo da Vinci's experiments on friction. In a) the determination of friction at different angles is shown, while b) shows experiments on the influence of the area of contact on the frictional force (Meyer et al. 1998).

Two laws postulated by Leonardo da Vinci were later reinforced by Guillaume Amontons (1663-1705) observations:

1. The frictional force F_F is proportional to the normal load F_N.

2. The frictional force F_F is independent of the area of contact A_0.

Both laws are still a good approximation for solids (Bowden and Tabor 1973). A sketch of Amontons' apparatus for measuring friction between two materials is shown in Figure 2.11:
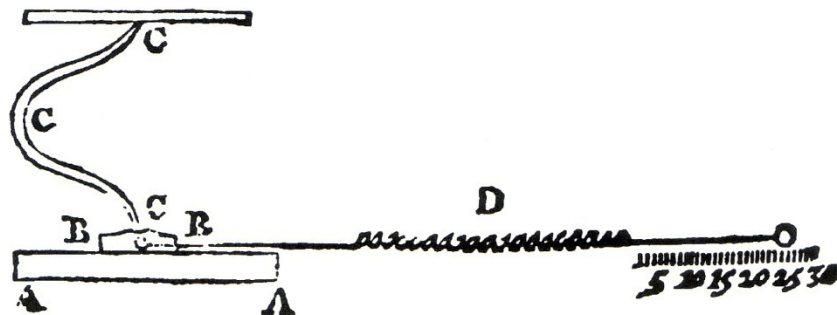
Figure 2.11: Experimental setup for Amontons' experiments on friction. A test body "B" contacts a surface "A", while a spring "C" is used to apply a normal force, acting perpendicular to force of spring "D", which is used for measuring the frictional force during the sliding process (Dowson and Higginson 1977).

Another scientist, Leonhard Euler (1707-1783), contributed to the understanding of frictional processes by firstly distinguishing between static and kinetic friction (Meyer et al. 1998). The static friction force is defined as the force required to put a body into motion, whereas the kinetic friction force is required to maintain a body in motion, as is shown in Figure 2.12. In (rubber) friction applications the static force is either equal to or higher than the kinetic friction force, as given in Equation (2.44).

$$F_{Static} \geq F_{Kinetic} \tag{2.44}$$
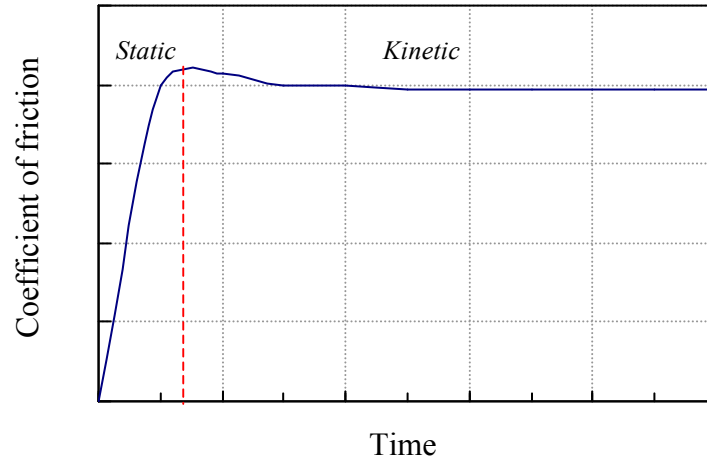
Figure 2.12: Schematic friction graph. The coefficient of friction increases up to a point until the static force is reached and then kinetic sliding occurs.

A former Russian student of Euler, Semen Kirilovich Kotel'nikov (1723-1806) is credited with adopting the Greek letter μ to represent the friction coefficient (Dowson and Higginson 1977). Kotel'nikov and Charles-Augustin de Coulomb (1736-1806) both developed independently from each other an equation to calculate friction, which was later credited only to Coulomb as 'Coulomb friction', given in Equation (2.45). The friction resulting from two moving surfaces, as shown in Figure 2.13, can be expressed as the coefficient of friction μ, which is a dimensionless variable relating the frictional force F_F, acting parallel to the surface, and the perpendicular normal force F_N.
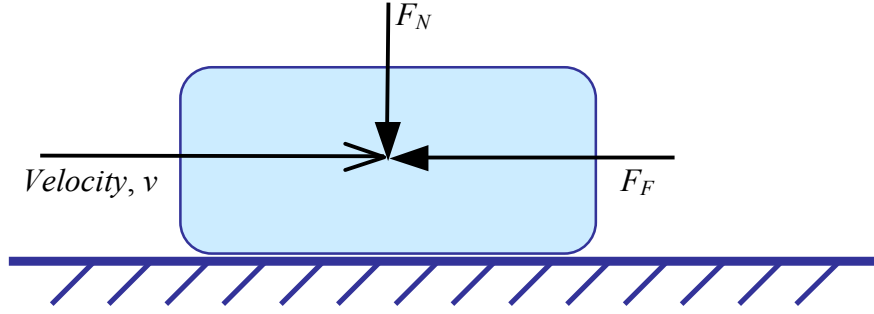
Figure 2.13: Basic principle of friction. A rectangular body, loaded with the normal force F_N is moved over a surface with a certain velocity. The frictional force F_F is acting against the movement of the sliding body.

While solids like metals obey this law with virtually no dependence on velocity or temperature, Equation (2.45) is not directly applicable to elastomers due to their viscoelastic nature (Bowden and Tabor 1954; Bowden and Tabor 1973; Grosch 2007).

$$\mu = \frac{F_F}{F_N}.$$

(2.45)

2.5.2   Rubber friction

The very low elastic modulus and the high internal friction of rubbers over a wide range of frequencies are both reasons for the difficulties encountered in the use of Amontons' friction laws in rubber friction (Persson 1998). Therefore, rubber friction is commonly described as a contribution of different factors, which form the frictional force F_F (Kummer 1966):

$$F_F = F_{ADHESION} + F_{HYSTERESIS} + F_{VISCOUS} + F_{COHESION}.$$

(2.46)

The adhesion term ($F_{ADHESION}$) is a surface effect resulting from the intermolecular interaction between two surfaces (Roberts and Thomas 1975) and the hysteresis term ($F_{HYSTERESIS}$), sometimes referred to as the deformation contribution, results from the irreversible viscoelastic energy dissipation through the bulk deformation of a certain volume of rubber (Grosch 1963; Roberts 1992). When lubricated, an additional factor $F_{VISCOUS}$ contributes to the reduction of the frictional force, due to the viscous shear of a fluid at the interface. In case the rubber loses contact with the surface completely

(aquaplaning), the frictional force is given by shear viscosity of the fluid alone. In case of abrasion a fourth cohesive factor ($F_{COHESION}$) is defined, due to the additional energy lost from crack initiation and wear (Southern and Thomas 1978; Fukahori and Yamazaki 1995). Complicating matters further, the four factors are not independent of each other, but are subjected to interaction as shown by Schallamach in Bateman (1963) and Muhr and Roberts in Roberts (1988).

Assuming a dry, smooth contact with reasonably low shear forces, hence no contributions from lubrication and wear, the total frictional force is considered to reduce to a combination of adhesion and hysteresis (Tabor 1960) and is given as:

$$F_F = F_{ADHESION} + F_{HYSTERESIS} \,. \qquad\qquad \textbf{(2.47)}$$

Moreover, suitable modification can reduce one or other of the two terms and, therefore, can change their ratio significantly. For example Fuller and Tabor (1975) as well as Persson (2001) have stated that adhesion is negligible for rough interfaces, as experienced in the tyre / road contact, so that the hysteresis term alone is the major contribution to the frictional force. In contrast, it is shown that adhesion is the main influence on rubber friction for very smooth contact situations (Roberts and Thomas 1975) and the hysteresis influence diminishes. For this reason the question arises, is it possible to describe the complexity of rubber friction by just a single term? If not, how might additional factors such as an entirely geometric contribution to the frictional sliding force, which are not encountered in Equation (2.46), contribute to the mechanics of rubber friction? This question is addressed further in Chapter 4.

An overview on the parameters influencing the frictional behaviour of rubber is given in Table 2.1 and the different parameters are discussed in the following sections: The contributions from adhesion at smooth surfaces and hysteresis at rough surfaces are discussed in Sections 2.5.3 and 2.5.4, while lubrication and abrasion are covered in Sections 2.5.8 and 2.5.9 respectively. A summary of several approaches unifying friction theories is given in Section 2.5.7.

Table 2.1: Factors influencing the frictional behaviour of rubber (Blau 2001).

Category	Factor
Material properties	Stiffness, elasticity and characteristic properties of a material.
	Ageing properties of the material.
Contact geometry	Conformity of the components (macro-scale mating of shapes).
	Apparent and real area of contact between the sliding bodies.
Surface geometry	Surface roughness and waviness (micro-scale features, asperity shapes, size distributions).
	Surface lay (directionality) with respect to relative motion.
Relative motion	Constancy of motion (accelerations, pauses, start-stop).
	Magnitude of relative surface velocity.
Applied forces	Magnitude of the normal forces (contact pressure).
	Constancy of applied forces.
	Adhesional forces resulting from surface energy.
Temperature	Thermal effects on material properties (thermo elastic instabilities).
	Friction induced temperature rise between the sliding objects.
Lubrication	Formation of friction-altering films (film thickness).
	Viscosity of lubricant (temperature and pressure dependence).
	Characteristics of particles entrained in the lubricant.
	Debris created by abrasion of one ore both of the surfaces.
Stiffness and vibrations	Contact compliance (stick-slip).
	Damping of frictional or external vibrations.
	Feedback between frictional stimulus and structural response.
Wear	Formation of wear patterns and the creation of debris.

2.5.3   Adhesion and frictional sliding on smooth surfaces

Static adhesion

Investigating static adhesion, Johnson, Kendall and Roberts (JKR) (1971) examined adhesion between an optically smooth rubber sphere and an optically smooth flat surface. It was shown in their experiments that two unloaded bodies were drawn into intimate contact by short-range surface forces enabled by the high elasticity of rubber, resulting in an increase in the area of contact. A certain force had to be applied to pull both bodies apart (Johnson et al. 1971), which was determined by the viscoelastic

response of the elastomer. From their findings, adhesion can be described as an intermolecular process at the interface, dependent on surface energies. The JKR approach is further discussed in Section 2.5.4. Extending the pioneering work of JKR, Roberts and Thomas (1975) related the adhesional work to the rate dependent peel energy, which was necessary to pull both surfaces apart. Further experiments in their study showed the large influence of rubber adhesion by using a small steel ball, which, when dropped on a rubber surface, rebounded if the surface was dusted but adhered without rebound on a clean surface. Consequently, lubrication (either liquid or solid in the form of powders) decreases adhesion, preventing the formation of intimate contact patches required to form intermolecular bonds. Lubrication is further discussed in Section 2.5.8.

Dynamic adhesion

When the dynamic contact between two smooth surfaces is considered, intimate contact patches between both surfaces constantly change within the contact area due to the relative displacement between both surfaces. By this a cyclic formation and breakage of molecular bonds between polymer chains and surface asperities are induced and associated with the dissipation of energy (Le Gal 2007). Schallamach developed a molecular mechanism describing this relative displacement mechanism. His displacement model for a single rubber polymer chain of a soft rubber in contact with another smooth, rigid surface in dynamic adhesion is schematically shown in Figure 2.14 (Schallamach 1963) and is still thought to be valid today (Persson and Volokitin 2006):
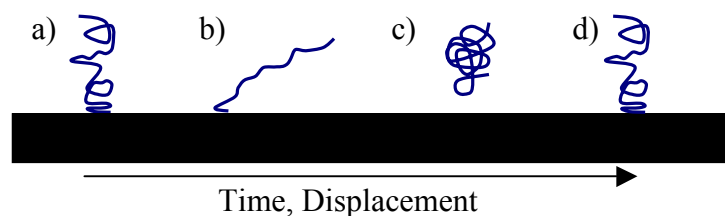
Figure 2.14: The stick-slip transition of a single rubber chain is shown when relative displacement occurs. The rubber chain a) sticks to the surface, b) stretches with increasing time, c) detaches from the surface and relaxes and d) reattaches to the surface to repeat the cycle. [Redrawn from (Schallamach 1963)].

A single rubber chain on the rubber surface is considered, which is in intimate contact with the rigid surface in a). When both surfaces are displaced relatively to each other, as shown in b), the adhering rubber chain is stretched. Due to this deformation the area of contact decreases, resulting in a decrease in adhesional force. When the rubber chain is considered to be an entropic spring according to rubber elasticity, the retraction force increases with deformation, so that if the adhesion force at the interface is less than the retraction force the rubber chain detaches from the surface and relaxes. Marking the end of the cycle the rubber reattaches at a new location, as is shown in d), and the cycle is repeated. Depending on the surface finish (smooth or rough), the rubber is either in intimate contact or only partially contacting the rigid surface, determining the amount of adhesional force resisting to relative displacement. For optically smooth and dry surfaces the adhesional part of the total rubber friction, as defined in Equation (2.46), is a dominant factor in sliding friction (Persson and Volokitin 2006).

Stick-slip motion

Based on the frequency independent displacement model proposed by Schallamach (1963), shown in Figure 2.14, the viscoelastic properties of the rubber and the surface topography determine different modes of this relative displacement at the interface. While at very low sliding velocities for both, smooth and rough surfaces the relative displacement is promoted by a constant unpeeling and re-adhesion processes between both surfaces, at higher sliding velocities different forms of surface instabilities promote relative displacement. For smooth interfaces wave-like wrinkles on the rubber surface, commonly described as Schallamach waves, are present over a broad range of sliding velocities, which are discussed further in Section 2.5.6 and which transform into so-called stick-slip motion at high sliding velocities. This matter is further examined experimentally in Chapter 6. For rough surfaces stick-slip motion is the only surface instability considered to provide relative motion. In stick-slip motion, occurring for both, smooth and rough interfaces the displacement results from the cyclically detachment and reattachment of the two surfaces at high frequencies. When in contact, no relative motion occurs at the interface (stick stage), whereas in the second stage relative sliding (slip stage) at the interface occurs, when a critical shear deformation is met.

Fukahori and Yamazaki (1994a) followed by Coveney and Menger (1999) investigated the stick-slip behaviour of a sliding rubber using an accelerometer to detect the time dependent periods of acceleration (slip) and zero displacement (stick). Their findings are shown in Figure 2.15, where a) shows the frictional force $F_F(t)$ for a normal load of 4 N and b) shows the acceleration. Graphs c) and d) show equivalent results for a normal load of 8 N. The 'stick' phase is marked as (I) and 'slip' is denoted as (II).
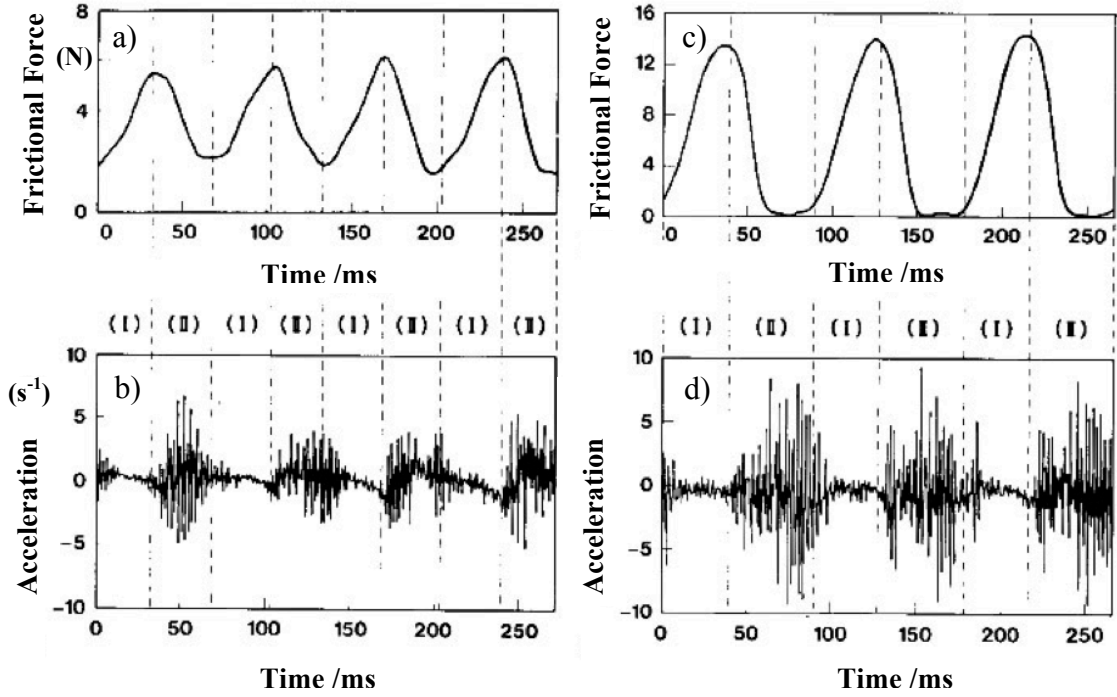
Figure 2.15: The change in frictional force and acceleration induced by stick-slip behaviour is shown. Graphs a) and b) (left) show the frictional force and acceleration for F_N=4N, while c) and d) (right) show the data for F_N=8N. In stage (I), marking the stick-stage, the frictional force increases until the critical shear stress for slippage is met and the rubber slips in stage (II). The acceleration increases only in stage (II) (Fukahori and Yamazaki 1994a).

Figure 2.15 shows the frictional force alters periodically due to the stick-slip motion. The acceleration measured at the slider in the slip-phase (II) corresponds well with the decrease in frictional force. The slippage causes the previously compressed rubber to relax partially and this induces a micro-vibration, which correlates with the natural resonance frequency of rubber. This micro vibration is similar in nature to a guitar string, which resonates at a high frequency, after it has been plucked. It was shown that when a rigid slider moves over a rubber surface, two kinds of vibration are generated: One being stick-slip motion in the range of 1-20Hz and the second being micro-vibrations in the range of 500-1000Hz (Fukahori and Yamazaki 1994a). When the frequency of stick-slip motion is considered, the mechanical resonance of the system

plays a significant role. If both frequencies are nearly the same the system can get into a highly excited resonance mode (Persson 2001b). For example the squealing noise of windscreen wipers indicate stick-slip motion at a very high frequency. The different frequencies encountered by stick-slip motion also depend on the surface finish at the interface and can result in either relatively smooth sliding or the catastrophic loss of contact (chattering). For example, when heavy stick-slip motion is experienced, the rigid slider may experience an uplift that changes periodically the vertical position together with the periodic stick-slip motion, moving upwards in the slip stage and downwards during the stick stage as is shown schematically in Figure 2.16.
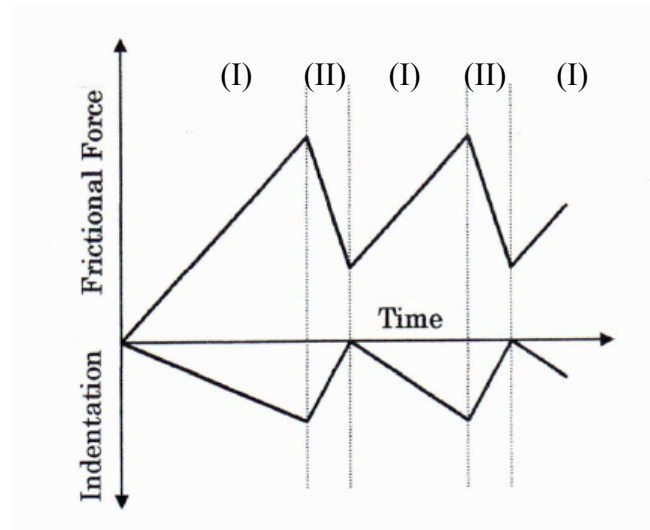
Figure 2.16: The slider is displaced vertically while horizontally sliding on a rubber block. The change in indentation correlates to a change in frictional force during the stick-phase (I) and slip-phase (II) (Fukahori et al. 2010).

Recently, a transition zone between Schallamach waves and stick-slip motion has been described briefly by Wu-Bavouzet et al. (2007) for smooth surfaces, as shown in Figure 2.17. This existence of this transition zone implies that Schallamach waves may affect the (coinciding) stick-slip motion. In their phase diagram Schallamach waves occur at low sliding velocities and positive normal loads, while stick slip occurs only at higher velocities. What is still not clear is how far this transition zone is affected by wave frequency and the wave progression velocity of Schallamach waves. This question is investigated further in chapter 6.
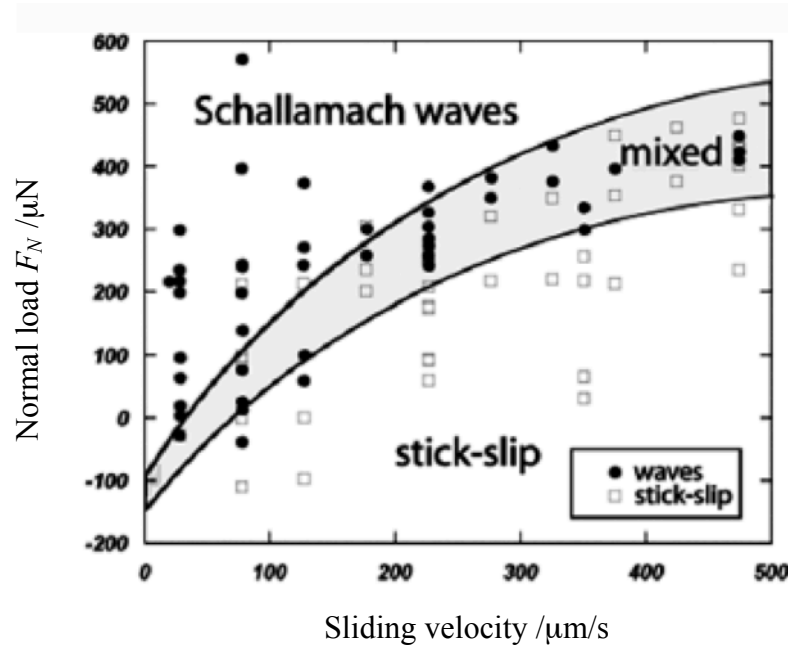
Figure 2.17: Phase diagram for frictional force F_N versus sliding velocity of a soft rubber lens (R=1mm) on a glass plate. The rubber used here is a Polydimethylsiloxane rubber with a Young's modulus of 0.1MPa (Wu-Bavouzet et al. 2007).

2.5.4   Hysteresis and frictional sliding on rough surfaces

In tribology research it is often distinguished between the nominal area of contact and the real area of contact. Even a surface that appears smooth to the eye on a macroscopic scale contains surface asperities on a microscopic scale. The resulting real area of contact between two bodies is, therefore, often significantly smaller than assumed, as contact patches are usually formed only at the top of surface asperities. Since the real area of contact is dependent on the length scale of interest, it is very difficult to give a value for it. For example, the nominal area of contact between a tyre and the road surface has a value around 10.000 mm² per tyre, whereas the real area of contact is around 18% of this (Bachmann 1998). Using a pressure sensitive contact film the real area of contact was measured, showing that contact is made only in discrete patches rather then as an interconnected region (Eichhorn 1993; Bachmann 1998). The real area of contact was measured for different surfaces by Bachmann, who showed that with increasing smoothness of the surface the values for the real area of contact range from 5% to 35% of the nominal area of contact (with an average of 18%). An example is shown in Figure 2.18.

Figure 2.18: The real area of contact between a passenger car tyre and a road surface was measured via a pressure sensitive film (Bachmann 1998).

In order to give an estimate of the real area of contact, most contact theories are based on the basic consideration of (static) contact mechanics firstly derived by Hertz (1896). The Hertzian contact theory describes the elastic contact of two smooth spheres, as shown in Figure 2.19.
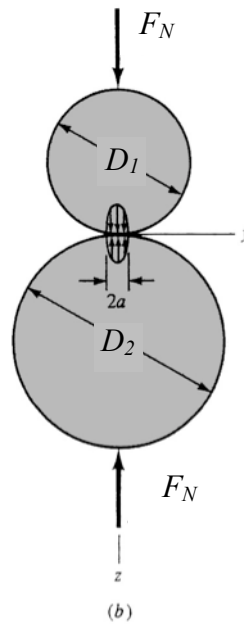
Figure 2.19: Schematic figure showing the elastic contact between two spheres proposed by Hertz. Two spheres are in contact and a normal load F_N is applied. The area of contact for both spheres with diameters D_1 and D_2 has a width of $2a$. The distribution of the contact pressure has an elliptical distribution at the face of the contact (Shigley and Mischke 1989).

The shown radius of contact *a* can be calculated by using the elastic Hertzian theory (Shigley and Mischke 1989) as

$$a = \sqrt[3]{\frac{3F_N}{8} \frac{(1-\rho_1{}^2)/E_1 + (1-\rho_2{}^2)/E_2}{1/D_1 + 1/D_2}} \; , \tag{2.48}$$

where F_N is defined as the applied load, ρ_i are the two Poisson's ratios, E_i the two values of Young's modulus for each sphere, and D_i gives the diameter of each sphere. Several conditions are required for this equation to apply including the dimensions of the contact area being small compared to the dimensions of each body (Johnson 1985). Also the Hertzian contact theory is only valid for frictionless, small linear elastic deformation (Hertz 1896). Great care has to be taken, if this theory is applied to low modulus materials like rubber, where deformations can exceed the restriction of a small strains theory. For the case of a sphere contacting a flat surface, the diameter of the latter can be assumed to be infinite ($D_1=\infty$). In addition, if one of the materials has a much higher modulus than the other, with $E_1 \gg E_2$ (for example steel compared to rubber) the deformation of the stiffer sphere becomes negligible (Tatara 1993) and, therefore, Equation (2.48) can be simplified as:

$$a = \sqrt[3]{\frac{3DF_N(1-\rho^2)}{8E}} \; , \tag{2.49}$$

The pressure *p* in Figure 2.19, in each sphere has a semi elliptical distribution with the maximum at the centre of the contact area (see also Figure 2.23), which can be expressed as:

$$p_{\max} = \frac{3F_N}{2\pi a^2} \; . \tag{2.50}$$

However, it was found by Johnson, Kendal and Roberts (JKR) (1971) that for small loads the contact area between two smooth elastic bodies is significantly larger than predicted by the Hertzian contact theory, as shown in Figure 2.20.
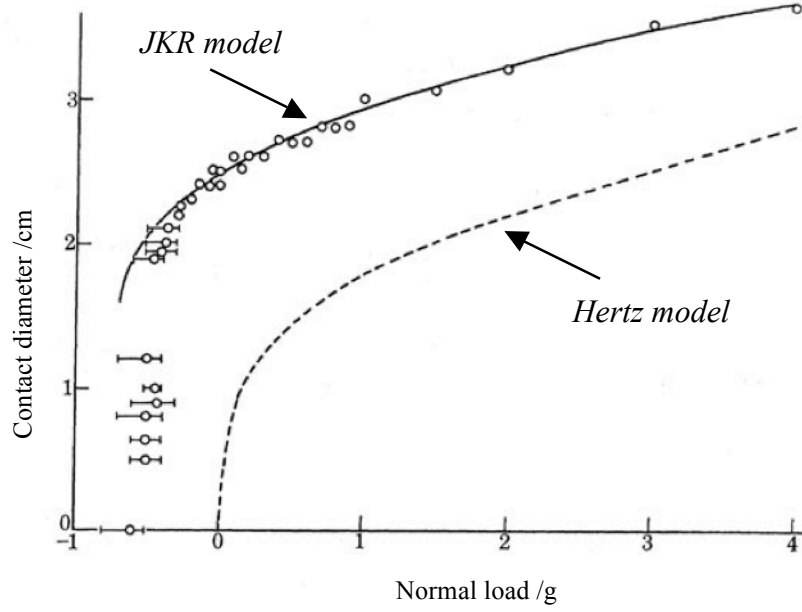
Figure 2.20: Experimental data points of the contact diameter of two contacting rubber spheres (*R*=22mm) compared to the contact diameter prediction by the JKR and the Hertz contact model. (Johnson et al. 1971)

They proposed the JKR model, which includes an adhesion contribution that was ignored in the Hertzian model. The radius of contact *a* between a sphere and a flat sheet is now given by

$$a^3 = \frac{R}{K}\left(p + 3\gamma\pi R + \sqrt{\left(6\gamma\pi Rp + \left(3\gamma\pi R\right)^2\right)} \right), \tag{2.51}$$

where γ is the surface energy, *K* is related to the elastic constants and *R* is the radius of the sphere. It is worth pointing out that if no load is applied, the contact area is not zero as suggested by Hertz, but Equation (2.51) reduces to

$$a^3 = R(6\gamma\pi R)/K, \tag{2.52}$$

so that a force has to be applied to break the contact between two bodies. This approach has also been adopted by Derjaguin et al. (1975) and Bradley (1992).

For a surface with a certain roughness, expressed as a (random) distribution of surface asperities, these theories for smooth surfaces have to be modified. Greenwood and Williamson (1966) described a contact theory depending on the surface topography distinguishing between plastic and elastic deformation. In their work they examined a smooth and a rough surface in contact as shown in Figure 2.21:
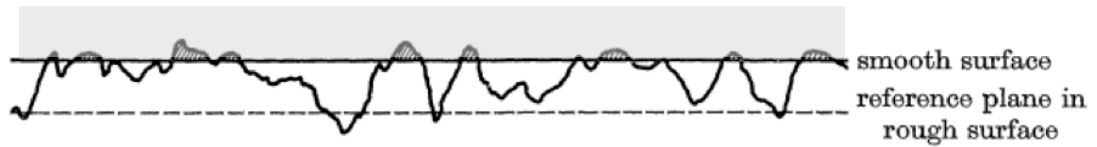
Figure 2.21: Contact of a smooth and a rough surface. The load is supported by the shaded asperities, which have a height greater than the separation between the reference plane (Greenwood and Williamson 1966).

Their theory assumed that the surface asperities all have the same radii in their summits with a random distribution in heights. Persson (2001c) extended this theory to include surface roughness at any length scale. Figure 2.22 shows a rubber block squeezed onto a substrate with roughness over two length scales (Persson 1998; Persson 1999; Persson 2001c). The rubber fills out a long-wavelength roughness profile, while it is not squeezed into the small-wavelength profile, especially at the bottom of the profile, where the pressure acting on the rubber is much smaller than at the top of the asperities.
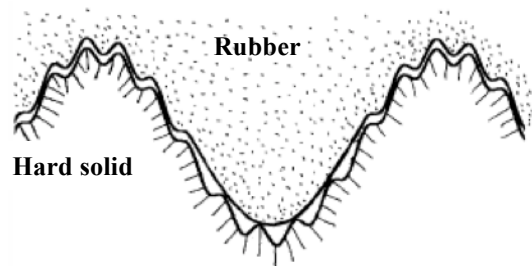
Figure 2.22: Schematic figure for a rubber block squeezed against a hard solid with surface asperities of two length scales (Persson 2001b).

Therefore, when a rubber block slides over a rigid, rough substrate, as in Figure 2.22 or as is the case of a tyre on a road, it is excited periodically by the deformation process of rough asperities, which lead to energy dissipation due to internal damping in the rubber material (Palasantzas 2005). Adhesional influences are thought to be negligible in a tyre/road contact (Persson 2001b), so that the resulting frictional force is often assumed to be almost entirely characterised by internal losses ($F_{HYSTERESIS}$) in the rubber (Persson 1998; Klüppel and Heinrich 2000). If the relative sliding velocity increases, the excitation of the rubber by surface asperities occurs at a higher frequency, so that the time available for the rubber to relax after the deformation decreases, and the elastic modulus increases. Therefore, it is likely that both the indentation depth as well as the

real area of contact decrease. This is schematised in Figure 2.23 for the same friction interface for two different sliding velocities, where velocity v_2 is larger than v_1.
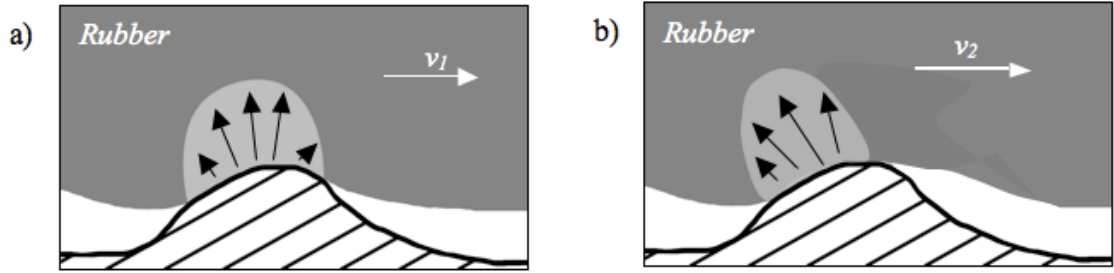
Figure 2.23: Schematic figure of a rubber (top) deformed by and sliding over a surface asperity. The main dissipation occurs in the volume element highlighted in grey, while sliding velocity v_1 in a) is lower than sliding velocity v_2 in b). Modification of (Persson 1998).

To complicate matters further, many length scales have to be taken into consideration for so-called self-affine surfaces, which are defined as self-affine, if a similar surface morphology is observed irrespective of the length scale (for example by magnification from macroscopic to microscopic). Consequently, at the dynamic friction interface each length scale contributes to the energy dissipation in the rubber, denoted as hysteresis in Equation (2.46), with a length scale dependent friction contribution at different specific sliding velocities as shown in Figure 2.24 (c).
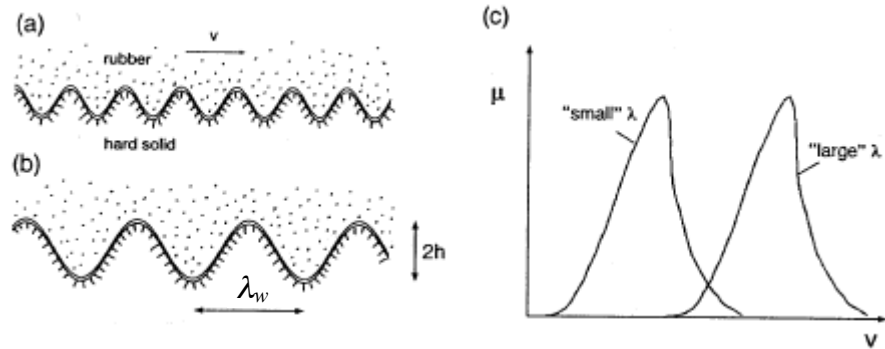
Figure 2.24: The ratio of amplitude h to wavelength λ_w is identical for both contact situations (a) and (b). Therefore, the contribution of internal damping to friction for both length scales is similar, however, as shown in graph (c), which shows the coefficient of friction $\mu(v)$ for the substrate profiles (a) and (b), the maximum energy dissipated occur at different sliding velocities (excitation frequencies) (Persson 2001b).

The surface topography of Figure 2.24 (a) and (b) can be expressed as the ratio between amplitude h and wavelength λ_w and is similar for both profiles shown. In the case that excitation time ($t_{ex}=\lambda_w v$) is similar to the relaxation time (t_{relax}) a maximum in the

coefficient of friction can be expected, as shown in c). Prior to Persson, Grosch (1963) showed that, $1/t_{relax}$ coincides with the frequency of the maximum loss modulus. The influence of surface topography is clearly of paramount influence on the frictional force and by considering this, the friction dependence on temperature and velocity can be considered. This is described in the next section.

2.5.5   *Friction dependence on temperature and velocity*

The viscoelastic nature of elastomers suggests that rubber friction depends up on temperature and the applied excitation frequency induced by a combination of the sliding velocity and the topography of the rigid surface. A comprehensive study on both parameters was firstly made by Grosch in 1963. Grosch found that experimental data points for the coefficient of friction, measured over a limited range of velocities (10^{-4} to 30mm/s) at different temperatures (-58°C to 90°C) using isomerised NR, can be shifted into a single master curve, by using the WLF time-temperature superposition (discussed previously in Section 0), as shown in Figure 2.25 a) and b). It was later found (Persson 2006), that testing at low sliding velocities also reduces the effect of local heating of the contact patch, described as the so-called flash temperature effect, as at velocities higher than 10mm/s local heating of the specimen alters the rubber friction.
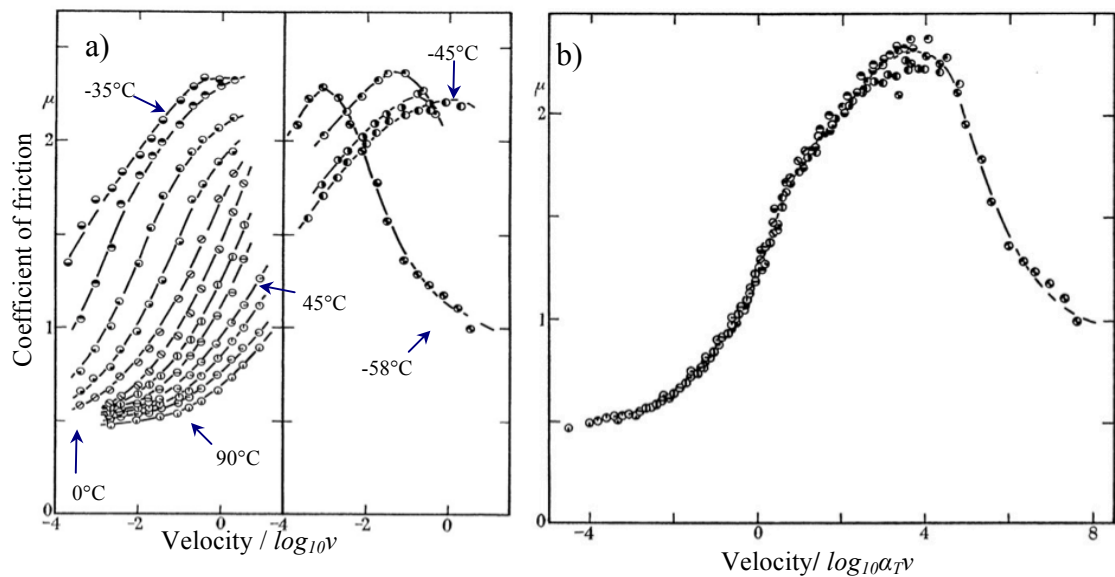
Figure 2.25: a) The friction curves of an isomerised natural rubber can be shifted into a b) master curve, in this case at a specified reference temperature of 20°C) (Grosch 1963).

The different segments of Figure 2.25 a) for an unfilled rubber were shifted only in the horizontal scale to create the master curve shown in b). For filled rubbers, the polymer behaviour is determined by the filler network at low frequencies, so that the conventional WLF shift fails to capture all the behaviour over the entire frequency region (Klüppel and Fritzsche 2009). Furthermore, at low deformations the compound's behaviour is influenced by the Fletcher-Gent effect (commonly known as the Payne effect). This can be explained by considering the polymer morphology, as the insertion of a filler structure into the polymer matrix modifies the polymer dynamics, because the interaction of the neighbouring polymer molecules with the filler surface hinders the chain mobility. So that in the case of filled rubber an additional vertical shift correction has to be introduced. The vertical shift factors are interpreted in terms of the thermal activation of glassy polymer layers between aggregated filler particles, which alter the stiffness of the filler network. The associated activation energy values relate to the filler type and polymer chain architecture. For the sake of readability the determination of vertical shift factors or WLF-correction functions are further described in literature (Ferry 1961; Le Gal et al. 2005).

Grosch's study showed further that the maximum of the master curve depends on the elastomers glass transition temperature (Grosch 1963). A comparison of different rubbers is given in Figure 2.26.
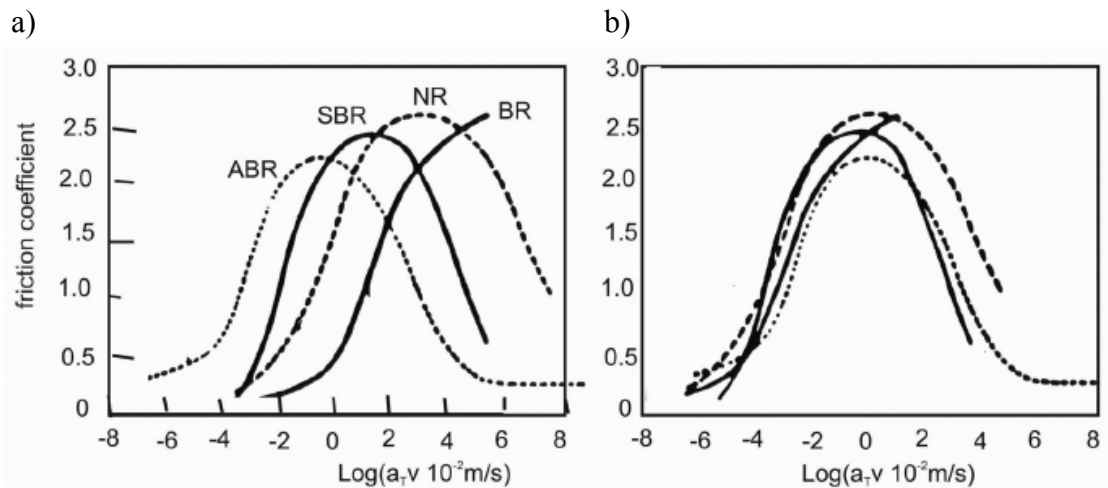
Figure 2.26: Master curves for different rubbers, shown at two different reference temperatures T_{Ref}, which were chosen to be for a) 20°C and for b) T_g +50°C. ABR=Acrylonitrile-Butadiene Rubber, BR=Polybutadiene Rubber (Grosch 2007).

Grosch showed further, that the maximum of the friction master curve for a rubber sliding against a smooth rigid surface corresponds to the maxima of the corresponding loss modulus E´´, as is shown in Figure 2.27 (Grosch 1996).
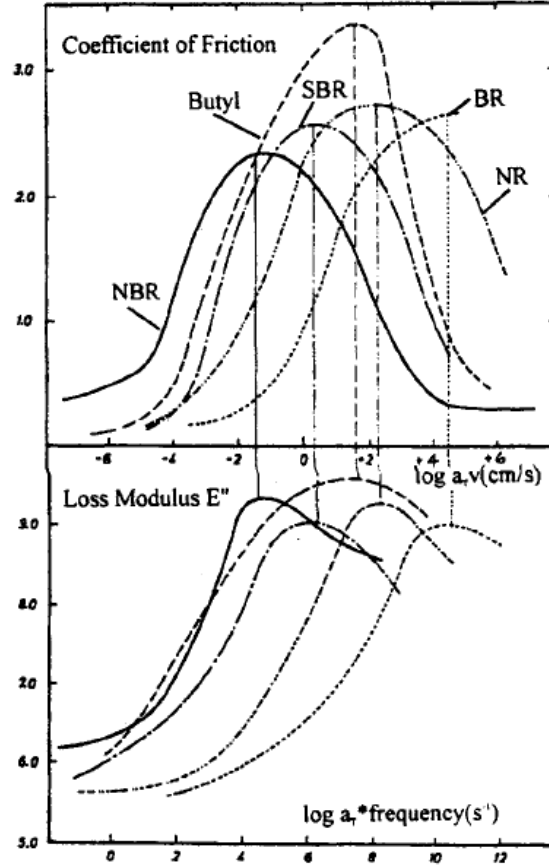
Figure 2.27: Comparison between friction master curves for smooth surfaces (top graph) and the corresponding loss modulus master curves (bottom graph). Reference temperature was chosen to be 20°C (Grosch 1996).

To relate both the velocity v_{max} at which the peak friction occurs and the frequency f_{max} at which the loss modulus $E´´$ is maximum, a characteristic length scale ζ needs to be introduced.

$$\frac{v_{max}(\mu)}{f_{max}(E'')} = \zeta. \tag{2.53}$$

For a smooth, rigid surface in contact with the rubber surfaces, used by Grosch, the dimension ζ is about 6nm, which is of the order of the molecular dimensions, showing the strong adhesional influence on rubber friction. In contrast, for a rough, rigid surface a similar analysis relates the frequency of the tan δ peak and the maximum friction velocity producing a much longer length scale of around 150μm, which corresponds to the spacing between abrasive particles, originally used by Grosch (1963).

This dependence on the surface topography of the rigid surface is emphasised in Figure 2.28. On smooth, rigid surfaces like dry glass, shown as curve A, friction increases from very low values up to a maximum followed by a decrease. In contrast, curve B shows that friction is much higher at low sliding velocities for rough surfaces and the peak is displaced to a higher velocity and is much sharper. If the rough surface is dusted with a fine powder, the adhesion term is removed and the friction is reduced, as is shown by curve C, for virtually the entire range of sliding velocities, while the position of the maximum remains in the same position. In contrast, if the smooth surface is dusted (not shown in Figure 2.28), all WLF dependence disappears and the coefficient of friction remains at a certain (small) value over the whole temperature/sliding velocity range. The maximum peak for smooth surfaces is attributed to an adhesion contribution and the maximum for rough surfaces is attributed viscous energy dissipation in the rubber.
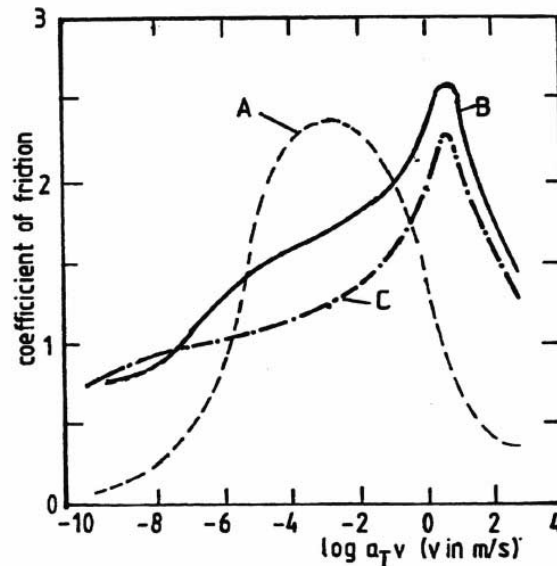
Figure 2.28: Master curves of an acrylate butadiene rubber on A) smooth glass, B) clean silicon carbide surface and C) dusted silicon carbide surface (Grosch 2007).

However, the pioneering experiments by Grosch (1963) were contradicted by Barquins and Roberts (1986), who were unable to reproduce his results under nominally similar conditions. A comparison of their test results with the Grosch data are shown in Figure 2.29 by Arnold et al. (1987), who showed, that the surface finish of the tested rubber sample (as well as the surface finish of the rigid surfaces) is of paramount importance. It is clear on careful rereading that the detailed nature of the rubber surface was not described by Grosch in his original paper. While Grosch described the employed rubber

surfaces only as smooth, it appears that he abraded the rubber in order to avoid heavy stick-slip motion, as it was revealed later in private discussion between the author of this work and A.D. Roberts. This confusion lead to the fact, that researchers such as Barquins and Roberts (1986), who used optically smooth surfaces, were not able to reproduce the same behaviour. Figure 2.29 shows that Grosch's test data follows a bell-shaped curve, whereas Barquins and Roberts' results were much less rate dependent. Furthermore, their test data had a much wider scatter at higher frequencies, making it difficult to judge if friction really decreases with increasing velocity, as was shown by Grosch (1963) for the highest frequencies.
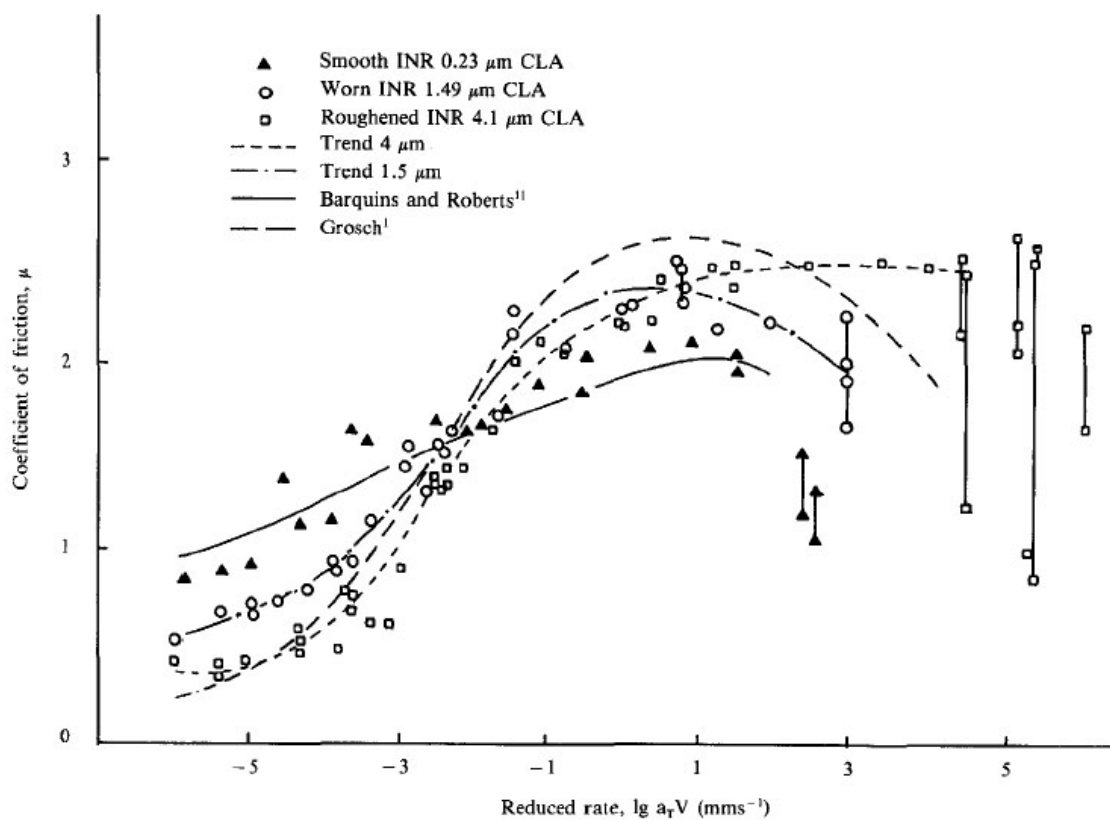
Figure 2.29: Comparison of the WLF shifts of the coefficient of friction versus sliding velocity by Grosch, Barquins and Roberts as well as Arnold et al. (Arnold et al. 1987).

In contrast to Grosch, Barquins and Roberts also examined the area of contact optically and reported the presence of wave like surface instabilities, so-called Schallamach waves, over a wide range of sliding velocities. The appearance of this stress-relieving displacement mechanism is believed to be one of the reasons for the contrasting findings between Grosch (1963) and Barquins and Roberts (1986). The conflict between these two key papers in rubber friction is considered further in this work: Different

surface finishes are used to reinvestigate the dependence on surface topography and the contribution to rubber friction of simplified surface asperities is examined in chapter 7. Schallamach waves and the different sliding mechanisms involved in these surface instabilities are investigated in Chapters 5 and 6. To understand more clearly the theory behind Schallamach waves is discussed in the next Section (2.5.6).

The early findings by Grosch and Barquins and Roberts are very significant in tyre research. In the case of a tyre road contact, the tyre compound is excited by a variety of road asperities at different frequencies. The sliding of fine structures with a short wavelength subjects the material to high frequency excitations, while larger asperities result in a lower frequency excitation. The proposed relationship between friction and the viscoelastic behaviour allows a classification of different frequency regions to different aspects of a compound's frictional properties. Figure 2.30 shows a schematic of this relationship for two different tyre compounds filled with carbon black and silica, respectively. In the case of wet-braking friction, the material is excited at higher frequencies. The paramount properties of the material at this situation should result in a maximum energy loss, which can be resolved from a combination of both, adhesion and hysteresis friction, highlighted in Figure 2.30. The graph indicates that this particular silica compound has higher energy dissipation in this region, improving the wet braking performance. Pan (2007) has suggested that silica filled rubbers have better wet grip properties than carbon black filled rubbers, indicating that in addition to bulk viscoelastic hysteresis, interfacial interactions between filler particles and the road surface might contribute to wet sliding friction of elastomer compounds on a rough surface.
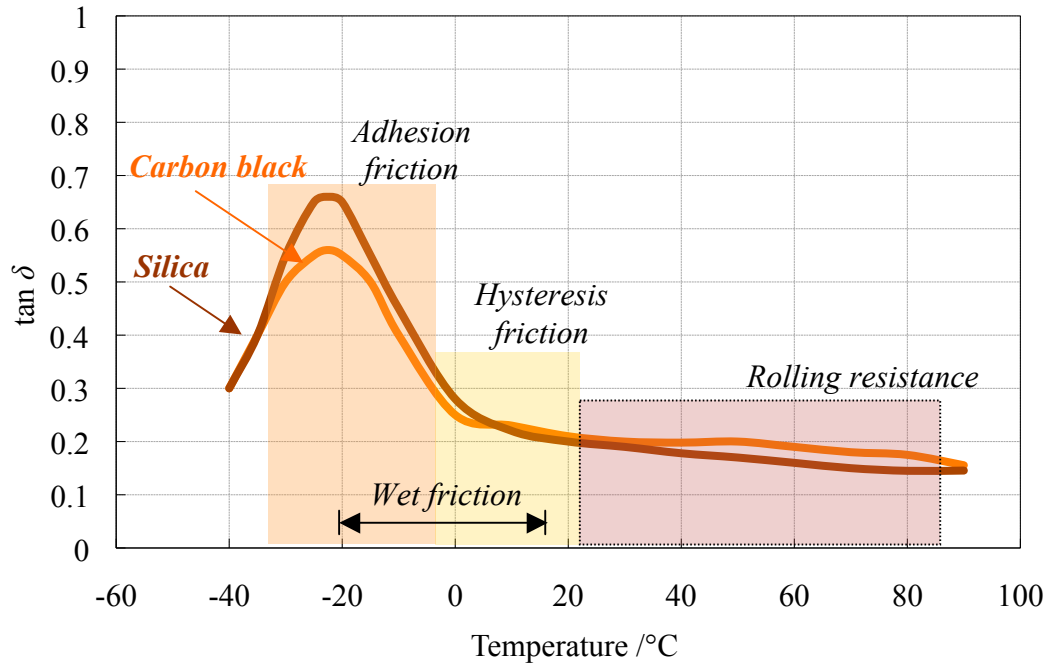
Figure 2.30: Schematic relationship between tan δ and temperature using WLF shift. The different friction properties experienced by a tyre can be classified to certain frequency regions. Modified and redrawn from (Schramm 2002).

An additional energy dissipation results from the tyre, being deformed cyclically by the rolling motion, however, this frequency is much lower than the frequency of surface vibrations during wet braking. According to the time-temperature superposition principle a lower frequency is equivalent to working at higher temperatures. Therefore, the rolling resistance is located at higher temperatures, shown in Figure 2.30 as the shaded (red) area. In this area, the carbon black compound shows a higher loss tangent, compared to the silica compound, resulting in higher rolling resistance and, therefore, higher fuel consumption. The green tyres, developed in the 1990s, exploited this finding to produce tyres with lower rolling resistance whilst maintaining wet grip.

2.5.6 *Waves of detachment*

When a smooth rubber like material slides over a smooth rigid surface, a phenomenon is sometimes observed, where waves of the rubber surface move rapidly through the contact region. A schematic of the process is shown in Figure 2.31.
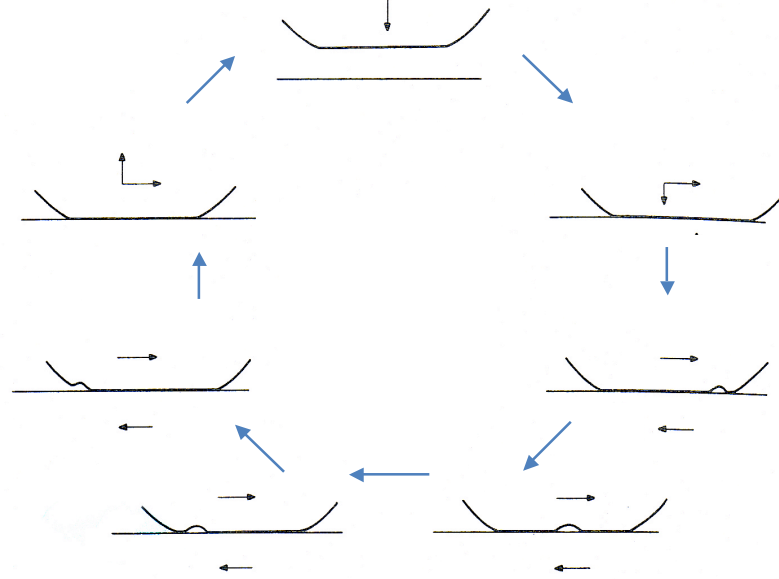
Figure 2.31: Schematic diagram of the propagation of one Schallamach wave (clockwise cycle). The rubber sphere is initially brought into contact with the smooth rigid surface and the rubber sphere is displaced to the right hand side. A wave of detachment forms at the front of the hemisphere and travels through the area of contact to the back (Briggs and Briscoe 1979).

A wave-like pattern is formed on the rubber surface, which moves rapidly through the contact region. First observed by Schallamach (1971), these 'waves of detachment' are often described as 'Schallamach waves' and are thought to be the only observable way for a relative displacement to arise between the two surfaces. The rationale behind this is commonly described in the literature (Best et al. 1981; Gent and Cho 1999), to result from a buckling instability (Biot 1965; Green and Zerna 1968), which occurs when the rubber at the front of a rigid slider attains a critical value of compressive strain. The compressive stress field at the front and the tensile stresses at the back of the contact region propagate the waves via a process of viscoelastic peeling and re-adhering. It was shown, that the frictional work could be derived from the rate-dependent surface energy, involved in the viscoelastic peeling and re-adhesion process of a Schallamach wave, where the regained energy from re-adhesion is neglected (Roberts and Jackson 1975; Roberts and Thomas 1975). It was found that the dissipated energy, described by $\Gamma(v)$, in the cycle shown in Figure 2.31 can be almost completely accounted for as the energy required to peel the rubber off the surface and then to re-form contact again. Roberts and Thomas (1975) proposed an Equation to calculate the tangential stress F:

$$F = \frac{\gamma\omega}{\lambda v},$$

(2.54)

where γ represents the rate dependent surface energy, ω the wave velocity, v the sliding velocity and λ the spacing between two waves. On this basis Briggs and Briscoe (1975) derived a hypothesis to calculate the work of adhesion of the Schallamach waves as:

$$\Gamma(v) = \frac{Fv}{nA}, \tag{2.55}$$

where n is the number of waves traversing the interface in unit time and A the area of contact. Roberts and Jackson (1975) and Roberts (1975) have shown, that Equation (2.54) holds over a wide range of velocities. Barquins (1993) observed that no Schallamach waves arise below a certain critical tangential stress, when the coefficient of friction is less than 2.0. However, care has to be taken in interpreting discrete friction values, as the coefficient of friction is highly dependent on the specific test conditions as is demonstrated in chapter 4. Furthermore a critical rubber thickness for wave appearance exists, as is shown by Koudine and Barquins (1997). The waves of detachment disappear if the sliding surface is contaminated or rough (Roberts and Thomas 1977; Best et al. 1981). However, throughout the findings of this research a sliding mechanism similar to Schallamach waves has been observed for rough surfaces and this is further described in Chapters 5 and 6.

In contrast to Barquins and Courtel (1975), who were not able to observe Schallamach waves using an unspecified lubricant, "wet Schallamach waves", using water, have been reported (Roberts 1979; Wu-Bavouzet et al. 2007), where the detachment waves contain water instead of air. It is understood that the state of lubrication f(v), hydrodynamic or boundary (Persson 1999), determines the separation of the two surfaces, hence, the ability to build up any buckling instabilities. Recent studies on Schallamach waves (Rand and Crosby 2006; Rand and Crosby 2007) revealed that the sliding velocity v is related to the wave periodicity λ:

$$\lambda \propto v^{1/3}, \tag{2.56}$$

Furthermore, they give a relationship between the periodicity of the waves and the surface energy γ and bulk viscoelastic properties E^* for a specific silicone rubber.

$$\lambda = \beta\left(\frac{\gamma}{E^*}\right), \tag{2.57}$$

where β is a geometrically dependent but not specified constant. This relationship suggests, that the periodicity of Schallamach waves will quickly approach nanometre

scales for stiff materials, explaining why Schallamach waves only form on smooth soft surfaces and do not form on stiffer materials such as filled rubbers. Only a few examples of possible applications for Schallamach waves have been mentioned in literature: Koudine and Barquins (1997) suggested Schallamach waves might act as test indicators for skin friction in rubber-like materials, where the occurrence of Schallamach waves might anticipate the failure of joints and seals. Generally, experimental investigations into the phenomenon of Schallamach waves can be summarised as follows (Schallamach 1971; Barquins and Courtel 1975; Briggs and Briscoe 1975; Roberts and Thomas 1975; Briggs and Briscoe 1979; Roberts 1979; Best et al. 1981; Roberts and Richardson 1981; Barquins 1983; Barquins 1984; Barquins 1985; Barquins and Roberts 1986; Arnold et al. 1987; Barquins 1993; Mori et al. 1994; Barquins et al. 1996; Grosch 1996; Koudine and Barquins 1997; Koudine et al. 1997; Gough et al. 2001; Gent 2005; Rand and Crosby 2006; Wu-Bavouzet et al. 2007; Maegawa and Nakano 2008):

1. A critical sliding velocity v_{crit} exists below which no Schallamach waves are observed (Barquins and Courtel 1975).
2. The critical sliding velocity v_{crit} decreases with a decrease in normal load F_N or temperature (Roberts and Richardson 1981) and increases with an increase in the slider radius R (Barquins and Roberts 1986).
3. The wave velocity and wave frequency, both increase with sliding velocity and temperature (Briggs and Briscoe 1975).
4. The wave velocity of each individual wave increases, when passing through the contact area (Barquins and Courtel 1975).

From these points, it can be concluded that the appearance of Schallamach waves is strongly dependent on the elastic and viscoelastic properties of the elastomer, the interface geometry, the normal load and temperature. Point 4 above has so far only been observed by Barquins and Courtel (1975) and has not yet been further investigated. The investigation on why an individual wave may increase in velocity over the area of contact is taken further in this thesis and this is described in Chapter 6.

The origins and mechanism of Schallamach waves are still debated. While Barquins and Courtel (1975) relate the instability to the viscoelastic properties of rubber, Best et al.

(1981) argued that it is purely elastic. A detailed FEA analysis is examined in this work, leading to a better understanding of this matter. Gent (2005) notes the possible relation of wear mechanisms to Schallamach waves. Supporting this, Fukahori et al. (2008) asked for further detailed observations on Schallamach waves in order to investigate their relation to crack initiation during rubber abrasion. Baumberger and Caroli (2006) state "no prediction relating material properties to the dynamics, nor even to the occurrence of Schallamach waves is available up to now".

2.5.7   *Unified theories for rubber friction*

According to Equation (2.46), the most important parameters for friction are adhesion, hysteresis, lubrication and wear. Different theories have been published attempting to produce a unified theory for rubber friction (Klüppel and Heinrich 2000; Persson 2001c; Lindner 2005). A brief overview on the different theories is given in this section:

In contrast to other solids, rubber does not obey Amontons' law, as given by Equation (2.45). Instead, the coefficient of friction (usually) decreases as normal stress increases. An empirical equation describing this characteristic was firstly given by Thirion (1946) as:

$$\frac{1}{\mu} = m_a + m_b \left(\frac{\sigma}{E} \right),$$

            (2.58)

where m_a and m_b are constants, derived from an extrapolation of the reciprocal of the coefficient of friction against pressure. The former is calculated from the ordinate at the origin, while the latter is derived from the slope. The elastic modulus E is incorporated in Equation (2.58) to make the equation dimensionless (Denny 1953). Like Thirion (1946), Schallamach (1952) investigated the dependence of frictional force in respect to the real area of contact. The experimental results shown in Figure 2.32 a) on three rubbers, differing in hardness, pointed out the dependence of contact radius a on the normal load F_N, expressed as:

$$2a \propto F_N^{\frac{1}{3}},$$

            (2.59)

which is similar to the Hertzian contact theory, given in Equation (2.49). If the contact area is given as a function of the normal load and a proportional relationship to the frictional force is assumed, Equation (2.59) becomes:

$$\mu = \frac{c_u a}{F_N},$$

<div align="right">(2.60)</div>

where c_u is an unknown factor. Substituting Equation (2.59) into Equation (2.60) and incorporating the Hertzian contact theory, allows the coefficient of friction to be described as:

$$\mu = c_v F_N^{-\frac{1}{3}},$$

<div align="right">(2.61)</div>

where c_v is an experimental parameter, which has to be measured for each velocity. The good agreement of Equation (2.61) with experimental data has been also confirmed later by other scientists (Barquins and Roberts 1986) as shown in Figure 2.32 b).
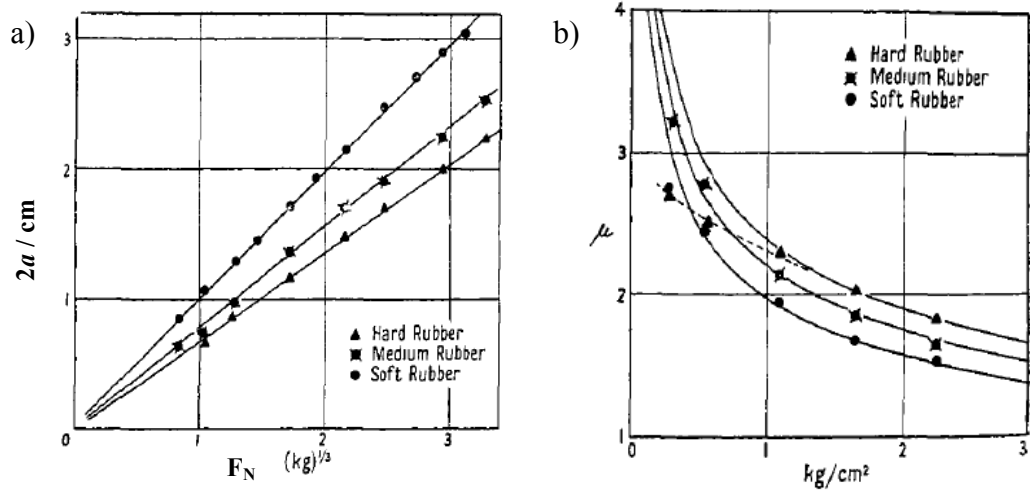
Figure 2.32: Graph a) shows the linear relationship between the diameter of contact (2a) and the load $F_N^{1/3}$ for different rubber spheres on a smooth surface and b) shows the coefficient of friction dependence on normal pressure. Single points denote experimental data, while thick lines represent the theory (Schallamach 1952).

It is worth noting that the empirical Equation (2.61) does not describe the frictional behaviour for all load cases, especially at very low or high pressures, as Equation (2.59) specifies the contact area to normal load relation only over a limited range of conditions. Furthermore, these first empirical equations do not incorporate this viscoelastic frequency dependence of elastomers and also assume the apparent area of contact to be equal to the real area of contact. Modifications of these first approaches are given qualitatively and theoretically in the literature, as is reviewed next.

Unified theory of Klüppel and Heinrich

Klüppel and Heinrich (2008) give a unified theory of rubber friction for dry and wet (rough) surfaces, assuming the total friction to be mainly influenced by adhesion and hysteresis, see Equation (2.47). They suggest the hysteresis part to be described as an integral over the interval of mechanical excitation frequencies and its amount is determined by load, velocity, temperature and the dependent length interval of contact (Klüppel and Heinrich 2008):

$$\mu_{Hysteresis} = \frac{F_{Hysteresis}}{F_N} = \frac{1}{2(2\pi)^2} \frac{\delta_t}{pv} \int_{\omega\,\min}^{\omega\,\max} d\omega G''(\omega) S(\omega) \quad , \tag{2.62}$$

where δ_t is the thickness of the excitation rubber layer, p is the normal pressure, v is the sliding velocity, G'' is the shear loss modulus and S is a complex parameter to describe the surface topography. The excitation frequencies are individually dependent on surface parameters: The minimum excitation frequency is defined as

$$\omega_{\min} = 2\pi\xi_{II}, \tag{2.63}$$

where ξ_{II} is the horizontal cut-off length of the roughness spectra, which is a surface descriptor. The maximum excitation frequency is defined as

$$\omega_{\max} = 2\pi v / \xi_{\min}, \tag{2.64}$$

where ξ_{min} the minimum coupling length, which is strongly dependent on the normal load. However, they note that for large contact pressures, as experienced for example in the footprint of a passenger tyre (p=0.3MPa) the integral value of Equation (2.62) is small and hence the hysteresis part is governed by δ_t/p. Both parameters can be derived from the Greenwood-Williamson theory on contact mechanics (see Section 2.5.4). With

$$(\delta) = \overline{p} f(x)_1 \left(\frac{d_m}{R_h} \right) \quad , \tag{2.65}$$

and

$$p = \frac{0.53\xi_{II} \left| G^*(\omega_{\min}) \right|}{\pi s^{3/2} \xi_{II}} f(x)_{3/2} \left(\frac{d_{ms}}{R_{hs}} \right) \quad , \tag{2.66}$$

where d_i is the load dependent mean gap distance between rubber and the mean height of the road track, R_h is the variance of height distribution, $|G^*(\omega_{min})|$ is the norm of the complex modulus at minimum excitation frequency, $\xi_\perp$ is the vertical cut-off length of the roughness spectra and the $f(x)_i$ is being defined by an equation proposed by Greenwood and Williamson (1966) to describe the contact between two surfaces of a

certain roughness. The index *s* in Equation (2.66) indicates a transition to the height distribution of the track summits on the largest roughness scale, which can be obtained by applying an affine transformation with an affine scaling factor, which is given by Greenwood and Williamson (1966). Complicating matters further, the surface descriptors are highly dependent on the actual distribution and shape of surface asperities, for example if an asperity is sharp or blunt.

If low pressures are considered, the integral of Equation (2.62) gains in significance and the minimum coupling length ξ_{min} is given as

$$\frac{\xi_{min}}{\xi_{II}} = \left(\frac{0.09\pi s^{3/2}\xi_{II}(2R_D - 4)|G*(\omega_{max})|F_0(d_m/R_h)}{\xi_{II}(2R_D - 2)|G*(\omega_{min})|F_{3/2}(d_{ms}/R_{hs})} \right)^{1/(3R_D - 6)} \tag{2.67}$$

where R_D is a surface descriptor, describing the fractal dimension.

For the description of the adhesion influence Klüppel and Heinrich (2008) suggest the following:

$$\mu_{Adhesion} = \frac{F_{Adhesion}}{F_N} = \frac{\sigma_\tau}{p}\frac{A}{A_0} \tag{2.68}$$

where σ_τ is the true shear stress in the real area of contact *A* and A_0 is the nominal area of contact. The true shear stress results from molecular energy dissipation mechanisms of the rubber contact patches, while the load dependence of the real area of contact is determined by the Greenwood-Williamson function *f(x)*:

$$A(\xi_{min}) = A_0 \left(\frac{(2D - 4)^2 \xi_{II} F_0^2(d_m/R_h)F_{3/2}(d_{ms}/R_{hs})|G*(\xi_{II})|}{808\pi s^{3/2}(2D - 2)^2 \xi_{II}|G*(\xi_{min})|} \right)^{1/3} \tag{2.69}$$

Klüppel and Heinrich draw the conclusion from Equations (2.68) and (2.69), that for sharp asperities the influence of adhesion decreases with increasing load. However, they also mention that blunt asperities show the opposite behaviour.

In order to use the approach given by Klüppel and Heinrich (2008), at least 19 parameters are necessary to obtain a prediction of the coefficient of rubber friction. The presented equations work under well-defined laboratory conditions, however, the question arises if it is applicable to engineering problems in every-day applications, where surfaces are not well defined and several other complications arise. It is further noticed, that Equations (2.62) and (2.68) are based in their fundamental form on the relationship, originally suggested by Amontons.

Different equations in similar complexity have been proposed by other scientists, for example by Persson (2001b), Persson and Volokitin (2006) and Pinnington (2009). In the last decade great effort has been undertaken to propose different approaches on rubber friction taking into account different parameters such as smooth or rough surfaces. However, the vast complexity of parameters still makes the overall description of rubber friction difficult.

2.5.8   Lubrication

As shown in Equation (2.46), the total friction force is influenced by lubrication. The investigations on additional geometric effects on rubber friction, conducted in Chapter 4, require the use of suitable lubricants to alter the frictional behaviour of the sliding interface, so that a brief discussion on lubrication is required in this review.

Nearly every surface is covered by a thin contamination layer, starting from condensed moisture to highly viscous oils or even solid powders. In technical applications lubricants are commonly used to lower interface friction, in order to avoid or reduce wear. In some applications lubrication is undesirable especially if the energy dissipated through friction, for example to stop a car, is further reduced resulting in a longer stopping distance. Even without external contamination from dirt and dust particles a thin layer of wax and other volatile components may constantly bloom out of the surface, which would tend to lower the friction. The viscosity $f(p,v,T)$ and chemical interaction of a fluid determines the thickness of the interface lubrication layer. At a suitable pressure, the surface layer in Figure 2.33 of a low viscosity liquid can be squeezed out of the contact and both surfaces are in intimate contact.
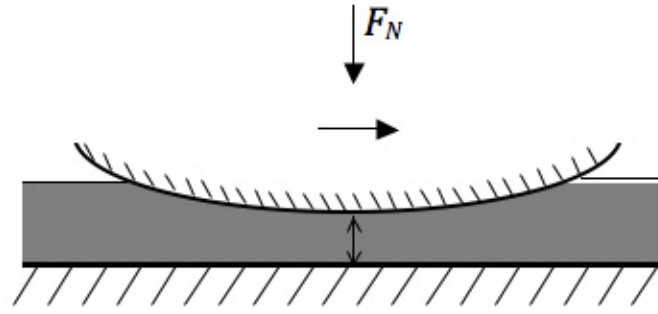
Figure 2.33: The thickness of a water film trapped between two surfaces is dependent on the normal load, the viscosity of the lubricant and the sliding velocity.

When (distilled) water is used as a lubricant, the presence of a soap alters the chemical interaction and this makes it harder to establish intimate contact, due to a change in surface energy and the wetability. In Figure 2.34 (a) a small layer of water and soap is trapped between rubber and glass, whereas in (b) the distilled water is fully squeezed out over most of the surface allowing contact to be established across most of the contact patch with just small-lubricated spots remaining. Roberts (1974) used Newton rings as a measure of film thickness and this is given in the graph below each photograph.
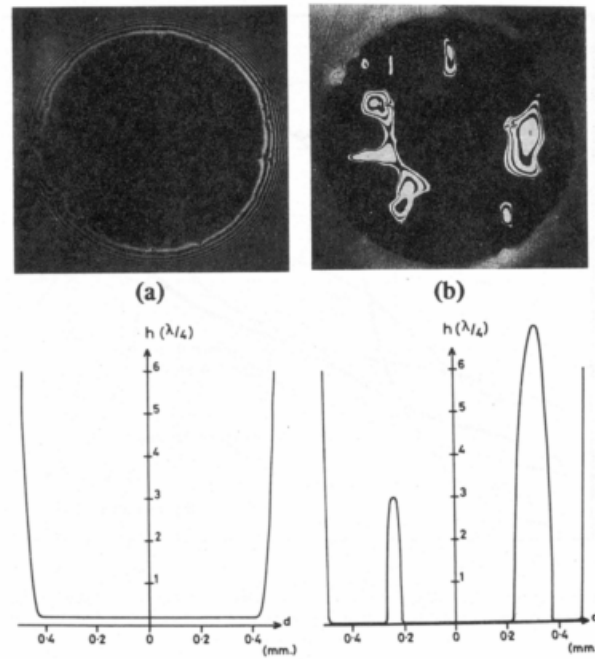
Figure 2.34: Photos of the interfaces of a soft rubber hemisphere and a transparent surface are shown. Two different lubricants were used here and the film thicknesses were measured by Newton rings. In a) a layer of water with soap prevents the contact between the two bodies, as is shown in the graph below photo a), while in b) distilled water is used. The correlating graph for b) shows that intimate contact patches are formed despite the presence of a lubricant (Roberts 1974).

If the velocity *v* of the rigid sphere is high, the time for the lubricant to squeeze out from the contact area is too short and liquid is trapped on the area of contact. This means that the lubrication layer between both surfaces is large and the sliding friction low. Conversely, if the sliding velocity is comparatively low, the lubricant can be squeezed out to a certain thickness resulting in close contact and higher sliding friction. The latter process is called *hydrodynamic* or *fluid lubrication*, whereas the former is called *boundary lubrication* (Persson 1999). Persson further states that hydrodynamic lubrication is well understood in contrast to boundary lubrication, where a few monolayers of lubrication molecules affecting the sliding friction and the behaviours is then independent of the fluid viscosity. It is also worth noting that the effect of lubrication on friction is much higher for smooth surfaces, than for rough surfaces, as tests on silicon carbide paper showed only a modest effect of lubrication on the total friction behaviour. This is due to high local pressures on surface asperities enabling the lubricant to squeeze out and form intimate contact patches.

2.5.9   *Abrasion*

Abrasion is defined as the process of material removal at a surface, due to the interaction with another surface and contributes to rubber friction due to the dissipated fracture energy (Equation (2.46)). In chapter 7 abrasion has been experienced for different slider geometries (cones and hemispheres) so that general abrasion mechanisms are hence discussed in this section.

Frictional stresses induce local mechanical failure of the elastomer, leading to the formation of micro-cracks and the initiation of abrasion (Schallamach 1958). Through this process energy is dissipated, contributing to the total experienced friction force (Greenwood and Tabor 1958). For a complete description of the mechanism of elastomer abrasion a series of factors, such as the coefficient of friction, pressure, surface texture, sliding velocity, operating temperature, elastic modulus and fatigue resistance have to be considered (Liang 2007). In the absence of transient effects, for example the initial formation of abrasion patterns, the amount of rubber abraded is proportional to the sliding distance (Roberts 1988).

The measure of abrasion is given as

$$\text{measure of abrasion} = \frac{\text{depth of abrasion}}{\text{distance of sliding}}.$$

(2.70)

The topography of the rigid slider is of great importance during abrasion and a significant difference in abrasion rate is observed between sharp and blunt sliders. By using a sharp slider the rubber is abraded by the single action of a counter face asperity, whereas on a blunt slider the rubber is only abraded after repeated slidings. It was found that for sharp sliders the measure of abrasion is proportional to the normal load (Grosch and Schallamach 1965). If a rubber is abraded in a constant direction, abrasion patterns are usually developed, manifesting in ridges normal to the sliding direction, as shown in Figure 2.35.
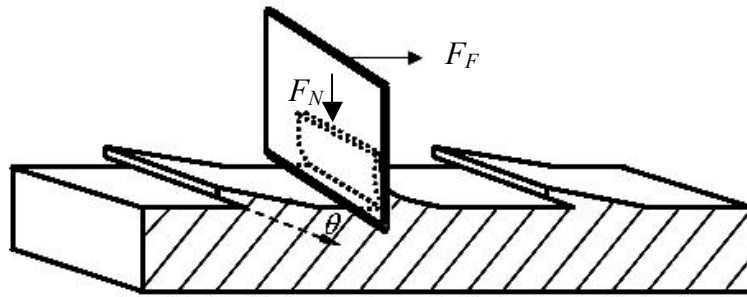
Figure 2.35: Schematic figure of a blade in contact with a soft rubber surface. An abrasion pattern is created by the repetitive sliding motion of the blade on the rubber. Cracks develop at an angle θ (Southern and Thomas 1978).

Figure 2.36 highlights the aspect of fracture mechanics on the magnification of Figure 2.35, where the rubber tongue is pulled with force F by the friction between rubber and blade, leading to a further crack propagation at angle θ.
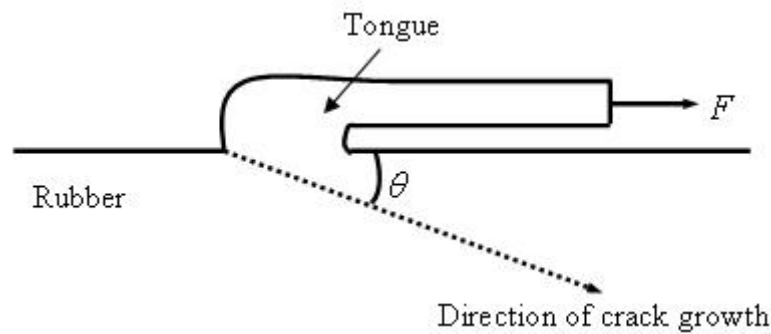
Figure 2.36: Schematic of a fracture mechanics model of a single ridge, which is pulled along the surface due to the blade motion. The direction of crack growth is indicated as angle θ (Southern and Thomas 1978).

2.5.10 Tyre road contact

The interaction between tyre and road is discussed briefly in this section. The tyre is a complex product consisting of several different rubbers, steel cord and other materials. The basic design for a radial car tyre is shown in Figure 2.37 and the various components are explained in Table 2.2.
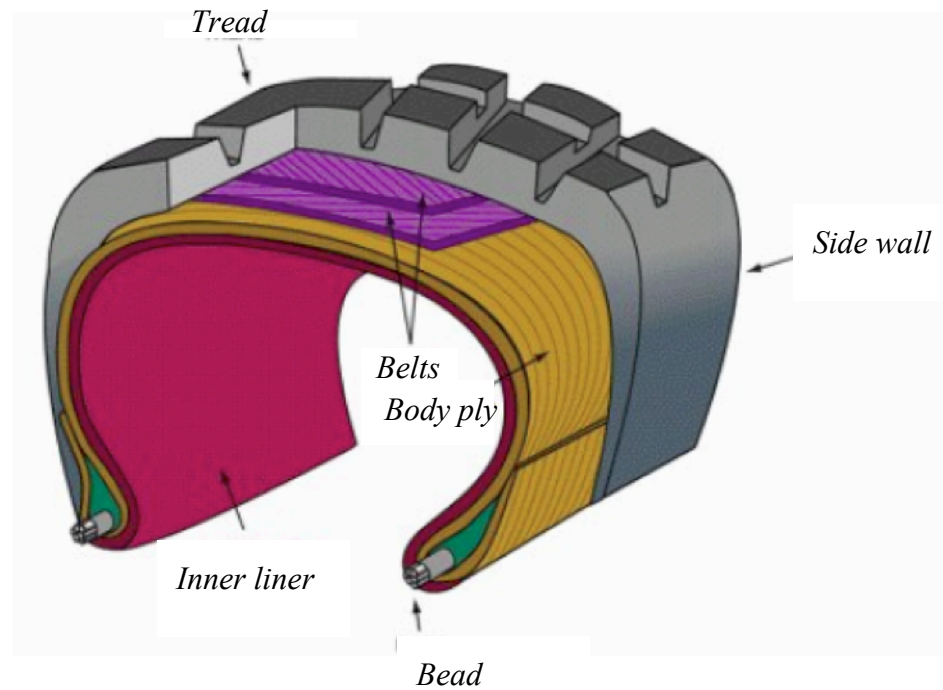
Figure 2.37: Typical structure of a radial tyre used for cars.[1]

Table 2.2: Main components of a radial tyre (Kumar 2007).

Component	Description
Tread	Directly in contact with the road. Providing cornering grip and traction. Usually made from SBR with high filler content. The tread profile is of great importance.
Sidewall	Reinforcement of the interface between tyre and wheel rim made from a blend of NR, BR and SBR.
Belts	Reinforcement of tread. Maintenance of tyre shape made from NR. Layers of rubber containing a metallic web.
Body ply	Flexible web out of polymer cords (nylon) strengthening the structure, coated with NR.
Innerliner	A thin butyl (IIR) layer with a low gas permeability used to ensure tyre pressure is fixed in service.
Bead	High strength steel wire coated with rubber that ensures an airtight fit between the tyre and the wheel and ensures the tyre stays on the wheel rim.

Several parameters affecting the tyre road contact are shown in Table 2.3.

---

[1] Image source: http://www.rma.org.

Table 2.3: Parameters and effects of the tyre road contact (Eichhorn 1993).

	Parameter	Effect
Vehicle	Velocity, wheel load, wheel toeing, camber angling.	Forces, slip, noise, abrasion rate, heat generation.
Tyre	Type, tread depth, Internal pressure.	Pressures, deformation, oscillation, damping.
Lubricant (wet / dry)	Type, film thickness, temperature.	Film squeeze out, tyre deformation, hydroplaning.
Road	Material, micro-/macro texture, age, drainage.	Abrasion, contact area, rolling resistance, tyre noise.

Many parameters affect the actual area of contact. Several parameters like wheel toeing are required to ensure directional stability in a vehicle or have a significant effect on the abrasion behaviour such as camber angling. During a tyres service life and due to the abrasion of the tread the contact area usually increases, but this may also result in aquaplaning being more readily established.

In general the three main indicators of tyre performance can be summarised by a triangular relationship, as shown in Figure 2.38. By changing the tyre properties in favour of only one of the parameters, the efficiency of one or both of the others may be decreased. For example if the frictional properties are increased, this usually results in lower abrasion resistance or an increase in fuel consumption. Consequently, in tyre design the overall aim is to improve all three properties.
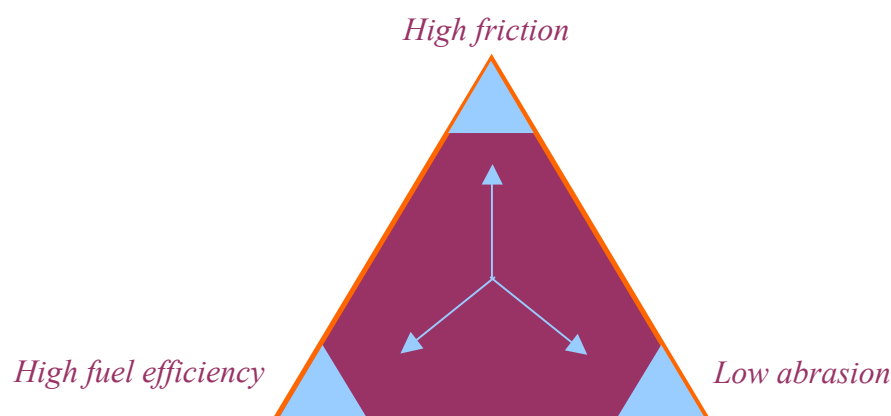
Figure 2.38: Each corner of the tyre performance triangle represents one (positive) property of the tyre. If the design of the tyre is altered, each of the properties might alter, changing the overall behaviour.

2.6   Finite element analysis

Finite element analysis (FEA), based on finite element methods is a valuable tool for the numerical solution of geometrically complex structural analysis problems. The ability to solve a complex problem without the necessity of developing and applying complex equations makes FEA a powerful technique for both engineering design and research (Gent 2001). Using software interfaces the engineer has to define the problem type accurately, but does not have to understand in detail the full mathematical complexity. Nevertheless, it has to be pointed out, that FEA results depend ultimately on the accuracy of the input and the skill and experience of the engineer. To be able to validate calculated results, an understanding of the basic concepts of FEA is required. The following section gives an overview of how solutions are achieved in FEA, highlighting the special requirements when modelling elastomer behaviour and rubber friction. A detailed discussion of the theory behind FEA can be found in various textbooks (Fenner 1987; Fagan 1992).

2.6.1   Fundamental concepts and terminology

In FEA an object is modelled by braking down the structure into a large number of so-called elements. As shown in Figure 2.39, these elements, usually triangular or rectangular in shape for 2D models, are connected to each other at connection points, called nodes. Some element types also contain nodes sitting between two element corners in order to increase the information output. All nodes can move in various directions, specifically translation or rotation, which are known as the degrees of freedom (DOF). By applying boundary conditions to the nodes the range of DOF can be defined. Boundary conditions are also used to apply loading to a body, for example displacement, pressures or forces, as shown in Figure 2.39.
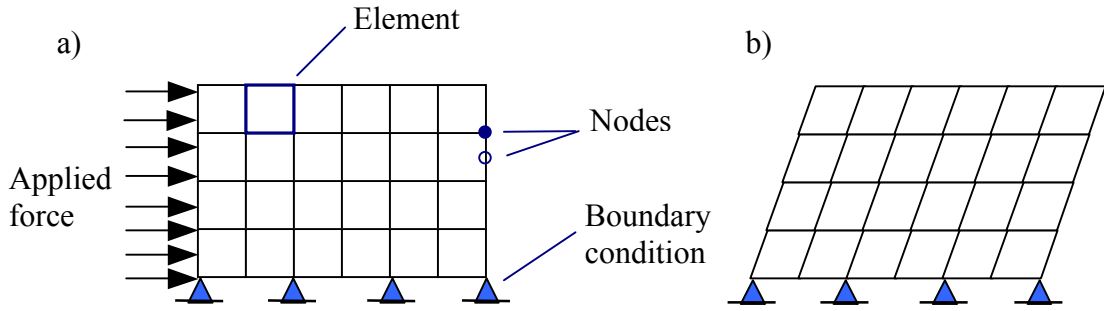
Figure 2.39: a) Example of a two dimensional mesh consisting of joined elements. b) Deformed mesh after analysis.

In order to calculate the mesh deformation a large number of complex equations with several unknowns have to be solved. In the simplest mechanical analysis these unknown are typically displacements and rotations (Liang 2007). A force displacement analysis is given by:

$$[K]\{U\} = \{F\} \, ,$$ (2.71)

where [K] is a square matrix or stiffness matrix derived from the models geometry and material properties, {U} and {F} are the vectors of (unknown) nodal displacements and the vector of applied forces, respectively. As described in Section 2.4, the force of an ideal spring is given by the deflection x multiplied by the spring stiffness k. When forces are applied to a FEA model the software inverts this relationship to calculate the displacement (Liang 2007). By employing a large number of equations, representing the model, the FEA software is able to calculate a deformation for an applied force at each node in the system. However, as the complexity of the model increases with the number of elements the computational costs increase as well. For this reason great care has to be taken when defining a complex model. Simplifications can be achieved by taking advantage of symmetries in the body. For example a cylindrical model can be reduced to two dimensions (2D) by using axial symmetry (Busfield 2000). Modelling is also possible in two dimensions for systems that exhibit either plain stress and plane strain conditions. Plane stress is used if the model has negligible dimension in one direction and is loaded in the plane of the body, while plane strain is used when the body is long and the geometry and loading does not vary significantly in the longitudinal direction. More complex situations, which cannot be simplified to 2D, have to be modelled three-dimensional (3D) and usually consume more time both to create and to solve the model. The software package ABAQUS 6.7 (Simulia 2009) used in this work offers two ways

to create the input for the solver. On the one hand a tabular text file can be created, while on the other hand, an interactive, graphically-aided pre-processor (ABAQUS/CAE) is also available. The tabulated file is known as an input deck, which contains typically 8 sections:

1. The **header** can be used to define the problem or make annotations to the following format.

2. The following **geometric definition** specifies the position, in coordinate space of nodes and spatial arrangements of the materials.

3. The **element properties** classify the dimensions of the model, being 1D, 2D or 3D.

4. The **material properties** describe the materials used. Elastomers are usually defined by density and a SEF, which is marked with the keyword *HYPERELASTIC (large strain elastic) in its basic configuration.

5. The **boundary conditions** specify the DOFs of single nodes or node groups in terms of global displacement.

6. The **Loading condition** specifies any forces, pressures or displacements wished to be applied to a model.

7. For the **analysis type**, either static, steady state dynamic or explicit dynamics can be chosen.

8. The **output request** characterises the required output variables, such as stresses, strains or energy.

A typical input deck used in this work is given in the appendix in Section 9.3. The models investigated in this thesis involve large deformations and contact as well as the implementation of sliding friction, leading to a dynamic, nonlinear problem. Consequently, either implicit dynamics or explicit dynamics techniques have to be used to derive solutions for these highly non-linear problems. Two different approaches exist: ABAQUS/Standard and ABAQUS/Explicit. In ABAQUS/Standard an implicit algorithm is used with an automatic increment strategy, based on the success rate of a full Newton iterative solution method, the ABAQUS/Explicit procedure is based on the implementation of an explicit integration rule along with the use of diagonal element mass matrices (Liang 2007; Simulia 2009). The former algorithm has been successfully implemented in fracture analysis (Busfield et al. 1996) and fatigue life prediction (Busfield et al. 2005). However, the unconditionally stable implicit method is likely to

fail in the case of the significant non linearity encountered around buckling type behaviour often seen in complex friction related contact problems. The reason for this comes from how implicit solutions are solved in ABAQUS. The solution is subdivided into small time steps, specified by the user. The state of each incremental step is updated from time t to $t + \Delta t$, so that the state of a following increment at $t + \Delta t$ is determined based on information at t. By this, the equilibrium solution is resolved, however, equilibrium throughout the whole calculation is not guaranteed especially in conditions when an instability is approached. An automatic time step control is introduced, which decreases the time increment whilst it tries to find a minimum energy solution (ABAQUS theory manual 2.2.1 (Simulia 2009)). If the time increments are reduced, then the computational costs increase dramatically and at an instability often a divergence can result so that the calculation fails. As no iterations are involved in the explicit method, convergence problems are not an issue. The advantage of the explicit method is, therefore, that it is conditionally stable. The stability limit for an explicit operator is that the maximum time increment must be less than a critical value of the smallest transition times for a dilatational wave to cross any element in the mesh (Sun et al. 2000). Secondly, the nature of the explicit method limits it to the analysis of short transient problems. During the analysis of rubber friction instabilities are encountered and hence explicit algorithms are used. Accelerations and velocities at a particular point in time are assumed to be constant during a time increment and are used to solve for the next point in time (Harewood and McHugh 2007). For explicit calculations the element sizes should be as regular as possible to maintain efficiency, as a single small element can reduce the time increment for a whole model. For the explicit solver a linear relationship exists between the solution time and the size of the model, as dictated by the characteristic element length and the number of elements in the model. For an implicit analysis, the solution time grows with the square of the problem size (Kim et al. 2002). In the post-processor ABAQUS/Viewer the calculated results can be graphically presented and interpreted and defined output requests, for example CAREA for the contact area at the interface between two bodies, can be monitored.

2.6.2   Rubber in FEA

FEA modelling of elastomers is a complex task due to the non-linear, viscoelastic behaviour. In Abaqus, rubber and rubber-like materials are modelled as broadly incompressible and hyperelastic materials. However, in Abaqus/Explicit it is not possible to model fully incompressible materials, as no mechanism for such a constraint at each integration point is given, whereas hybrid elements exist in the implicit solver (specifically) for these materials. To represent the elastomeric behaviour in explicit dynamics models, a small but realistic finite compressibility has to be introduced as the bulk compliance D_{com}, which is defined as:

$$D_{com} = \frac{2}{E_B},$$

(2.72)

where E_B is the bulk modulus of the rubber.

The energy stored per unit volume in a material in its unstrained configuration, is defined as a function of strain. The material properties of the rubber are represented by a stored energy function and the material density. The type of SEF used has great influence on the material output used for the calculation. For example the Neo-Hookean SEF, defined in Equation (2.7), represents the rubbery behaviour well at moderate strains, but fails for very small or larger extension ratios (see Section 2.3.1). Other, more complex, SEFs also account for viscoelasticity or hysteresis (Mullins effect), but might be over engineered for a simple, unfilled rubber (Gough et al. 1999). Therefore, it is advisable to evaluate the suitability of a SEF and to verify the output by comparison to experimental data. The coefficients for the different SEFs can be either derived manually by the user or derived from a large set of experimental results by the software automatically. The Neo-Hookean SEF relies on one coefficient only, being equivalent to one-half of the shear modulus, as its second coefficient equals to zero. The calculated data for the one-term Neo-Hookean SEF correlate well up to an extension ratio of 1.4 with experimental results in uniaxial tension, while the two-term Mooney SEF shows a good agreement up to an extension ratio of 2.0 (Gent 2001). The derivation of coefficients for the SEF used in this work is described further in Section 3.6.

2.6.3   Rubber friction in FEA

The ability to establish contact between two or more bodies requires the FEA software to be eligible to distinguish if and where contact is established, to avoid the interpenetration of the bodies and to identify the sliding direction. As a complicating matter friction has to be defined for the contacting partners. As stated previously, rubber friction depends not only on various parameters, including surface topography, test temperature, sliding velocity and lubrication, but also the commonly assumed proportionality between frictional shear stress and normal stress is not generally obeyed (Gough et al. 1999; Liang et al. 2009). Therefore, it has to be borne in mind that specific values for the coefficient of friction (as a constant) are only valid for the modelling of one particular situation. If rubber friction were to be modelled successfully over, for example a range of velocities, the change in μ according to the velocity has to be implemented. In addition, if rubber is only modelled as a hyperelastic material, viscoelastic losses due to hysteresis deformation are not accounted for when modelling rough surfaces, so that the coefficient of friction and the model would have to be modified. In ABAQUS the interacting surfaces have to be defined and a contact interaction property has to be set up, in order to implement friction. By default, frictionless contact is assumed at the interface. If friction is included, then the friction can be defined either by a limiting shear force or by a single value in the software interface. The value of this constant defines the ratio between the horizontal and the vertical reaction forces. While the horizontal force is calculated by the FEA software, the vertical force is typically defined in the model. In order to increase the convergence rate, the load can be applied using displacement control (Lin and Hwang 2004). In reality, load control would reflect a sliding contact more appropriately, however, it is likely for a complicated FE simulation involving frictional contact that convergence issues might arise if load control is used. Detailed advice is given in Section 30.4.1 "Defining contact pairs in Abaqus/Explicit" of the Abaqus user manual (Simulia 2009). If viscoelastic behaviour shall be modelled, then, besides the hyperelastic model, time-dependent data sets have to be included. This can be done via 'time domain viscoelasticity', 'frequency domain viscoelasticity' or 'hysteresis', which are all described in the Abaqus user manual.

2.7 Sustainability and recycling aspects

The global production of rubber is approximately 20,000,000 tonnes annually (Shulman 2004). With 75% of the rubber consumed by the automotive industry, tyres can be considered to be not only the greatest use of rubber but it is also the greatest source of waste rubber. Since 2006 the disposal of tyres in landfills / waste sites has been prohibited in the European Union under the landfill directive (1999/31/EC). Despite the possibility of some tyre disposal by exporting tyres for retreading to poorer countries in Africa or Asia, recycling is the only sustainable solution to cope with increasing waste tyre production. However, tyres consist of blends of elastomers that are vulcanised with strong chemical crosslinks that are intended to be stable and irreversible. This makes the prospect of tyre recycling difficult. The challenge is to look at cost–effective, energy-efficient and environmentally benign methods to reduce, reuse, recycle or recover rubber (Kumar 2007). Different approaches exist, ranging from the introduction of rubber granules into new rubber components (Kumar et al. 2007), tyre material use in architectural engineering, for example in noise barriers, to devulcanisation, where for example NR can be recycled at 200°C by using diphenyldisulfide (Verbruggen et al. 1999). Some of the different approaches are summarised in Figure 2.40 for the recycling of tyre compounds (Shulman 2004).
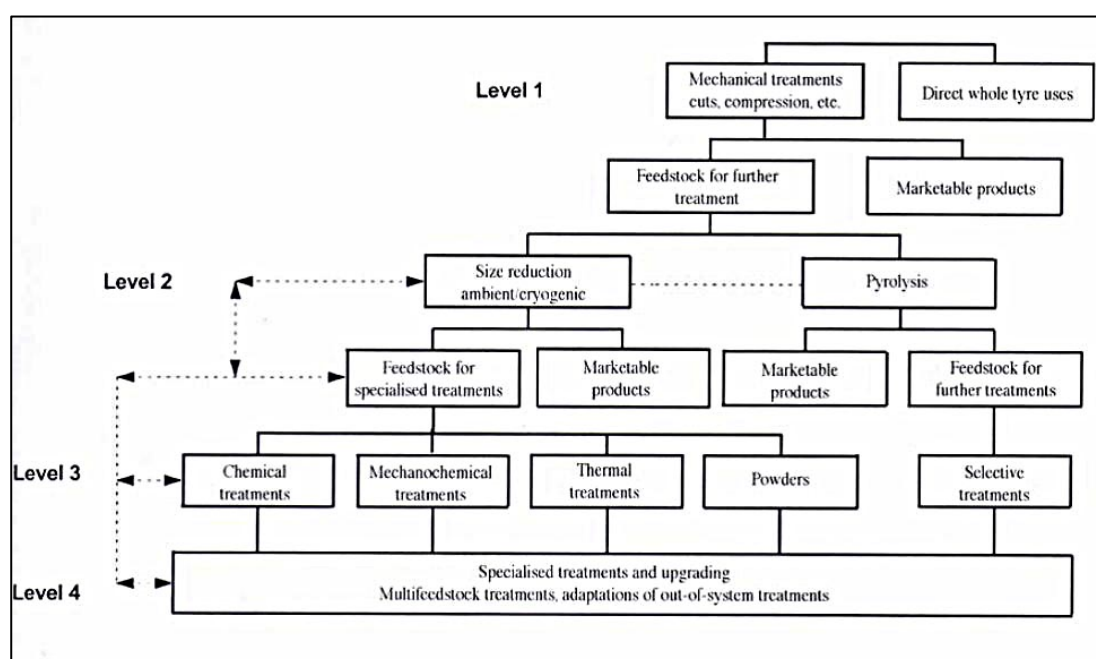
Figure 2.40: Various treatments and technologies used to recycle post-consumer tyres (Shulman 2004).

Not only used materials, which have reached their end of life, but also finished industrial rubber products, for example latex gloves, which do not meet the required standards can be recycled, for example by chemical reclamation (Rajan et al. 2006; Rajan et al. 2007). Another way to reduce the complexity of recycling or at least decreasing the hazards coming from waste material is to limit the amount of chemicals used prior to production. For example, furnace carbon black is partly replaced by precipitated silica, exhibiting improved wet traction performance (Pan 2007). In addition, it was shown by Heideman et al. (2004) that the amount of zinc oxide, which is incorporated at up to 5phr in common compounding formulations, could be reduced to just 2phr, with negligible changes in cure characteristics and physical properties. Furthermore, they showed that for a pronounced reduction of zinc levels, smaller particles and a high surface area are the most important parameters.

2.8   Aims and objectives

The hypothesis of this work is that the geometry of the rubber and rigid surface interfaces influences the rubber friction at macro and micro length scales.

In this literature survey a brief introduction to elastomers is made and it is shown that rubber friction is dependent on many parameters such as sliding velocity, temperature, normal load, abrasion or lubrication due to the viscoelastic nature of rubber. The most critical parameter is the area of contact, or more specifically, the real area of contact. It is affected by each of the above-mentioned parameters in different ways, however, the paramount factor determining the real area of contact is the geometry of the interface in terms of the different length scales of interest such as macro and microasperities. The different effects of these geometrical surface parameters and the resulting displacement mechanisms on different length scales is the principal subject of this investigation.

Many approaches exist trying to describe the phenomenon of rubber friction and due to the complexity of the problem these typically require a very large number of parameters to fit experimental behaviour well (Klüppel and Heinrich 2000; Persson 2001c). Probably the most common of these descriptions of the total friction is given by Kummer (1966) as the sum of adhesion, hysteresis, cohesion and lubrication. By

elaborate modifications, this sum of the total resulting friction can be reduced to just one of the main factors, adhesion (Roberts and Thomas 1975) or hysteresis (Persson 1999). One of the aims of this study is to address the question: is it possible to describe the complexity of rubber friction by a single parameter or are other parameters required such as consideration of the macroscopic shape of the interface? It is thought likely that an entirely geometric effect, similar to the wrapping of a rope around a capstan, contributes under certain conditions, increasing the shear forces between two contacting bodies. The influence of this macroscopic geometric effect at the interface on the measured rubber friction is further addressed in Chapter 4.

Complicating matters further, many of the above mentioned parameters, for example sliding velocity and temperature, interact with each other, making it impossible to give one universal constant for the coefficient of friction, as it is sometimes given for rigid materials. Therefore, it is essential for every test setup that all the relevant information on the adopted parameters is available in order to be able to reach a conclusion. One example of how an imperfect description of the full test parameters can create confusion, are the apparently conflicting data sets proposed by Grosch (1963) and Barquins and Roberts (1986) on the sliding velocity dependence of rubber friction. The outcome of this conflict is that especially the microscopic surface finish of the rubber (either smooth or rough) is of paramount importance and this dependence on the micro-roughness of rubber is re-examined here in Chapter 7 to gain better insight into the dependence of rubber friction on surface preparation.

The effect of macro and micro-asperities also alter the displacement mechanisms at the interface. For rough rubber surfaces in the range of millimetres or tens- or hundreds of micrometers, usually only smooth sliding or stick-slip instabilities arise. For smooth surfaces, where microasperities are at the order of a few micro or nanometres not only smooth sliding and stick-slip is experienced, but also surface instabilities, known as Schallamach waves are seen (Schallamach 1971). Despite a large amount of experimental results on Schallamach waves having been presented in the literature, virtually no information is available on the modelling of these surface instabilites. Furthermore, there is still a significant debate about whether the formation and progression of Schallamach waves are subject to either elastic or viscoelastic properties or a combination of both. This is examined in this work by investigating a

microscopically smooth interface and a FEA modelling approach is undertaken and described for the first time in Chapter 5.

Furthermore, the different sliding mechanisms (smooth sliding, stick-slip and Schallamach waves) are investigated experimentally in terms of surface topography of the rubber, by comparing a microscopically rough surface with an optically smooth surface and the effects of these differences in asperity size on the exhibited sliding mechanisms are compared. In addition, the mechanics of Schallamach waves are investigated, in terms of a transition zone between Schallamach waves and stick-slip motion, which has been recently mentioned by Wu-Bavouzet et al. (2007). From their findings the question arises in how far this relationship to stick-slip motion can be investigated in terms of wave frequency and wave progression velocity and this is discussed in Chapter 6.

3 Materials and methodology

The aim of this work is to investigate the mechanics of rubber friction between a soft rubber and a rigid surface on different length scales of interest in order to investigate the effects of both macro and microasperities on the total frictional force. The purpose of this chapter is to describe the methodologies used for rubber characterisation, starting with a description of the rubber compounding (Section 3.1), followed by the basic mechanical (3.2), thermal (3.3), chemical (3.4) and optical (3.5) analysis of the compounds and their viscoelastic behaviour. The approach required to measure the relevant parameters required for elastomer materials to be modelled using FEA are explained in Section 3.6. Finally, in Section 3.7 the characterisation of rubber friction is described and the friction testing devices developed and used in this work are introduced. If it is not specified then it can be assumed that tests have been done at room temperature (23°C ±3°C).

3.1 Compounding and vulcanisation

In their pure form, raw rubbers are after a large strain inelastic and exhibit poor mechanical properties due to microscopic slippage between polymer chains, leading to a macroscopic, irreversible plastic behaviour. The properties of a rubber are changed remarkably by the addition of various ingredients followed by vulcanisation. A typical list of additives for a practical rubber compound is shown in Table 3.1. Under the combined action of heat and pressure the curing agents form crosslinks between the molecules, strengthening and enabling the rubber to exhibit elasticity. The most common vulcanising agent is sulphur, which demands a rubber containing double bonds with allylic hydrogen. The rubber materials used in this work, SBR and NR, both satisfy this requirement. To increase the time efficiency of the sulphur vulcanisation, accelerators, for example Mercapto Benzothiazyl Disulphide (MBTS) are introduced in the compound (Gent 2001).

Table 3.1: Components of a typical rubber formulation (Sircar 1997).

Component
1. Elastomer
2. Curatives (sulphur, accelerators, peroxides, sulphur-donor systems, etc.)
3. Cure-system activators (zinc oxide, stearic acid etc.)
4. Fillers and reinforcing agents (carbon black, mineral fillers, short fibres etc.)
5. Plasticisers, process oil
6. Other additives (antioxidants, antiozonants, softeners, tackifiers, peptizers, scorch inhibitors, flame retardants, colorants, blowing agents, process aids, etc.)

Activators like zinc oxide (or stearic acid) are introduced into the compound to make accelerated sulphur vulcanisation more efficient, enhance the vulcanizite properties and reduce the vulcanisation time (Heideman et al. 2005). Fillers, such as carbon black, are added to the compound to improve tensile strength or to increase the modulus. A change in properties will be noticed by the amount of filler used, particle size (typically less than $1\mu m$), specific surface area or structure of the filler system (Busfield 2010). The most frequently used fillers are carbon black and silica. While carbon black is directly introduced into the compound, silica has to be used in conjunction with a coupling agent in order to increase the compound properties (Reuvekamp et al. 2009). In addition, process aids such as oils and waxes are used to lower the viscosity of the compound and, therefore, increase the processability. Some additives are used to enhance specific properties or increase resistance against environmental influences such as ozone or oxidation degradation. Extenders, used as either liquid or solid particles (>1 μm), are also used to reduce costs.

The most common rubber types (used in tyre production) are natural rubber, butadiene and styrene-butadiene rubbers. In order to correlate the findings of this work to tyre behaviour, the materials used are natural rubber NR CV 60 and an emulsion styrene butadiene rubber E-SBR 1500, both supplied by the Tun Abdul Razak Research Centre (TARRC) and they will be referred to as NR and SBR in this work from now on. Both unfilled and filled rubbers, with carbon black of the type 'high abrasion furnace' (HAF N330), have been used. In addition, a rubber with a high glass transition temperature was needed for the test setup investigated in Chapter 8. A 3,4 polyisoprene rubber (IR), with the trade name Isogrip, supplied by Lehmann & Voss[2] was used for this reason. A

---

[2]Lehmann & Voss Co. KG, Hamburg, Germany.

brief overview on the general properties and molecular structure of the rubbers is given in Section 2.2. Formulations for sulphur based compounding are given in Table 3.2, while the number behind the abbreviation, for instance NR-50, denotes the amount of the filler in parts per hundred rubber mixed into the compound. The optimum cure times, given Table 3.2 and Table 3.3, were measured using a rheometer, which is further explained in Section 3.3 on thermal analysis.

Table 3.2: Compounding recipes for elastomers in parts per hundred of rubber (phr).

Ingredients	NR-0	NR-50	SBR-0	SBR-50	IR
Natural rubber CV 60	100	100	-	-	-
Styrene butadiene rubber 1500	-	-	100	100	-
3,4 Polyisoprene	-	-	-	-	100
Carbon black (HAF N330)	-	50	-	50	-
Zinc oxide	3	3	3	3	3
Stearic acid	2	2	2	2	1.5
Antioxidant (6PPD)[3]	3	3	3	3	1.5
Accelerator (CBS)[4]	1.5	1.5	-	-	2
Accelerator (MBTS)[5]	-	-	1	1	0
Accelerator (DPG)[6]	-	-	1.3	1.3	0
Sulphur	1.5	1.5	1.5	1.5	1
Curing time /min	7	7	50	50	60
Curing temperature /°C	140	140	160	160	160

For the observation of Schallamach waves, rubbers were needed, which exhibit a high elasticity and stickiness. For these compounds dicumyl peroxide was used as a curing agent. In contrast to sulphur-crosslinks, simple carbon-carbon crosslinks are established by the peroxide vulcanising agent via a free radical process (White and De 2001). The formulations for peroxide compounds are given in Table 3.3, while the number, for example NR1, indicates the amount of peroxide in phr.

---

[3] N-1.3-dimethylbutyl-N'-phenyl-p-phenylenediamine Flexsys (2005). *Safety data sheet on Santoflex 6PPD (Product code 460921)*, Dublin, Flexsys.
[4] N-Cyclohexyl-2-benzothiazyl-sulfenamide
[5] Mercapto benzothiazyl disulfide
[6] Diphenyl guanidine

Table 3.3: Compounding formulations for translucent NR.

Ingredients	NR1	NR2	NR3
Natural rubber	100	100	100
Dicumyl peroxide	1	2	3
Curing time /min	40	40	40
Curing temperature /°C	150	150	150

The unfilled rubbers were compounded using a two-roll mill at QMUL, while the filled rubbers were masterbatched with the aid of an internal mixer and provided by TARRC, as higher shear forces are needed to ensure a dispersion of the carbon black filler. A programmable hot press[7] in combination with a flat sheet mould (200x200x2mm³) were used to vulcanise the rubber at high pressure as shown in Figure 3.1.
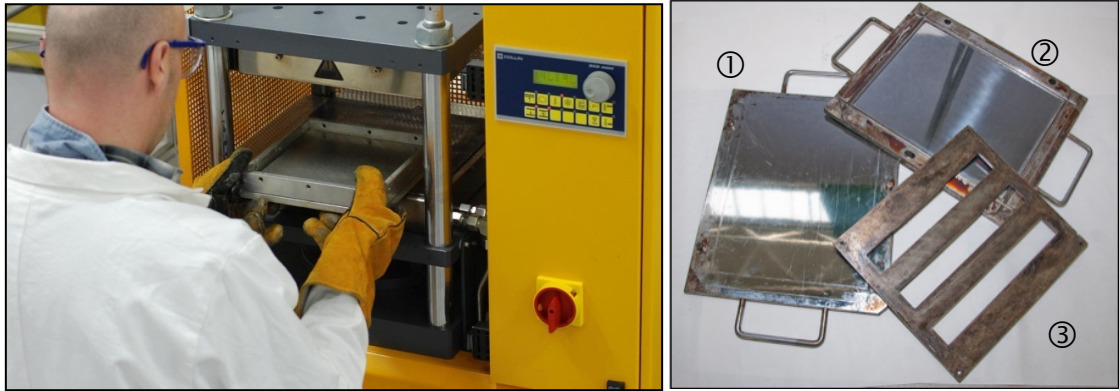
Figure 3.1: Pneumatic hot press used for rubber vulcanisation (left) with flat sheet rubber moulds (right). The polished flat sheet moulds ① and ② can be used together to vulcanise flat sheets of 200x300x2mm3 with a mirror like surface, while ③ functions as an inlay in order to vulcanise test strips of 200x30x5.5mm³. Similar moulds were used to vulcanise rubber with a rough surface.

The cured sheets were used in uniaxial tests used to characterise the rubber behaviour, as well as to investigate the frictional sliding behaviour. As the surface preparation has a fundamental influence during frictional sliding, both smooth and rough rubber surfaces were manufactured. For a smooth surface finish the rubber was cured against a mirror-like, polished steel mould, as shown in Figure 3.1. For a rough surface finish the rubber was vulcanised against a steel mould, which was grit-blasted by using a grit of the granularity specified as P40. The optical difference between the two roughnesses is further analysed in Section 3.5.

---

[7] Dr. Collin GmbH, Ebersberg, Germany, type: P 300 E

3.2   Mechanical analysis

3.2.1   Hardness testing

A Shore A scale durometer[8] was used to characterise the hardness of the entire test compounds (Wallace 1997). The minimum dimensions for a sample are 35mm in width and a minimum of 6mm in thickness, as given by ASTM D 2240 – 02b (ASTM 1999). If the sample has an inadequate thickness, several sheets of the same sample were stacked together. To ensure reliable results the points of indentation have to be at least 12mm distance to the sample edge. Six points of measurements were taken per sample and the mean values for each are given in Table 3.4. As expected, filler increases the modulus and the hardness of an elastomer.

Table 3.4: Shore A hardness values for the tested rubber samples.

	NR-0	NR-50	SBR-0	SBR-50	IR
Hardness [Shore A]	29.8	66.0	42.1	63.6	30.4
Standard deviation (n=6)	0.1	0.2	0.2	0.1	0.2

The measured Shore A hardness value Sh_A can be transferred into the Young's modulus, using an equation given in the literature (Kunz and Studer 2006) as

$$E = \frac{1-\rho^2}{2RC_c} \times \frac{C_a + C_b Sh_A}{100 - Sh_A} \quad , \tag{3.1}$$

where E is the Young's modulus, C_a, C_b and C_c are constants with the values -0.549N, 0.07516N and 0.025mm, respectively. R is the radius of the indenter and ρ is the Poisson's ratio.

3.2.2   Tensile testing

The most common technique used in mechanical characterisation is tensile testing, giving a whole range of material properties in a relatively short time frame, including tensile strength, elastic modulus, elongation to break and yield strength. The Young's

---

[8] Wallace Instruments, Kingston, United Kingdom: Type H17A.

modulus E is given by the initial slope of the engineering stress σ versus engineering strain ε curve:

$$E = \frac{\sigma}{\varepsilon}. \tag{3.2}$$

Dumbbell specimens were stamped from flat rubber sheets using an ASTM D412, type C dumbbell cutter. The thickness of each dumbbell specimen was measured before each test at both ends of the reduced section and in the centre of the sample (ASTM 2002). The average of three measurements is used to calculate the cross sectional area. Other dimensions of the dumbbell specimen are given in Figure 3.2.
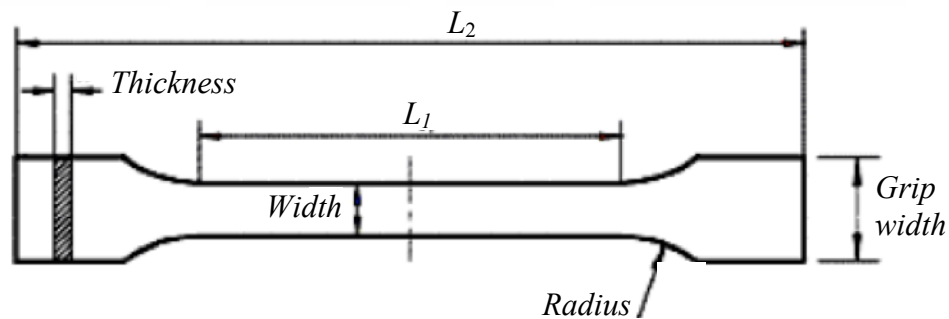
Figure 3.2: The dimensions of the dumbbell specimen used in the tensile tests are given as test length L_1 = 33mm, dumbbell length L_2 = 115mm, dumbbell width = 6mm, grip width = 40mm, radius = 14mm and specimen thickness (ASTM 2002).

An Instron 5567[9] tensile test machine with a 1kN load cell was used, as this machine offers two methods of strain measurements, either from a measure of the crosshead displacement or by using an external video (laser) extensometer, shown in Figure 3.3.

---

[9] Instron, Norwood, USA; type: table top, 5567

Figure 3.3: Tensile test machine with optical following red-laser unit (left) and dumbbell specimen with black dotted benchmarks, specifying the unstrained length H_0 (right).

For rubber materials, which exhibit large strains as well as viscoelastic behaviour, a video extensometer was the method of choice. Before testing, two small points were drawn on the dumbbell shaped samples, acting as bench marks for the optical following unit, as shown in Figure 3.3 (right). These marker points for the optical following unit were either applied by using black ink on unfilled rubbers or applied by using a white correction fluid[10] on filled (black) samples. A difficulty arising from the stretching of the ink marker points can be neglected up to λ=2.0, but will affect the measurement at larger strains, however, measurements of the cord modulus are not affected by this. The initial distance between the benchmarks was measured by the laser extensometer as unstrained length H_0, while H is the instantaneous length, defining the extension ratio λ as:

$$\lambda = \frac{H}{H_0}.$$

(3.3)

Five dumbbell specimens were tested for each different material with a speed of 500mm/min. The mean values of the Young's modulus and a comparison with calculated values, using hardness test results, are given in Table 3.5. All the tests were

---

[10] Bic Deutschland GmbH & CO., Liederbach, Germany; Type: TippEx

carried out according to the ASTM D 412 – 98a. An example stress-strain curve for SBR compared to NR is shown in Figure 3.20.

Table 3.5: Cord modulus for the rubbers over an uniaxial extension ratio λ=1.0 to 1.2.

	NR-0	NR-50	SBR-0	SBR-50	IR
Cord Modulus E [MPa]	1.0	2.3	1.7	4.0	1.0
Standard deviation (n=5)	0.05	0.06	0.05	0.05	0.04
E from hardness tests [MPa]	0.9	4.9	1.7	4.5	0.9

The deviation of the experimentally measured values of cord modulus for NR-50 and the values calculated from hardness tests using Equation (3.1) may result from the fact that NR exhibits a non-linear behaviour at large strains, while the hardness tests only reflects a measurement over a small strain. Therefore, it is likely that small strain non-linearity of the stress-strain curve is responsible for this deviation. The cord modulus for each of the peroxide cured natural rubber samples is given in Table 3.6.

Table 3.6: Cord modulus for peroxide cured rubbers (λ=1.0 to 1.2).

	NR1	NR2	NR3
Cord modulus E [MPa]	0.7	1.2	1.6

3.2.3   Dynamic mechanical analysis

The importance of the glass transition temperature T_g on rubber friction behaviour was first investigated by Grosch (1963) (Section 2.5.5). Several different ways exist for measuring this transition temperature. In this work both dynamic mechanical analysis (DMA) as well as differential scanning calometry (DSC) were used. Both methods can offer specific information on the elastomer. The DMA is a sensitive analytical technique for measuring the modulus (stiffness) and damping (energy dissipation) properties of the materials under a periodic (oscillatory) stress over a wide range of temperatures (Foreman and Reed 2005a), while DSC analyses phase transitions in the compound from an energetic point of view.

The DMA[11] used in this work adopted a tension film clamp, as shown in Figure 3.4, where a rectangular rubber specimen is mounted in uniaxial tension clamps, of which one is oscillated sinusoidal at a frequency of 1Hz and an amplitude of 15μm. In order to determine the viscoelastic properties and the glass transition temperature, the temperature range is varied from -140°C up to 90°C at a heating rate of 3°C/min.
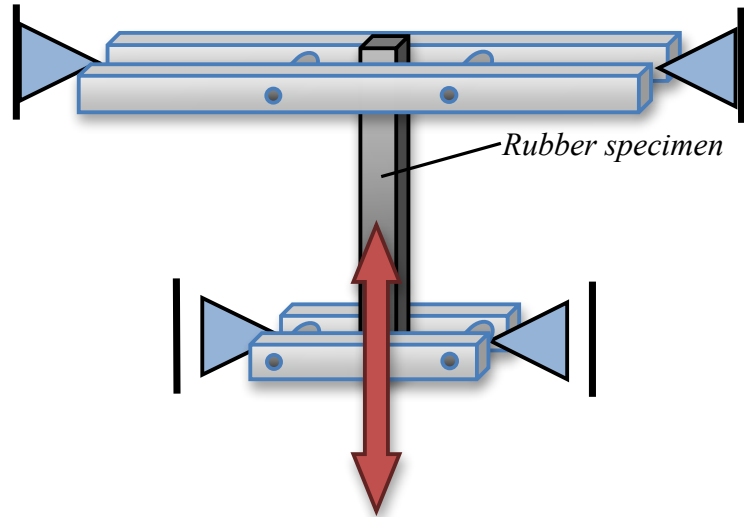
-*Rubber specimen*

Figure 3.4: A rectangular rubber specimen is clamped in tension mode between an upper fixed clamp and a lower oscillating clamp to determine the T_g.

A typical graph showing the temperature dependence of the mechanical properties of an elastomer is shown Figure 3.5. As the sample passes through its glass transition temperature, the storage modulus E' decreases by several orders of magnitude and the loss modulus E'' and tan δ (E''/E') both pass through a maximum (Haines 1995). Commonly, T_g is determined as the onset of the large drop in the storage modulus, which can be specified by the point, where two tangents, drawn to the graph, cross each other (here -56.67°C).

---

[11] TA-Instruments Ltd., New Castle, USA; type:Q-800
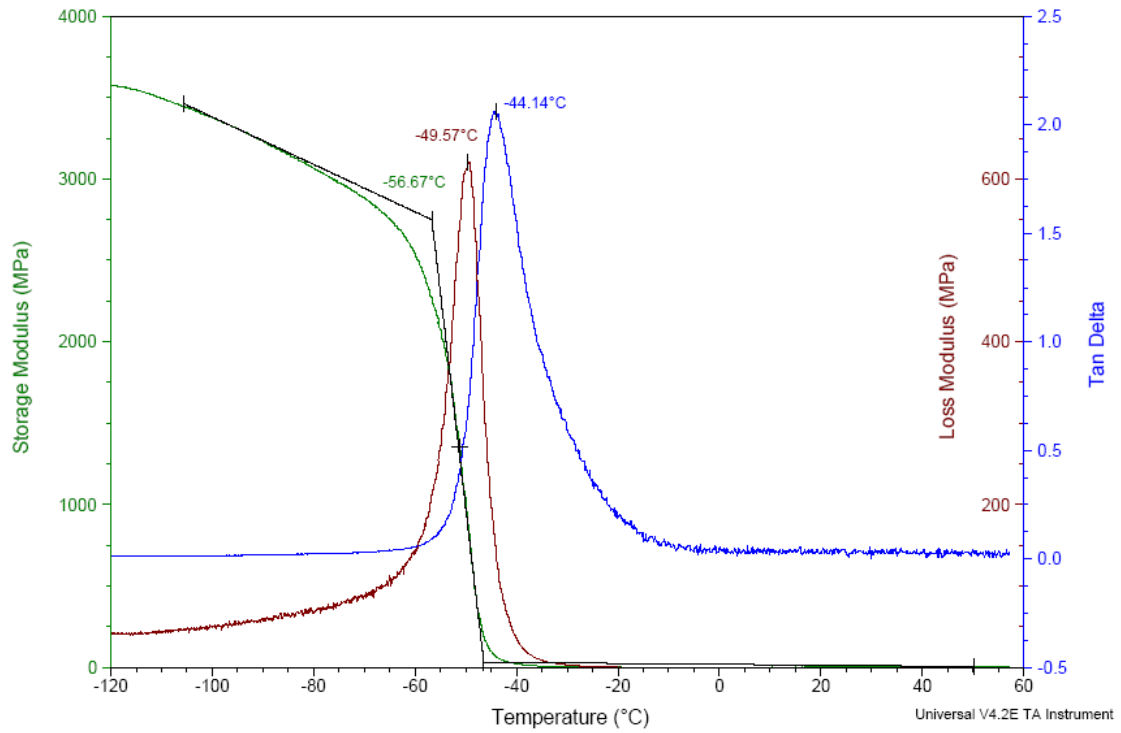
Figure 3.5: Typical DMA graph for an unfilled NR to determine the glass transition temperature T_g. The T_g is usually given as the crossover of two tangents, here given as -56.67°C.

Sometimes the peak in loss modulus is used to define T_g and on other occasions the peak of tan δ is used (Turi 1997). As the three values typically cover a range of about 15°C it is of great importance to know which transition point is specified as the temperature range of usage for an elastomer is usually limited by significant stiffening below T_g (Foreman et al. 2005b) or respectively softening above T_g for a rigid plastic. The measured glass transition temperatures, using the three parameters (for the four tested rubbers) are given in Table 3.7:

Table 3.7: Glass transition temperatures for the tested rubbers (Dick 2001).

	NR-0	NR-50	SBR-0	SBR-50
T_g *Storage Modulus [°C]*	-57	-49	-42	-41
T_g *Loss Modulus [°C]*	-50	-45	-35	-35
T_g *tan δ [°C]*	-44	-41	-30	-29
Literature values	-70	-70	-50	-50

It has to be noted, that the glass transition temperatures of both NR and SBR are not in accordance with the glass transition temperature given in literature. The reason for the deviations is that the transition point is a rate dependent process with segmental motion,

involving a molecular relaxation. If the frequency is for example increased, the molecular relaxations can only occur at higher temperatures and consequently T_g increases (Turi 1997; TA-Instruments 2005a). As an example this is shown for Polyethyleneterephthalate in Figure 3.6 (Thomas 2005). Similar behaviour is experienced when the test frequency is changed for a rubber sample.
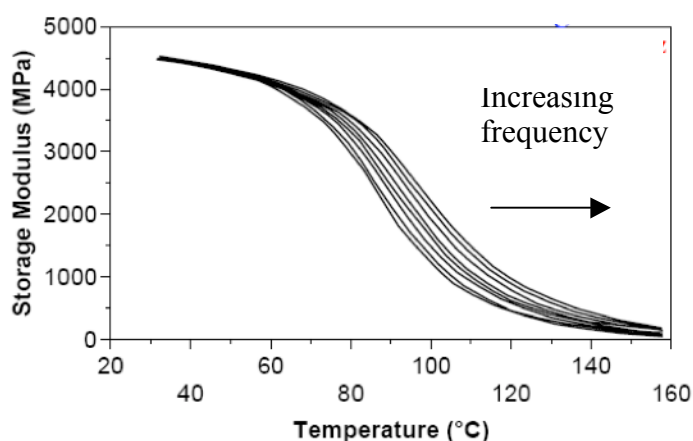
Figure 3.6: With an increase in test frequency the values for T_g shift to higher temperatures. The graph shows frequencies from 0.1 Hz (left curve) up to 20 Hz (right curve) (Thomas 2005).

For this reason, DSC was used as a second test of T_g as is described later. A further application of the DMA test is given in Chapter 4 in Figure 4.15 and Figure 4.16, where the hysteresis curves, measured on the DMA are shifted into a mastercurve using a WLF approach.

3.2.4   Resilience testing

A resilience test was used as another method to measure the dynamic properties of a compound (Southern and Thomas 1972). Commonly, this test can be either executed by a commercially available pendulum tester or with a simple ball drop setup, both of the employed machines in this work are shown in Figure 3.7.
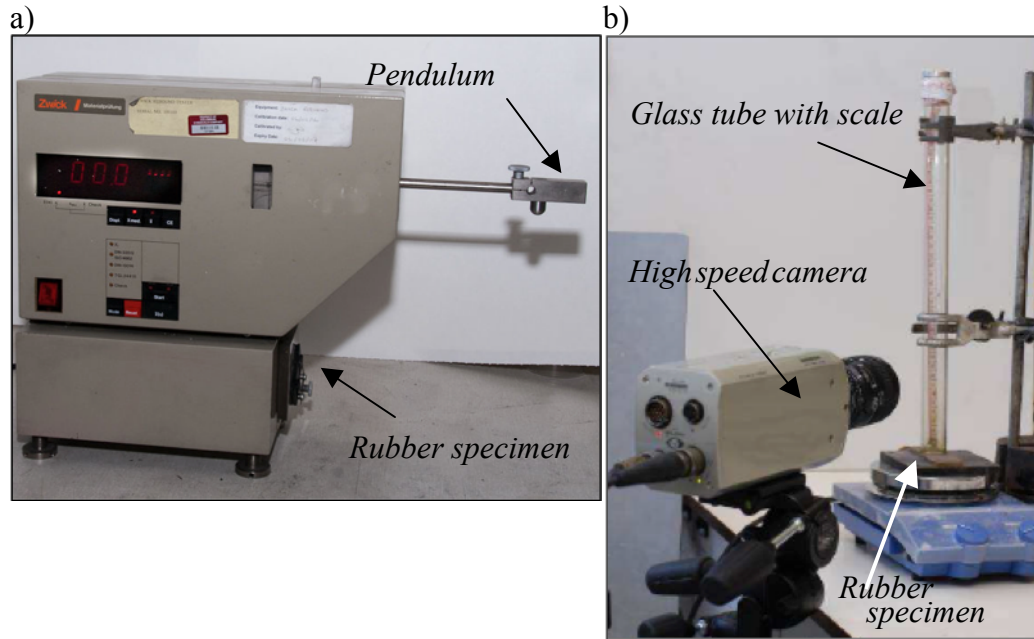
Figure 3.7: a) Zwick resilience tester and b) high-speed camera with ball drop tester. The Zwick tester measures the resilience as the rebound height of a pendulum after the impact with a rubber specimen. The ball drop tester measures the rebound height of a steel ball dropped on a rubber specimen mounted on a temperature control unit (blue).

The pendulum tester[12] measures the hysteresis loss, through the ratio of the rebound height of the pendulum arm after impacting with the rubber specimen to the initial release position. In contrast, for the ball drop setup the hysteresis is defined as the ratio of rebound height, of a small steel ball (R=3mm) to the initial release height. Consequently, the resilience can be defined as:

$$Resilience = \frac{Rebound\ Energy}{Initial\ Energy} \quad . \tag{3.4}$$

The pendulum test has fixed parameters (impact weight, radius of impacting rigid body, drop height) and follows common test standards, while the ball drop setup had to be tested and evaluated first. Both test setups have been examined in terms of comparability and reproducibility and the procedure adopted is explained in detail by Baumard (2009). This study showed that the tackiness, or surface adhesion, of a compound affects the resilience measurement and to avoid this complication, measurements on a talcum dusted rubber specimen were recommended. The measured

---

[12] Zwick GmbH & Co. KG, Ulm, Germany. Type:

results for both test methods for unfilled and filled NR and SBR rubbers are shown in Chapter 4.

3.3   Thermal analysis

3.3.1   Cure rheometry

In order to cure an unvulcanised rubber masterbatch, the optimum cure time was measured using a moving die rheometer (MDR). The employed MDR[13] is designed to measure the change in rubber stiffness over time using maximum torque measurements from an oscillating rotor encapsulated in a sealed die (Dick 2001). To prevent the rubber from slipping on the surface, the rotor is corrugated. The upper die of the rheometer, shown in Figure 3.8 a), can be lowered pneumatically in order to enclose the rubber under pressure with the lower die in a test cavity, as shown Figure 3.8 b).
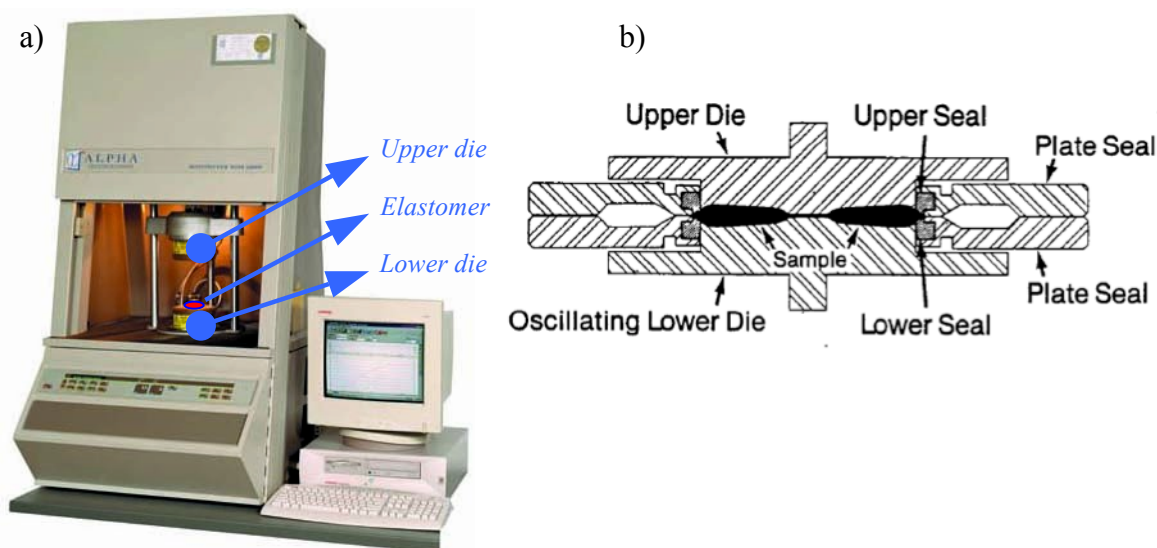
Figure 3.8: a) Rheometer MDR2000E[14]. b) Schematic figure of the test cavity shown in a) (Sezna 1991).

Some of the parameters, which can be deduced from the rheometer, are shown in Table 3.8 (Sezna and del Vecchio 2003).

---

[13] Alpha Technologies, Swindon, Wiltshire, United Kingdom
[14] Image courtesy of Alpha Technologies, United Kingdom.

Table 3.8: Parameters, which are given as an output by the MDR2000E.

Cure parameter	Description
M_L	Minimum peak torque per angle
M_{HF}	Maximum torque when curve plateaus
M_{HR}	Maximum torque of a reverting curve
M_H	Highest torque during test when no plateau or maximum is reached
t_X	Minutes to x% of M_H

Three typical graphs for the cure rheometer are shown in Figure 3.9:
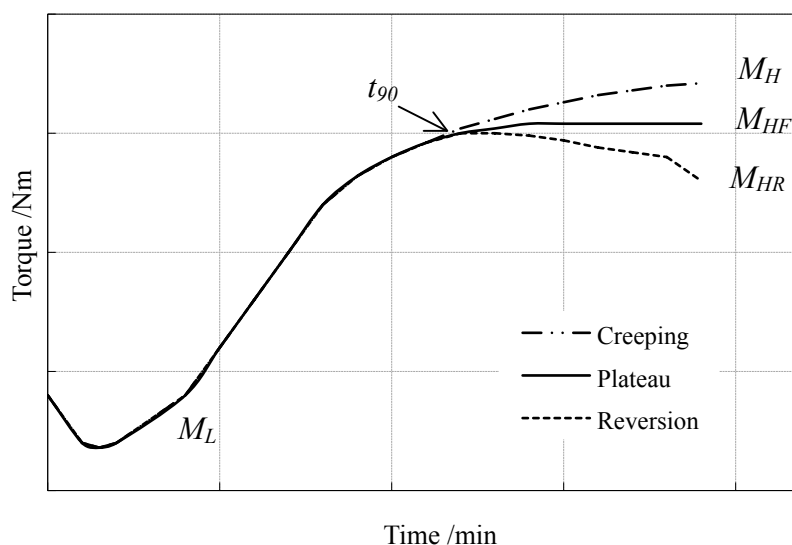
Figure 3.9: Schematic graph of cure time versus torsion. Redrawn and modified from (Gent 2001).

For rubber materials that exhibit a plateau or reversion type cure, the t_{90} value determines the time at which the compound reached 90% of the highest torque measured, and this is often used as the criterion for setting moulding cure time. For rubber sheets with similar dimensions to the rheometer test pad, typically with a thickness of 2mm, this cure time can be used, however, if the sample geometry is larger, then in practice longer cure times are required. The optimum cure times for the materials employed in this work are given in Table 3.9, where NRx denotes the peroxide cured natural rubbers, and NR-x and SBR-x the sulphur cured systems.

Table 3.9: Optimum cure times at different temperatures for a 2mm rubber sheet.

Rubber /phr	Cure Temperature /°C	t_{90} /min
NR1	140	21
NR2	140	21
NR3	140	21
NR-0	140	7
NR-25	140	7
NR-50	140	7
SBR-0	160	50
SBR-25	160	50
SBR-50	160	50

As shown in Table 3.9, the ideal cure time for natural rubber at 140°C is quite short, when a sulphur system is used. In order to establish a homogenously cured sample, especially for thicker sample geometries, a longer cure time is advisable, therefore, a lower cure temperature should be used. By using an Ahrenius law (McNaught and Wilkinson 1997), over a relatively narrow temperature range a decrease of 10°C doubles the reaction time, as can be seen in Figure 3.10. In contrast, for industrial purposes, short processing times are desired for cost efficient production, which can be established by using chemical accelerators (Section 3.1), however, for thicker geometries or for particularly complex components, such as tyres, longer cure times are needed in order to establish a homogenous cure. Moreover, cure kinetics of rubber are complicated as different chemical reactions are happening simultaneously, so it is advisable to experimentally determine the optimum cure state (White and De 2001).
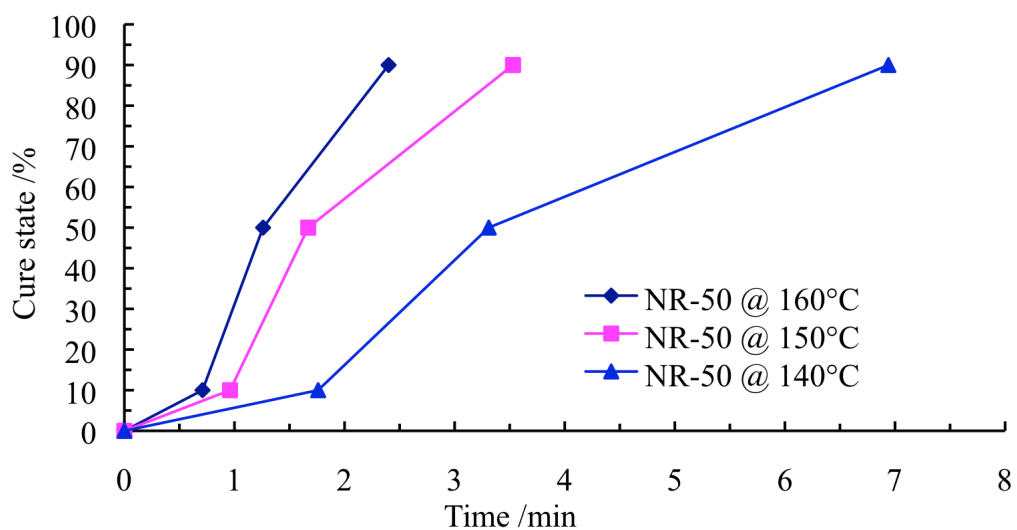
Figure 3.10: Cure state versus time for NR-50 at three different temperatures.

3.3.2   Thermogravimetric analysis

High-resolution thermogravimetric analysis (TGA) was used to determine the type of polymer and the amount of carbon black used in a rubber sample in order to validate the master batch formulations, which were provided externally. The principle of TGA is based on the measurement of change in weight loss with increasing temperature. Figure 3.11 shows the schematic working principle of the used TGA[15].
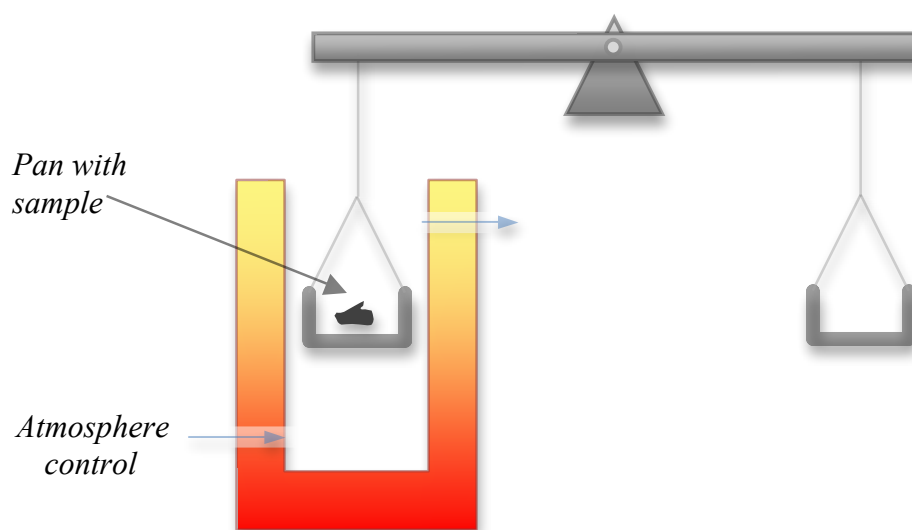
Figure 3.11: The schematic working principle of the TGA Q500 used in this work is shown.[16] A specimen in the pan (left) is heated under a controlled atmosphere and the weight loss is measured by a balance using an empty reference sample (right).

Prior to analysis, possible resins (for example oils or waxes) in the compound were extracted using a Soxhlet extractor, described in Section 3.4 and especially used in chapter 7. This procedure was necessary, as some volatile resins camouflage the rate in weight loss of other ingredients during the decomposition. Consequently, two samples of the same compound, one extracted and one virgin, were tested via TGA to monitor possible differences. A heating rate of 40°C/min was used, which automatically reduces to 0.01°C/min as a response to an occurring weight loss (Fernández-Berridi et al. 2006). A typical graph for a sample (±5mg) of SBR-50 is shown Figure 3.12. While the ordinate on the left hand side denotes a measure of weight lost, shown as the green line, the right ordinate depicts the ratio of weight loss per degree centigrade, shown as the blue line. Firstly, the low molecular weight volatiles (for example the low boiling

[15] TA Instruments, New Castle, USA
[16] Image courtesy of TA Instruments

temperature plasticizers and oils) are decomposed (4.9% weight loss) until the main component SBR (61.2% weight loss) degrades over a temperature range that is specific for the polymer. The temperature is increased up to 600°C in an inert atmosphere in this first step. When no further weight loss occurs, the temperature is reduced to 400°C and then the atmosphere is switched from nitrogen to oxygen and organic fillers such as carbon black is oxidised (31.9% weight loss) in a second heating period up to 800°C. The remaining residues (2%) are ashes, which include inert additives like zinc oxide. Inorganic fillers such as silica would increase the amount of residue, as they would also not decompose.
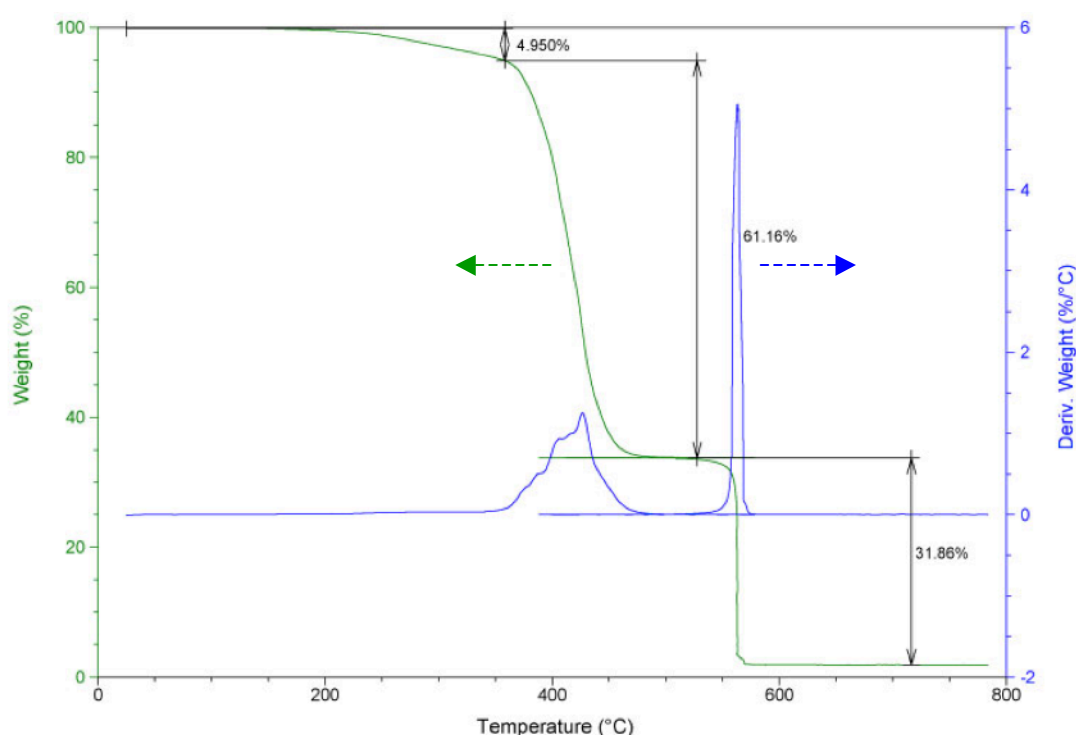
Figure 3.12: Typical TGA graph, showing the weight loss [%] over temperature [°C] for SBR-50.

Figure 3.12 shows that the claimed carbon black content (50phr) in the compound is accurate as supplied. Equivalent tests for the other elastomers NR-0, NR-50 and SBR-0 were done and the results are shown in Table 3.10. Soxhlet extraction of the four model compounds showed only subtle differences between virgin and Soxhlet extracted samples.

Table 3.10: Amount of filler in used rubber samples, determined by TGA.

	SBR-0	SBR-50	NR-0	NR-50
Polymer [phr]	100	100	100	100
Filler [phr]	---	48	---	54
Residue [phr]	8	8	7	8

The polymer degradation temperature can be used to identify the type of polymer. Typical degradation temperatures T_{DEG} for SBR and NR are given in Table 3.11 (Agulló and Borrós 2002; Fernández-Berridi et al. 2006) and compared to the experimentally observed temperatures.

Table 3.11: Tested degradation temperatures compared to literature values.

	SBR	NR
Literature value T_{DEG} [°C]	420 – 460	350 – 380
Test result T_{DEG} [°C]	417	320

The deviation in temperatures from the literature values in Table 3.11 was probably due to the fact that high resolution TGA was used, in which the heating rate is decreased to 0.01°C/min as soon as a change in weight is noticed. In contrast, the literature values are based on constant heating rates of 10°C/min. With an increase in heating rate the degradation of the polymer is shifted to higher temperatures, as shown in Figure 3.13 (Seidelt et al. 2006). The degradation maximum for NR measured at 2°C/min shifts about 40°C to higher temperatures when a rate of 10°C/min is used. Consequently, the Hi-Res TGA used here gives a more accurate analysis of the degradation temperature for the polymer.
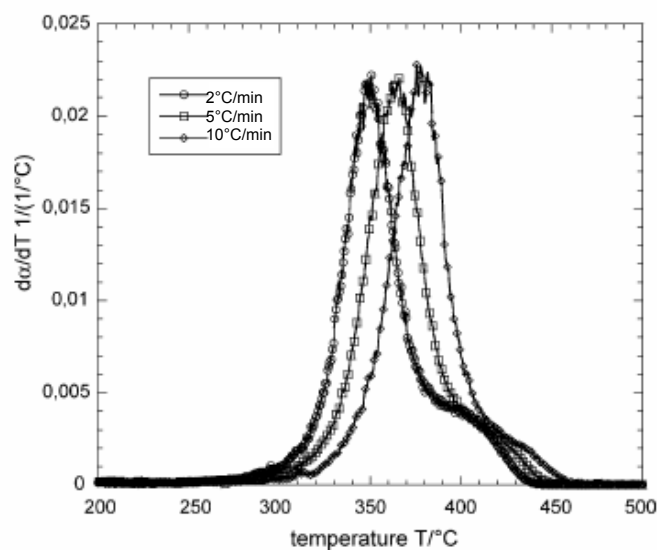
Figure 3.13: Degradation maximum (dα /dT) for NR at different heating rates (Seidelt et al. 2006).

From this brief description it can be argued that TGA is a valuable tool to investigate decomposition temperatures of polymers and to evaluate the ratio of the different components in the compound. This technique is used in chapter 7.

3.3.3 Differential scanning calorimetry

As an additional method to DMA, DSC[17] was also used to characterise the glass transition temperature. DSC compares the difference in energy required to heat both, a sample portion in a heating pan and an empty reference pan as a function of temperature (Blaine 2005). The schematic test principle of the DSC is shown in Figure 3.14:
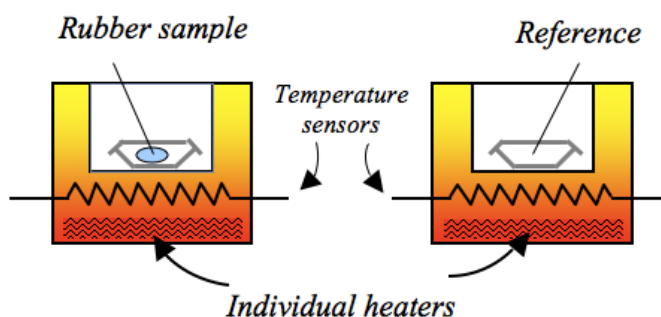
Figure 3.14: The DSC measures the heat flow in a sample pan compared to an empty reference pan. The difference in heat absorption is measured with temperature sensors. Redrawn from Blaine (2005).

---

[17] Mettler Toledo, Inc., Columbus, Ohio, USA; type: DSC822^{e}

A glass transition temperature shows as a change in heat flow, manifesting as a sigmoidal shift in the baseline (ΔY) as shown in Figure 3.15. The extrapolated onset, determined with two tangents similar to DMA, is denoted as T_g.
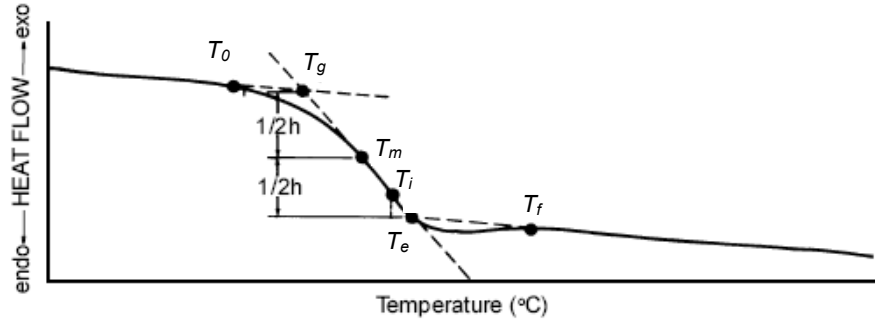
Figure 3.15: A typical DSC graph used to determine the glass transition temperature T_g. To is the temperature of first deviation, Tm the midpoint temperature, T_i the inflection temperature, T_e the extrapolated end set temperature and T_f the return to baseline temperature (TA-Instruments 2005b).

The minimum working temperature of the available DSC is -60°C. At low temperatures, close to the maximum cooling temperature of the DSC it was advisable to choose a low heating rate in order to get a moderate baseline (first part of the graph before the transition, see Figure 3.15). A heating rate of 5°C/min was chosen and the results are given in Table 3.12:

Table 3.12: Glass transition temperatures determined using DSC (Dick 2001).

	NR-0	NR-50	SBR-0	SBR-50
Glass transition T_g [°C]	T_g< -60	T_g< -60	-50	-51
Literature value T_g [°C]	-70	-70	-50	-50

Only results for SBR are gained accurately via DSC, as the NR curves do not show any point of transition. The reason for this is the lowest working range of -60°C, which is higher than the referenced literature value for NR of -70°C. The DSC does depict the T_g for SBR in accordance to the literature (Dick 2001), with an accuracy better than the DMA (see Table 3.7). As a result it is shown that the values for the transition given by the DMA are too high, due to the frequency dependence of the test. The values for T_g are used later in Chapters 4 and 7 as part of the WLF time-temperature superposition.

3.4   Chemical analysis – Soxhlet extraction

Soxhlet extraction techniques are used to remove the organic additives from polymer/black/inorganic components without simultaneously removing significant amounts of the polymeric phase (Loadman 1998). In Figure 3.16 a schematic figure of the extractor apparatus is shown.
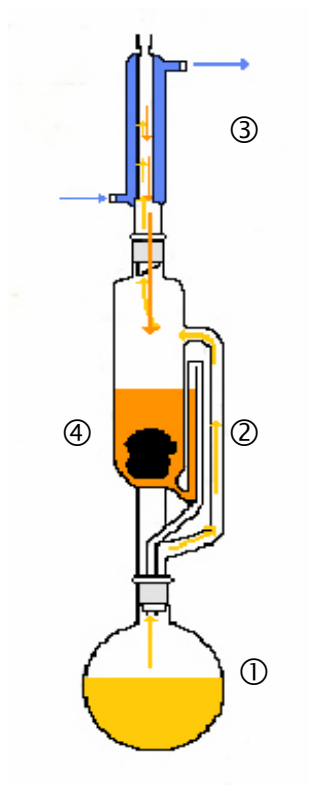
Figure 3.16: Soxhlet extractor. The solvent cycle is indicated by arrows and numbers (Baumard 2009).

The solvent is heated until its boiling point in flask ①, so that solvent vapour rises up in the distillation arm ②. With the aid of a water-cooling unit ③ the solvent condenses and flows back into the sample chamber ④, where the rubber sample swells and soluble components are extracted. If a critical volume of solvent is reached, it empties via a siphon-mechanism and the cycle ① to ④ is repeated. For solvent extraction Loadman (1998) suggests 2-propanol for unvulcanised synthetic rubbers, or either butanone or acetone for vulcanised synthetic rubbers. Analytical acetone (Propanone) 99.8+% (GLC) 0.791g/ml, (FisherScientific 2007)) was used as a solvent. In the extraction process the rubber acts as a gel in which the level of swelling depends on the number of

crosslinks. According to ASTM D 297-93 (ASTM 2004a) the extraction should undergo at least 300 cycles, while ISO 1407:1992 (ISO 1992) suggests a minimum of 160 cycles. In this work the sample was extracted for 24 hours, allowing for about 300 cycles. However, it was validated to assure that all soluble components were extracted completely after this time period. For this reason samples were each marked with a number of cuts, so that they could be differentiated after the acetone extraction. Different samples were left in the extraction process for up to 72 hours. It was found that overnight extraction (24 hours) achieves complete solvent extraction with a good reproducibility. The extracted rubber samples were tested further in DMA and TGA. If the extracted solvent were of interest, thin layer chromatography could be used for separation of different phases and the further analyse of other components (Sherma 1991).

3.5   Optical analysis

As described in Section 3.1, two rubber surface finishes, rough and smooth, were moulded onto the tested rubbers throughout this work. For the optical analysis a scanning electron microscope (SEM)[18] as well as a non-contact three dimensional surface measurement instrument[19] were used.

3.5.1   Scanning electron microscope

The imaging process of a SEM[18] is based on raster scanning of the sample surface by a high-energy beam of electrons. The interaction between surface atoms and the electron beam produces signals, which can be interpreted in terms of surface topography. The used samples in this work were cleaned with propanol and acetone and were cut to a square shaped specimen with a length of 5mm in order to be glued with conducting glue to a sample holder. For the SEM a sample or at least the sample surface must be electrically conductive to prevent the accumulation of electrostatic charge, so that all samples used in this work were coated with a thin layer of gold. The information on magnification and energy of the electron beam (typically 10keV) are both given in the

[18] FEI, Hillsboro, Oregon, USA. Type: Quanta 3D ESEM
[19] Scantron Ltd., Taunton, UK. Type: Proscan 2000

SEM pictures for a) the rough and b) the smooth surface in Figure 3.17.

a)   b)
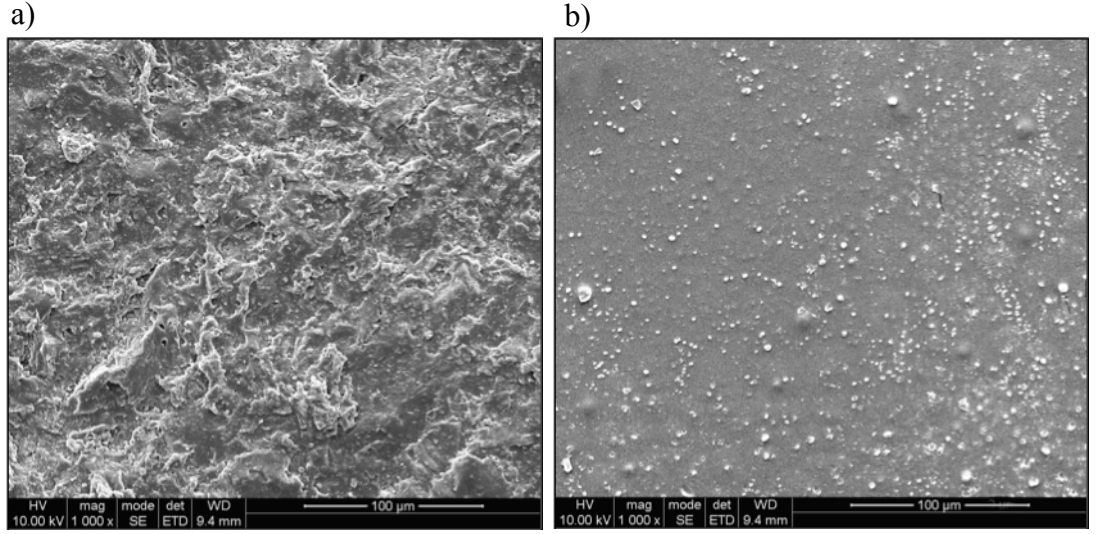
Figure 3.17: SEM surface scans of a) a rough and b) a smooth NR-0 rubber sample.

3.5.2   Topography characterisation

A non-contacting surface roughness measurement instrument[19] (Scantron Proscan) was used to measure the three-dimensional topography of a surface of interest. By measuring the intensity of light reflections of a focussed light beam on a given surface an evaluation of different roughness parameters is possible. Two roughness parameters were chosen to characterise the roughness of the rubber surface. The universally recognised roughness average R_a measures the arithmetic mean of the absolute values of profile deviations from the mean line and is given as

$$R_a = \frac{1}{L} \int_0^L |z(x)| dx \quad ,$$

(3.5)

where L is the assessment length. The second parameter R_{max} determines the maximum peak to valley height. Both parameters are also schematised Figure 3.18.
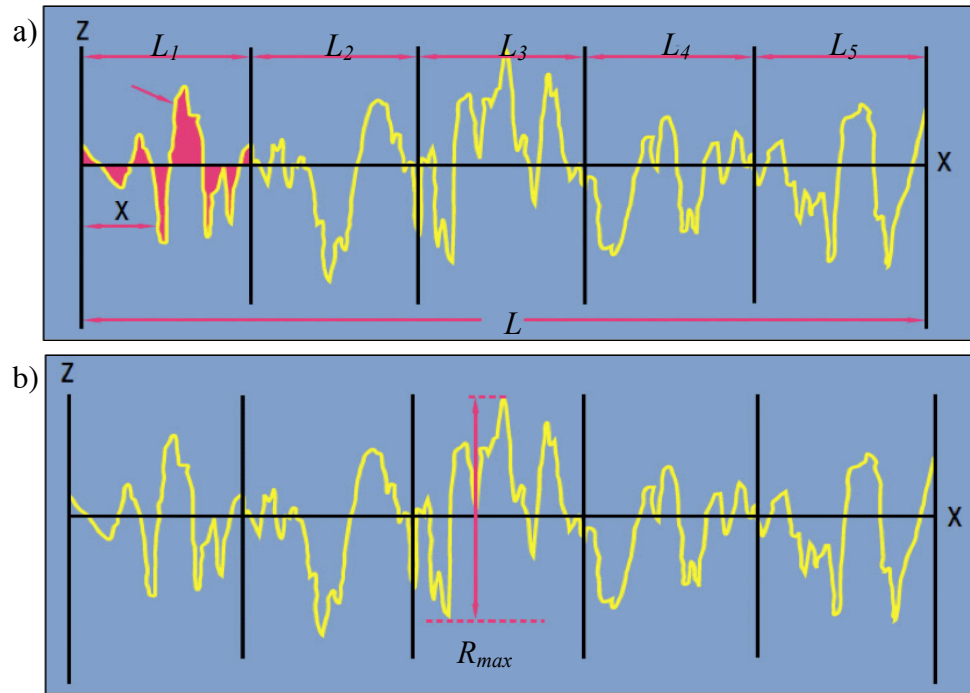
Figure 3.18: The schematic figure in a) and b) show the characterisation of a randomly rough surface. a) The roughness average R_a determines the arithmetic mean of the absolute values of profile deviations from the mean line (coincident with the X-axis), where L is the assessment length and L_i are the sampling lengths. The coloured area highlights deviating peaks from the mean line (black) In b) R_{max} measures the maximum peak to valley height (Hobson 2005).

The rubber profiles, shown in Figure 3.19, were measured over a square of 5mm length. The rubber was fixed at the bottom of the Scantron using double sided tape to avoid movement during the measurement. The optical head had the specification 'L25/2H' and offers a resolution of 0.1μm. The value of R_{max} is 21μm for the rough and 12μm for the smooth surface, and the roughness average R_a, for the rougher surface has a value of 3.2μm and the smooth surface has a value of 1.8μm. While an optical difference is clearly seen from the SEM images in Figure 3.17, the surface roughness values determined via the surface measurement instrument are only of minor difference. The frictional behaviour of both surfaces is further examined in Chapters 6 and 7.
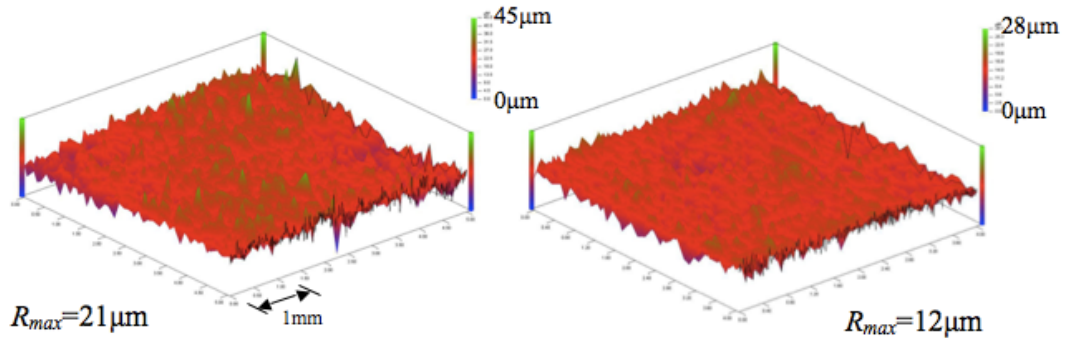
Figure 3.19: Both a) rough and b) smooth NR-0 rubber surfaces are shown as 3D topography scans.

3.6   Derivation of FEA parameters

3.6.1   Stored energy functions

The following section describes how coefficients for SEFs were derived in order to describe the elastomeric behaviour for use in FEA. As shown by Kumar (2007), Liang (2007) and Jha (2009), unfilled materials (NR-0 and SBR-0) can be satisfactorily described by a simple, two-coefficients Mooney SEF, while filled elastomers, are more appropriately described by a more complex Yeoh SEF. Both of the SEFs are implemented in the software package Abaqus 6.7. The Mooney SEF is given as:

$$W = C_1(I_1 - 3) + C_2(I_2 - 3), \tag{3.6}$$

while the Yeoh SEF is represented by

$$W = C_{10}(I_1 - 3) + C_{20}(I_1 - 3)^2 + C_{30}(I_1 - 3)^3, \tag{3.7}$$

While the strain invariants I_1 and I_2 are defined according to Equations (2.10) to (2.12) in Section 2.3. The coefficients C_i and C_{i0} are the coefficients for the Mooney and Yeoh SEF respectively, and can be determined via the stress-strain data gained from a uniaxial tensile test. Rivlin (1956) proposed the relationship between the principal true stresses (σ_{T1}, σ_{T2} and σ_{T3}), principal extension ratios (λ_1, λ_2 and λ_3) and the partial derivates of the strain energy W, given in Equation (2.17). For a uniaxial, simple extension test the relationship is given as the reduced stress (Rivlin 1956):

$$\sigma^* = \frac{\sigma}{\left(\lambda - \lambda^{-2}\right)} = 2\left[\left(\frac{\partial W}{\partial I_1}\right) + \frac{1}{\lambda}\left(\frac{\partial W}{\partial I_2}\right)\right]. \tag{3.8}$$

where σ is the engineering stress, defined as the ratio of force and the unstrained cross sectional area of a test piece. If a Mooney SEF is desired, Equation (3.8) can be rearranged to give the reduced stress as:

$$\frac{\sigma^*}{2} = \frac{\sigma}{2\left(\lambda - \lambda^{-2}\right)} = C_1 + \frac{C_2}{\lambda}. \tag{3.9}$$

Typical stress-strain curves are given in Figure 3.20:
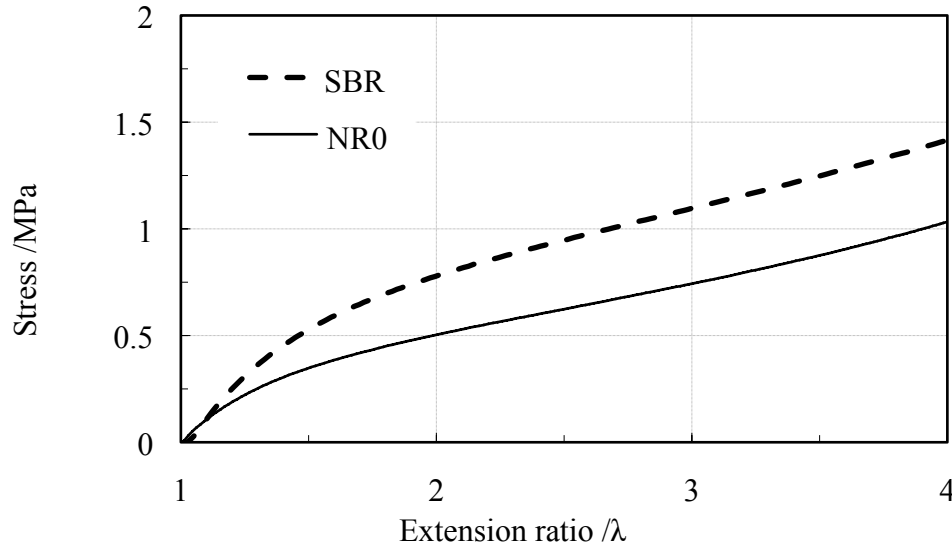
Figure 3.20: Typical stress strain curve for unfilled SBR and NR measured using tensile testing (Section 3.2.2) until λ=4.0. The (video) extension ratio is limited to extensions up to 200mm, which is the maximum observation field of the laser extensometer. At higher extension ratios NR shows a stiffer behaviour than SBR.

From Equation (3.9), the data for unfilled rubbers can be plotted as half of the reduced stress versus $1/\lambda$ as shown in Figure 3.21, where the linear fit for the FEA is shown:
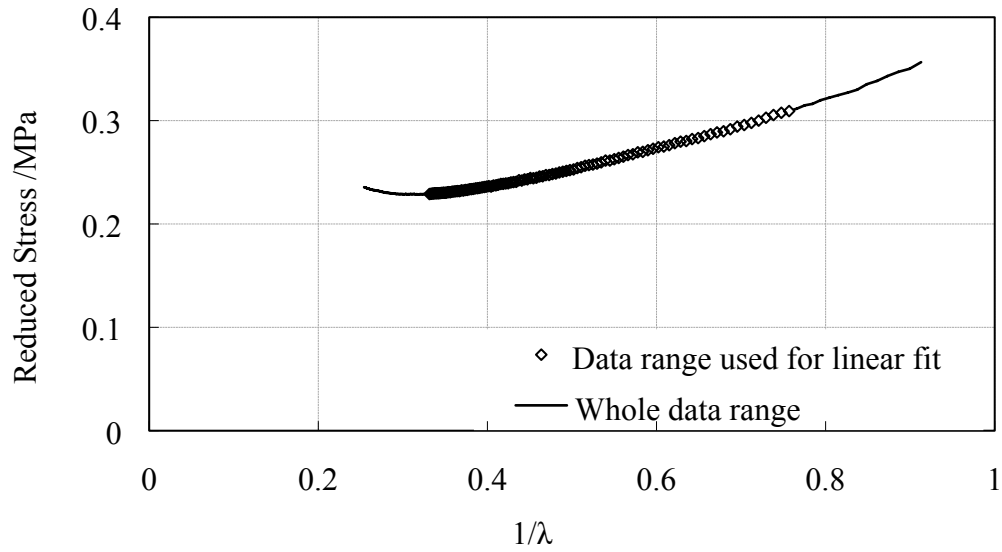
Figure 3.21: Reduced stress σ^* vs. $1/\lambda$ for NR-0.

The coefficient C_1 is given by the intercept of the trend line with the ordinate, while C_2 is derived as the slope of the straight part of the curve. The calculated coefficients are given in Table 3.13. The bulk compliance D_{com} is calculated by Equation (2.72) and the density was determined experimentally as is described in Kumar (2007).

Table 3.13: Parameters used in the FEA model and for the Mooney SEF.

Materials	C_1 /MPa	C_2 /MPa	D_{com} /(MPa)$^{-1}$	Density /10^3 kgm^{-3}
NR-0	0.0835	0.1165	0.065	0.996
SBR-0	0.1279	0.2012	0.07	0.998

The good correlation between FEA and experimental data up to an extension ratio of 2.0 is shown in Figure 3.22.
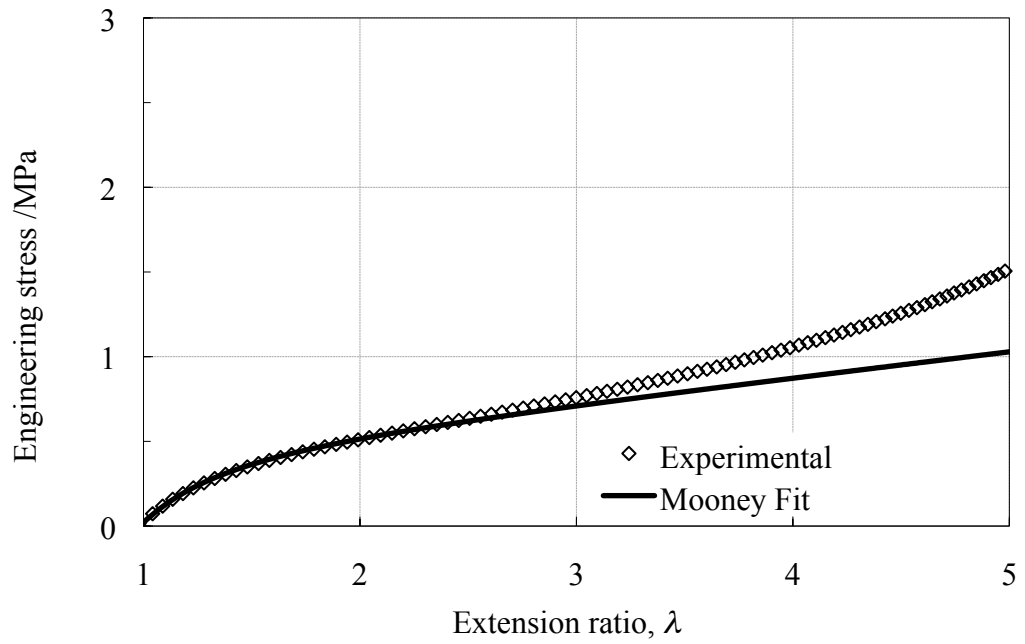
Figure 3.22: Comparison between Mooney fit by FEA software and experimental data for NR-0.

In case of carbon black filled elastomers, which cannot be represented well by the Mooney SEF, the Yeoh SEF was employed. Equation (3.8) can be rearranged in combination with Equation (3.7) to derive the reduced stress as:

$$\frac{\sigma^*}{2} = \frac{\partial W}{\partial I_1} = 3C_{30}\left(I_1 - 3\right)^2 + 2C_{20}\left(I_1 - 3\right) + C_{10}. \tag{3.10}$$

Similar to the Mooney-fit, the reduced stress is plotted against (I_1-3) as shown for SBR-50 in Figure 3.23:
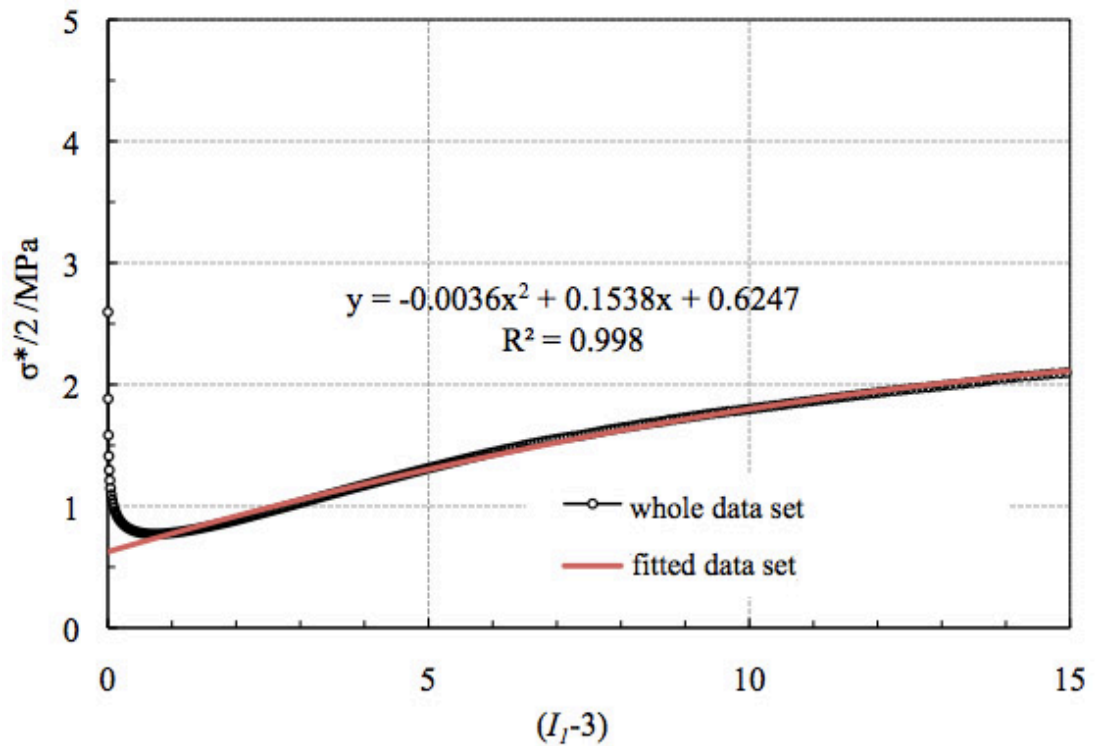
Figure 3.23: Half of reduced stress versus I_1-3 for filled SBR-50 to determine the Yeoh-SEF coefficients.

Ignoring the small strain complication the equation gives a good quadratic fit as shown in Figure 3.23 so that the curve can be fitted for SBR-50 as

$$\frac{\sigma^*}{2} = \frac{\partial W}{\partial I_1} = -0.0067\left(I_1 - 3\right)^2 + 0.3057\left(I_1 - 3\right) + 1.2396, \tag{3.11}$$

allowing the coefficients to be deduced according to Equation (3.10) and given in Table 3.14.

Table 3.14: Parameters used in the FEA and in the Yeoh SEF.

Materials	C_{10} /MPa	C_{20} /MPa	C_{30} /MPa	D_{com} /MPa^{-1}	Density /10^3 kgm^{-3}
NR-50	0.6177	0.0879	-0.0015	0.052	1.119
SBR-50	0.6120	0.0772	-0.0012	0.03	1.123

The FEA models in which these parameters are applied are discussed separately in the relevant chapters 4 and 5 and the input decks are given for both chapter in the Appendix in Sections 9.3 and 9.4 respectively.

3.6.2   Mesh convergence

Due to the nature of the finite element approach the accuracy of a model improves as the number of elements is increased. There is a convergence point, at which a further increase of mesh density no longer results in a change in the calculated output. Figure 3.24 gives a representative example on the mesh size dependence when using FEA models. The contact area of a spherical rigid slider indenting into a rubber block is shown for different element sizes for SBR-0. At small deformations the contact area is supposed to increase linearly. However, for large elements (length=0.3mm), a step like graph is obtained, as the contact area is measured by the sum of the surface area of all elements in contact. With a decrease in element size, a more accurate result is gained and below an element length of 0.1mm the calculated results converge. Consequently an element length of 0.1mm was chosen for this type of analysis to obtain accurate results without an excessive increase in computational costs. Similar procedures were conducted for each of the different models used in this work in order to decide on an appropriate mesh size to represent the model.
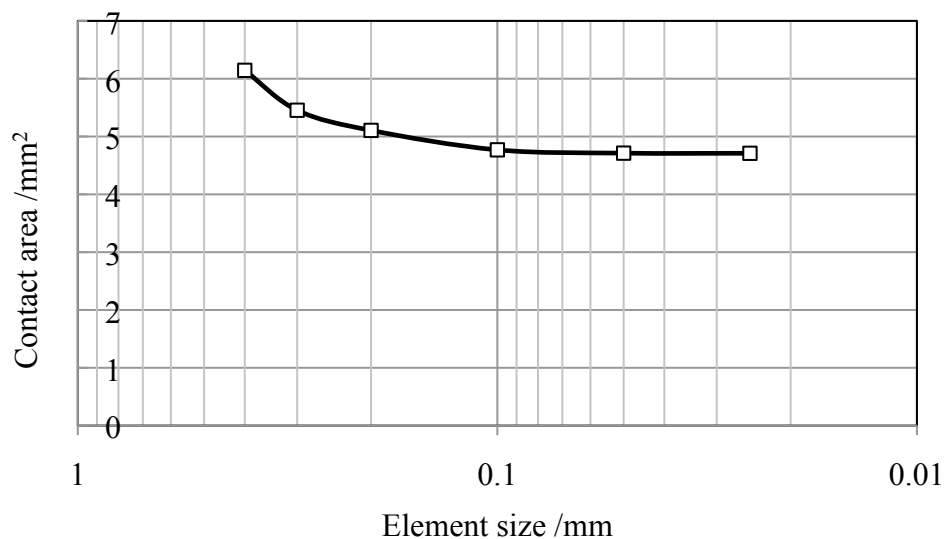
Figure 3.24: An example for the convergence of an FEA model is shown as the calculated contact area is predicted more accurately as the element size is reduced. Further reduction of the element size does not alter the result significantly, but increases computational costs. The shown contact area is calculated for an indentation of d=0.4mm with a sphere of R=6mm on NR-0.

3.7 Ways of measuring friction

Several methods of measuring the frictional behaviour of rubbers were available throughout this work due to a collaborative agreement allowing access to facilities at the Tun Abdul Razak Research Centre (TARRC). However, as rubber friction is sensitive to many parameters, the utilisability of a certain test method has to be carefully considered. In the following section a brief description and evaluation of the available techniques is given.

3.7.1 QMUL friction tester

In literature many test setups have been used to measure friction. Several pin on disk systems have been designed by scientists (Schramm 2002; Lindner 2005). Grosch (1963) used a system based on two flat surfaces in contact with each other, similar to the pin on plane system. Torsion-based setups have been used as well, either with two flat surfaces in contact (Lazeration 1987) or a (rough) rotating pin indenting into a rubber block (Scherbakov and Gurvich 2003; Scherbakov and Goodyear 2004). However, most of these machines are complex in design and typically require very large rigid supports due to the inertia of the moving parts.

One task of this work was to design a friction tester that was a simple adaptation of existing facilities at QMUL. Very simple setups, similar in principle to Leonardo da Vinci's initial experiments (shown in Figure 2.10), are reported in literature (Klüppel and Heinrich 2000; Budinski 2001; Axel 2006), as illustrated in Figure 3.25:
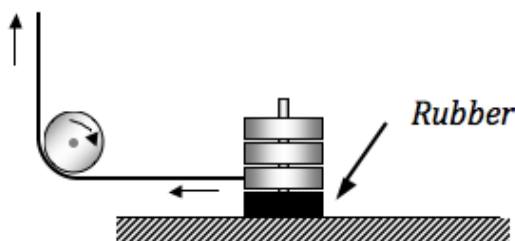
Figure 3.25: Simple friction tester using a pulley system and tensile test machine.

In the shown setup, a stiff string is attached to a screw-driven test machine that pulls a rubber block, loaded via a dead weight, over a surface. One disadvantage is that edge

effects are present due to the shape of the rectangular specimen. In order to avoid additional frictional losses due to the mounting system, for example by using linear ball bearings, the block is usually unconstrained in all directions. Consequently, only planar blocks with a sufficiently large surface area to support the dead weight can be used. Resulting from this, hemispherical shaped test bodies for example can not be supported, however, this geometry is required to observe Schallamach waves in this work. Therefore, the task was set to design a new friction tester, which could be easily mounted onto existing test machines.

The driving unit of the friction tester was chosen to be a simple screw-driven (tensile) tester, which has the advantage of having an existing software interface and a load cell, which can be used to measure the frictional force. In order to develop a practical device, several designs were considered, which differ in the way the normal load is applied and how the resulting frictional force is measured. An early design is shown in Figure 3.26. A friction tester is schematised on the right, where a rubber sample is mounted on a fixed frame, while the upper part (shown in turquoise) can be displaced using the tensile tester frame with velocity v. A hemispherical slider connects to a load cell through a flexible spring, which allows for deflection perpendicular to the rubber surface, needed for the application of a normal load F_N, but remains stiff in the direction parallel to the rubber surface so that a frictional force F_F can be measured. The normal load is applied either via a spring system, as schematised in the figure, or possibly using a pneumatic system. As a modification, which does not need a load cell to be provided by the tensile tester, the magnification of the flexible spring steel in Figure 3.26 shows two strain gauges #1 and #2, which can be used to measure both, horizontal and vertical forces.
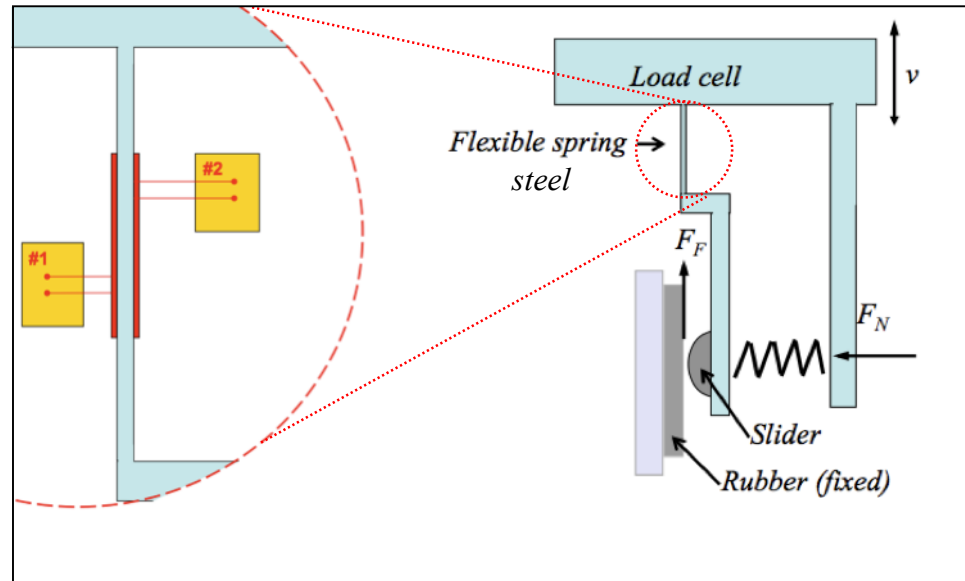
Figure 3.26: Schematic figure of an early design concept of the QMUL friction tester. The frictional force F_F is measured using the load cell of the tensile tester or, as shown in the magnification of the flexible spring steel, by two strain gauges. The normal load F_N is either applied using a spring or pneumatic system.

The use of strain gauges, however, requires an additional software interface and the application of the normal load using a spring complicates matters, as springs with different stiffness have to be provided. In general, application of the normal load using a pneumatic system is favourable, nevertheless, the complexity of the machine would be increased by the need of a compressed air supply and a control interface. The final design of the friction tester was constructed to be mountable on a tensile tester as an independent test unit, which does not require any additional (software) interfaces or external supplies as for example compressed gas. A schematic figure of the friction tester is shown in Figure 3.27. It consists of two separate parts, only contacting at the frictional interface: The upper part (grey), the main frame, is connected to the load cell (here: 100N or 1kN) at point ① and it can be displaced using the tensile test machine. Its load arm ② connects to the main frame via two low-friction ball bearings and transmits the force of a dead weight ③ into the normal force F_N at the slider ④. The slider ④ contacts the rubber pad ⑤, resulting in a frictional force F_F when the main frame is displaced. The rubber pad ⑤ includes a mounting system, described in Section 3.7.3, so that different rubber specimen can be quickly replaced. The second part, ⑥ (dark grey) remains fixed and acts as a mounting frame for different rubber samples. A second force is applied to the main frame in ⑦, acting as a counter balance in order to reduce the torsional moment at the load cell, induced by the dead weight ③ of the load arm ②.
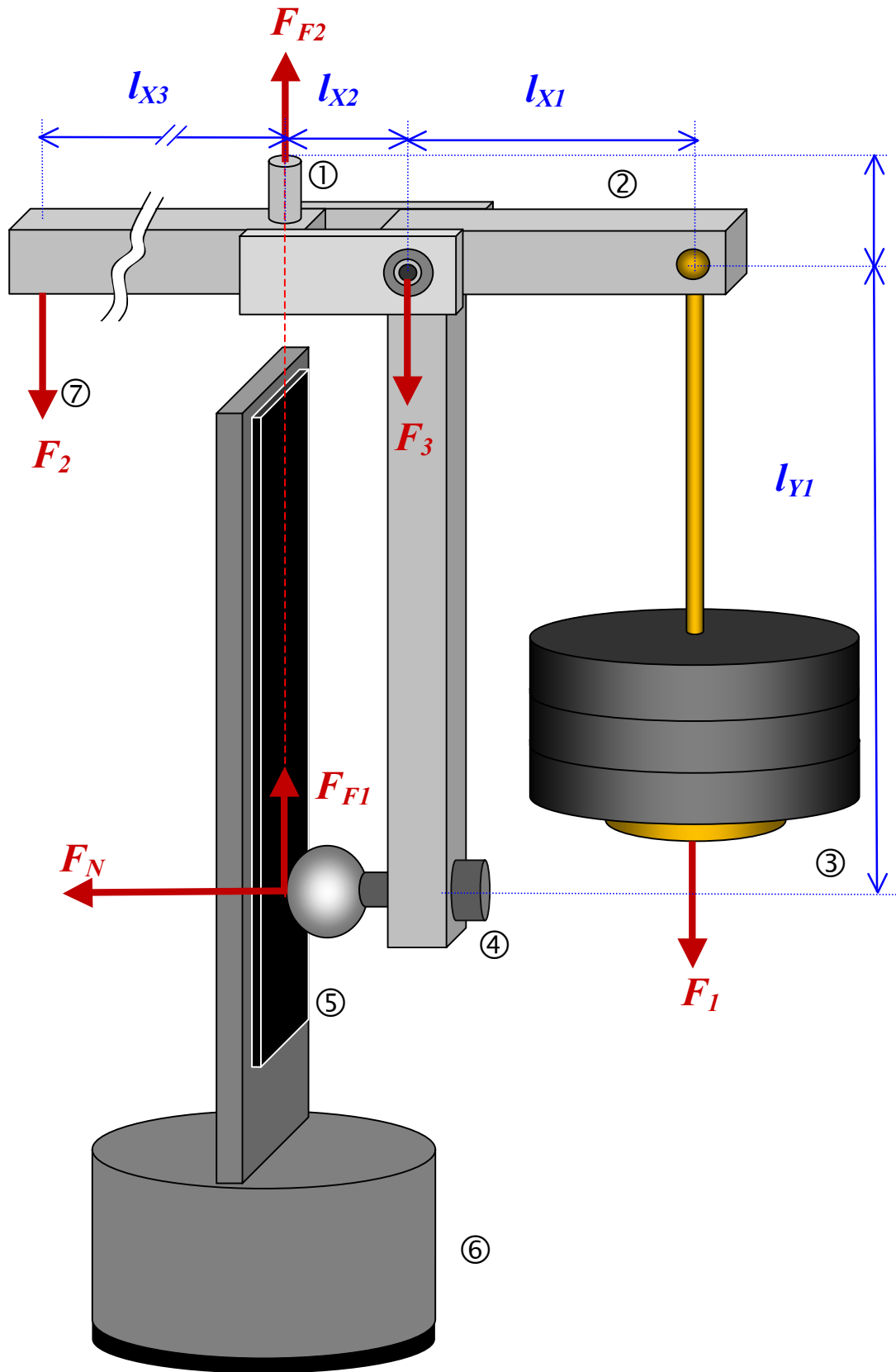
Figure 3.27: QMUL friction tester, with ① load cell connection, ② load arm, ③ variable dead weight, ④ indenter, ⑤ rubber strip, ⑥ mounting unit and ⑦ counter balance to avoid moments on load cell.

The forces F_i (with $F_1 = F_2$ and F_3 equalling the weight of the load arm) are applied via dead weights. The frictional force at the interface is denoted as F_{Fi}. The dimensions are given by:

Table 3.15: Dimensions of QMUL friction tester.

	l_{X1}	l_{X2}	l_{X3}	l_{Y1}	l_{Y2}
Length /mm	70	25	95	210	11

From the schematic free body diagram shown in Figure 3.27 the resulting forces and moments can be calculated. The normal load F_N is given by:

$$F_N = \frac{F_1 l_{X1}}{l_{Y1}}.$$

(3.12)

The force in the load cell F_{F2} is given by:

$$F_{F2} = (F_1 + F_2) - F_{F1},$$

(3.13)

while the sum of F_1 and F_2 are equalised to zero via the software interface prior to experimental testing, so that F_{F2} is (virtually) equivalent to the frictional force F_{F1}, acting at the interface between rubber and slider. The forces F_1 and F_2 should be taken into account for the choice of load cell, as the frictional force can exceed the normal force by a factor of 4 to 5, to ensure that the total force F_{F2} does not exceed the load cell protection limit. Due to the test geometry the load cell is subject to a moment by the applied normal forces and the weight of the load arm. The moment in the load cell ① can be calculated as:

$$(l_{Y1} + l_{Y2})F_N = l_{X3}F_2 - (l_{X1} + l_{X2})F_1 - l_{X2}F_3,$$

(3.14)

so that the force F_2 can be chosen to account for the induced moments.

A photograph of the friction tester in combination with the tensile tester and the high-speed video camera is shown in Figure 3.28:
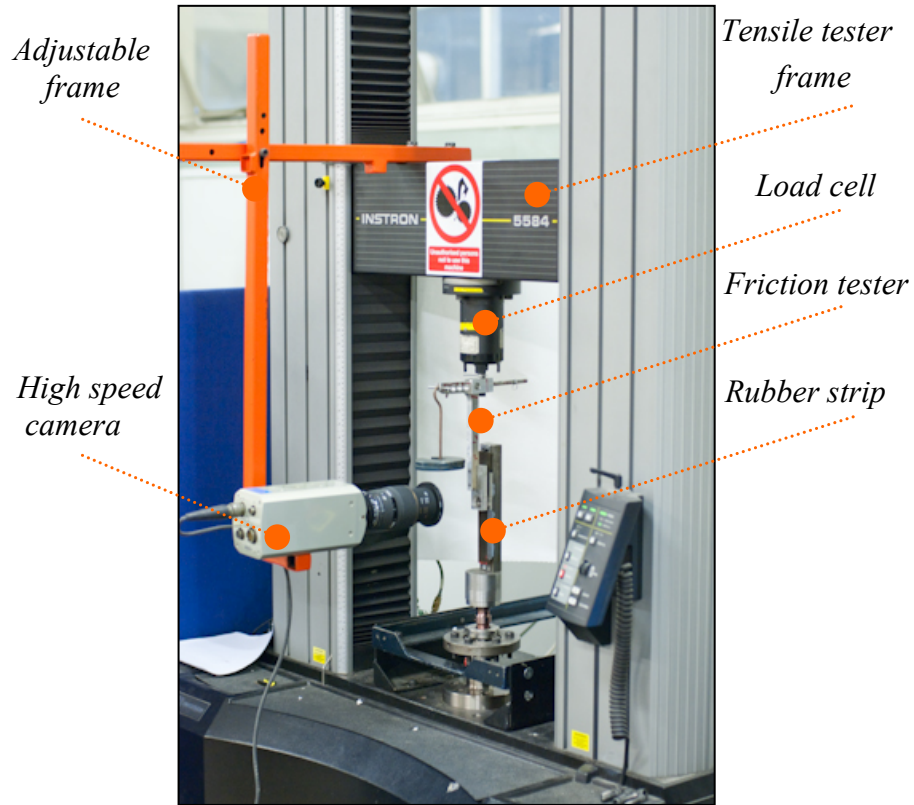
Figure 3.28: The developed friction tester mounted on tensile test machine with high-speed camera. The frame for the camera can be adjusted vertically and horizontally to cope with different friction setups and lens-systems. Each frame of the high-speed video can be linked to the friction data acquired by the load cell, measuring the frictional force.

Several slider geometries were manufactured for the friction tester, and their relevant geometry is defined in as shown in Figure 3.30.
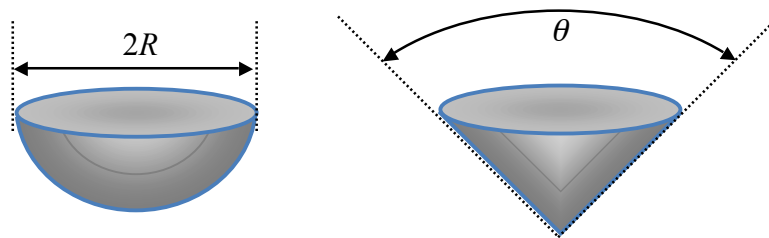
Figure 3.29: The slider / indenter geometry is defined for (hemi-)spheres as the radius *R* and for cones as the angle *θ*.

Different conical sliders were made ranging from 10° to 170° which could be mounted via a quick-fit system. Hemispherical sliders were also made with radii ranging from 6mm up to 240mm some of which had optically smooth glass lens at one extreme to a rough slider at the other. The glass lens as well as a glass wedge were both used to observe Schallamach waves.
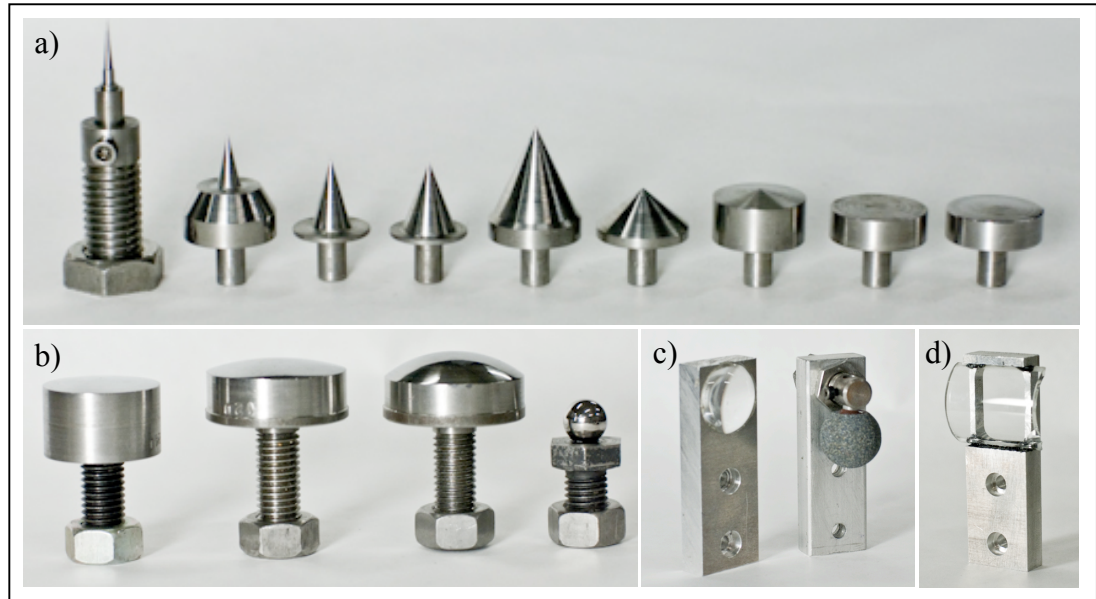
Figure 3.30: Different sliders, which can be supported by the Plint and the QMUL friction tester. a) different cones from α=10° (left, with mounting system) to 170° (right), b) hemispheres from R=240mm to 6mm, c) glass lens and rough slider and d) glass wedge.

Rubber hemispheres were also used to observe Schallamach waves. In this case the rubber pad on the fixed lower part ⑥ of the unit was replaced by a transparent Perspex glass, while the contact area was observed with a high-speed camera.

For validation purposes of the QMUL friction tester, the measured friction data were compared under same test conditions to values obtained by the Plint friction machine based at TARRC (Roberts 1994), which is described next. A good correlation between the two techniques is shown when the friction between a rough hemispherical slider and a flat sheet of SBR-0 is compared, as shown in Figure 3.31:
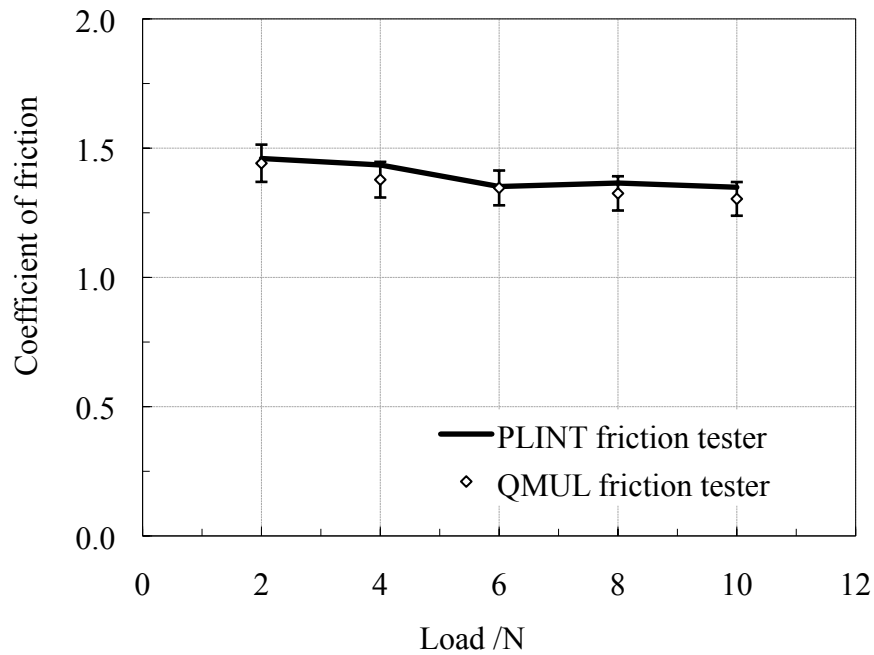
Figure 3.31: Comparison of Plint- and QMUL friction tester at 1mm/s with a rough, hemispherical slider at room temperature on SBR-0 for various normal loads.

This friction tester was also extensively used and validated in the co-supervised diploma thesis of Baumard (2009) on the degradation behaviour of touring car racing tyres.

3.7.2   The Plint friction tester

The Plint friction tester uses a test body sliding over a planar rubber block. The slider is loaded via a dead weight and the resulting frictional force parallel to the sliding direction can be measured. The Plint friction tester and its frictional setup are shown in Figure 3.32. Further information on the principal operation of this equipment can be found in the literature (Roberts 1994; Plint-Manual 1997) and are explained in the next section in comparison to the QMUL friction tester.
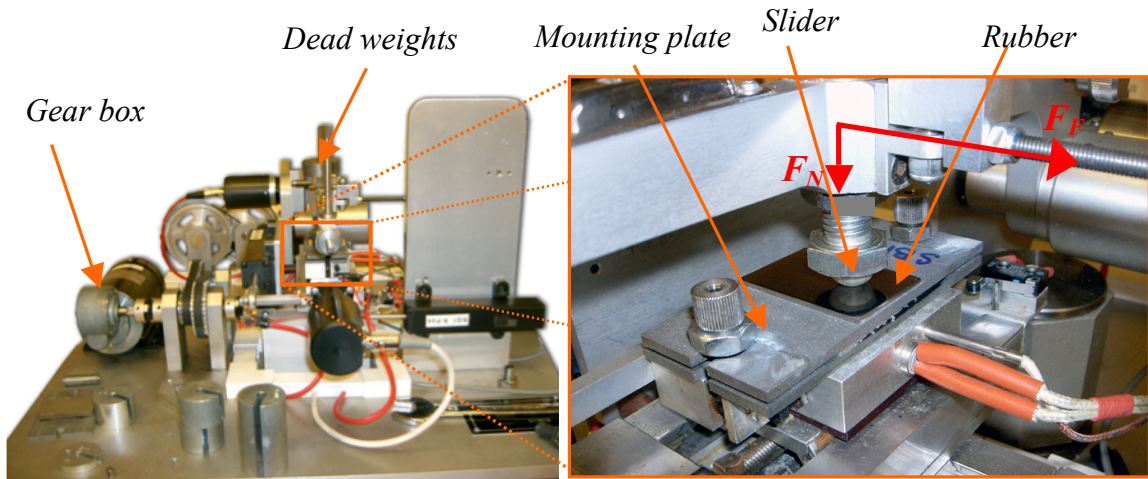
Figure 3.32: Plint friction tester (left) with magnification of the frictional sliding stage with SBR-50 rubber mounted (right).

3.7.3   *General description of a friction test*

Both machines, Plint and QMUL friction tester, are similar in their working and operational principles. Prior to every test, rubber samples were cleaned with ethanol and acetone to remove surface oils and any surface bloom, which may act as a lubricant. Laboratory friction tests with and without cleaning as well as a choice of cleaning agents and evaporation/drying times, showed a considerable difference in their measured friction values, as is shown later. The rubber is glued[20] to a rigid steel plate, which is mounted on the machine via a quick release system. The dimensions of the steel plate are shown in Figure 3.33, where l_x and l_y are 90x60mm² for the Plint and 200x40mm² for the QMUL friction tester, respectively.

---

[20] Henkel, Loctite Adhesives Ltd., Welwyn Garden City, Great Britain. Type: Instant adhesive 480.
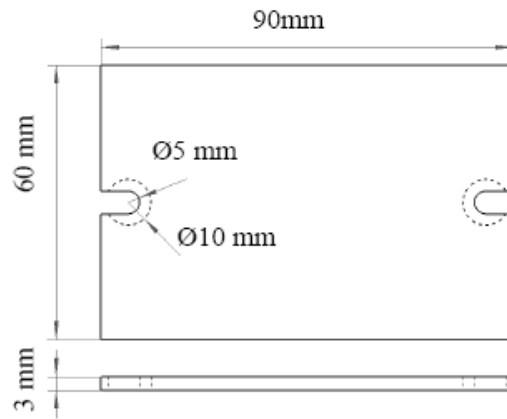
Figure 3.33: Dimensions of the steel plate used to attach the rubber sheet in the frictional sliding stage.

Figure 3.34 depicts a Plint friction test schematically: In the preparation period t_1 the slider is lowered onto the rubber sample, t_2 marks the time when sliding is started as an increase in the coefficient of friction and marks the static friction. When sliding starts, the measuring period at which the coefficient of friction is averaged over is noted as t_3, whereas the end of the test is noted as t_4, when the slider is lifted up.
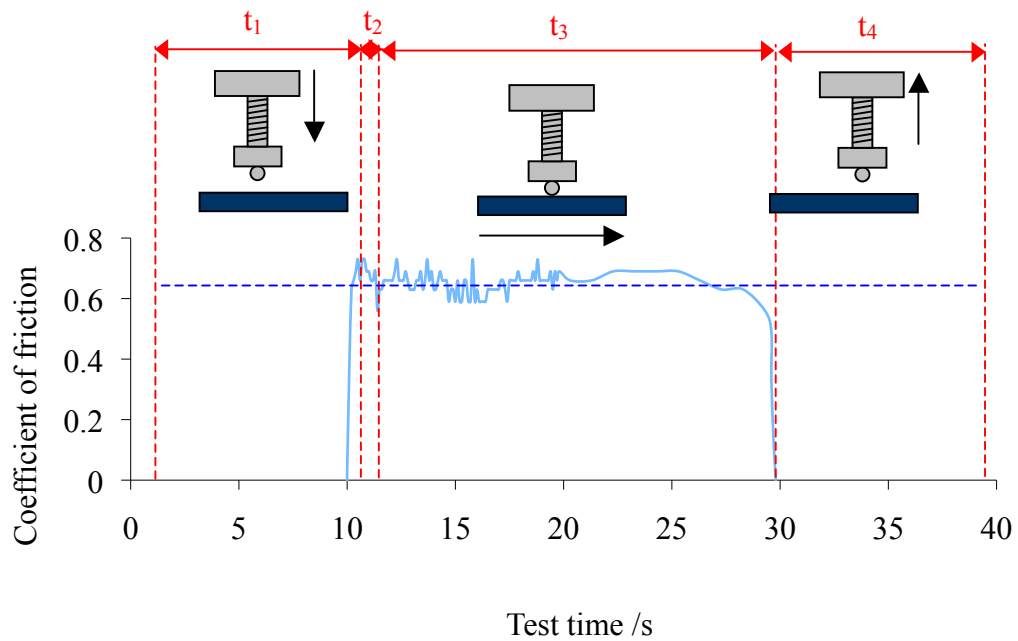
Figure 3.34: The procedure of a friction test and the correlating friction versus time graph is shown. In time period t_1 the spherical slider is lowered to the rubber surface (dark shade), while t_2 denotes the static coefficient of friction when no relative displacement occurs. The time period t_3 shows the kinetic coefficient of friction and t_4 marks the end of the friction test, when the slider is lifted up (v=1mm/s, SBR-0, steel sphere R=6mm, F_N=1N, measured on the Plint friction tester).

The graph in Figure 3.34, measured over a total sliding length of 20mm, shows a smoother curve after $t=20$s, or to an equivalent length of 10mm. This is due to a software regulation, which automatically decreases data capture rate from 10 to one data point per second (1/s). The reason for this was historic and reflected that when the machine was built in about 1990, disc capacity was still a premium. In contrast the QMUL friction tester plots up to 1000 data points per second (1000/s).

The significant effect of cleaning is shown Figure 3.35: Six tests were conducted for each state – uncleaned and ethanol cleaned. A much lower standard deviation and a higher coefficient of friction due to less contamination on the surface were observed after the surface was cleaned. All friction values obtained in this study are taken as an average of five passes over the rubber surface.
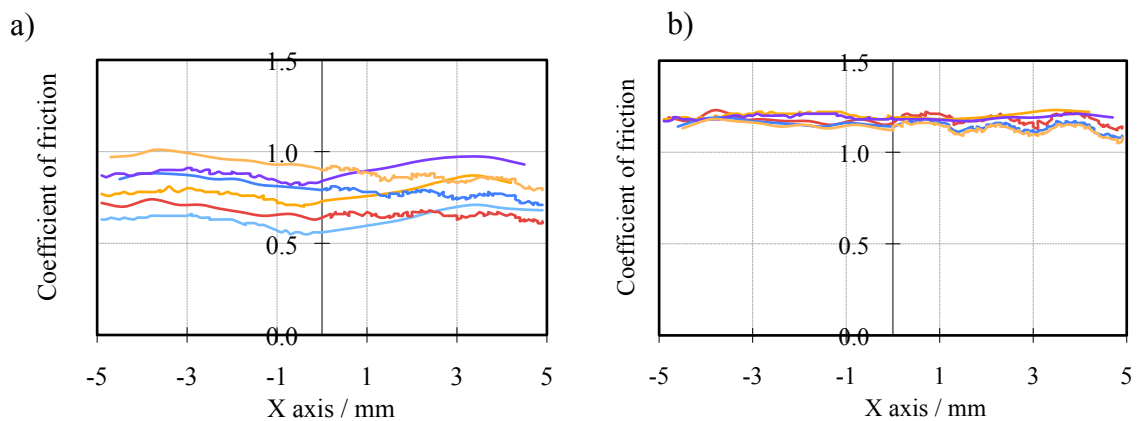
Figure 3.35: The difference in the measured friction of a) an uncleaned and (b) a cleaned surface is shown (v=1mm/s, SBR-0, steel sphere R=6mm, F_N=1N, measured on the Plint friction tester).

Several problems of the Plint friction tester were experienced in the initial test- and validation phase of the machine, which are discussed next.

Test parameter evaluation

The Plint friction tester measures the friction coefficient of a rigid slider and a rubber block over a sliding length of 20mm by displacing the rubber block relative to the fixed rigid slider in a forward and backward motion. Differences in the frictional forces measured between forward and backward passes were noticed and were investigated first. Several test parameters, for example normal load, sliding velocity or test

temperature, were checked individually, but the problem appeared to be parameter independent. A reason for this might be due to the design of the friction tester, a schematic of which is shown in Figure 3.36. It is shown that the load cell is not in line with the actual point of contact at the interface, so a different force for both directions was possible due to induced moment on the system. Furthermore, due to the repeated forward and backward passes on the rubber surface the rubber might be deformed by the forward action but can not relax before the backward pass commences. These design issues were all addressed in the design of the QMUL friction tester.
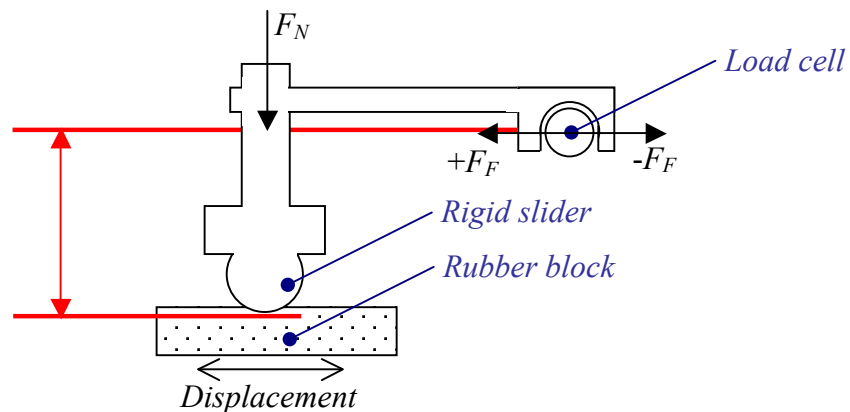
Figure 3.36: Schematic figure of the way of measuring the frictional force with the Plint friction tester. A fixed hemispherical indenter, loaded with a normal force F_N, contacts a rubber block, which can be displaced forwards and backwards over 20mm. The resulting frictional force is measured using a frictionless connection to a load cell.

Nevertheless, for most rubber surface and rigid indenter combinations these differences were only small, so that it was reasonable to give the average friction coefficient, averaging the different friction values measured for the forward and the backwards pass.

A second problem was differences noticed between the chosen sliding velocities in the software interface and the apparent sliding velocity. The deviation between the input and apparent sliding velocity was shown to be dependent on the operated gearbox. Three different gearboxes were available, while each gearbox is designed to cover a range of sliding velocities and were distinguished as 'slow' for 0.01mm/s to 0.1mm/s, 'medium' for 0.1mm/s to 1mm/s and 'fast' to cover 1mm/s to 10mm/s. The fast gearbox also showed an apparent difference in the velocities for the forward and backward passes. To evaluate the scale of these differences, the gearboxes were checked with an external linear variable differential transformer (LVDT). It can be seen from Figure 3.37

that for the fast gearbox deviates clearly from its nominal input velocity, shown as a thick black line. However, it is shown that the differences in input and output sliding velocity are negligible at 10mm/s and the medium gearbox with a velocity range of 0.1 to 1.0mms/s is in good agreement with the input velocity. The main sliding velocities, which are operated throughout this work are 0.01mm/s, 0.1mm/s, 1.0mm/s and 10mm/s, which show no or negligible deviation from the input value. When other velocities were required in this work, the sliding velocity was corrected according to the values measured with the LVDT. A more detailed analysis of this problem can be found in the work of Qui (2007).
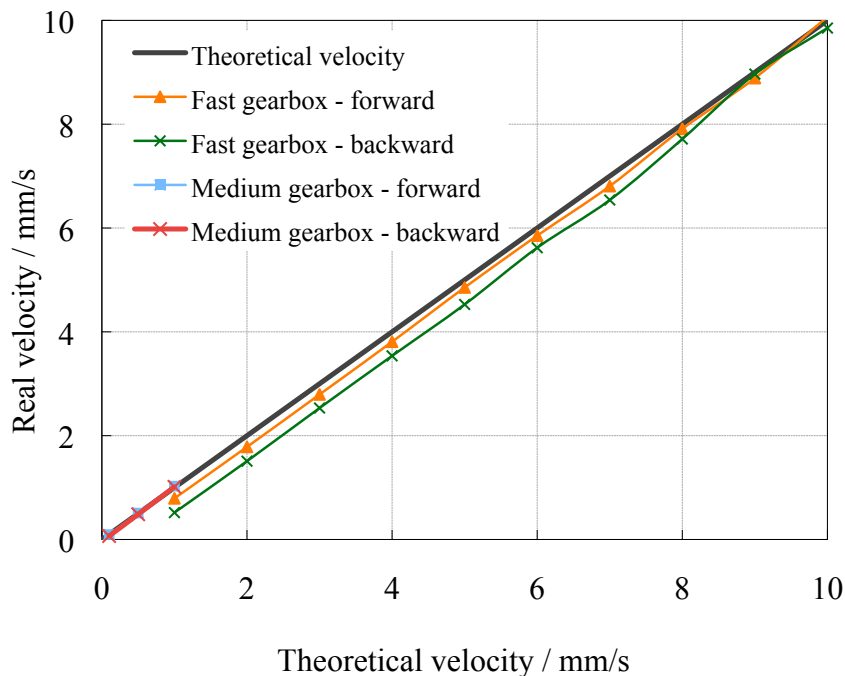
Figure 3.37: The velocities both, medium and fast, gearboxes of the Plint friction tester have been checked using a LVDT. Deviations from the theoretical velocity, shown as a straight black line, for the fast gearbox can be noticed, so that the real velocity for each sliding test had to be corrected.

Moisture at testing below ambient temperature

The temperature control system of the Plint friction tester operates from ambient temperature to 100°C. In its standard configuration testing below ambient is not provided, however, a Peltier cooler was adapted as part of this work, which was capable of cooling down a surface to 40°C below the ambient test temperature. The working principle of a Peltier cooler is described in the literature (Kutz 1998) and results from

energy transformation into heat at one side of the interface and cooling at the other. A complication was noted that by cooling down the rubber sample, condensation was built up on the rubber surface and if cooled under 0°C, an ice layer developed. This additional lubrication changed the coefficient of friction significantly. The build up of moisture or ice may be avoided by either operating friction tests in vacuum or in an inert atmosphere without humidity or by using silica gel trays to dry the environment. Neither of the mentioned options was available in the standard test setup of the Plint friction tester. A system using a continuous flow of nitrogen was tried, however, the operation of a constant nitrogen purge in a limited room capacity was impracticable and the limited amount of test time at TARRC limited the scope of this investigation and restricted testing only at room temperature or above.

4   Influence of interface geometry on rubber friction

4.1   Introduction

The origins of the influencing parameters that affect rubber friction and their related mechanisms are still a subject of debate. Various friction theories have been developed in order to describe or model the total of rubber friction (Kummer 1966; Moore 1972; Roberts 1988; Persson 1999; Sills et al. 2007). Summarizing these models, a general description for the total friction force (F_{TOTAL}) is commonly described as given in Section 2.5.2:

$$F_{TOTAL} = F_{ADHESION} + F_{HYSTERESIS} + F_{VISCOUS} + F_{COHESION}. \tag{2.46}$$

Assuming a dry, smooth contact with reasonably low shear forces, the total frictional force is considered to reduce to a combination of just two mechanisms (Tabor 1960):

$$F_{TOTAL} = F_{ADHESION} + F_{HYSTERESIS}. \tag{2.47}$$

The adhesion term ($F_{ADHESION}$) is a surface effect resulting from the intermolecular interaction between two surfaces (Roberts and Thomas 1975) and the hysteresis term ($F_{HYSTERESIS}$) results from the energy lost through the bulk deformation of a certain volume of rubber (Roberts 1992). It is worth emphasizing that both factors are not independent as shown by Schallamach in Bateman (1963) and Muhr and Roberts (in Roberts 1988). However, suitable modification can reduce one or the other of the two terms and, therefore, can change their influence significantly. For example Fuller and Tabor (1975) as well as Persson (2001b) have stated that adhesion is negligible for rough interfaces, as experienced in the tyre / road contact, so that the hysteresis term alone is the major contribution to total friction. However, it is shown that adhesion has the main influence on rubber friction in very smooth contact situations (Roberts and Thomas 1975) and the hysteresis influence diminishes. For this reason the question arises, is it possible to describe the complexity of rubber friction by just a single term? If not, how might additional factors, such as an entirely geometric contribution to the frictional sliding force, contribute to the mechanics of rubber friction? The following chapter, based on the publication by Gabriel et al. (2010a), addresses the question in

how far the macroscopic geometry of the frictional interface affects the total frictional force. The abstract of this paper can be found in the appendix in Section 9.1. The microscopic influence of rubber friction is discussed later in Chapter 7.

4.2   Theory

4.2.1   Basic considerations on rubber friction

When a rigid hemisphere slides on top of a flat, elastic material, large (tensile) stresses are observed at the rear of the slider, whereas compressive stresses are built up in front (Schallamach 1952). The stresses are considered to result from a combination of adhesion and hysteresis, as defined in Equation (2.47). A model experiment depicts the stresses schematically in Figure 4.1. In Figure 4.1 a) the unloaded, hemispherical slider rests on the rubber surface, while in b) a normal force is applied perpendicular to the rubber surface. This produces a symmetrical stress field around the contact area, which is highlighted by the distorted reflection of the grid in the background on the mirror-like rubber surface. When the slider is displaced relative to the rubber to the right hand side, the stress field becomes asymmetric and sliding occurs, measurable as a horizontal frictional force. In c) a compression zone is developed to the front, as well as a tension zone at the back.
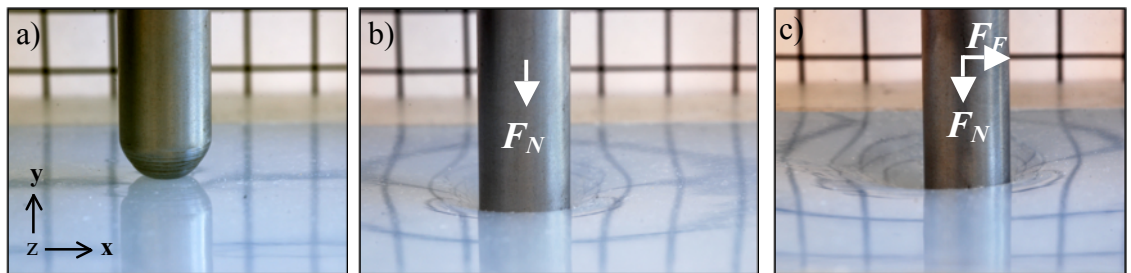
Figure 4.1: Model experiment on the sliding of rubber friction with a rigid slider a) in contact with a soft rubber, b) indenting and c) sliding along the surface. The reflexions of the background grid on the smooth rubber surface show the deformation of the rubber.

The involved stresses in the scenario described in Figure 4.1 are more readily observable using a 2D FEA simulation, as shown in Figure 4.2.
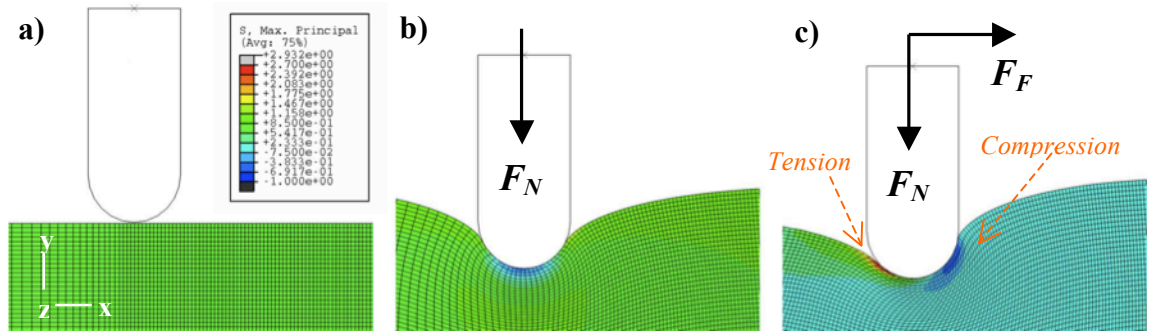
Figure 4.2: FEA model highlighting the stresses in the rubber from the model experiment (Figure 4.1). After the contact between the rigid hemispherical slider and the rubber in a) is established, a compression zone underneath the slider is shown in b) due to indentation and this compression zone moves to the front in c) while a tensile zone builds up in the rear of the contact.

The FEA simulation allows the stresses inside the rubber bulk to be monitored, which would otherwise be difficult to be deduced directly from the deformations of the surface shown in Figure 4.1. FEA is able to monitor stresses also in 3D, as shown Figure 4.3, where the simulation of Figure 4.2 is analysed from a bird's eye perspective, highlighting the distortion of the mesh due to the tension zone shown in red and the compression shown in blue.
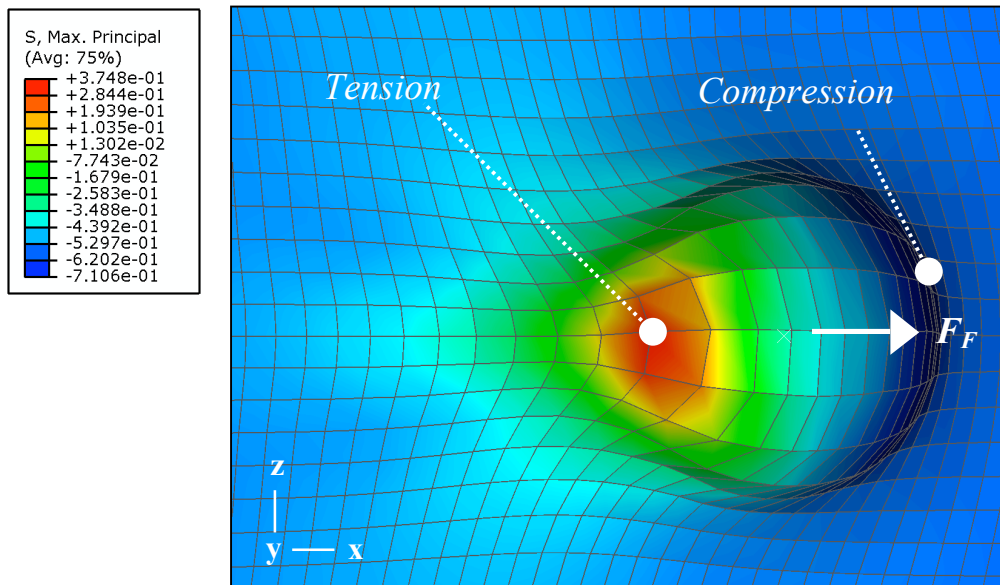
Figure 4.3: 3D FEA simulation of the model experiment shown in Figure 4.1, shown from above with the slider removed.

Huffington (1961) showed that these friction induced stresses can be resolved into horizontal and vertical directions by his considerations of a rigid, prismatic sliders with an angular front edge of 70° in contact with a rigid solid. His analysis is limited though,

as he assumed that the friction increases to infinity, if the frontal edge of a rectangular slider contacts the horizontal surface at an angle of 90°, as shown in Equation (4.1).

$$\mu = \frac{F - p\sin\beta}{p\cos\beta}.$$

(4.1)

Schallamach (1969) refined these findings for soft, elastic materials by investigating the resulting frictional forces and geometry further. He proposed that the contact between the rubber and the slider is not confined to the leading face of the slider (as assumed by Huffington), but continues around its edge and along part of the rear slope. For this reason the frictional stresses are resolved due to the tension zone at the rear of the contact and can not become infinite (Schallamach 1969). By considering a prismatic slider with a rounded edge he proposed the stresses were resolved as shown in Figure 4.4:
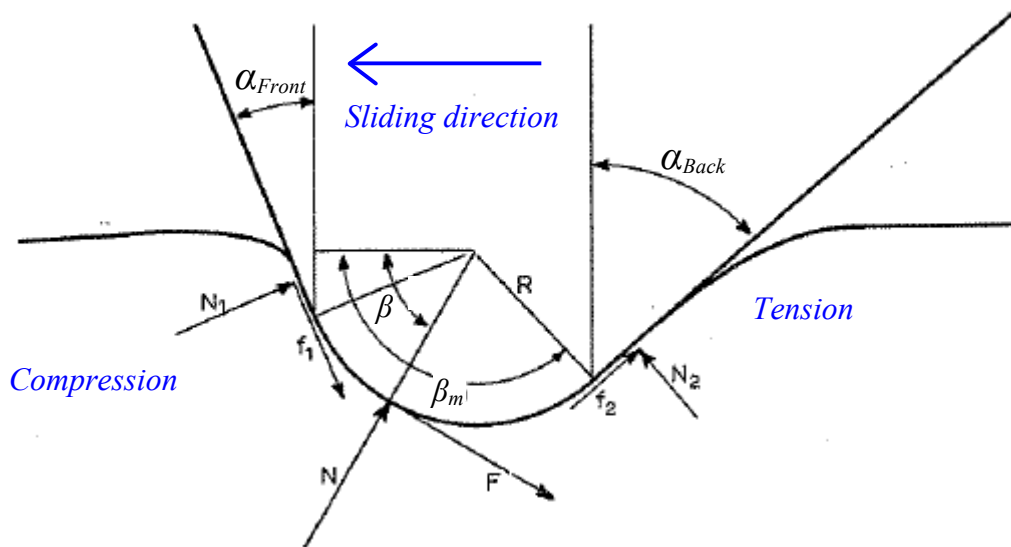
Figure 4.4: Tip of a prismatic slider in contact with rubber sliding towards the left. Adapted from Schallamach (1969).

While the angles α_{Front} and α_{Back} define the slider geometry, β_m specifies the angle of contact. The related frictional forces are denoted with f_i and F, while the forces normal to the contact are defined as N_i. Schallamach acknowledges that rubber friction is not governed by Amontons' friction law, however, he defines the friction by a single constant μ, so that the relation between the forces is given by Schallamach (1969) as:

$$\mu = \frac{f_i}{N_i},$$

(4.2)

For a sharp edge and under the assumption of the Hertzian contact theory, given by Equation (2.48) he assumed, that the total tangential force can be expressed as

$$F = f_1^{\mu(\beta - \alpha_{Front})}. \tag{4.3}$$

This equation is similar to equation derived by Euler-Eytelwein to describe a capstan effect, which is derived in the next section (Euler 1769; Eytelwein 1808). Schallamach referred to an apparent capstan effect in order to explain the general phenomena of rubber wrapping around a rigid surface, however, no corroborating evidence for the effect was presented. Furthermore, to account for a possible wrapping effect he finally derived an equation for a revised form of the friction coefficient μ as the friction ratio φ of the total horizontal and vertical forces shown in Figure 4.4, given as

$$\varphi = \frac{\cos\alpha_{Front} - \left(\dfrac{N_2}{N_1}\right)\cos\alpha_{Back} + \mu\sin\alpha_{Back}\left\{\left(\dfrac{N_2}{N_1}\right) + \exp\mu(\pi - \alpha_{Front} - \alpha_{Back})\right\}}{\sin\alpha_{Front} + \left(\dfrac{N_2}{N_1}\right)\sin\alpha_{Back} + \mu\cos\alpha_{Back}\left\{\left(\dfrac{N_2}{N_1}\right) + \exp\mu(\pi - \alpha_{Front} - \alpha_{Back})\right\}}. \tag{4.4}$$

Equation (4.4) includes the parameters N_i to describe the arising forces at the rear and the front of the slider, which cannot be measured from experiment, so that this equation remains solely theoretical. A finite elements approach can help to resolve this problem and the relation to the capstan effect can be extended.

4.2.2   The relation between friction and the capstan effect

If a string is wrapped around a capstan, it requires very little force on one side of the string to hold a much larger force on the other end in place without sliding. The underlying mechanics are based on the relationship between wrapping angle and friction between the string and the capstan. Figure 4.5 shows the schematic of a string in contact over a certain angle with a static capstan of radius R. The forces in the string are defined as F_1 and F_2, where F_1 is assumed to have a constant value. Dependent on the angle of contact β and the friction coefficient μ between the string and the pulley, the force F_2 is considerably higher than F_1.
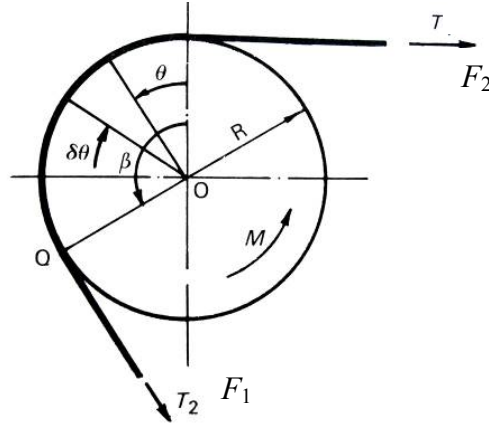
Figure 4.5: The capstan effect shows that force F_1 does not equal F_2 and that their ratio depends on the angle of contact β (Budinski 2001).

The free body diagram of Figure 4.5 is shown in Figure 4.6:
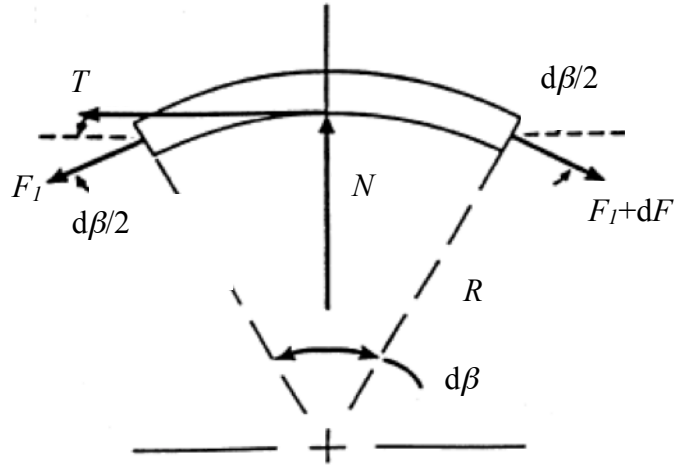
Figure 4.6: Free body diagram of the string in contact with the round pulley shown in Figure 4.5 (Budinski 2001).

While the constant force is marked as F_1, the end of the string F_2 is more accurately described as $F_1+\mathrm{d}F$. The angle of contact β is given in radians. N is the radial outward normal force and μN is the friction force, with μ as the coefficient of friction. The pressure p in a small increment of length $r\mathrm{d}\beta$ of the angle can be expressed as (Budinski 2001; ASTM 2004b):

$$p(\beta) = \frac{N(\beta)}{R}.$$

(4.5)

When the string slides over the capstan, the resulting tangential friction force T is given as:

$$T(\beta) = \mu p(\beta) \cdot \qquad \text{(4.6)}$$

The equilibrium of forces along the differential string increment is given as:

$$dN = T(\beta)Rd\beta = \mu p(\beta)Rd\beta, \qquad \text{(4.7)}$$

so that a combination with Equation (4.5) eliminates the dependence on the radius R and leads to

$$dN = \mu N(\beta)d\beta \qquad \text{(4.8)}$$

It is shown that the force in the string has to decrease due to the friction between the string and the capstan, however, no relationship to the radius exists. The differential of Equation (4.8) is given as:

$$N'(\beta) = \mu N(\beta). \qquad \text{(4.9)}$$

To solve the differential Equation (4.9), it can be rewritten as:

$$\frac{dN}{N} = \mu d\beta, \qquad \text{(4.10)}$$

so that integration leads to:

$$\ln N = \mu \beta + C, \qquad \text{(4.11)}$$

with C being a constant, which is written as $K=e^{C}$, after the antilogarithm of Equation (4.11) is taken:

$$N(\beta) = Ke^{\mu \beta}. \qquad \text{(4.12)}$$

Equation (4.12) leads to an equation firstly derived by Euler (1769) and later promoted by Eytelwein (1808), known as the Euler-Eytelwein equation, when $N(\beta)=N(0)=K=F_1$, so that:

$$F_2(\beta) = F_1 e^{\mu \beta}, \qquad \text{(4.13)}$$

and F_1 and F_2 are the two forces shown in Figure 4.5. In an experiment, with fixed environmental parameters and a constant sliding velocity the coefficient of friction μ is constant. According to Equation (4.13) the force F_2 increases significantly by an increase of the angle of contact when F_1 is constant. The above named relationship is usually assumed to be true only for $0<\mu<1$ so that the applicability for rubber friction, experiencing coefficients of friction with values up to 4 or 5, has to be validated.

4.3 Experimental background

The above described theory on basic considerations of rubber friction and a possible connection to the capstan effect is evaluated in this work. For initial observations, the capstan effect is investigated to explore if this mechanism is also adaptable to rubber friction. The findings are thought to be useful in order to investigate the macroscopic geometric wrapping effect of rubber around any rigid surface, as described in the introduction.

4.3.1 Capstan friction tester

A schematic of the setup used to investigate the capstan effect is shown in Figure 4.7 a). An polymer string (Polypropylene, E=1.5GPa) is wrapped around a fixed capstan (A) for specific angles of contact (Figure 4.7 b)) and is assumed to be inelastic at small loads (1N to 20N). One end is loaded with dead weights, acting as force F_1 while the other is pulled around a freely rotating pulley (B) to the load cell of an Instron 5584 tensile test machine, measuring the resulting force F_2 when pulled.
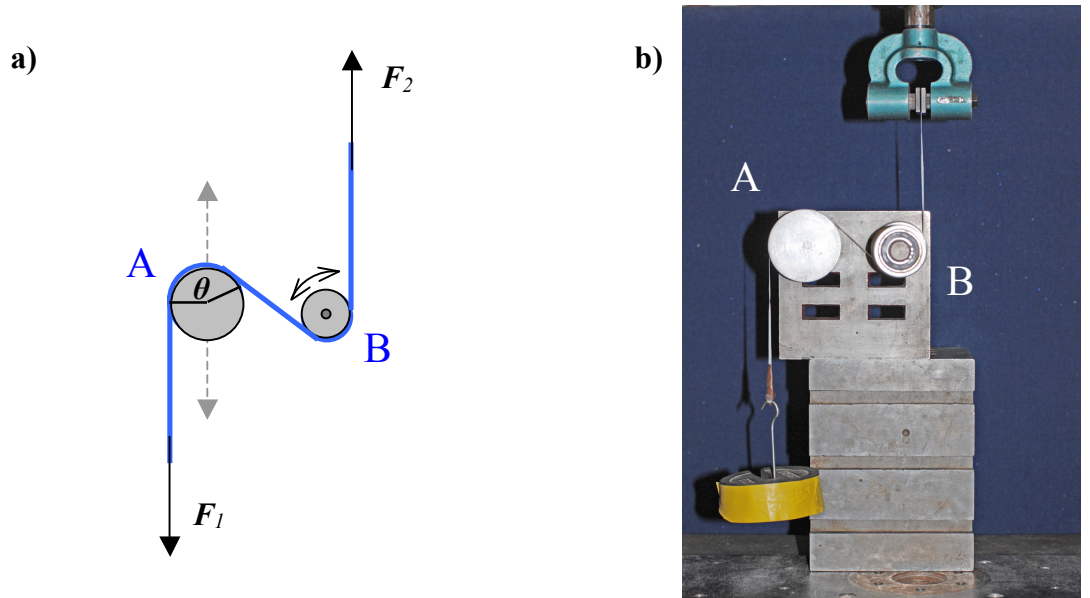
Figure 4.7: a) Schematic of the designed capstan tester and b) setup used to investigate frictional forces. The angle of contact θ is changed by varying the positions of A or B, while the force F_1 is applied using a dead weight and force F_2 is measured using a tensile tester.

The positions of the capstan (A) and the bearing (B) are variable, allowing for different angles of contact to be examined. In order to validate and investigate the designed test

setup, two initial loading conditions (10 and 20N) in combination with two different velocities (60 and 600mm/min) were used with the polypropylene plastic band. The results are shown in Figure 4.8, where it is observed that only load dependence, but no velocity dependence exists, as is anticipated by Equation (4.13).
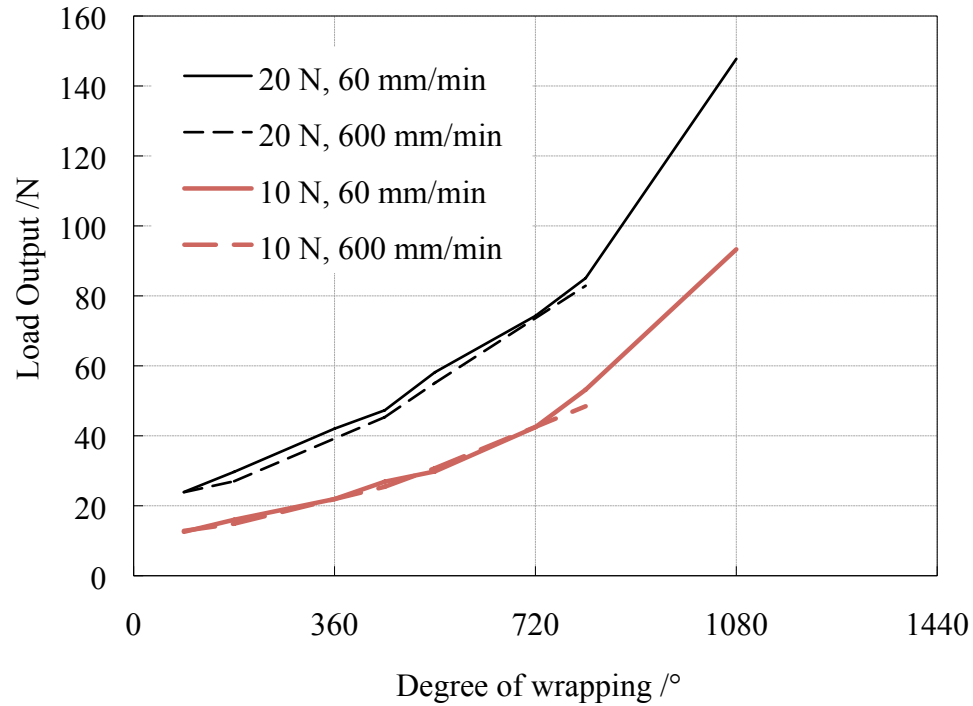
Figure 4.8: The velocity and load dependence of the capstan effect for different wrap angles using a polypropylene band is shown.

In order to investigate the behaviour of rubber, using a capstan friction test setup, a rubber band was moulded in a custom-built mould, shown in Figure 4.9. Two flexible steel cables, each with a thickness of 1.2mm, were moulded inside a transparent silicone rubber to limit the excessive stretching of the sample.

a)
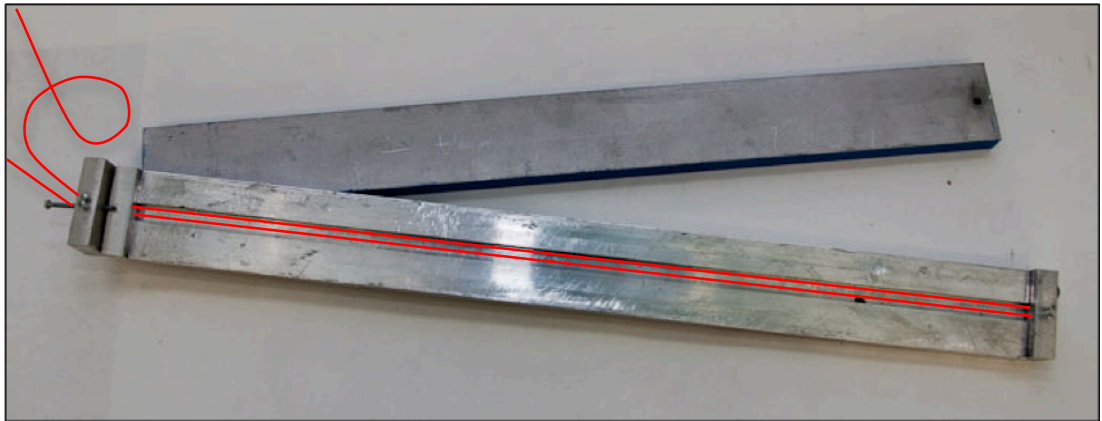
b)
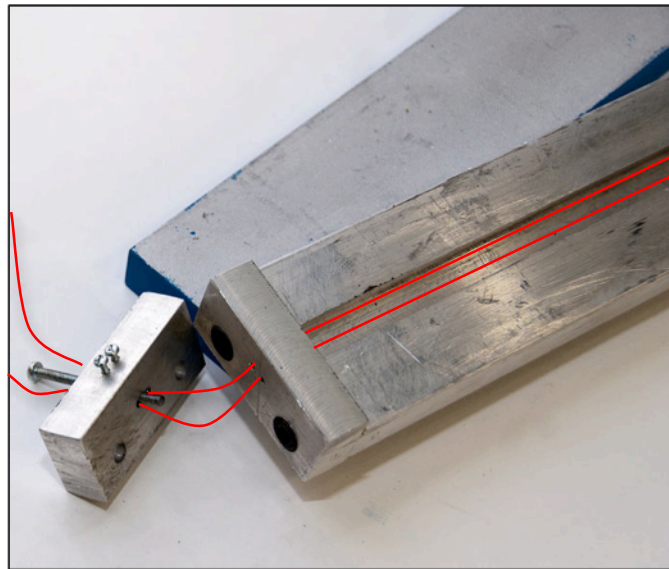
Figure 4.9: a) By incorporating two steel cables in the mould tearing of the rubber band (width=10mm) is prevented. b) The steel cables (red) in the centre of the aluminium mould can be fixed at one end of the mould and strained on the other, to ensure that the cable is centred.

The measured experimental data from the rubber and plastic band are shown in Figure 4.10, at a fixed velocity of 60mm/min and load of 10N. The data points fit the Euler-Eytelwein theory given in Equation (4.13) well and the resulting coefficients of friction are μ=1.04 for rubber and μ=0.12 for polypropylene. The value for polypropylene is in an acceptable range experienced for stiff polymers. From these coefficients it is show that under the same normal load and similar contact area between the capstan and the 10mm wide rubber or plastic band, the effect of adhesion exhibited by the rubber becomes much more significant than the adhesion experienced by the polypropylene band.
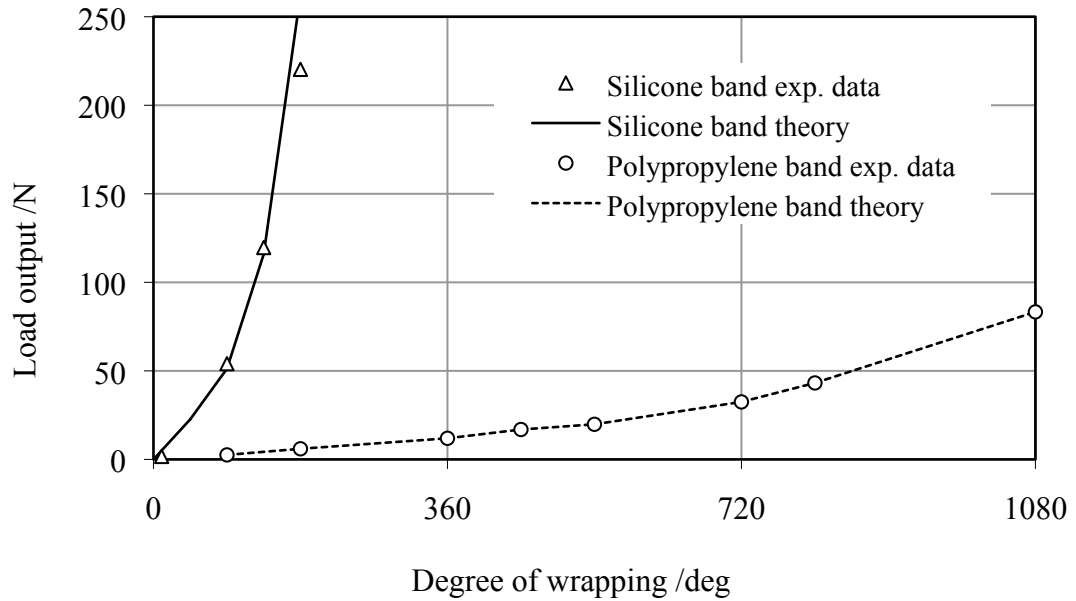
Figure 4.10: Capstan test data for a silicone rubber band compared to the theory (thick line) and a polypropylene band compared to the theory (dotted line) (Euler 1769).

The fundamental mechanics of this effect may become important when a spherical indenter slides over a rubber surface, so that the rubber wraps around the rigid surface in a similar way. This proposal is thought to be appropriate, as even at very small angles of contact, large forces for a rubber material arise when compared to a rigid plastic band. For the further investigation the cylindrical interface geometry is considered to be inappropriate, as if used as a slider edge effects can complicate the contact situation. Therefore, the interface of two materials contacting and sliding relative to each other is considered next.

4.3.2   *Definition of the required geometries*

To investigate the initial problem of possible geometric influences on rubber friction, two basic configurations are required. A hemispherical slider is thought to be appropriate to be used for the investigation, as both experimental and computational experiments can be conducted without problems such as edge effects or excessive wear caused by sharper indenters. One configuration is needed, in which a wrapping of rubber around a rigid hemisphere is developed, and one in which a hemisphere is deformed into a flat configuration and no wrapping is possible. A FEA schematic of both configurations is shown in Figure 4.11. The schematic figure a) shows a rigid spherical slider indenting into and sliding along a rubber block where the rubber wraps

around the indenter. This contrasts well schematic b) where a rubber sphere of the same diameter D is deformed to conform to the flat shape of the rigid contact surface (without wrapping) as it slides over a smooth rigid surface. The first case can be considered similar to the behaviour of a smooth rubber tyre surface sliding over an individual asperity in a road surface. Throughout this work the test geometries, shown in Figure 4.11 a) and b), is denoted by configuration 1 and 2 respectively:
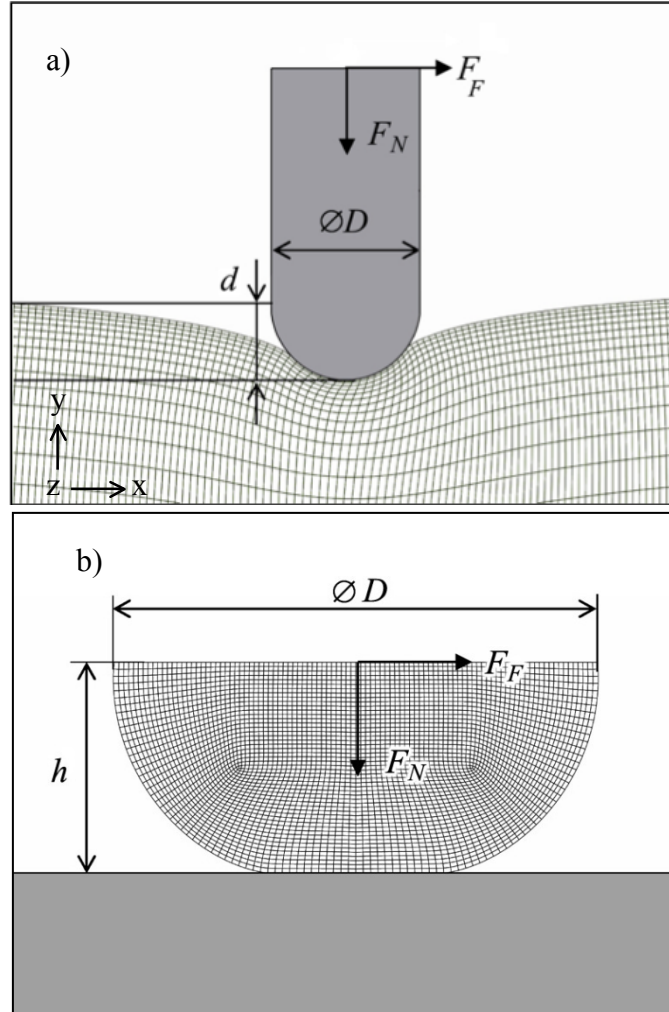
Figure 4.11: Geometric definitions of the FEA models to show the geometric influence on rubber friction. a) Model of a rigid hemispherical slider indenting into and sliding along a rubber. b) Model of a rubber sphere compressing onto and sliding along a flat rigid sheet.

F_N and F_F are the normal load and frictional force. In configuration 1 the diameter of the rigid slider D and the depth of deformation d are defined, as shown in Figure 4.11 a). For configuration 2 shown in Figure 4.11 b) D is now the diameter of the rubber hemisphere and the depth of deformation d is defined as:

$$d = \frac{D}{2} - h,$$ **(4.14)**

where *h* defines the height of the deformed sphere. Both, experiments and FEA models, use a spherical steel slider with *D*=12mm on a 5mm thick rubber block for configuration 1 and a rubber hemisphere with a diameter *D*=12mm on a steel track for configuration 2. The test configurations 1 and 2, defined in Figure 4.11, are shown as 3D models in Figure 4.12 a) and b) respectively.

a)
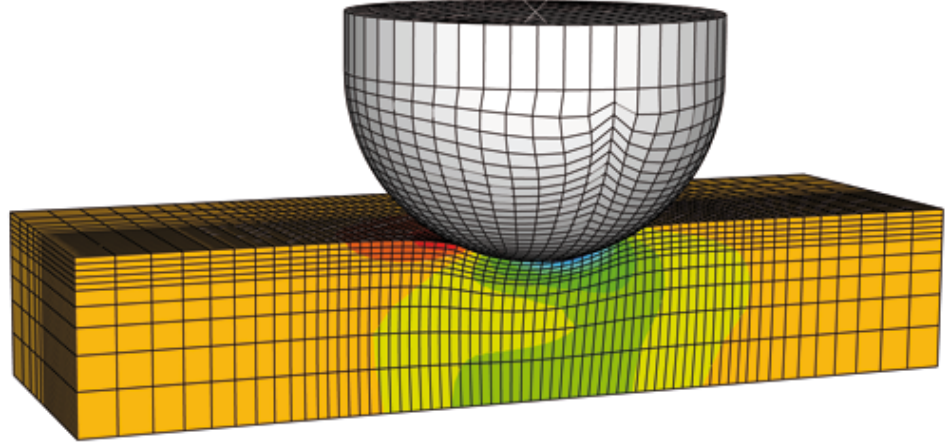
b)
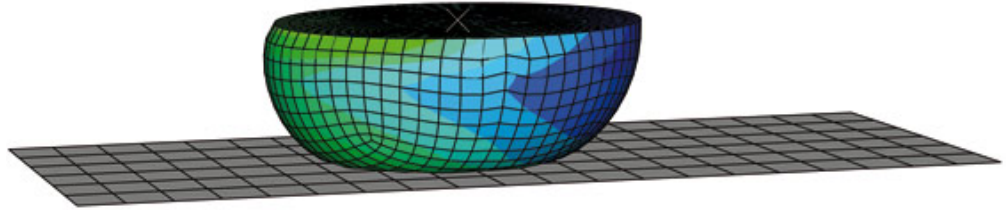
Figure 4.12: Three-dimensional hemispherical test bodies sliding along the interface modelled using FEA. a) is a model of rigid hemispherical indenter representing configuration 1 and b) is a model of a rubber sphere conforming onto a flat rigid sheet. The compressive stresses are shown in blue in front of both hemispheres, sliding to the right hand side.

4.3.3   *Experimental investigation on geometric effects*

The PLINT friction tester, developed by Roberts (1994) and which is described in Section 3.7.3, was used to investigate the two different geometrical configurations. The experimental coefficient of friction μ_{exp} is derived as the ratio of frictional force F_F to normal load F_N. In order to address whether a geometric contribution exists, the

different influences described by Equation (4.2), which affect rubber friction, have to be controlled carefully as they might camouflage a possible geometric contribution. As reviewed in Section 2.5, adhesion and hysteresis can be reduced by several modifications, so that the influence of a geometric factor can be observed clearly and these modifications are described next. In addition, considerations on the requirements of the rubber compound and the influence of fillers are made.

Decreasing hysteresis

For the test series presented here, this hysteresis term is required to be as low as possible, so that such does not camouflage a geometric contribution to rubber friction. In order to choose suitable rubber compounds in preliminary experiments the influence of a filler on the hysteresis, when used in rubber was investigated. A simple resilience test was used to examine the resilience as a measure of hysteresis. Both resilience setups, described in Section 3.2.4, were employed to measure the resilience for unfilled as well as filled NR and SBR compounds, to show the influence of a carbon black filler (HAF-N330) on the resilience. The results, shown in Figure 4.13 clearly demonstrate the effect of fillers on the resilience.
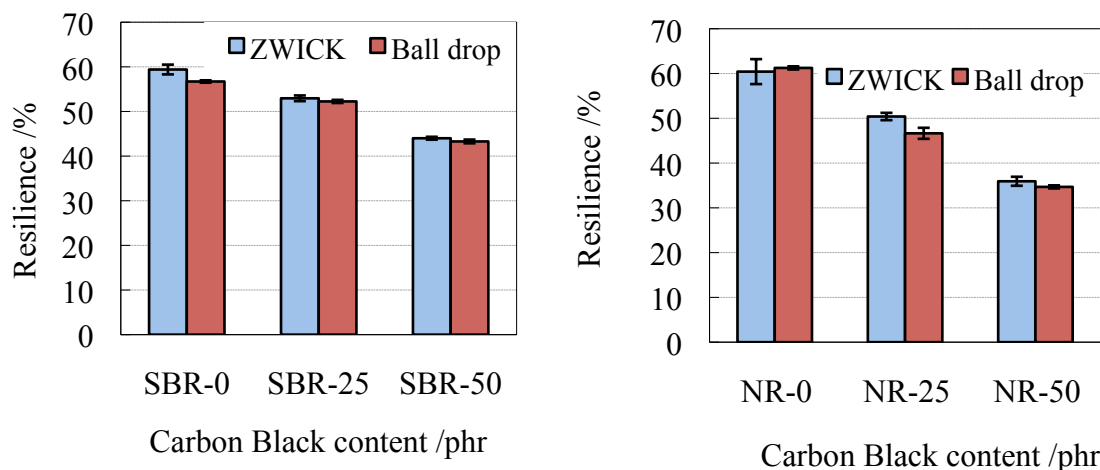
Figure 4.13: Comparison of a resilience test using a Zwick pendulum tester and a simple ball drop test for different NR and SBR rubbers.

While the unfilled rubbers exhibit a resilience of around 60%, the introduction of a carbon black filler decreases the resilience of the compound, so that more energy is dissipated through internal friction by the filler-filler and filler-rubber network. Consequently, in order to limit the viscoelastic losses through hysteresis, only unfilled rubbers (NR-0 and SBR-0) were used in this part of the investigation.

To decrease the hysteresis losses further, the specific excitation frequency of the compound is of great importance. In order to examine the frequency response, the unfilled elastomers were tested using DMA measurements, which are described in Section 3.2.3. These tests over a limited frequency and temperature scale were transformed into a mastercurve using the WLF time-temperature superposition, as described in Section 0. Both unfilled rubbers were tested in a frequency range from 0.1 to 100 Hz at isothermal temperatures ranging from T_g to $T_g+100°C$. A reference of 23°C was chosen for all mastercurves. The horizontal shift factors a_T were obtained according to Equation (2.35). The values given for both materials in Figure 4.14 as a function of temperature are in good agreement with similar values in literature (Klüppel and Fritzsche 2009). For NR-0 the constants obtained had the values C_{W1}=8.86 and C_{W2}= 125.6°C, while the constants for SBR-0 were C_{W1}=4.3 and C_{W2}= 114.4°C, which are also in good agreement with literature values (Shaw and MacKnight 2005).
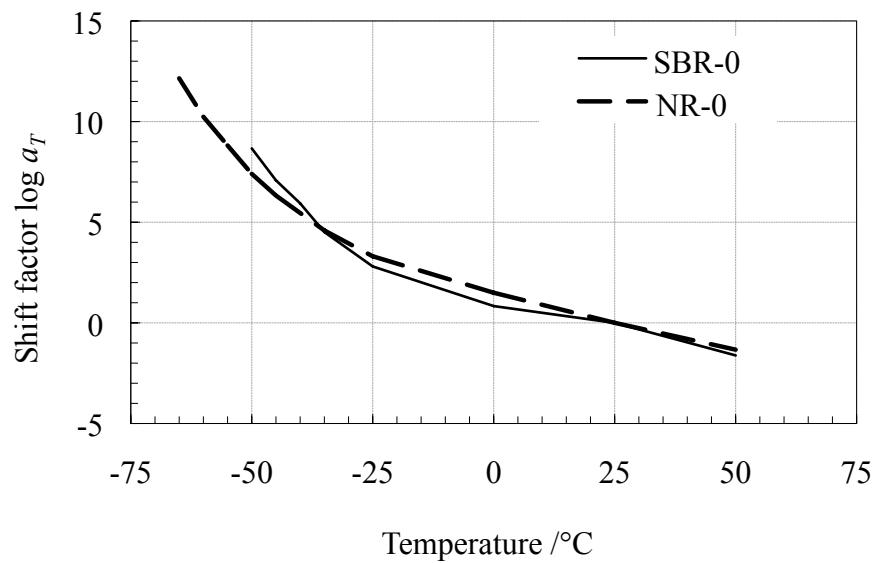
Figure 4.14: Horizontal shift factors $\log a_T$ for NR-0 and SBR-0 obtained from the WLF equation in relation to the temperature given for the range of T_g until $T_g+100°C$.

The shifted master curves of the hysteresis losses for NR-0 and SBR-0 at a reference temperature of 25°C are shown in Figure 4.15 and Figure 4.16. A characteristic maximum hysteresis peak is shown, which correlates to the compound's glass transition temperature (see Sections 0 and 2.5.5). At low frequencies (or at higher test temperatures) the SBR-0 compound shows a slightly higher hysteresis loss when compared to NR-0. Due to its higher glass transition temperature, the maximum occurs at lower frequencies than that of NR.
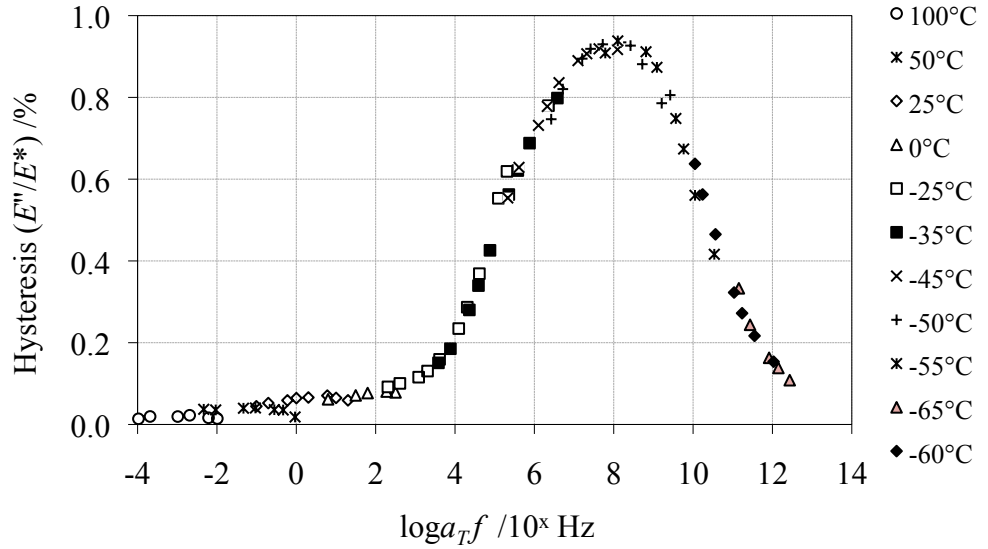
Figure 4.15: Hysteresis master curve for NR-0 gained from the WLF shift.
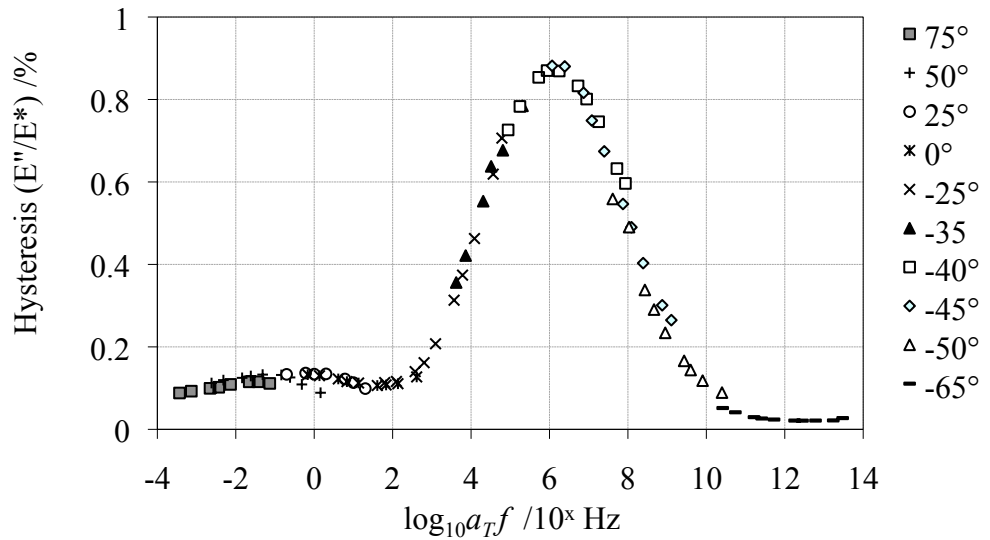
Figure 4.16: Hysteresis master curve for SBR-0 gained from the WLF shift.

Grosch (1963) showed the direct relationship between the viscoelastic properties of rubber to the sliding velocity (see Section 2.5.5). For the friction testing conducted here, the hysteresis contribution should be as low as possible, so that from both figures it can be concluded that this is accomplished at low frequencies only. This is of importance, as a minimum hysteresis contribution is then expected, as long as the sliding velocity (and excitation frequency, induced due to possible stick-slip) is low. Therefore, the minimum operating velocity of 0.01mm/s of the friction tester was chosen, operated at room temperature in an temperature controlled room held at 25°C. This way an almost static

friction measurement could be assumed. Therefore, the direct viscous or hysteretic contribution to rubber friction was as low as possible.

Decreasing adhesion

As mirror-like surfaces exhibit very high adhesion, which can result in large stick-slip instabilities (Thirion 1946) or Schallamach waves (1971) the rubber materials were vulcanised against a roughened surface as described in Section 3.1 and analysed in Section 3.5. By this, the adhesion was considerably decreased and a complete study of this is described in Chapter 7.

The remaining hysteretic contribution would only be through an indirect contribution to adhesional effects and this was assumed to be negligible, as the adhesional contribution was decreased by using a suitable lubricant. As is described in Section 2.5.8, a lubricant hinders the direct interfacial molecular bonds, leading to a large reduction of the adhesional influence. Firstly, distilled water, being a commonly used lubricant (Roberts 1974; Pan 2007), was used in order to decrease the adhesional influence on friction. However, both rubbers, NR and SBR, exhibit a hydrophobic nature and the pressure at the interface was sufficient to squeeze out the water from the contact area, establishing dry contact patches, so that only little change in the frictional force was noted. In order to avoid this complication, a solution of soap and distilled water was tried (Roberts 1974; Schramm 2002), as soap reduces the surface tension of water, so that a better contact between water and the interface is established. Furthermore, pure soap has been used before as a lubricant (Tabor 1960). However, a solution of water and soap reduced the friction to zero. It is assumed that a hydrodynamic boundary condition was established, resulting in a total loss of contact, as was shown by Roberts (1974) in Figure 2.34. As a soap solution was unsuitable, and other liquids like oil or chemical solvents would swell the compound, a dry lubricant was used instead, as suggested by Grosch (1963) and also (Barquins and Roberts 1986). In this work a thin layer of talcum powder was used. Due to this measure, adhesional effects were reduced but the friction was still measurable. The untreated surface, showed a coefficient of friction around μ=0.8, while the powdered surface had a value of around μ=0.2 under otherwise similar test conditions, as shown in Figure 4.17. Also for this chosen test configuration the friction coefficient complies with Amontons' law, as it is virtually independent of

normal load. However, it is acknowledged that elastomers usually exhibit load dependence, as is discussed in chapter 2.
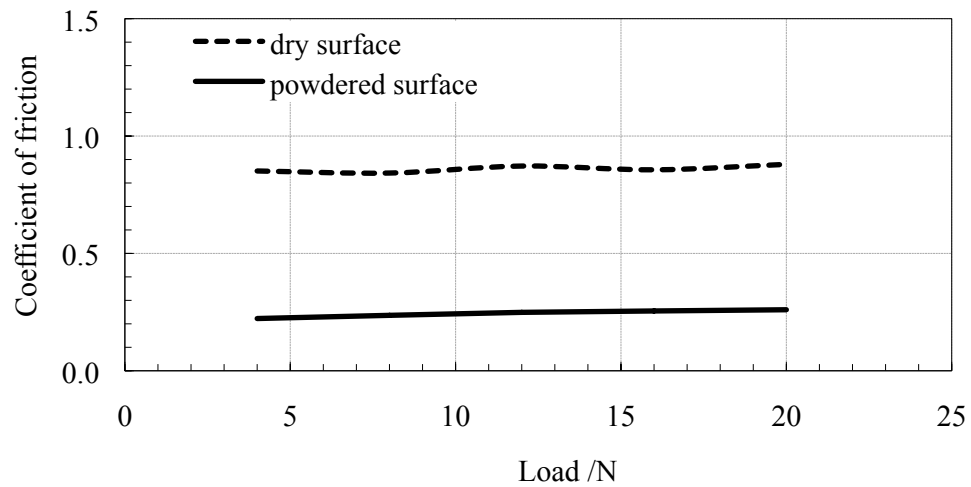
Figure 4.17: A dry surface exhibits higher friction than a powdered surface (v=0.01mm/s, R=6mm, SBR-0).

The choice of rubber compounds and the modifications described here were made to ensure that only the intrinsic coefficient of friction was measured. The compounding formulation and the measured properties of the unfilled rubbers are analysed in Chapter 3 and the specific test parameters used in this study are listed in

Table 4.1: Test parameters used to characterise the frictional behaviour.

Rubber compounds	NR-0 and SBR-0
Sliding velocity	0.0001m/s
Test temperature	25°C
Normal load	1N to 20N
Interface geometry	Hemisphere (R=6mm) on flat surface

4.3.4   *FEA investigation on geometric effects*

Both configurations 1 and 2 were modelled and analysed in 3D using ABAQUS (Explicit) version 6.7, using C3D8R elements with hourglass control (Simulia 2009) using the geometric parameters defined in Table 4.1. The simplified input deck of the model used here is given in the appendix in Section 9.3. As discussed in Section 2.6.3, this software works well for models subjected to a very large deformation and where complicated contact with high friction is encountered (Sun et al. 2000; Kim et al. 2002).

Due to the considerable decrease of the hysteresis contribution and to eliminate time dependent behaviour, the elastomer was modelled with elastic properties. As the results presented here are on unfilled rubbers deformed to relatively modest strains, the Neo-Hookean or statistical theory of rubber elasticity (Treloar 1975) can be used in the finite element models to describe the rubber behaviour. The shear modulus was taken to be 1/3 of the tensile modulus, measured using a tensile test over an extension ratio range of 1 to 1.2 and the derivation of the coefficients, describing the SEF used, is given in Section 3.6. It was considered that the detailed form of the stored energy function used in this work would not be a significant factor. For a simple comparison and following the recommendation of Kumar et al. (2007), finite element models were adopted that used other stored energy functions such as the Mooney SEF with coefficients fitted over a much larger range of strain. The results obtained were all essentially identical to those produced by the Neo-Hookean SEF confirming that the exact form of the stored energy function was not significant in this work. Therefore, only the results obtained using the Neo-Hookean SEF are presented.

In the FEA the steel components, used in the experimental investigation, are modelled as rigid bodies, due to the large difference in modulus compared to rubber. This means that no deformation of the rigid bodies was assumed which saved computational costs. The FE analysis is divided into two steps, which control the displacement of the slider. In first step contact was established and the rigid slider indents into the rubber as shown in Figure 4.2 a) and b). Secondly, the slider is displaced along the rubber surface, as shown in Figure 4.2 c).

FEA step 1 – indentation

The FEA approach used here uses displacement control as an indirect application of the normal load on the slider as described in Section 2.6.3. Therefore, prior to modelling, the values for the indentation depth used in the FE models had to be measured. The PLINT friction tester does not measure any vertical displacement resulting from either the indentation or any subsequent uplift during sliding. Therefore, additional indentation tests were conducted for the 12mm hemisphere on a 5mm thick rubber sample in order to validate the subsequent calculations and FEA models. As described in Section 2.5.4, the indentation depth can be also predicted by using the Hertzian theory, however, earlier work by Busfield and Thomas (1999) showed that for soft materials the ratio of rubber thickness to the diameter of circular contact must be at least 10:1, to avoid complications arising due to the supporting (rigid) boundary conditions underneath the rubber block contributing. For the employed test geometry, this ratio is less than the proposed ratio, so that a lower indentation is expected than is calculated using Hertz' theory (Waters 1965). For this reason a custom-made setup was designed and used to measure the indentation independently, shown in Figure 4.18.

Figure 4.18: Setup to measure the indentation depth of indenters (see Figure 3.30) on rubber samples. A counter weight is used to balance the load and zero out the initial load induced by a micrometer gauge, which measures the depth of indentation. Dead weights (not shown) are used to change the normal load.

Figure 4.18 shows a balanced, rigid beam supported by a knife-edge, which minimises frictional losses. Indenters of different shapes (see Section 3.7) can be attached to the left hand side of the beam and loaded with dead weights. So that a contacting micrometer gauge measures the deflection of the beam due to the indentation of the indenter into the rubber. In order to avoid preload, the spring in the gauge was removed

and the weight of the gauge, resting on the beam, was accounted for. Similar indentation tests were conducted using FEA. As is shown in Figure 4.19, the experimental results are in good agreement with the FEA for a 5mm thick rubber block. However, if the results are compared to the prediction by Hertzian theory for the tested geometry, then a large discrepancy is observed, as the Hertz model assumes an infinite thickness for the deformable material (Gent 2001). Additional tests with a rubber block of 10mm thickness have been conducted experimentally and using FEA, to further examine the problem. Nevertheless, not until a rubber block with a thickness of 20mm is used, does the FEA prediction become close to the Hertzian theory, as the rigid substrate is not felt by the indenter any longer. However, a 20mm unfilled rubber block is unsuitable for friction tests due to large shear deformations that would be encountered.
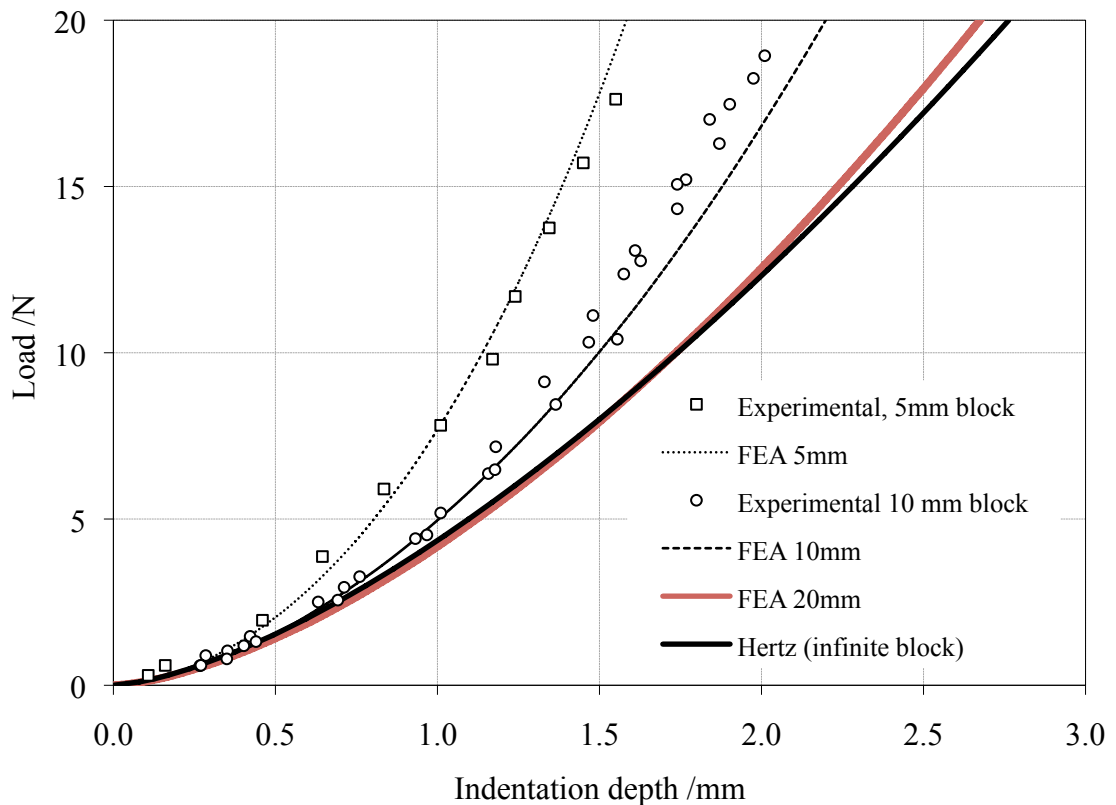
Figure 4.19: Experimental data points and the corresponding FEA calculations (thick lines) are compared to the theoretical prediction after Hertz (1861) for NR-0 using a rigid hemisphere (*R*=6mm).

A comparison of the measured experimental and finite element computational results between a NR-0 and a SBR-0 for the indentation test geometry is given in Figure 4.20.
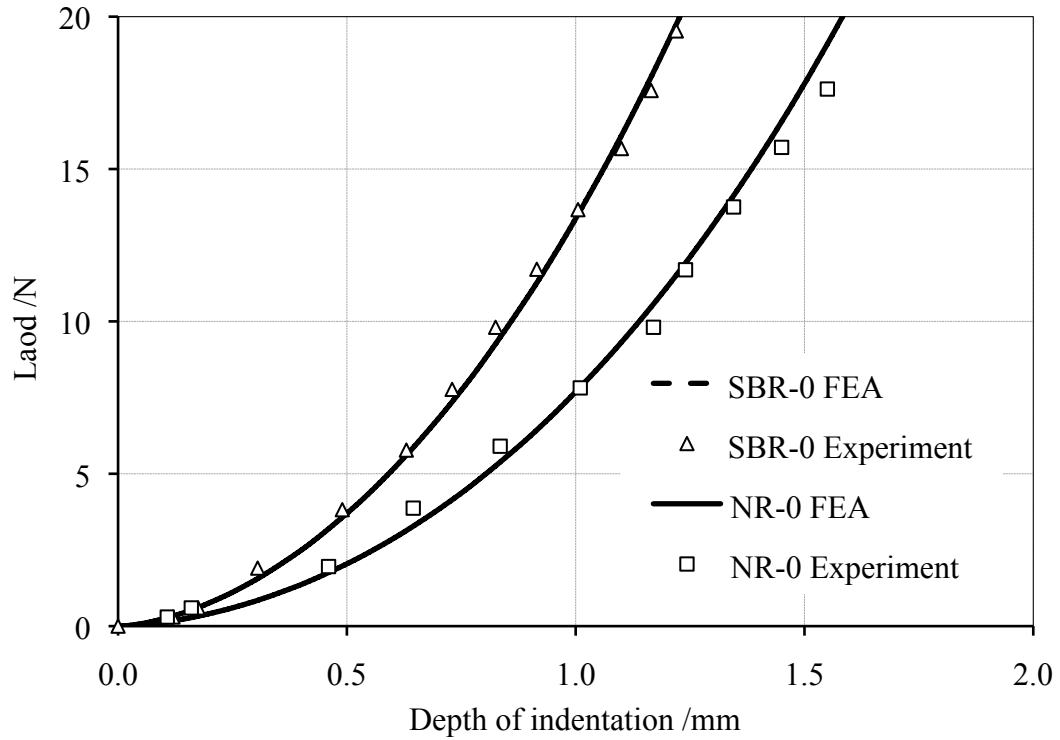
Figure 4.20: Comparison of FEA and experimental results for an indentation test of a rigid sphere (*R*=6mm) on a 5mm thick rubber block for NR-0 and SBR-0.

As expected from results of the hardness and tensile tests in Section 3.2, SBR-0 has a lower indentation when compared to NR-0 due to its higher modulus. The good agreement with the FEA confirms the suitability of the chosen stored energy function for this analysis. Further tests with different indenter geometries have been also conducted throughout this work and can be found in Chapter 7.

FEA step 2 – sliding friction

Amontons' friction model (Amontons 1699), also known as Coulomb friction, is employed at the interface in the FEA software as a single input parameter, the input coefficient of friction μ_I. Even though Amontons' friction model, originally designed for metals, is thought to be not applicable for rubber friction, as it assumes that μ is largely independent of the normal load (Smith 2008), it is still used for many industrial (Axel 2006) or engineering and scientific applications (Budinski 2001; Gough 2003; Uchiyama et al. 2005; Liang et al. 2009). In addition it is readily available in the most common FEA packages (Fukahori et al. 2008; Simulia 2009). As described in Section 2.5.2 rubber friction depends on various parameters, including surface topography,

temperature, sliding velocity and lubrication, so that the commonly assumed proportionality between frictional stress and normal stress is not generally obeyed (Gough et al. 1999). However, it is valid to use specific values for the coefficient of friction (as a constant) if it is borne in mind, that only one particular sliding condition is modelled. In this study it is shown that under the above described conditions and over the tested range, Amontons law holds for test configuration 2. The input coefficient of friction μ_I in the FEA model is defined as the ratio of the frictional force divided by the normal force, as applied by Fukahori et al. (2008):

$$\mu_I = \frac{F_F}{F_N},$$

(4.15)

The value of the input coefficient of friction μ_I is chosen according experimental investigations, using the same experimental test conditions as explained previously. The resulting output coefficient of friction μ_R calculated from the FEA model is therefore the result of dividing the calculated output frictional sliding (reaction) force, RF_F, by the calculated output normal (reaction) force RF_N

$$\mu_R = \frac{RF_F}{RF_N},$$

(4.16)

This means that the output coefficient of friction should be independent of any strain imposed in the sample.

4.4   Results and discussion

If Equations (4.15) and (4.16) are considered, at first sight it would appear, that the resulting calculated output friction ratio μ_R should equal the input coefficient of friction μ_I, as both the input parameters μ_I and F_N in Equation (4.15) define F_F via the FEA input deck. However, this is not borne out for test configuration 1 when examining the comparison of experimental and computational results as shown in Figure 4.21 and Figure 4.22 for NR-0 and SBR-0 respectively. In both figures the ratio of μ_R divided by μ_I is plotted against the normalised depth of penetration d/D, in order to remove any effect of geometric scaling for NR-0 and SBR-0. For test configuration 2, where a rubber sphere conforms to a flat rigid surface and the resulting contact is over a plane interface, the ratio between μ_I to μ_R is an approximately unity irrespective of the depth of deformation, while for configuration 1 the ratio increases with the d/D. The apparent

increase in friction of test configuration 1 can not easily be attributed to the increase in contact area or change in normal stress, as the contact area increases with increasing normal load for both configurations. As viscoelasticity is not included in the FEA model this difference cannot be due to hysteresis losses but has to be entirely geometric in origin.
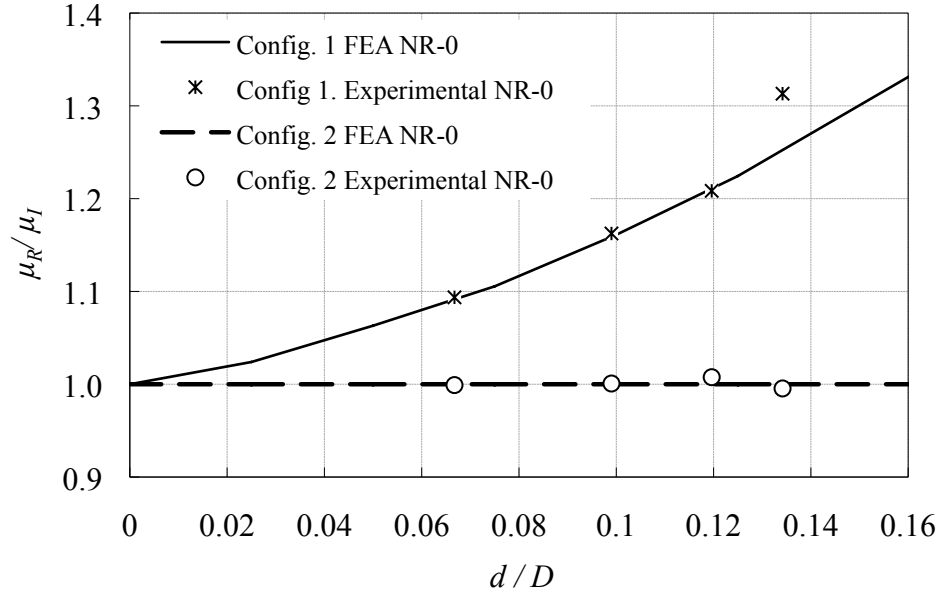
Figure 4.21: The ratio of μ_R/μ_I plotted against the depth of penetration/indenter diameter for NR-0. While for configuration 2, where a rubber sphere conforms to a flat rigid substrate, no alteration in the ratio of input to output friction exists, configuration 1 shows a distinct dependence on the indentation depth.
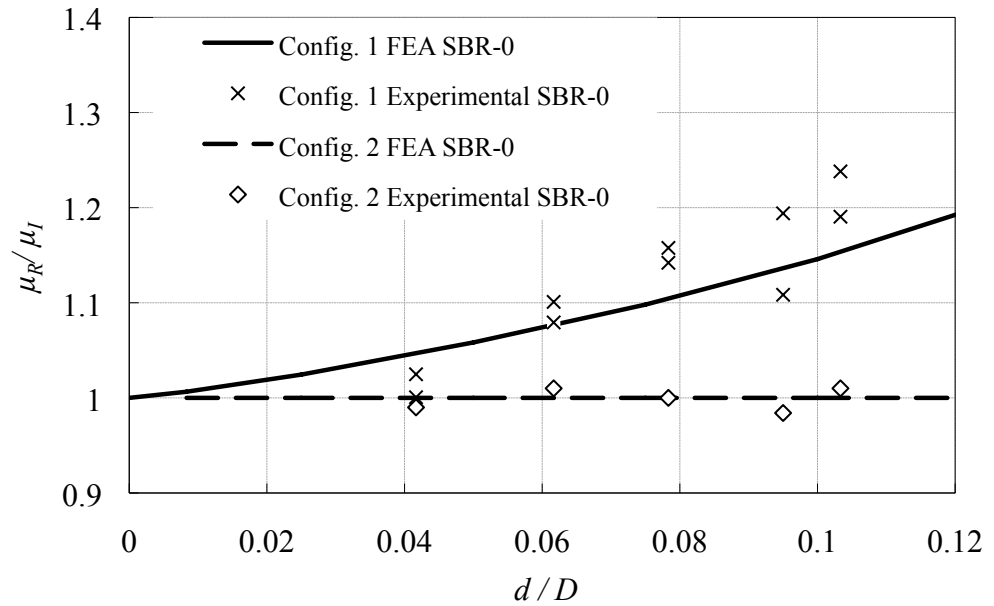
Figure 4.22: The ratio of μ_R/μ_I plotted against *d/D* for SBR-0.

A very good agreement between the experimental and calculated FEA data for NR-0 is shown in Figure 4.21. In Figure 4.22 the experimental scatter is somewhat larger for the SBR-0 compound.

The geometric effect of deforming the rubber surface onto the curved rigid profile has the effect of adding a significant additional contribution to rubber friction. This behaviour can be considered similar to the increase in friction resulting from the previously made considerations of a string being wrapped around a capstan. The increase in indentation depth creates an increase in the angle of contact even when the imposed friction coefficient remains the same at the interface. This additional entirely geometrical effect increases the total friction force as shown in Figure 4.21 and Figure 4.22, so that for the described geometry of configuration 1 the friction output is higher than that experienced for configuration 2 where the surfaces remain flat. This factor can be of considerable practical significance for example in explaining the increased friction that is experienced with certain types of road surface containing sharp asperities. It is evidently more complex in practice as many asperities on the road surface interact with small local regions on the rubber surface, also as the modulus is higher in a tyre tread compared to the unfilled samples, the depth of penetration will be smaller. One other factor of interest is that the coefficient of friction measured in many instances might be higher than if the friction had been measured using a flat surface contact. Therefore, as reviewed in Section 2.5, it is crucial to identify a suitable test geometry when measuring the friction behaviour.

4.5   Conclusions

Commonly, for the case of a dry friction interface without wear, the total friction is typically attributed to result from both, adhesion and hysteresis. The adhesion contribution to friction is related to the intermolecular process taking place on the interface surface and the frictional contribution resulting from hysteresis is due to the viscoelastic energy lost by the deformation process of a certain volume of rubber. It was proposed by Schallamach (1969) in a two-dimensional consideration of the interface, that a wrapping of the rubber around a rigid prismatic slider might also influence the total frictional force. Nevertheless, no confirming experiments were carried out so that this study on the (geometrically) macroscopic influence on rubber friction remained only theoretical, as in 1969 no suitable techniques existed yet to analyse the stresses in the test geometry.

In order to further develop an understanding on the problem presented by Schallamach, firstly, the main factors influencing the total frictional force, adhesion and hysteresis, were examined for two unfilled model materials, SBR-0 and NR-0 by various techniques. Specially designing and modifying the frictional interface decreased the influence of both, adhesion and hysteresis, so that in the work presented here it was confirmed for the first time that an additional geometrical factor also exists. The friction experiments presented validate a three-dimensional entirely elastic FEA model. It was shown that the geometrical contribution to the total frictional force for a hemispherical rigid indenting and sliding on a soft rubber, is dependent on the depth of penetration of the rigid surface into the elastomer, which changes the angle of contact between both surfaces. In contrast, tests using a different geometry, where a rubber hemisphere of the same dimensions conforms to a rigid flat surface, did not show this effect. The work presented here has shown that the entirely geometric contribution on a macroscopic level considerably increases the measured resulting coefficient of friction and is anticipated to make a significant contribution to many every-day frictional sliding applications.

5 FEA modelling of Schallamach waves

5.1 Introduction

In Chapter 4 it has been shown that a macroscopic wrapping effect contributes significantly to rubber friction depending on the exact interface geometry. If the micro-roughness of this interface is considered to be optically smooth, a different displacement mechanism to microscopically rough surfaces occurs over a large range of sliding velocities. This displacement mechanism is commonly described as Schallamach waves or waves of detachment and this chapter outlines an attempt to model the wavelike surface instability. As was discussed in Section 2.5.6, extensive research on the origins of Schallamach waves has been done experimentally. However, virtually no information has been published on the modelling of these waves of detachment. This is confirmed by Baumberger and Caroli (2006) who stated that "no prediction relating material properties neither to the dynamics, nor even to the occurrence of Schallamach waves is available up to now". Nevertheless, in (industrial) applications, where Schallamach waves are observed or at least anticipated, FE modelling might significantly enhance the understanding of this type of surface instability. Furthermore, the use of FEA allows for a detailed stress and strain analysis to be made at the interface.

The following chapter is based on a paper accepted by Rubber Chemistry and Technology for publication by Gabriel et al. (2010b).

5.2 Theoretical background

Basic instabilities in rubber are examined here first, leading towards an understanding of the origins of Schallamach waves. The phenomenon of surface instabilities under large static or dynamic elastic deformations have been observed both, in tension and compression, for example during the inflation of rubber shells (Gent and Cho 1999), at

a very high frequency during relative stick-slip sliding in rubber friction (Fukahori and Yamazaki 1995) or as a static surface configuration during the surface wrinkling of compressed rubber (Biot 1965). The latter occurs in rubber materials under uniaxial or biaxial compression at extension ratios that range from about λ=0.54 to 0.45, depending upon the exact boundary conditions applied. The detailed nature of this instability has not been totally resolved as Southern and Thomas (1965) as well as Gent and Cho (1999) reported experimental results that deviate from Biot's initial theoretical predictions. However, very recently Hong et al. (2009) suggested that this discrepancy is due to two different modes of instabilities, occurring at different strains and this is discussed later. Prior to modelling a complex instability like a Schallamach wave, it was thought necessary to validate the explicit dynamic FEA method when used to model typical rubber buckling phenomena, therefore, this simple compression buckling was modelled and the FEA predictions compared with the theoretical predictions of Biot and the experimental findings of Gent and Cho.

Previous attempts to mathematically investigate the onset of surface instabilities have been made: A static, numerical analysis on the initiation of surface instabilities was described by Best et al. (1981). In their mathematical study the onset of wave formation depended on the amount of compressive pre-strain. They neglected inertia effects and assumed the boundary of the elastic half-space as stress-free in their analysis, hence their results can only apply to regions outside the contact area. Désoyer and Martins (1998) took these factors into account and extended the numerical analysis to surface instabilities. Gough et al. (2001) discussed the modelling of Schallamach waves using a finite element approach, however, only information of a descriptive nature was given. Ashraf et al. (2007) claim to have modelled a Schallamach wave during their studies on wear, however, no specific details on how the instability was modelled nor other information on the model itself was given. It is suspected that due to the coarse nature of the element geometry, only a meshing problem was in fact reported. Up to now, no dynamic FEA approach has been reported, tackling the difficulties of modelling dynamic surface instabilities, such as Schallamach waves.

5.3   Experimental background

5.3.1   Experimental investigation of general buckling instabilities

To investigate general buckling instabilities, similar to the experiments by Gent and Cho (1999), a rectangular rubber block (200x30x5mm³) was compounded from SBR-0 as described in Section 3.1. The compounding formulation is given in Table 3.2. An unfilled rubber was chosen, as it provides highly elastic properties, while exhibiting complete recovery after a large deformation. In order to restrict the degrees of deformation to plane strain, the rubber slab was glued to a flexible metal plate of similar dimensions with a thickness of just 0.5mm. An adjustable clamp, shown in Figure 5.1 a), was used to push the ends of the rubber slab together. At a critical degree of bending, sharp creases appeared on the inner (compressed) surface of the rubber slab, as is shown in Figure 5.1 b). The creases, which formed in the pole, where the bending was the greatest, were orientated almost parallel to each other and only disappeared a couple of seconds after the rubber was released from the clamps.
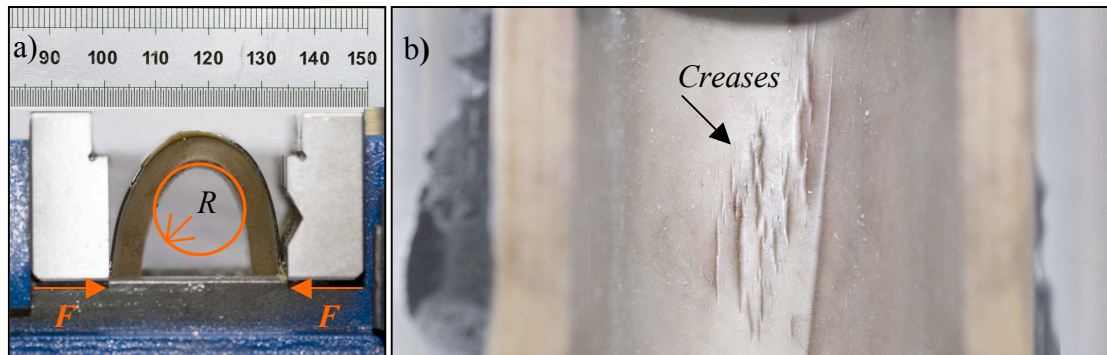
Figure 5.1: A bending experiment of a slab of rubber similar to Gent and Cho (1999) is shown. a) The radius of bending *R* of a rubber bonded to a flexible metal plate is measured. b) At a critical degree of bending surface instabilities manifest as creases on the inner surface of the bent rubber.

The critical bending ratio, at which creases were formed, was measured by applying fine lines on the rubber surface and measuring the decrease in the correlating distance to each other, which was induced due to the surface compression.

5.3.2   Experimental investigation of Schallamach waves

Several experimental findings on Schallamach waves are discussed in Section 2.5.6 and also have been conducted parallel to the work presented in this chapter. As the focus of this chapter is of the modelling of surface instabilities, the detailed description of the experimental investigation on Schallamach waves is not presented until the following chapter, where an extensive experimental examination is undertaken.

5.3.3   Computational investigation of buckling instabilities

Either implicit dynamic or explicit dynamic finite element methods can be used to model the non-linear dynamics models encountered in buckling problems. Implicit methods struggle to solve the highly non-linear contact problems, which are developed during sliding rubber friction (Sun et al. 2000; Kim et al. 2002; Harewood and McHugh 2007). An initial attempt to use an implicit dynamics model did not succeed, as the model could not pass through the point of instability. Resulting from the fundamental theory on how results are obtained from an implicit dynamic FE approach, the implicit dynamic approach for energy minimisation can not resolve that around instabilities multiple energy minimisations might exist. Consequently, all the models used in this thesis were created and analysed using the software package ABAQUS/Explicit (version 6.7), which is suitable for complicated, dynamic contact where high friction and large deformations are encountered (Simulia 2009). The following properties of the FEA model were used for both the compression model and the Schallamach wave model.

The properties measured in Section 3.2.2 for an unfilled SBR were used in the FEA package for describing the material model. The rubber was modelled as a semi-infinite, homogenous and isotropic body. The neo-Hookean strain energy function (SEF) was used to model the behaviour of the rubber (Treloar 1975), because it is the simplest available SEF and for this type of elastic analysis the detailed form of the SEF was thought to be unimportant (Gent and Cho 1999). The SEF is represented by the equation given in Section 2.3 as

$$W = \frac{G}{2}\left(\lambda_1^2 + \lambda_2^2 + \lambda_3^2 - 3\right),$$

(2.7)

where W is the strain energy density, λ_i are the principal stretch ratios and G is the shear modulus. The shear modulus of G=0.54MPa was taken to be 1/3 of the tensile modulus, measured using a tensile test over an extension ratio range of 1.0 to 1.2 on a typical unfilled SBR, as also applied for the models in chapter 4. The employed elements for the bulk material were two dimensional plane-strain, reduced integration elements with hourglass control (type: CPE4R). Quiet boundaries were introduced using semi-infinite elements (type: CINPE4) (Simulia 2009). The output contours and values presented here are all maximum principal stresses (true stresses). For the FE analysis the geometry of a rigid, hemispherical wedge (*R*=3mm) on a rubber block (thickness=5mm), has been chosen. In this plane strain model both the slider and rubber block were meshed with an element size of 25μm. For reasons of convergence and to replicate the experimental conditions, the normal force was applied via displacement control, so that a vertical displacement of the wedge produces a specific normal load F_N, which depends on the rubber block thickness. A two-step displacement model was used, where in the first step (indentation) contact was established and in the second step (sliding) the slider was displaced parallel to the rubber surface. The resulting shear stress between the smooth rubber surface and the smooth rigid, slider was applied using Amontons' friction law. By using a single value for the coefficient of friction (as a constant) the model can only be used to represent simple conditions. If rubber friction was to be modelled for example over a range of velocities, the dependence of μ on the velocity would have to be implemented, but this was not of primary interest in this study. A simplified input deck is shown in Appendix 9.4.

5.3.4   *Investigation on surface adhesion*

In order to characterise the adhesion properties of the compound modelled in this work, a peel test was designed to measure the rate dependent surface energy similar to the test used by Roberts and Thomas (1975). In this test, which is shown as a schematic test setup in Figure 5.2, a glass cylinder rolls down a smooth rubber surface with a velocity, which is both dependent on the slope of the rubber surface as well as its adhesive

properties. For the tests an unfilled rubber was vulcanised with a mirror-like, smooth surface.
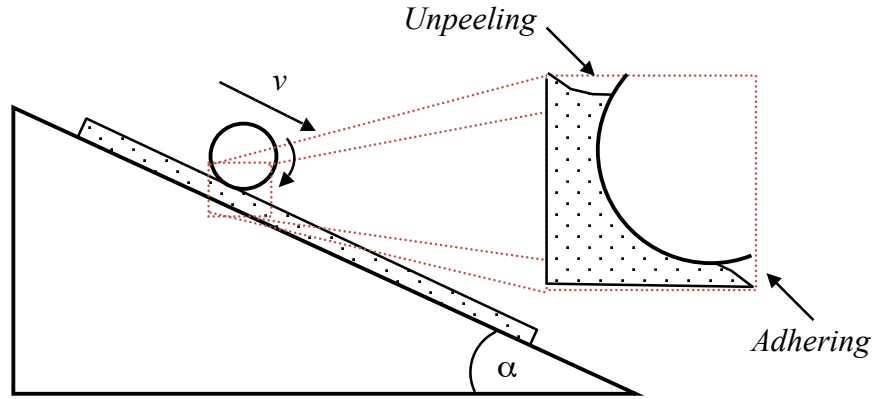
Figure 5.2: A glass cylinder of length L_{Roller} rolling over a smooth rubber surface at a certain velocity *v*. The slope of the rubber surface, measured at an angle α determines the rolling velocity. In the schematic magnification of the point of contact of the rubber surface and the cylinder, the unpeeling zone at the back as well as the adhering at the front are shown.

When the cylinder rolls down the rubber block, energy is dissipated by the unpeeling process at the rear of the contact, while a certain amount of energy is gained in the adhering process at the front, however, this gain in energy is assumed to be small and is neglected in the relationship given by Roberts and Thomas (1975), which can be related to the surface energy γ and is given as

$$\gamma = \frac{Mg\sin\alpha}{L}, \tag{5.1}$$

where M is the mass of the cylinder, α is the slope of the rubber surface and L is the length of contact between the rubber and the cylinder. When the rubber samples used in this work were tested using the setup shown in Figure 5.2, however, there was a wide variation in measured rolling velocities. While the total time needed for the cylinder to roll a length of 100mm for example at a slope of 25°, a time of around 200s was measured for the first of a repeat set of five, while the following rolling times decreased significantly down to an average of 55s, with a lowest value of only 10s. The large deviations on the time scale made a systematic scientific examination of the behaviour very difficult. It was also noted, that the cylinder did not roll constantly over the rubber surface but in sequences. Several reasons are likely to influence this behaviour. Tabor and Fuller (1975) describe this "sequentially (but) not simultaneously" behaviour to be caused by the irregular contact area which might be experienced when a cylinder rolls

down a surface with non-consistent adhesional properties. Prior to testing all the samples were cleaned with acetone and isopropanol, to remove any possible surface contaminations. However, it is believed that an inconsistent sticky layer on the rubber surface was present, which significantly influenced the adhesion properties but was not removed by the cleaning procedure. For this reason any contaminating layer, which might still be present after cleaning was also removed by Soxhlet extraction. However, after extraction the rubber surface lost virtually all adhesional properties, so that no surface energy could be measured. Furthermore, electrostatic charges on the rubber surface might have influenced the rolling behaviour, as rubber is a very good insulator, so that a surface charge may remain after or due to the cleaning process (Roberts 1971). For an initial investigation into the modelling of Schallamach waves adhesional effects were not included in the proposed FEA model.

5.4   Results and discussion

5.4.1   Experiments on general buckling instabilities

The critical bending ratio of the compressed rubber block at which surface wrinkling instabilities occurred in the form of parallel creases on the inner surface, was measured experimentally to be λ=0.64±0.007. The measured value agrees well with the value of λ=0.65 measured by Gent and Cho (1999), for a similar geometry. However, the critical deformation is considerably smaller then the value of λ=0.54, as predicted by Biot (1965). Gent and Cho stated that "it is not clear why the instability occurs so much sooner than expected". Nevertheless, the reason for this is discussed in the next section on the modelling of general buckling instabilities.

5.4.2   Modelling of general buckling instabilities

The buckling of a rubber surface in equibiaxial compression was modelled first to validate the application of the explicit finite element model prior to investigating Schallamach waves. Green and Zerna (1986) predicted a critical compression ratio at

which the rubber bulk becomes unstable. They proposed that the resistance to a small surface indentation for an equibiaxial compressed rubber block reduces with compression. This reduction in indentation force reflects the onset of a surface instability and it becomes zero at 33% compression (λ=0.67), resulting in a surface instability due to the equibiaxial compression. This initial theory by Green and Zerna can be modelled using FEA, by adopting an axis symmetric model of a half-space under equibiaxial compression. The diameter of the hemispherical indenter was chosen to be 0.2mm with a small indentation of 0.06mm applied for each level of compression, while the undeformed element length for the FEA was chosen as 0.04mm. The whole FEA model is shown in Figure 5.3. In a first step ① the model is compressed in the R-axis, while in a second step ② a spherical indenter is brought into contact with the compressed rubber surface, indenting into the rubber bulk. Figure 5.4 a) shows the maximum principal stresses for a model precompressed by λ=0.9 with a superimposed indentation.
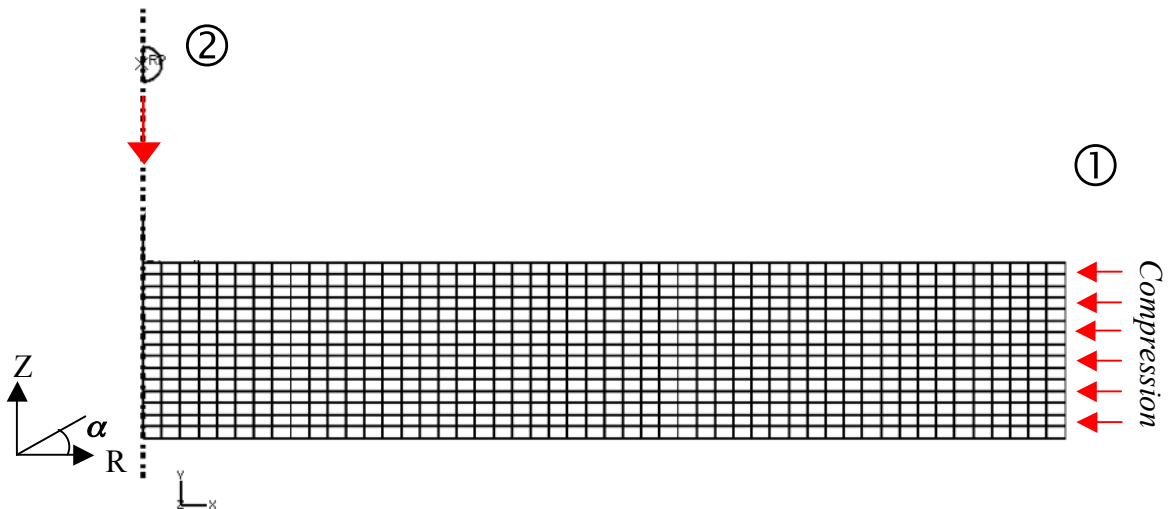
Figure 5.3: Unstressed axis-symmetric model for ① equibiaxial compression and ② infinitesimal indentation of a sphere into the rubber.

a)

b)
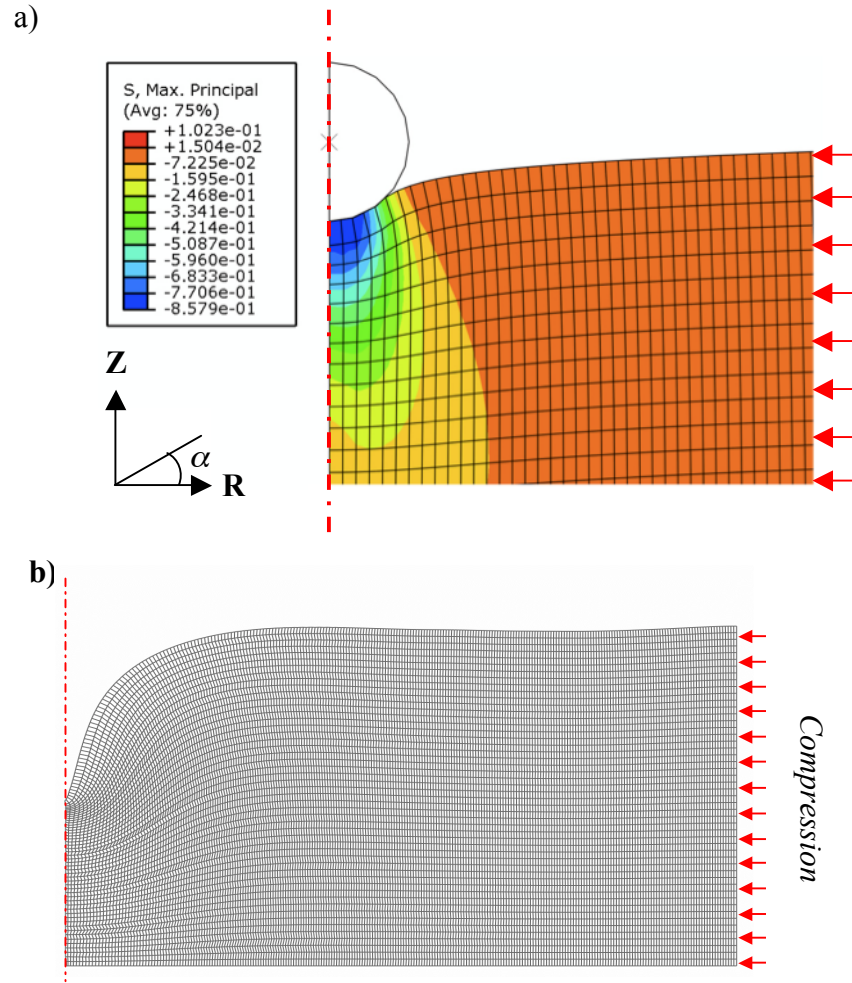
Figure 5.4: a) Magnification of the contact region when a rigid sphere indents into a soft rubber block. This is an axis symmetric model with a 10% biaxial compression. b) Buckling of the entire model without indentation at 30% (no stress contours).

Figure 5.4 b) shows that a buckling instability arises in the model at the axis of symmetry at a compression where $\lambda=0.7$. The surface buckles at this strain prior to indentation. The ratio between the resistance to indentation F_N at a certain compression to the initial resistance to indentation F_0 for an uncompressed state ($\lambda=1$) is given in Figure 5.5:
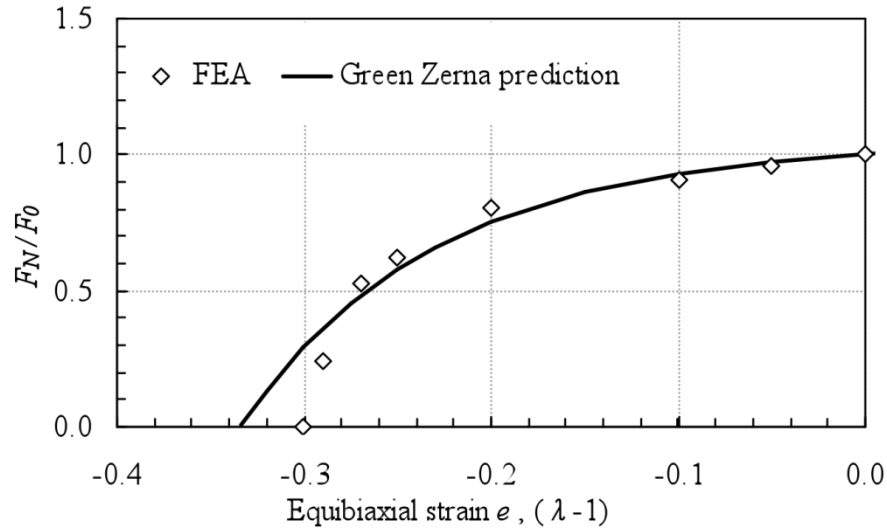
Figure 5.5: The ratio of resistance force F_N under prestrained conditions to the resistance F_0 without compression decreases with compression under equibiaxial strain.

The reasonable agreement between the Green and Zerna theory and the FEA prediction for the reduction in indentation force with prestrain validates the FEA software's capability to predict these general instabilities. The FEA deviates somewhat from the theory at larger compression ratios, predicting the point of instability to occur slightly earlier than in the theory. This is similar to the earlier onset of creases measured on the compressed inner surface of a bent rubber block, discussed earlier. It has been shown by various researchers in the past (Southern and Thomas 1965; Gent and Cho 1999) that measured buckling instabilities on unconstrained rubber surfaces do tend to arise earlier than predicted. This often-neglected disagreement between theoretical predictions and experimental observations is usually assumed to be too small to be of concern. A reason for this deviation might be that buckling instabilities in rubber often form creases or wrinkles rather than having a sinusoidal or wavelike shape, as is required by the general buckling instability theories. From an energetic point of view, creases may be more stable and energetically favourable than the build up of the sinusoidal waves and hence might arise at smaller precompressions. This assumption was confirmed very recently by Hong et al. (2009), who addressed this problem by using the same FEA software and SEF as were used in this work. Their considerations on differences in the elastic energy of the creased state and the homogeneous (unbuckled) state also confirmed that a crease is formed earlier than predicted by Biot's theory, as they showed that at the point of instability the creased state has the same energy as the homogeneous state.

5.4.3 Instabilities related to Schallamach waves

Best et al. (1981) confirmed the relation between the occurrence of buckling instabilities under a certain compressive stress and Schallamach waves, by using a static buckling approach. This work was extended to a dynamic consideration of wave-like buckling instabilities here. For the occurrence of Schallamach waves it was considered, that the strain induced by the slider is of great importance. Therefore, a series of different shear deformations, hence from low to high friction, was modelled in this work. For low friction, no buckling is expected, while for larger coefficients of friction, a buckling of the surface due to the large compressive strains was thought to be likely. A moderate shear deformation (μ=0.3) of the rubber bulk is considered first and is shown in Figure 5.6. After the initial indentation the stresses change position, due to the relative displacement, so that compressive stresses shift towards the front, while tensile stresses are built up behind the slider.
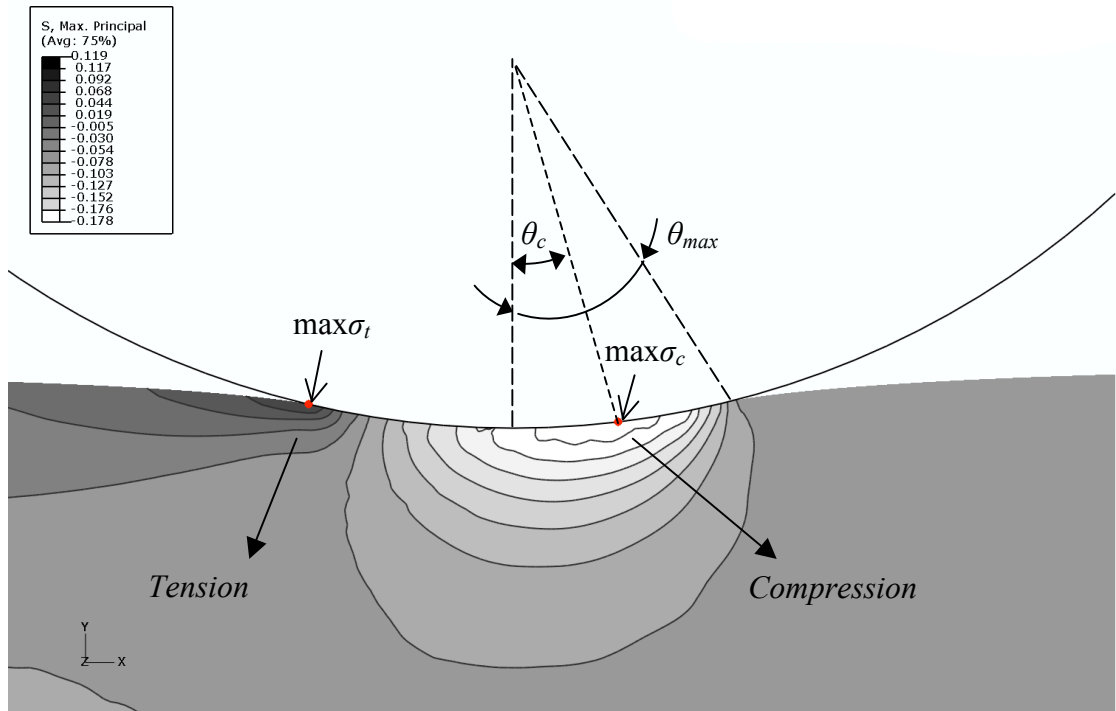
Figure 5.6: The FEA simulation shows of a rigid hemisphere indenting and sliding over a rubber block. Compressive and tensile stresses at a low friction coefficient (μ=0.3) are shown. The angle θ_c defines the position of maximum compression maxσ_C, while θ_{max} defines the angle between the contact at the front and the middle of the contact area.

In contrast to the maximum tensile stress max σ_t, Figure 5.6 indicates that the maximum compressive stress max σ_c is inside the contact zone, at an angle θ_c. The point of contact at the front between the rigid slider and rubber is denoted as angle θ_{max}. If zero friction

is assumed, with purely elastic behaviour for the rubber, the value of angle θ_c equals zero and a pure indentation with pressure distribution similar to Figure 5.4 a) is established even during sliding. The hypothesis proposed here is that the location of maximum compressive stress θ_c has to be close to θ_{max} in order to form Schallamach waves. Figure 5.7 shows that as the coefficient of friction increases, the ratio of θ_{max} to θ_c asymptotes to a value of 1, confirming that the location of the maximum compressive stress changes to the region at the front of the contact area.
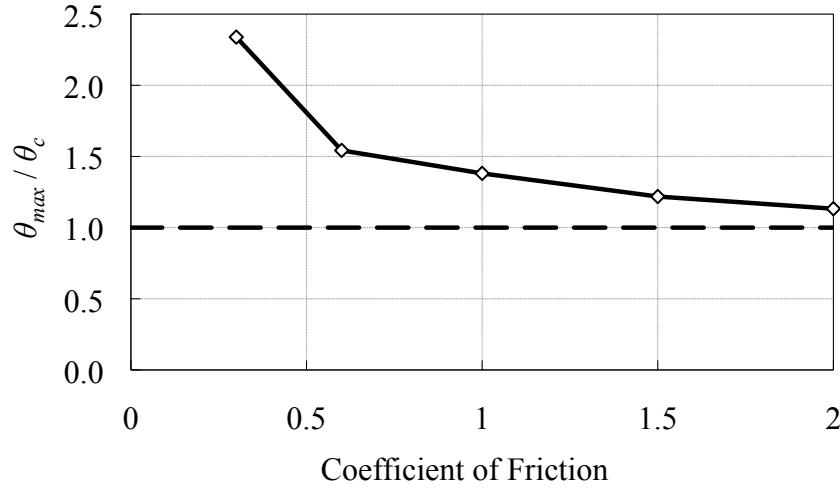
Figure 5.7: The ratio of angles θ_{max} and θ_c decreases with increase of coefficient of friction μ.

A high friction (μ>2.0) results in large compressive stresses at the interface causing the rubber surface to buckle at a critical value of the compression ratio. Such a buckling is necessary for the formation of Schallamach waves as shown in Figure 5.8, using a coefficient of friction μ=4.0. Figure 5.8 a) shows only the region of interest of the rubber block in the FEA model (dotted lines), while the dashed, magnified rectangles highlight b) the compression zone (light shade) in front and c) the tensile zone (dark shade) at the rear of the contact.
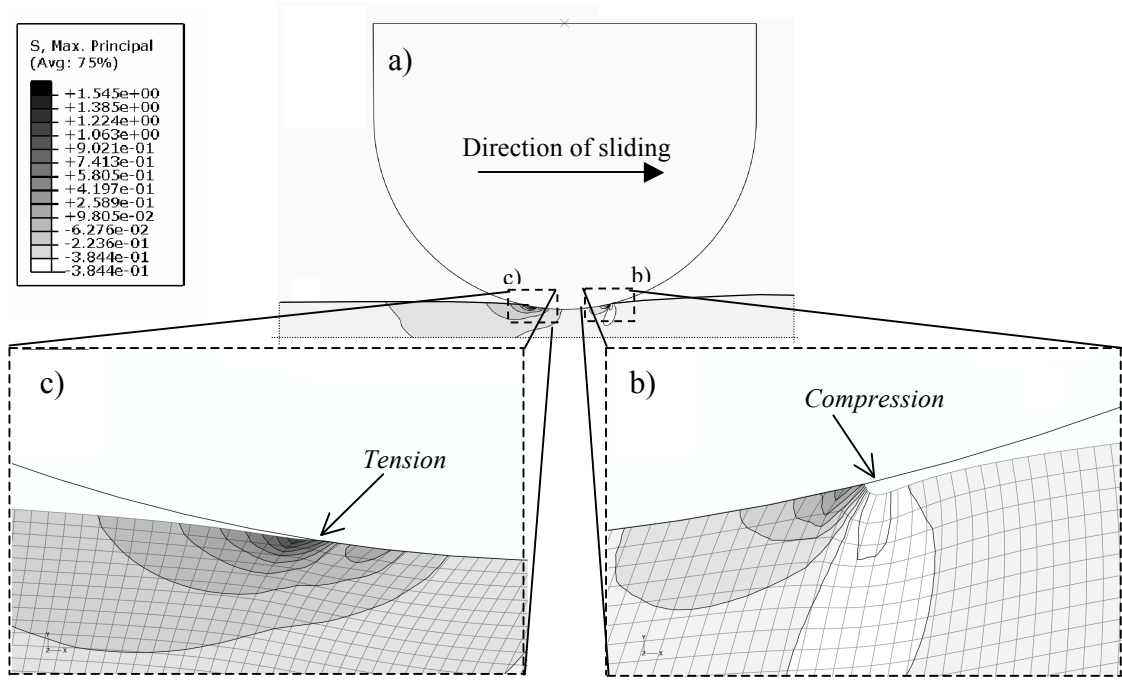
Figure 5.8: a) High friction (μ=4.0) at the interface of an indenter sliding to the right on a rubber block. While figure b) shows compressive stresses (light shade) at the front of the slider leading to buckling of the rubber surface, figure c) indicates the tensile stresses (dark shade) at the back of the contact.

It is interesting to note that in Figure 5.8 b) not only compressive stresses, but also moderate tensile stresses are generated, resulting from the buckling of the surface. These tensile stresses in addition to the contribution of sliding, supply the driving force to progress the Schallamach wave. In contrast, Figure 5.8 c) is entirely dominated by tensile stresses at the rear of the slider as expected from general considerations of the stress fields. Once the buckling in front of the slider is formed, a further increase in tangential stresses leads to the full formation of the instability and a Schallamach wave is formed and progressed.

By considering the maximum compressive strains of the above model, Figure 5.9 shows that an increase in the coefficient of friction induces an increase in maximum compression ratio σ_0/σ_c of unstrained to strained elements at θ_c, due to the higher tangential stresses. The maximum compressive strain σ_c in the elements close to the front at θ_c is monitored throughout the analysis, by using a strain control in Abaqus. As soon as a compressive strain of around λ=0.68 is reached, a buckling instability appears in the shaded area. This is in good agreement with experiments on the buckling under unidirectional compression, which showed the onset instabilities arise at around

$\lambda = 0.65 \pm 0.07$ (Gent and Cho 1999). However, according to Biot's theory a surface becomes unstable under unidirectional compression only when the critical strain ratio for λ is as low as 0.54 (shown as a dashed line in Figure 5.9) (Biot 1965). The reason for this apparent deviation from Biot's theory is not confirmed (Gent and Cho 1999), however as the correlation is good between the experiments and the FEA, it is thought likely to be due to the fact that real surface instabilities form as cusps or wrinkles, rather than as the sinusoidal waves, which were assumed by Biot.
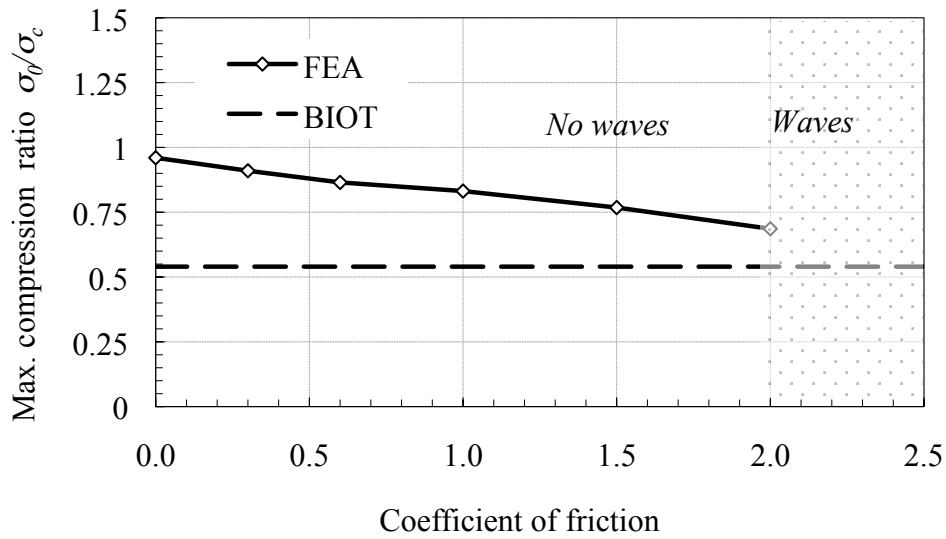
Figure 5.9: The thick line represents the FE prediction of maximum compression ratio versus coefficient of friction, while the dotted line is the critical compressive stress for buckling under uniaxial compression, predicted by Biot (1965). The maximum compression ratio was measured at the position of θ_c.

The analysis shows that to generate a sufficient tangential stress at the interface to create a buckle, requires the coefficient of friction to be greater than 2.0, confirming the earlier observation of Barquins (1993) and Gough et al. (2001), who experimentally observed the same value.

5.4.4   Propagation of Schallamach waves

Wave velocity

The progression of a single, successive wave from the right to the left hand side is shown in Figure 5.10, confirming the elastic nature of the buckling instability in the model:
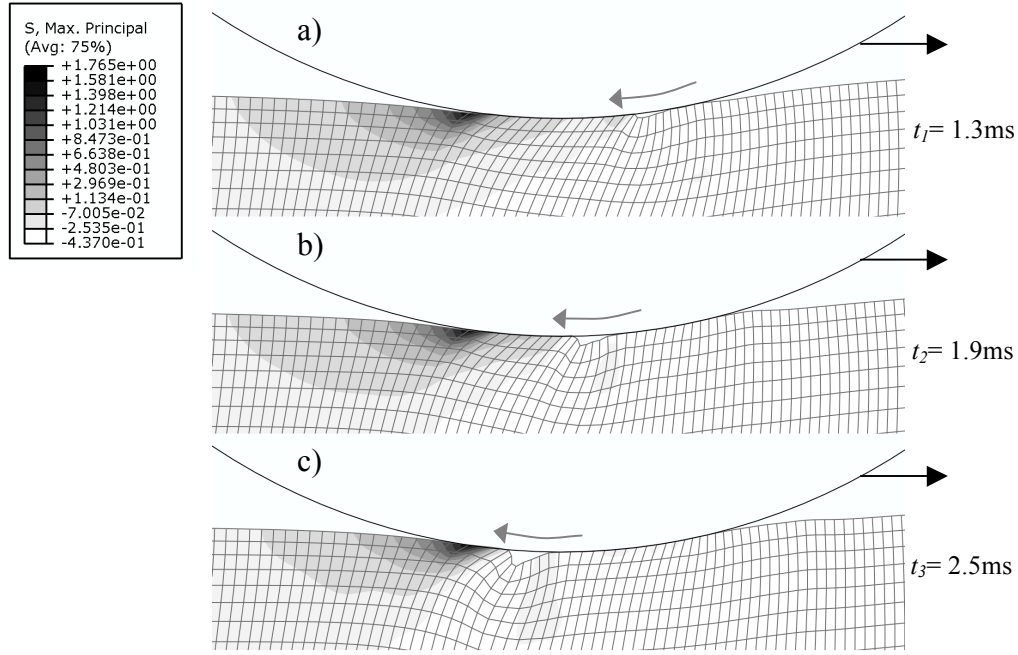
Figure 5.10: a) shows the progression of the wave, just after its formation and t_i indicates the time. Pictures b) and c) show the further development of the instability (grey arrow) throughout the area of contact, while the rigid wedge is sliding to the right hand side (black arrow).

The model described here is purely elastic in order to establish a first model of Schallamach waves. Surface adhesion and, therefore, the rate-dependent peeling energy is not included in the model, so that the velocity of wave progression velocity underlies no frequency dependent viscoelastic damping. Therefore, no relation to the experimentally observable wave progression velocity can be drawn. For this reason the wave progression velocity is considered to be comparable to the shear wave speed of the material ω_M, given as (Arfken et al. 1989):

$$\omega_M = \sqrt{\frac{G}{\rho}},$$

(5.2)

where ρ is the density of the material. As the depth of penetration scales with the contact area and the block is semi-infinite, the length scale for an individual wave is arbitrary. If a rate dependent peel energy were introduced, then the surface energy γ would generate a characteristic length scale ψ (Rand and Crosby 2006) as

$$\psi = \beta \frac{\gamma}{E*},$$

(5.3)

where β is an unspecified geometrically defined constant and $E*$ is the complex tensile modulus. As only the elastic behaviour is modelled, it is not possible to interpret the resulting size of the wave as a realistic representation.

The wave progression velocity was measured over the length of contact in the FEA model, and the results are shown in Figure 5.11. As this model is purely elastic, the wave progression velocity is linear and does not increase with distance, in contrast to what has been observed in experiments (Barquins and Courtel 1975). Furthermore, the slope of the linear fit shows a wave progression velocity of 22 m/s, which is in very close agreement to the relationship for the shear wave velocity ω_M, calculated as 23m/s according Equation (5.2).
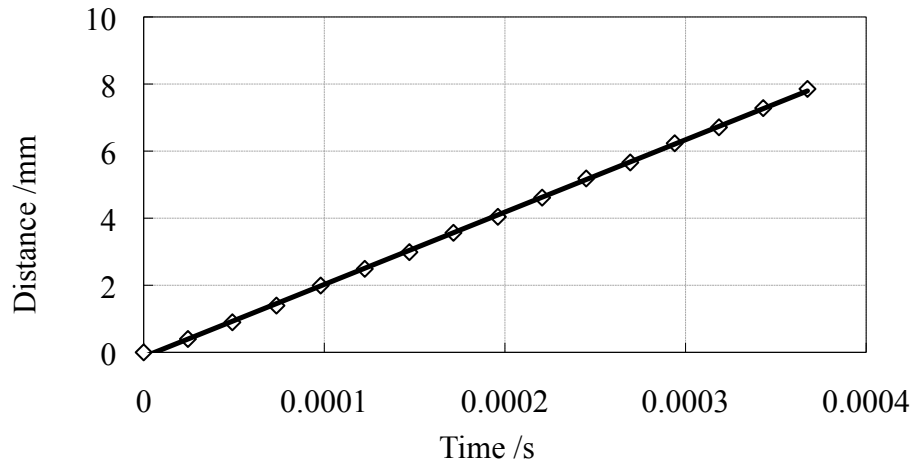
Figure 5.11: The wave progression velocity in Figure 5.1 was measured in the FEA model.

Despite the fact, that the predicted wave progression velocity is obviously not representative of the real Schallamach wave speed, as a first step in ongoing investigations on the FEA modelling of Schallamach waves, a purely elastic model was shown to be sufficient to introduce and satisfactorily progress a buckling instability, confirming the possibility that the wave can be established as a purely elastic instability (Best et al. 1981). It is acknowledged that experimental observations showed that Schallamach waves are, however, dependent on different parameters such as viscoelasticity of the material and the rate-dependent surface properties, which determine the progression of the buckling instability, these would have to be introduced to extend this work further.

Displacement through wave propagation

Schallamach waves are also termed waves of detachment, as they are thought to provide the (only) relative displacement between the rubber and the rigid surface (Barquins 1985), similar to a ruck in a carpet or the motion of a caterpillar. It was proposed by various researchers (Schallamach 1971; Barquins and Courtel 1975; Barquins and Roberts 1986; Barquins et al. 1996) that stick-slip is not present, but the total displacement results entirely from the progression of the waves of detachment between a slider and a rubber specimen. The common understanding is that the adhesional bonds at the interface are high enough to remain intact, even if the shear forces are large. This results from experimental observations of dust particles inadvertently trapped between the contact area of a sliding rigid profile on rubber specimen. The particles were only displaced by the waves passing the contact area, but remained motionless in the intervening areas. In the past, the displacement resulting from Schallamach waves, has been observed using various techniques, for example by applying a square lattice onto the surface (Schallamach 1971), which is similar to the passing-line technique (Barquins and Courtel 1975) or by observing Newton-rings (Barquins 1993). However, it is important to note that even Schallamach (1971) emphasized that it was not possible to rule out the existence of undetected true sliding in these segments (Smith 2008). In addition, only observations perpendicular to the rubber surface were possible, requiring the use of a transparent rubber or a transparent rigid surface. The introduction of FEA techniques to study the phenomenon of Schallamach waves allows the detachment folds to be observed from all angles for the first time.

When a low coefficient of friction is considered first (μ=0.2), the typical stick-slip motion at the sliding interface is experienced. Figure 5.12 shows the horizontal displacement of a single node over time when it is in contact with the hemispherical slider. In the first step, the node is displaced due to the friction at the interface (static friction) and when sliding at the interface occurs (kinetic friction) the horizontal displacement is shown as a repetitive cycle of stick-slip motion.
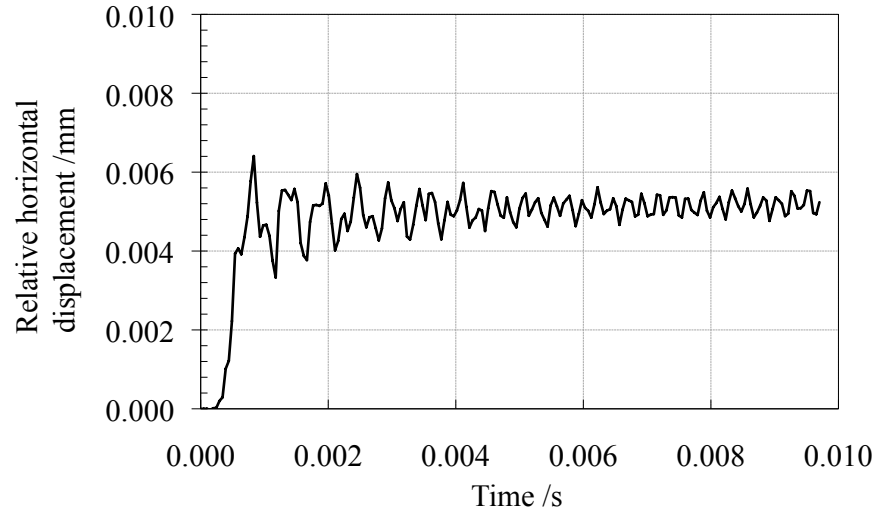
Figure 5.12: Typical stick-slip motion of a rigid slider on a rubber block (μ=0.2) shown as the relative vertical displacement.

This stick-slip motion, exciting the rubber at a high frequency, results from the loss and build up of adhesional bonds, further described in Section 2.5.3. In contrast, when high friction is considered (μ=3.0), the adhesional bonds are larger and intimate contact between the rubber and the smooth interface is built up, leading to large shear stresses, which can result in the creation of buckling instabilities. Figure 5.13 shows a close up of the rigid slider (sliding on top of the rubber), similar to the situation shown in Figure 5.10. The displacement of a single highlighted node, which is in contact with the slider was monitored here. Figure 5.13 a) shows an image of the wave before it has passed the highlighted node, while b) illustrates the situation where the node is being dragged across the contact area by the wave. In Figure 5.13 c) the wave progresses and the node is reattached with the rigid slider and is displaced from its original position a) to c) as is shown by the length *L*.
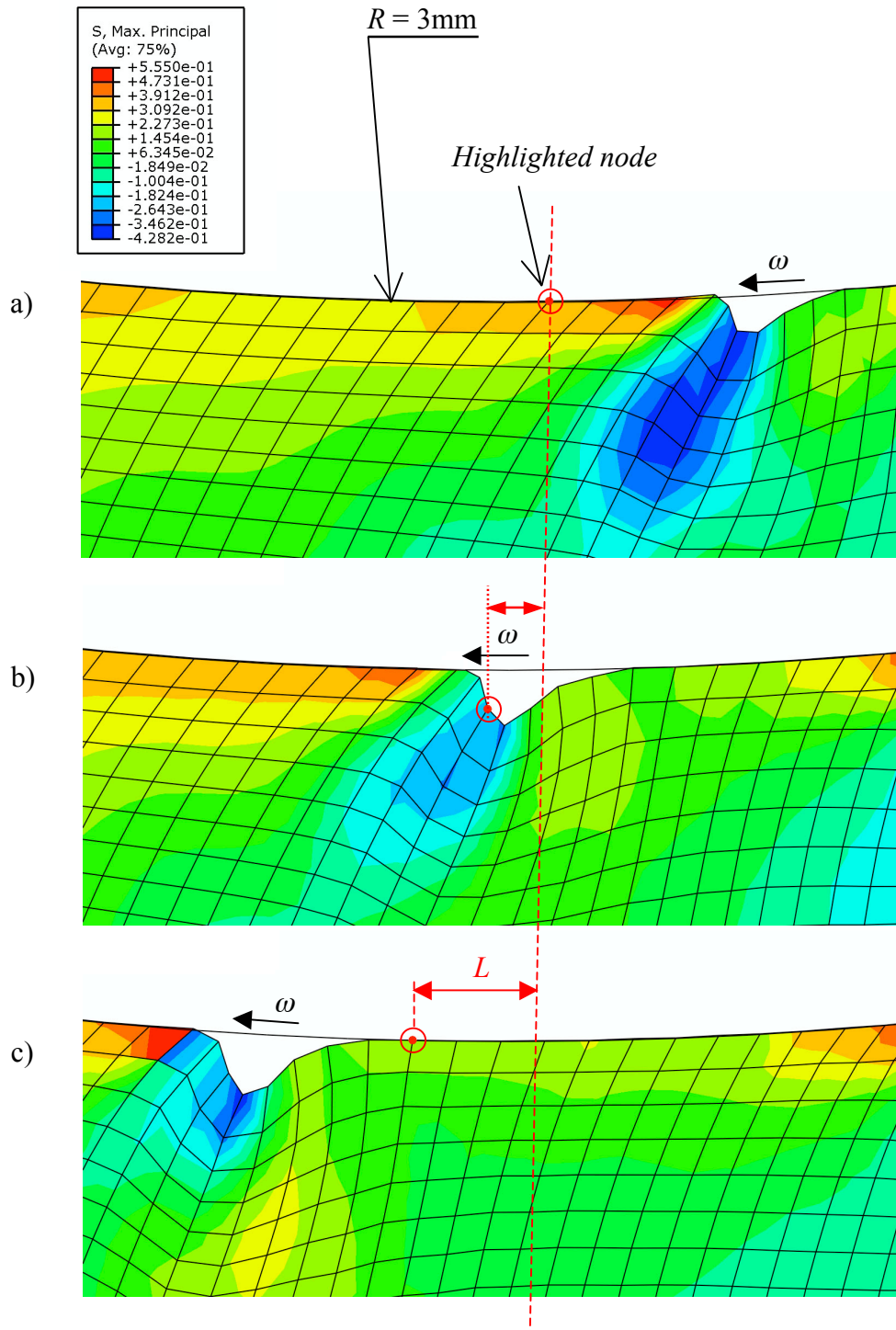
Figure 5.13: The initial position of a single node is highlighted with a red circle and a dashed line. When a wave progresses with a wave progression velocity ω over the contact area the initial position of the node is changed by a distance L. The time period from image a) to c) is 1.1ms.

The relative displacement of the highlighted node is plotted as the total displacement of the node to its original position in the mesh in Figure 5.14. Without wave progression the relative displacement between the node and the slider is zero, however, as soon as a wave passes through the area of contact, the node is displaced for a certain distance.

This is shown as a step in the graph for each wave passing through the area of contact in Figure 5.14.
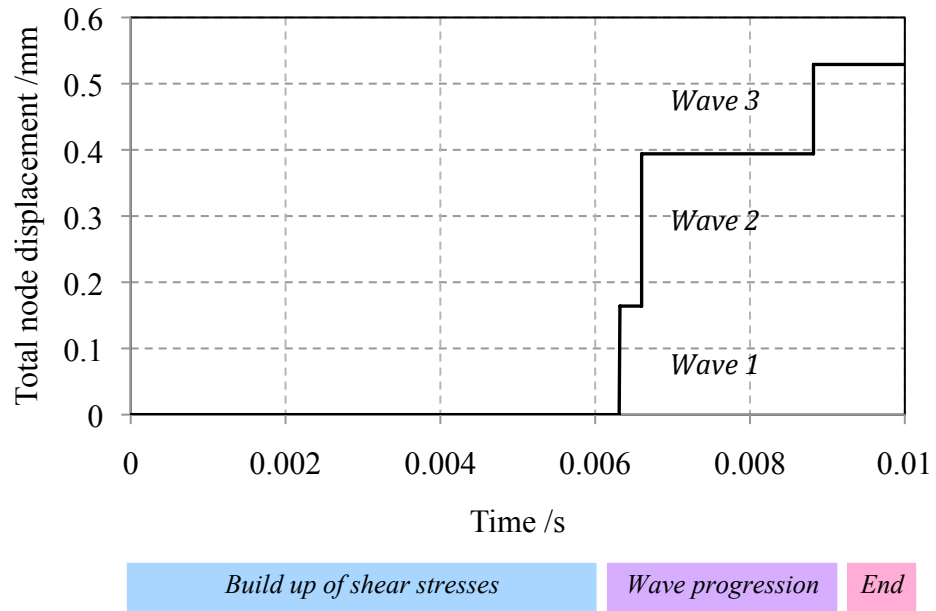
Figure 5.14: Displacement of a single node versus time by consecutive Schallamach waves.

The time period until 0.006s denotes the build up of shear stresses induced by the high friction between the slider and the rubber. As soon as the critical compression ratio is reached and the buckle in front of the slider is build up, a wave passes through the area of contact, denoted in Figure 5.14 as "wave progression". From the observation in Figure 5.14 it can be concluded that at large coefficients of friction, the only relative displacement in the FEA model is by the waves of detachment when a stick-slip FEA model is used and no frequency dependent peeling energy is introduced to the system, as it is assumed in the literature.

5.5 Conclusions

When a microscopically smooth interface is considered between a rubber and a rigid slider, surface instabilities occur as a result of large tangential shear forces. General surface buckling under compression has been investigated experimentally and compared to the instability theories of Biot and Gent. Furthermore, equibiaxial FEA models validate the capability of explicit dynamics to model an elastic instability in rubber, such as Schallamach waves. The experimental and computational observations confirmed that buckling instabilities tend to occur at an extension ratio of $\lambda=0.68$, which is earlier than predicted by Biot's theory with a value of $\lambda=0.54$. It was assumed that buckling instabilities, which form as creases rather than sinusoidal waves, were energetically more favourable and this was confirmed very recently by Hong et al. (2009).

When considering a sliding friction interface, it was shown from the FE analysis that the local compressive stresses underneath a slider on a rubber block are shifted towards the front of the contact region as the friction coefficient is increased. Consequently, high coefficients of friction induce sufficiently large compressive strains at the front to create a surface buckle, which propagates as a wave in a direction opposite to the sliding direction through the area of contact. Using a purely elastic explicit dynamics FEA approach, the build up and successive propagation of a buckling instability, similar in its nature to a Schallamach wave, has been shown successfully for the first time. In the literature Schallamach waves (when present) are considered to provide the only relative displacement at the interface, based on experimental observations from still images. In this study it was confirmed using FEA that a wave of detachment provides the only relative displacement between the slider and the rubber at very high coefficients of friction. Due to experimental difficulties and in order to simplify the model of the buckling instabilities, the peeling energy, necessary for a representative prediction of the wave progression velocity, was not introduced in this work. For this reason the wave progression velocity of 22m/s is determined by the material's shear wave speed, which has a value of 23m/s for the modelled rubber. By the introduction of a peeling energy at the interface, a more realistic prediction of the wave progression velocity might be expected.

Furthermore, when general buckling instabilites on the rubber surface are considered, a repetitive folding and unfolding of surface instabilities (creases) might result in fatigue failure or promote abrasion by the introduction of micro-cracks to the surface. The ability of modelling these surface instabilites, such as Schallamach waves, helps to gain a better understanding of applications, which exhibit large shear stresses at the rubber surface, so that surface instabilities are likely. Especially in industrial applications it is often not possible to observe the interface of two contacting friction partners, so that FE modelling can help to resolve these issues.

6   Investigation on the sliding mechanism of rubbers
- in relation to the presence of Schallamach waves

6.1   Introduction

The different sliding mechanisms related to rubber friction are still a subject of debate in the literature. For microscopically rough surfaces commonly only smooth sliding or stick-slip displacement mechanisms are mentioned in literature. On the other hand, for microscopically smooth surfaces, three different mechanisms of sliding are observed. At very low sliding velocities, commonly described as smooth sliding, the relative displacement is provided by a constant peeling and un-peeling process at the sliding interface. At higher sliding velocities and in the presence of Schallamach waves it is assumed that the relative displacement at the sliding interface is provided only by local waves (Smith 2008), as is discussed previously in Section 2.5.6 and Chapter 5. At much higher velocities, where Schallamach waves are not present, relative displacement is provided by stick-slip motion, as is discussed in Section 2.5.3. Recently, a transition zone between Schallamach waves and stick-slip motion has been described briefly by Wu-Bavouzet et al. (2007) for smooth surfaces, as shown in Figure 2.17. The existence of this transition zone implies that Schallamach waves may have some relationship to stick-slip motion. What is still not clear is how far can the transition zone be investigated in terms of the wave frequency and the wave progression velocity? This chapter investigates this relationship between the mechanisms of Schallamach waves and stick-slip motion further to examine, if the phenomena of stick-slip and Schallamach waves have a common origin.

To allow better understanding of the viscoelastic behaviour of these surface instabilities, general experimental observations on the formation criteria of Schallamach waves are undertaken. A purely elastic computational stress analysis on this problem has been discussed separately in Chapter 5. This is extended experimentally in this chapter to examine wave progression phenomena. Barquins and Courtel (1975) were the first to

note the increase in the progression velocity of single Schallamach waves over the area of contact. Initially, the wave progression velocity is nearly constant over a certain length of the contact area, however, this velocity increases significantly when the wave reaches the rear of the contact area. This phenomenon was also reported by Briggs and Briscoe (1975), however, they commented that the reason for this is not fully understood.

Furthermore, it is reported in literature that no Schallamach waves can build up when the frictional interface is contaminated (Briggs and Briscoe 1975) or the surface topography is rough (Barquins and Roberts 1986; Grosch 2007). While surface contaminations are acknowledged to reduce the shear stresses at the interface and hence prevent the build up of buckling instabilities, it was found in this work that even for a rough rubber surface a phenomenon similar to Schallamach waves occurs, which has not been described in relation to Schallamach waves previously. This phenomenon is discussed in this chapter and is directly compared to Schallamach waves.

The following chapter is in part based on the submitted and co-authored paper by Fukahori et al. (2010).

6.2 Experimental background

The material used in this work was a dicumyl peroxide cured natural rubber (NR) which was compounded with varying levels of crosslinking agent: NR1 (1phr), NR2 (2phr) and NR3 (3phr). The amount of crosslinking agent was changed to modify the modulus of the rubber as well as the adhesion at the surface. Two model surfaces, one smooth and one rough, were prepared. The full description of the compounding formulation and the surface preparation are found in Table 3.3 of Section 3.1 and in Section 3.5.

The Plint friction tester (Section 3.7.2), based at TARRC, was found to be incapable of observing stick-slip motion as the data capture rate is only 10 data points per second over 10mm of sliding and 1 data point per second over the next 10mm of sliding. In contrast, the QMUL friction tester was designed to provide a much more rapid data capture rate of 1000 data points per second, which is sufficient to observe the high

frequency stick-slip behaviour. Consequently, to observe Schallamach waves and possible stick-slip motion the QMUL friction tester was used in combination with a high-speed camera, as described in Section 3.7.1.

A hemispherical glass slider with a radius of 19mm, shown in Figure 3.30 c), was slid against a flat rubber surface over a wide range of velocities (0.01mm/s to 10mm/s). The contact area was observed through the glass slider using a macro-lens system[21]. In order to observe the detachment waves together with micro slip-processes at high frequencies, an image-capturing rate of 1000 frames per second was chosen. Initial experimentation showed that fairly low normal loads from 0.6N to 1.3N cover a reasonable experimental range. Larger normal loads resulted in the tearing of the rubber samples because of the high shear forces created due to the high adhesion with the smooth surface finish in combination with the low strength of peroxide cured rubbers. Moreover, it was shown that a rigid hemisphere on rubber is preferable to a rubber hemisphere on a rigid track. The former setup creates a fresh and clean rubber surface, which is constantly renewed, while for the latter setup surface contaminations and abrasion on the restricted area of contact of the rubber hemisphere become apparent after only a few sliding experiments.

6.3   Results and discussion

A detailed elastic stress analysis necessary for the Schallamach wave initiation is described in Chapter 5. The main outcome of this investigation shows that a specific surface compression is necessary to generate the sliding Schallamach waves. This compression is due to large shear forces generated by the intimate contact between two sufficiently smooth surfaces, so that the adhesive component of the surface finish becomes a fundamental criterion for the formation of Schallamach waves. As reviewed in Section 2.5.6 it is commonly assumed that Schallamach waves are present only for optically smooth surfaces. However, for comparison reasons two surfaces, rough and smooth, were investigated here. Both surfaces are shown as scanning electron microscopy (SEM) images as well as a topography scan in Section 3.5. While the maximum peak to valley height R_{max} is 21μm for the rough and 12μm for the smooth

---

[21] Sigma GmbH, Rödermark, Germany. Type: f2.8, EX DG 105mm lens.

surface, the roughness average R_a, measured as the arithmetic mean of the absolute values of profile deviations from the mean line, for the rougher surface this has a value of 3.2µm, for the smooth surface this has a value of 1.8µm.

6.3.1   Schallamach wave initiation

When both surfaces were investigated in a friction test under the same experimental parameters, the influence of this change in surface roughness became apparent, as is shown in Figure 6.1. The graph shows a comparison of compound NR3 at a normal load of 1.3N over a range of sliding velocities. The smooth surface experiences higher friction than the slightly rougher surface, as the apparent real area of contact is larger. Therefore, more intermolecular bonds between both smooth surfaces can build up, which require more energy to break than is required for the smaller area in the case of the rougher contact. Hence, the intimate contact also induces higher (compressive) shear forces, which lead to the formation of Schallamach waves. As expected from literature, for the rough surface no Schallamach waves were observed under the described experimental conditions, while they were visible for the smooth surface over the whole range of sliding velocities tested. In contrast to the literature though, for the rough surfaces using the compound NR1 a previously unmentioned phenomenon was also noticed, which might be similar to the wave progression in Schallamach waves and this is discussed separately in Section 6.3.3.
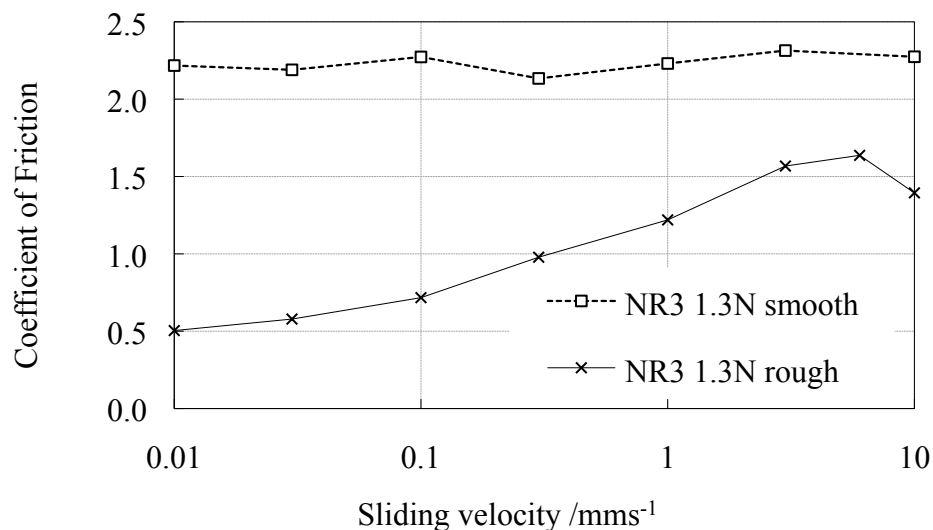
Figure 6.1: The measured coefficient of friction for a dry, rough surface is less than that for a smooth surface. (NR3, rigid slider R=19mm, F_N=1.3N, v=0.01-10mm/s).

In contrast to the rough surface, the friction values exhibited by the smooth surface were independent of sliding velocity. The reason for the constant friction values for the smooth surface is the energy dissipating process by Schallamach waves. This depends on the number of Schallamach waves over the contact length per unit time. Both the wave progression velocity and frequency increase with the sliding velocity, so that the frictional force remains constant and this will be further described in Section 6.3.5. For the rougher surface a viscoelastic frequency dependency of friction is experienced. This has been extensively discussed in literature (Grosch 1963; Barquins and Roberts 1986) and is part of the discussion given in Chapter 7.

The three compounds NR1, NR2 and NR3 were each tested further on the smooth surface for comparison reasons under the same conditions as in Figure 6.1 and the results are shown in Figure 6.2. It was found that Schallamach waves only occur at a coefficient of friction around 2.0 or greater, confirming literature values, which quote the same value (Barquins 1985; Gough et al. 2001). In addition, this value was also confirmed via computational FE analysis in Chapter 5 for the formation of buckling instabilities similar to Schallamach waves. Nevertheless, it has to be borne in mind, that the coefficient of friction and its derivation is dependent on various parameters, so care should be taken, as not all of these are known for the values given in the cited literature. Furthermore, the coefficient of friction is not a measure of the appearance of Schallamach waves, but the shear stresses generated during sliding. Nevertheless, these are not easily experimentally measurable, as the real area of contact can differ significantly from the apparent area of contact.
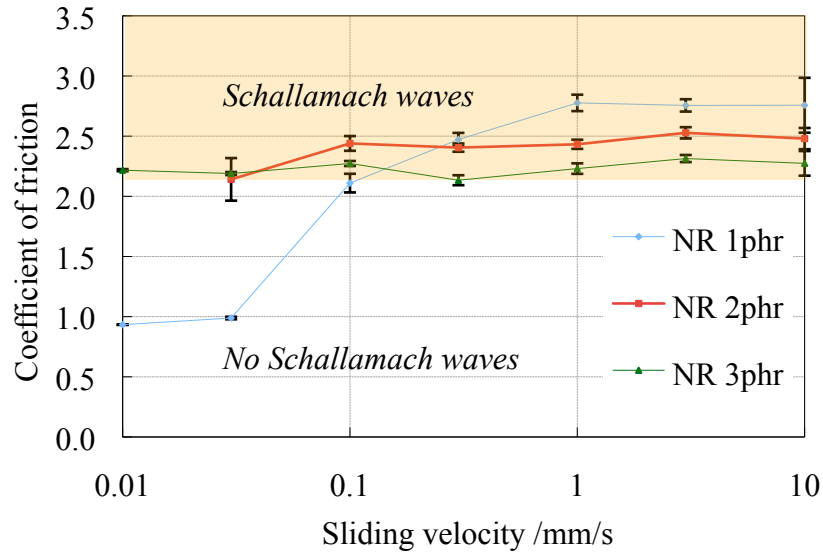
Figure 6.2: In presence of Schallamach waves the coefficient of friction is independent of velocity. A smooth, glass hemisphere (R=19mm) contacts an optically smooth rubber surface (NR1, NR2, NR3) under a normal load of 1.3N.

It is shown for NR1 that a critical sliding velocity exists, at which Schallamach waves occur. This is in accordance with the literature (Barquins 1985), which describes the critical sliding velocity being dependent on the compound's adhesional properties. With increasing sliding velocity the rate dependent peeling energy increases, which leads to the surface becoming unstable for a specific compressive stress. Figure 6.2 shows that Schallamach waves are present over the whole range of sliding velocities for NR2 and NR3. It is believed that the critical sliding velocity for both compounds occurs at lower sliding velocities, as qualitatively preliminary experiments showed that both samples experienced a higher adhesion than NR1.

6.3.2 Schallamach wave progression

The Schallamach wave progression has been widely described in the literature, as is discussed in Section 2.5.6, however, the sliding velocity regime, where the sliding mechanism transitions from smooth sliding to Schallamach waves and then from Schallamach waves to stick-slip motion has not been fully resolved. The aim of this section is to describe and analyse these three different sliding mechanisms and their transitions in more detail.

Transition from smooth sliding to Schallamach waves

For very low sliding velocities, in the range from 0.01mm/s to 0.03mm/s, the observed instabilities appeared as unconnected wavelets rather than coherent waves, as shown in Figure 6.3. Single wavelets are indicated by the yellow arrows, while the direction of sliding for the hemisphere is given as an indication of front and rear of the contact in Figure 6.3 a).

| *t=0ms* | *t=32ms* | *t=46ms* |
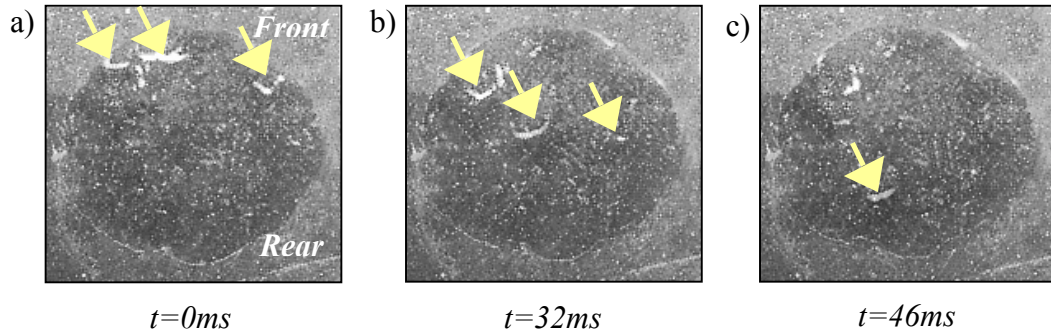
Figure 6.3: a) to c) Motion of small, unconnected wavelets on the surface, indicated by yellow arrows, are predecessors to Schallamach waves. The sliding direction is indicated in a). (NR3, F_N=0.6N, v=0.03mm/s).

These small wavelets that are similar to Schallamach waves travel independently of each other through the area of contact and are usually ignored in the literature. They mark the transition from smooth, which means for the eye undetectable, sliding to Schallamach waves. Usually it is assumed, that as soon as Schallamach waves appear, they are the only source of relative displacement. But as the observed wavelets do not cover the whole width of contact zone and only travel across certain areas of the area of contact, smooth sliding has to occur in parallel to the relative displacement provided by the wavelets, which remains undetected to the eye. In the experiments, however, it was neither possible to detect this smooth sliding mechanism by carefully monitoring changes in the contact area, nor from observed changes to the frictional force. Only the constant change in relative displacement of both surfaces in contact gave an indication that sliding had occurred.

Schallamach waves

With increasing sliding velocity, starting from around 0.1mm/s, the wavelets form single waves, which extend over the whole contact width. A representative example for

a progressing, coherent Schallamach wave is shown in Figure 6.4 for a relative sliding rate of 0.3mm/s. Several Schallamach waves are present on the circular contact area. To emphasise the motion of a single Schallamach wave, one progressing wave has been highlighted in orange. When Schallamach waves occurred no relative displacement between the rubber and the slider was observable beside the displacement provided by Schallamach waves, as dust particles, which were inadvertently trapped in the contact area, were only displaced by the relative motion provided by moving Schallamach waves and remained motionless between two successive waves.

| t = 0ms | t = 30ms | t = 66ms | t = 123ms |
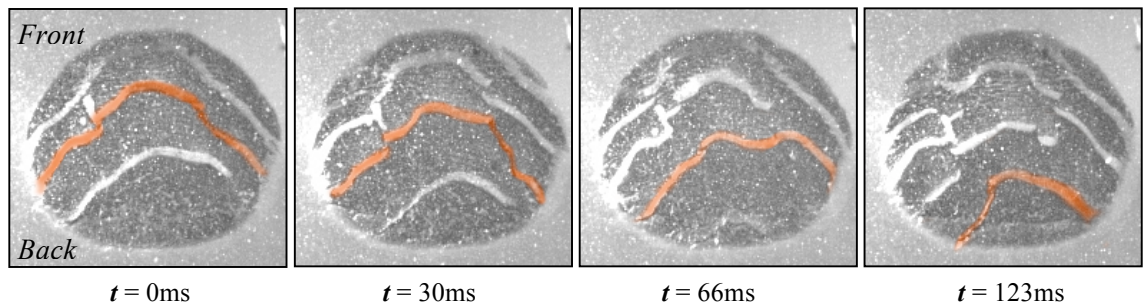
Figure 6.4: One Schallamach wave progressing over the area of contact is highlighted in orange to increase clarity (NR3, F_N=0.6N, v=0.3mm/s).

An additional video of the progression of Schallamach waves for the compound NR3 at a sliding velocity of 1mm/s and F_N=0.6N is provided on the DVD (Section 9.5) attached to this work (filename: Smooth_NR3_1mms_0.6.N.avi).

Various values for Schallamach average wave progression velocities have been published, which are individually dependent on the detailed experimental conditions. Some of the most common literature values (Schallamach 1971; Briggs and Briscoe 1975; Koudine et al. 1997) are plotted along with the experimental results of this work in Figure 6.5:
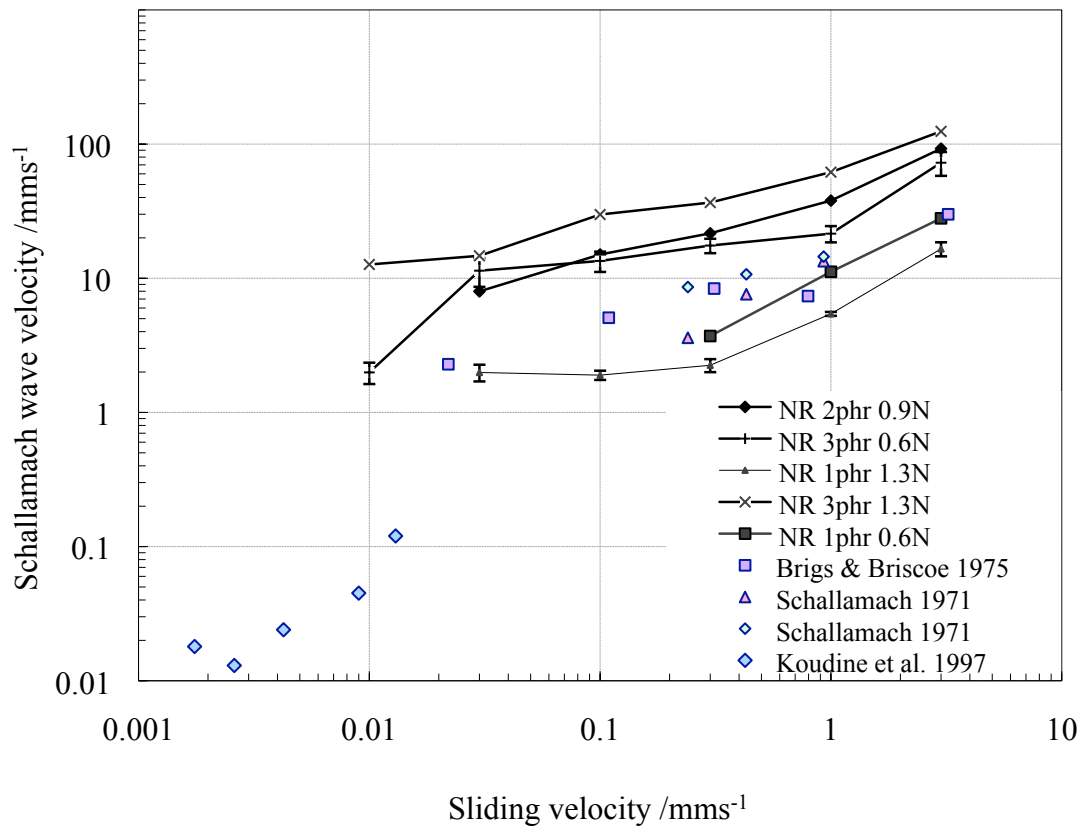
Figure 6.5: Common literature values for wave velocity versus sliding velocity compared to the experimental results gained throughout this work. Literature values by Schallamach (1971), Briggs and Briscoe (1975) and Koudine et al. (1997).

It is clear, that Schallamach waves can arise at very low sliding velocities (Koudine et al. 1997), so that the commonly quoted critical sliding velocity, is thought not to be a sufficient criterion for the initiation of Schallamach waves. The frequency dependent shear stress (or the resulting coefficient of friction) should be given in addition, if the critical appearance of Schallamach waves is described. The presented data of wave velocity versus sliding velocity show a similar trend to these found in the literature. The wide scatter in the data sets is due to the fact that different interface geometries as well as different materials have been used. It becomes apparent that NR1, the compound with the lowest modulus, also shows the lowest value for the wave progression velocities for any given sliding velocity, while the stiffest compound, NR3, has the highest wave progression velocity. This relationship between modulus, sliding velocity and propagating wave velocity reflects the viscoelastic behaviour of the material. When the excitation frequency (sliding velocity) increases, the rubber has less time to respond to an applied deformation, so that the force opposing deformation increases as the

modulus increases. For the same reason the real area of contact decreases with increasing sliding velocity as is discussed in the section on the transition of Schallamach waves to stick-slip motion later in this chapter.

Unfortunately, from the data presented in Figure 6.5 a qualitative relation between wave velocity and sliding velocity can not be easily drawn, as many parameters affect the wave progression velocity. However, when the log-log plot is extended over an even wider range, a power law relationship exists over several decades of velocities. The resulting trend line for each set of experiments may be given as:

$$\omega = Cv^{m}, \qquad\qquad\qquad \textbf{(6.1)}$$

where ω is the wave velocity, C is a coefficient, v is the relative sliding velocity and m is the slope of the log plot. The coefficient C and the slope m are unknown and they are both dependent on several parameters. For example, it was reported in literature that the slope decreases with the radius of curvature (Wu-Bavouzet et al. 2007). Furthermore, the normal load at the interface influences the coefficient C (see Figure 6.5 and Figure 6.16). As a further complication, frequency dependent properties such as the modulus or properties such as temperature dependence also influence the wave progression velocity (Briggs and Briscoe 1975). Nevertheless, as a first attempt to describe the Schallamach wave frequency dependency it might be reasonable to express the behaviour by Equation (6.1). The experimental data presented in Figure 6.5 cover a sliding velocity range from 0.01mm/s up to 3mm/s. Starting from around 1mm/s a slight decrease in contact area was noticed, which started from the rear of the contact area. This oscillating decrease and increase of the contact area at the rear of the slider was described by Barquins (1993) and termed as the so-called 're-attachment' waves. At 3mm/s a further decrease was noticed and the waves progressed faster and less uniformly over the area of contact. This change in contact area marks the transition from Schallamach waves to stick-slip motion, which can be further examined, when the frictional force for the shown data is analysed: The experimental data for the coefficient of friction related to the occurrence of Schallamach waves, shown in Figure 6.1, are re-examined only for the smooth surface of NR1 as the frictional force versus time in Figure 6.6. Schallamach waves start to occur around 0.3mm/s.
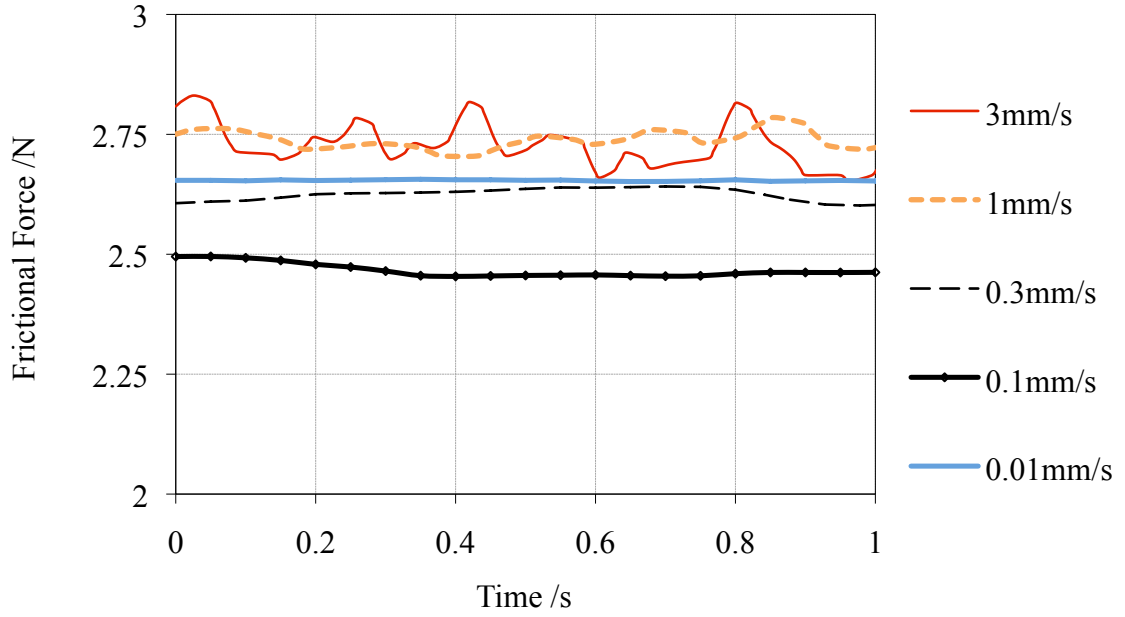
Figure 6.6: The oscillation of the frictional force output increases with sliding velocity, while the magnitude of each line is considered not to be significant. A smooth NR-1 rubber surface is in contact with a glass lens of R=19mm (F_N=0.6N).

It is noticed that by increasing the sliding velocity the shape of the frictional force output gains in oscillation amplitude and frequency. A periodic alteration in frictional force usually indicates stick-slip behaviour due to an alternating change in the area of contact (see Section 2.5.3). Although the stick-slip curves shown in Figure 6.6 are not necessarily completely regular in their appearance, (at the faster velocities from 0.3mm/s onwards) it is acknowledged that an oscillation in frictional force is generated due to the frictional sliding at the interface even when the Schallamach waves are present. An increase in the oscillation amplitude and the oscillation frequency indicates that the resistance to sliding changes, which marks the transition from Schallamach waves to stick-slip behaviour and this is considered next.

Transition from Schallamach waves to stick-slip

If the sliding velocity is further increased, the wave frequency increases until a second transition zone, which has recently been observed in literature by Wu-Bavouzet et al. (2007), who only briefly described this second transition. An example series of images for this transition between Schallamach waves and the stick-slip motion is shown in Figure 6.7 for NR3 at 10mm/s and 1.3N. The initial area of contact is shown as a red circle and the direction of sliding is indicated in image ① by defining the front and the

rear of the contact zone. Images ① to ⑤ (with a total time of 6ms) indicate a decrease in the area of contact (dark, circular area) as is highlighted by the red arrows. It is important to note, that the decrease in the area of contact is not a peeling process progressing only from the back (Barquins 1993), but a circular reduction caused by the uplift of the slider. Images ④ to ⑥ (3ms) show a single Schallamach wave, starting from the right hand upper corner, indicated by dashed blue arrows. The Schallamach wave does not appear as a thin clear line, as for example in Figure 6.4, but as a blurred, unclear large wave (or a combination of many small waves) through the area of contact. The change in appearance of the Schallamach wave is a further indicator of the transition to stick-slip motion. The images ⑦ to ⑨ (7ms) depict the subsequent increase in area of contact and mark the end of a single cycle, which is then repeated. In addition to the still images shown in Figure 6.7, a video of this transition zone is provided on the DVD with the filename 'Smooth_NR3_10mms_1.3N.avi' (see Section 9.5).
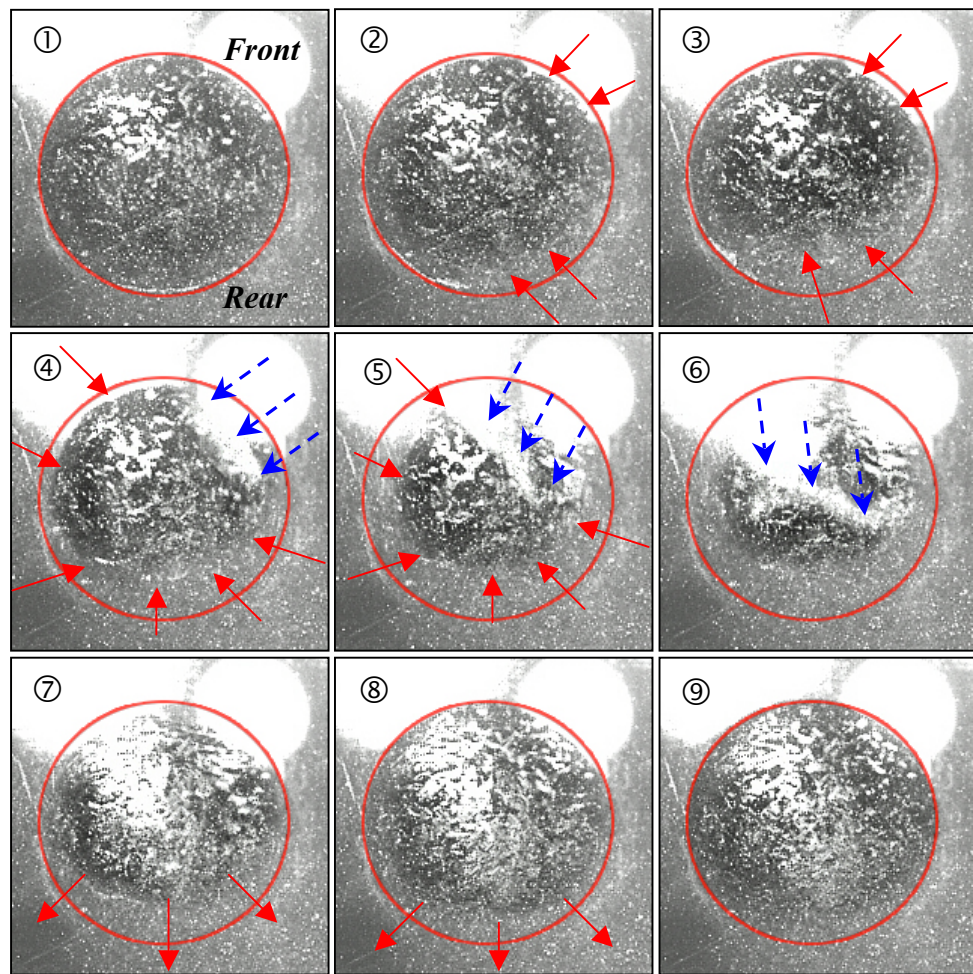
Figure 6.7: A transition between stick-slip motion and Schallamach waves correlates to the contact area. Red arrows show the decrease and increase in area of contact, while dashed blue arrows highlight a single Schallamach wave. The white circles in the upper part of each picture are light reflections. Rubber NR3 at a sliding velocity of 10mm/s and FN=1.3N is used.

The rationale behind this can be explained by the uplift (and down-lift) motion of the rigid hemisphere on the rubber created by the tangential stress field at the frictional interface, shown in Figure 2.16 (see also Chapter 4 and Schallamach (1969)). This oscillating up- and down-lift relates to an alternating increase and decrease in the area of contact, which leads to the stick-slip phenomenon and which can be observed at higher sliding velocities, as described next.

Stick-slip

The phenomenon shown in Figure 6.7 of a transition zone from Schallamach waves to stick-slip behaviour was at the sliding velocity limit for the friction tester so it was not possible to test at higher sliding velocities and, therefore, reveal true stick-slip motion. However, one way to induce stick-slip motion was to decrease the normal force, as this promotes the up and down lift of the slider, so that stick-slip arises at lower sliding velocities. For this reason the same parameters were used at a lower normal load of 0.6N and this allowed full stick-slip cycles to be observed. Figure 6.8 shows one such full stick-slip cycle under otherwise the same parameters as used in Figure 6.7. In the shown series of images, the decrease of the contact area is started from the rear of the contact zone (stick-phase) from ① until ③ (15ms), similar to Figure 6.7, followed by a sudden dramatic relative sliding (slip-phase). The time between images ④ to ⑥ only lasts 2ms. In the centre of image ⑤, when the slip occurs, the contact area seems to be rippled, which is an indication of a small surface instability still occurring in parallel to the macroscopic sliding process, while in image ⑥ the contact between slider and rubber appears to be totally lost. After this, the contact area increases again (⑦ to ⑨) and the cycle is repeated continuously.
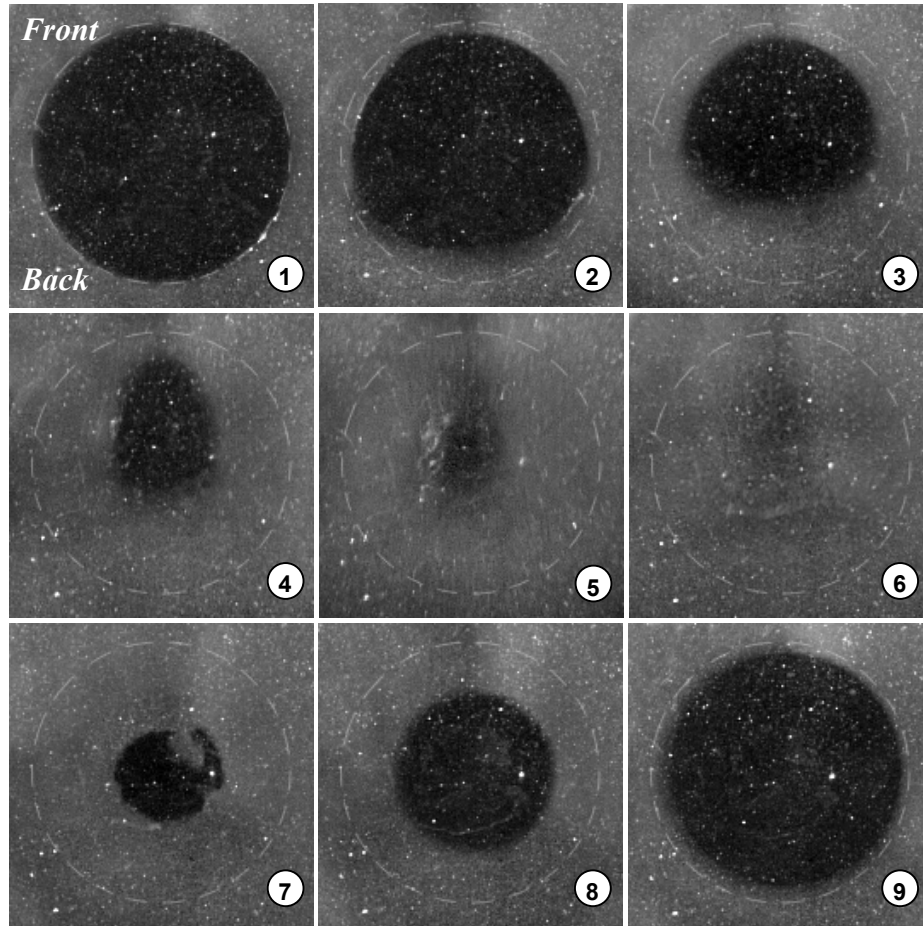
Figure 6.8: Correlating pictures to frictional force and contact radius measurement in Figure 6.9. A stick-slip cycle for the hemispherical glass lens (R=19mm) contacting an optically smooth NR3 surface at 10mm/s and FN=0.6N is shown from ① to ⑨.

The change in contact radius and the coefficient of friction over time for Figure 6.8 is plotted in Figure 6.9, in which the numbers relate to the images identified in Figure 6.8. Figure 6.9 shows that when the contact area becomes semicircular in shape in Figure 6.8 the sudden slipping at the interface correlates with a simultaneous drop down of the tangential frictional force. This phenomenon yields a fluctuation in the frictional force, which confirms the relative stick-slip motion between the two surfaces. Figure 6.9 shows that the stick-phase is much longer than the actual slip-phase and it also shows the coefficient of friction depends upon the apparent contact area. From the graphs it can be concluded that a close relationship between the contact area and alterations in the force exists. This also supports the argument given for Figure 6.6, where the frictional force gains in frequency and amplitude with increasing velocity, while Schallamach waves still occur.
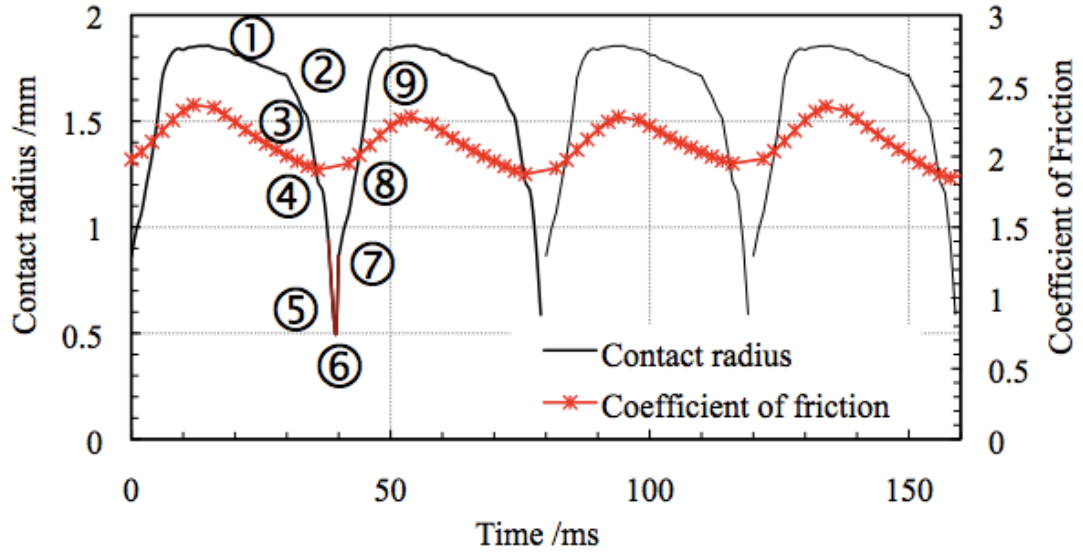
Figure 6.9: The change in contact radius and coefficient of friction for the stick-slip cycles are shown. The test was measured at *v*=10mm/s and *F_N*=0.6N for NR3. The numbers on the graph relate to different states shown in Figure 6.8.

6.3.3 A new phenomenon in rough sliding friction

The observations from Figure 6.3 to Figure 6.8 show that for smooth surfaces sliding undergoes several transitions: Starting from smooth sliding, a transition is noticed, where on certain parts of the contact area wavelets occur, which increase in size with sliding velocity to coherent Schallamach waves. A second transition is noticed at higher sliding velocities, where Schallamach waves co-exist with stick-slip motion. After this transition pure stick-slip motion is the only form of relative displacement at the interface and can result in the total loss of contact at the interface.

In contrast, for rough surfaces only smooth sliding and stick-slip motion occurs as described in Section 2.5.3 and commonly it is assumed that no Schallamach waves can manifest. This is because rough surfaces have a much smaller real area of contact, so that the adhesion on the surface is insufficient to lead to buckling instabilities. In order to investigate the transition from smooth sliding to stick-slip motion for rough surfaces, similar to Figure 6.6, the frictional force versus time for the rough surface of NR1 is shown in Figure 6.10 a). It is observed that no oscillation with time in the frictional force occurs up to a value of about 1mm/s, reflecting smooth sliding, while at higher sliding velocities an oscillation in the frequency of the frictional force increases,

providing evidence for the transition to stick-slip behaviour. Figure 6.10 b) shows the correlating frictional force versus sliding velocity, where the typical rate dependent friction behaviour for rough surfaces is reflected, which was also shown in Figure 6.1 and which is also discussed in Chapter 7.
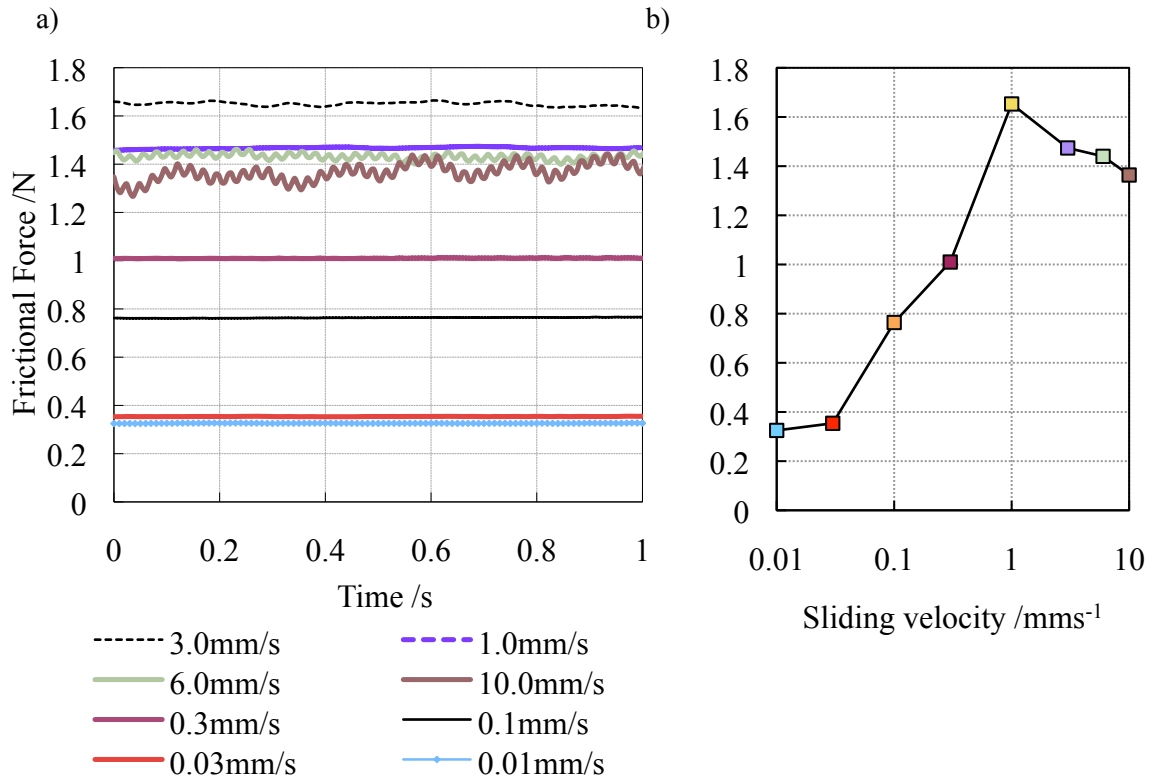
Figure 6.10: a) The increase in oscillation of frictional force output with increasing sliding velocity is shown for rough NR-1 surface (F_N=0.6N), while in b) graph the correlating frictional force for a) is shown versus sliding velocity.

If the region between 1mm/s to 6mm/s is investigated with a high-speed camera, a clear transition between smooth sliding and stick-slip can be also confirmed visually. From observations of the contact area a periodical decrease in the area of contact is expected, however, surprisingly another slip-process, which is similar in its appearance to Schallamach waves occurred. In this sliding velocity range, the displacement on the area of contact only occurred in sudden wavelet-like motions, which start from the front of the area of contact to the rear. These wavelets show the same increase in progression velocity with sliding velocity as experienced for Schallamach waves and they result in true stick-slip motion with a periodical alteration of the contact area at the highest sliding velocity observed (10mm/s). Due to the blurred nature of these wavelets, it was impossible to capture the motion in still images, as was possible for Schallamach waves on smooth surfaces. For this reason, two observation videos are attached to this thesis

on a DVD. The description of all DVD content is given in Appendix 9.5. The first video (filename: 'Rough_NR1_3mms_1.3N.avi') shows single blurred wavelets progressing over the area of contact of a rough rubber surface. The second video (filename: 'Rough_NR1_10mms_1.3N') shows similar stick-slip behaviour for the rough surface as shown in Figure 6.8 for the smooth surface. The supposition is made, that these wavelets, which travel across the area of contact in a similar manner than Schallamach waves, are connected to the general behaviour of Schallamach waves and also mark a transition between smooth sliding and stick-slip sliding. It is noted that the coefficient of friction for the rough surface is maximum at a value of $\mu = F_F/F_N = 1.6N/1.3N = 1.23$ according to Figure 6.10, so that the benchmark of $\mu = 2.0$ for the build up of surface instabilities is not met. However, as suggested previously, the coefficient of friction alone is not a sufficient measure to describe the threshold for the onset of Schallamach waves. In the presented phenomenon of slip-waves on rough surfaces, local stress maxima due to compression of single rubber surface asperities may lead to a build of shear stresses sufficient for the progression of surface instabilities.

In order to compare the average progression velocity of the wavelets on the rough interface with the values acquired for the wave progression velocity of Schallamach waves for the smooth surface, both compared for NR1 with $F_N = 1.3N$ in Figure 6.11.
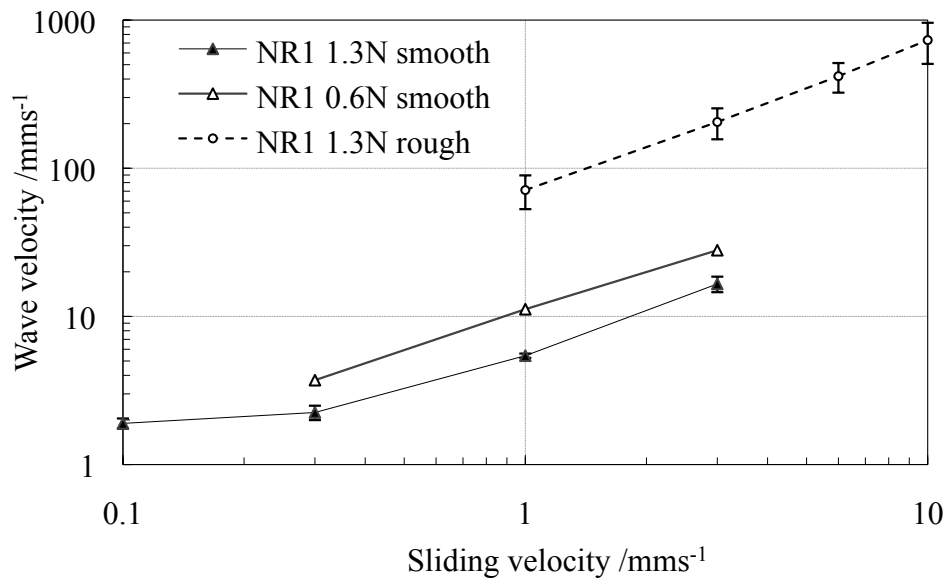
Figure 6.11: Progression velocity of Schallamach waves and rough surface waves versus sliding speed.

It is apparent that, for otherwise the same parameters, the surfaces waves on rough rubber travel at an about ten times higher velocity then Schallamach waves on a smooth rubber surface. This higher progression velocity can be explained in terms of the adhesional properties and its relation to the real area of contact. While the smooth surface is in intimate contact with the optical smooth rigid hemisphere, the rough surface has a much smaller real area of contact. This can be qualitatively observed, as the smooth contact interface is shown as a dark, circular contact patch, while the contact patch for the rough surface is much lighter but having the same contact radius. Therefore, for the rough surface the adhesional bonds at the interface are small and weak, so that adhesional effects less damp the wave velocity. Due to this, the wave velocity can travel at higher speeds and it is more dependent on the wave speed determined by the elastic modulus. The fact that the elastic modulus increases with sliding velocity, due to the viscoelastic properties of the elastomer, determines the velocity dependence of both, smooth and rough surface wave phenomena.

If the wave frequency of both is compared, an interesting relationship is revealed: Figure 6.12 shows the frequencies observed for the smooth surface (frequency of Schallamach waves and frequency of stick-slip motion at higher sliding velocities) in comparison with these for the rough surface (frequency of slip-waves and stick-slip frequency). The graph shows the transition from Schallamach waves to stick-slip behaviour, so that the data points at 10mm/s for the smooth surface represent the frequency of stick-slip.
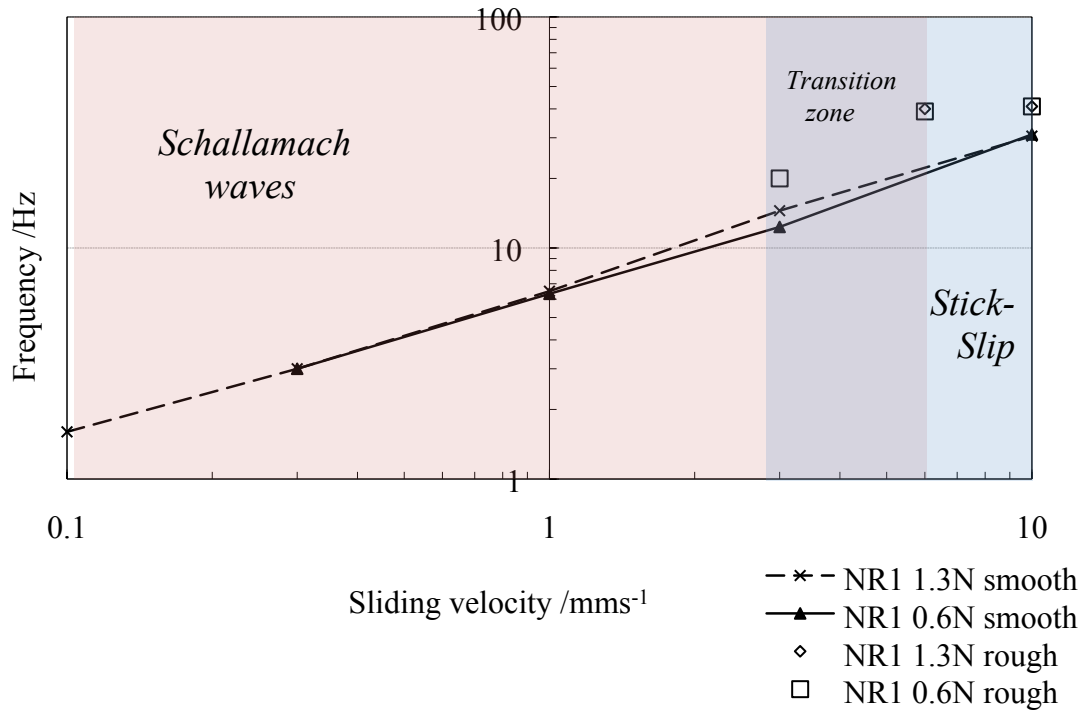
Figure 6.12: Comparison of Schallamach wave frequency (for smooth NR1, *F$_N$*=0.6N & 1.3N) with frequency of stick-slip motion for the rough surface.

The single data points on the graph in the region from 3mm/s to 6mm/s represent the frequency of the wavelets experience on the rough surface, while the values for 10mm/s represent true stick-slip motion. It is revealed, that for rough and smooth surfaces the frequency of surface waves are surprisingly similar and follow the same trend line, so that a direct relationship is shown here. As discussed in Figure 6.11 the higher frequency of the wavelets of the rough surface is due to the differences in rate dependent surface properties.

6.3.4   *Schallamach wave progression velocity*

In addition to the increase of wave progression velocity with sliding velocity, another phenomenon of Schallamach waves, which was only mentioned but not further investigated by Barquins and Courtel (1975), is the increase in the wave velocity throughout the contact region. It is reported, that the wave velocity is initially nearly constant over a certain length of the contact area, however, an order of magnitude increase in the velocity is seen at the rear of the contact area. This phenomenon has also been reported by Briggs and Briscoe (1975), however, they state "the reason for the

shape of the (wave progression velocity versus contact length) profiles is not fully understood".

In the presented work of this thesis the high frame rate setting of the high-speed camera also allowed for the measurement of the progression velocity of a single wave. It was confirmed that each wave increased in velocity while passing through the area of contact, as shown for NR1 (F_N=0.65N) for two different relative sliding velocities in Figure 6.13. The observed wave travels from the front of the contact zone (0mm in Figure 6.13) to the back (about 2.7mm in Figure 6.13). The graph further indicates the frequency dependence of the Schallamach waves, which was previously discussed in the context of Figure 6.5.
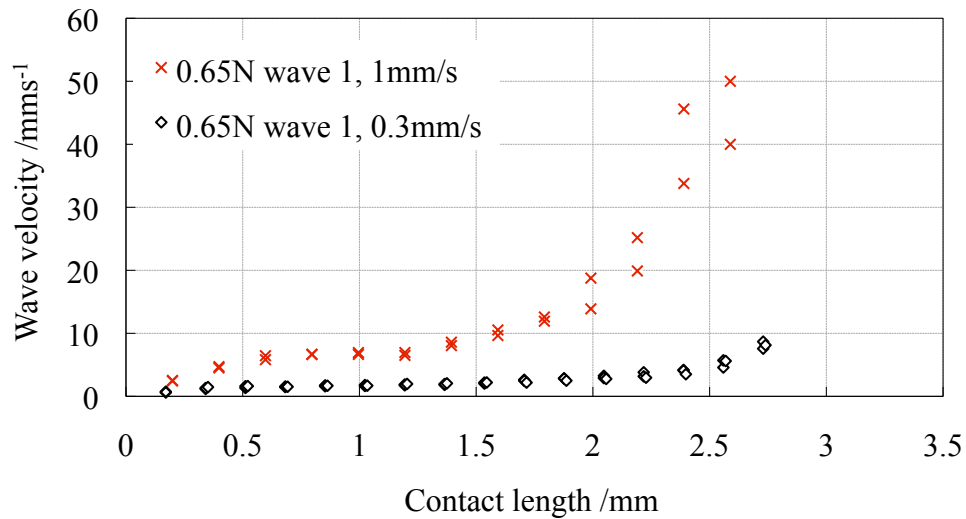
Figure 6.13: Wave progression velocity versus length of contact for two different sliding velocities for NR1 and F_N=0.65N.

From Figure 6.13 it can be concluded that in approximately the last third of the contact length the wave progression velocity increases significantly. The stresses at the sliding interface for rubber friction can be visualised using a FEA model such as that shown in Figure 6.14, taken from the FEA model previously described in Section 5.3.3.
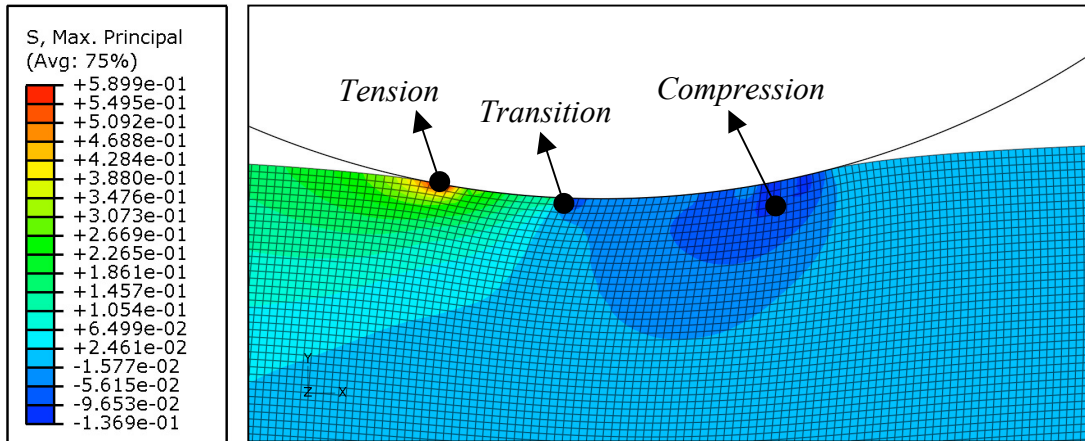
Figure 6.14: A rigid wedge slider (*R*=3mm) on a rubber block with *μ*=2.0 showing compressive and tensile stresses at the contact area.

The large compressive stresses in the front of the contact area govern almost two thirds of the entire contact area until the stress field undergoes a transition to tension in the last third of the contact length. In this tension zone the stress maximum is located near the edge of the contact area, so that the tensile stresses increase towards this edge. The stress distribution for Figure 6.14 is shown in Figure 6.15:
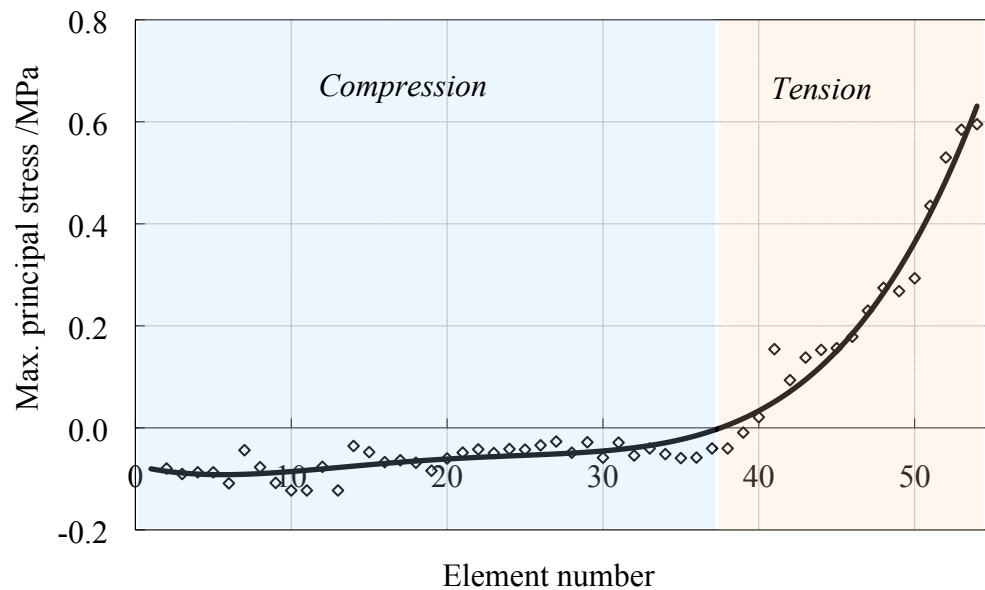
Figure 6.15: The maximum principal stress is shown versus element number. Element 0 is in front of the contact zone and element 54 is at the rear of the contact zone in Figure 6.15 and relate to a total length of 2.6mm. The compressive stresses are shown to be nearly constant over most of the contact zone, while the tensile stresses increase with increasing element number (contact length).

From Figure 6.15 it becomes apparent that the compressive stress in the contact area stays remarkably constant over two thirds of the contact length and only increases in the last third of contact due to the transition to a positive tensile stress. If Figure 6.15 is

compared to Figure 6.13 it can be concluded that the explanation for the increase in the wave velocity over the contact length is governed by this change in the stress field. Therefore, the compression zone is thought to govern the first, constant wave progression velocity, while the decrease in pressure gradient and increase in 'pulling' tensile stresses results in an increase in wave progression velocity.

6.3.5 Schallamach wave dependence on normal load

The compressive stress field influence on the wave velocity of Schallamach waves becomes even clearer when different normal loads are examined for the same compound NR1. It is described in literature, that Schallamach waves appear as the load is decreased. This is confirmed by experiments shown in Figure 6.16.
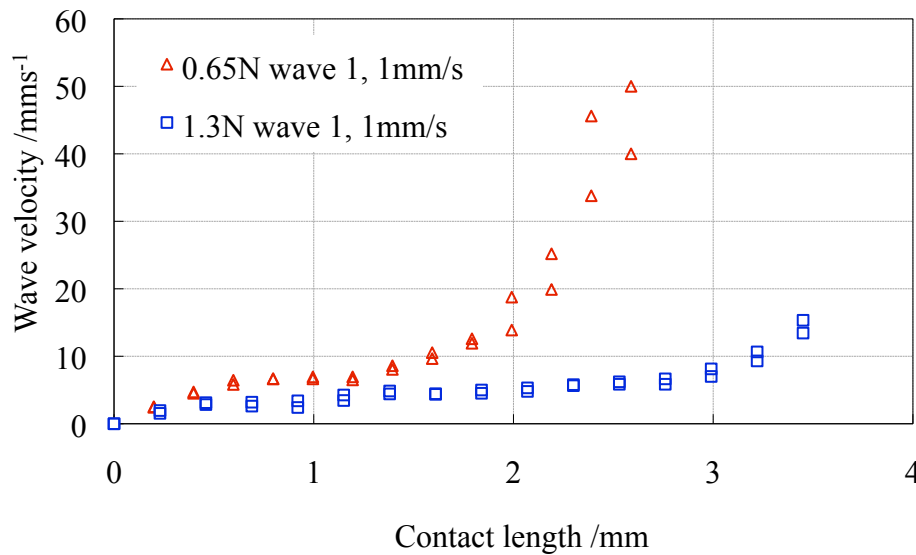
Figure 6.16: Wave progression velocity versus contact length for NR1 (F_N=0.65N&1.3N, v=1mm/s).

It is interesting to note, that for the normal load of 0.65N an average of two waves were present in the contact area, whereas for the normal force of 1.3N an average of three waves were present. The average wave progression velocity ω of the normal load 0.65N is higher than that velocity for F_N=1.3N, which was also shown in Figure 6.5. This increase in wave velocity with decreasing normal load can be explained qualitatively in terms of the energy balance (Barquins 1985; Barquins 1992). At a given time a number of n waves propagate through the area of contact, with a wave progression velocity of ω, when the slider slides with a velocity v at the interface. The apparent horizontal

frictional force F_F must satisfy the energy balance, which was given by Koudine et al. (1997):

$$vF_F = nF_C \omega, \tag{6.2}$$

where F_C is the applied force to a crack of length L. In the case of Schallamach waves, L can be defined as the diameter of the contact area. For a hemispherical rigid body on a soft rubber block, the equation can be rewritten as:

$$vF_F = n\omega^{\frac{8}{5}} \left(\frac{L\gamma\kappa}{1 - \cos\beta_P} \right). \tag{6.3}$$

where γ is the surface energy, κ is a temperature dependent parameter and β_P is the angle of peeling ($\beta_P = \pi/2$ for detachment waves). This approach suggests, that the tangential force F_F is directly proportional to the frequency-dependent surface energy and the number of waves apparent on the contact area in combination with the wave progression velocity ω f(v). Therefore, with an increase in normal load, hence an increase in frictional force, more waves travel through the area of contact at the same time in order to satisfy the energy balance.

6.4   *Conclusions*

Schallamach waves have been investigated experimentally by using the QMUL friction tester, which was designed and build as part of this research. The use of a high-speed camera allowed for precisely timed observations of the wave progression behaviour in relation to sliding velocity and length of contact for smooth rubber surfaces. The employed load cell, capable of storing data at a high rate, made the correlation of the observed images and the observed frictional force possible.

In the first part of this chapter the general sliding behaviour at the interface of a rigid hemisphere contacting a rubber block with a microscopically smooth surface was observed over three decades of sliding velocities. For these 'smooth' surfaces two sliding transitions have been described, where firstly smooth sliding transformed to Schallamach waves in the form of non-coherent wavelets. This is an indicator that, for the eye undetectable, smooth sliding exists parallel to the presence of these wavelets. Secondly, with increasing sliding velocity Schallamach waves transformed into stick-

slip motion. With increasing velocity a change in the frictional force (increase in frequency and oscillation amplitude) was noticed, which was also noted for rough surfaces, confirming the suggested relationship to stick-slip behaviour. Furthermore, a direct link between the contact radius and the frictional force was drawn.

For microscopically rough surfaces it is commonly assumed that only smooth sliding or stick-slip motion occurs. In contrast to this, slip waves have been observed in this work, which are similar in their nature to Schallamach waves. These waves on microscopically rough surfaces were compared to Schallamach waves for microscopically smooth surfaces and it was shown that a direct relationship exists between both progression frequencies. While Schallamach waves on smooth surfaces are damped due to the peeling energy, which is directly linked to the adhesional properties of the surface, the waves on rough rubber surfaces can travel at a higher velocity as the real area of contact is much smaller and, therefore, adhesion has a minor influence. The investigation confirmed the transition zone suggested by Wu-Bavouzet et al. (2007) and directly related the stick-slip behaviour to the surface instabilities of Schallamach waves.

In the second part of this chapter a phenomenon, firstly mentioned by Barquins and Courtel (1975) and Briggs and Briscoe (1975), was investigated, in which the wave progression velocity over the length of contact of a single Schallamach wave was monitored. It was shown by experimental observations and with the aid of FEA that the initial slow propagation of the wave is governed by the compressive stress field, while the increase of progression velocity is dominated by tensile stresses.

By the presented analysis several new insights were gained in the understanding of the sliding mechanism of rubber friction in the presence of Schallamach waves and in the understanding of wave propagation.

7 Surface preparation and indenter geometry influence on rubber friction

7.1 Introduction

It was found by Grosch (1963) that rubber exhibits distinct viscoelastic behaviour over several orders of magnitude of sliding velocity, while Barquins and Roberts (1986) were not able to replicate these key findings by Grosch. It was found later by Arnold et al. (1987) that the surface finish of the examined rubber samples was of great importance. Firstly, this conflict between Grosch's data and that of Barquins and Roberts is re-examined in this chapter by testing the frictional behaviour of different rubber samples with surface finishes differing in their microscopically roughness in contact with a optically smooth rigid slider. A WLF time-temperature superposition is examined for both surface finishes. As an extension of this investigation, the friction of a smooth rigid slider is compared to that of having the same microscopically roughness as the rubber surface.

Secondly, in this chapter the influence on the resulting frictional force of different rigid surface geometries with conical and hemispherical shapes, chosen to represent the different ideal macro asperities found in practice for example in a road surface, is investigated to examine how both very smooth as well as extremely rough indenters can exhibit a high coefficient of friction.

The following chapter is based on the publication in Constitutive Models for Rubber VI, by Gabriel et al. (2009)

7.2   Experimental background

7.2.1   Characterisation of model materials

Four model materials were compounded at QMUL using the compounding methodology described in Section 3.1 and the mechanical characterisation is discussed in Section 3.2 and the methodology used to measure T_g is described in Section 3.2.3. Each rubber surface was vulcanised with a specific roughness, which was analysed by the process described in detail in Section 3.5. A modest roughness of the surface was chosen to reduce the complications that arise for mirror-like surfaces when the velocity dependence of the frictional sliding is examined: While Grosch (1963) showed bell shaped master curves for the coefficient of friction versus sliding velocity for different rubber compounds, friction tests of Barquins and Roberts (1986) were not able to reproduce these results. They did, however, note Schallamach waves, as discussed in Section 2.5.5. It was later shown by Arnold et al. (1987) that a difference in surface finish, which was originally not described by Grosch (1963), might be the reason for the discrepancy between these two data sets. In order to avoid complications arising through Schallamach waves and heavy stick-slip motion experienced specifically on very smooth surfaces (Thirion 1946), as examined in Chapter 6, a mould with roughened surface was used for the majority of tests described in this work. However, to examine the complication experienced by Barquins and Roberts (1986), and to further investigate the discrepancy between their findings with Grosch (1963), a smooth surface was also investigated.

7.2.2   Friction testing

The frictional characterisation of the model materials and the tyre compounds was examined on the Plint friction tester, which is described in detail in Section 3.7.2. The test parameters for the friction tests examined in this chapter are given in Table 7.1.

Table 7.1: Range of parameters used for different friction tests.

Parameter	
Velocity	0.01mm/s to 10mm/s
Normal load	1N to 20N
Temperature range	22°C to 80°C
Rigid slider geometries	
Cones	10° to 160°
Hemispheres	*R*=6mm to 240mm

7.3   Results and discussion

7.3.1   Time-temperature superposition

In order to classify the frictional behaviour, the model materials were tested at a broad range of sliding velocities from 0.01mm/s to 10mm/s over a range of temperatures up to 80°C. A smooth rigid steel slider with a radius of 96mm was used with a normal load of 1N in order to test under a normal pressure of 0.3MPa, similar to the pressures experienced in tyres for motor sports. The coefficient of friction was shifted using the WLF time-temperature superposition, described in Section 0.

Figure 7.1 shows the time-temperature superposition principle for the frictional data of SBR-0. In a) the coefficient of friction for SBR-0 is plotted versus the logarithmic sliding velocity, while b) shows the same data set multiplied with the WLF shift factors gained from the time-temperature superposition principle. The good shift-behaviour for all four model compounds is shown also for SBR-50 (Figure 7.2) as well as NR-0 and NR-50 (Figure 7.3).
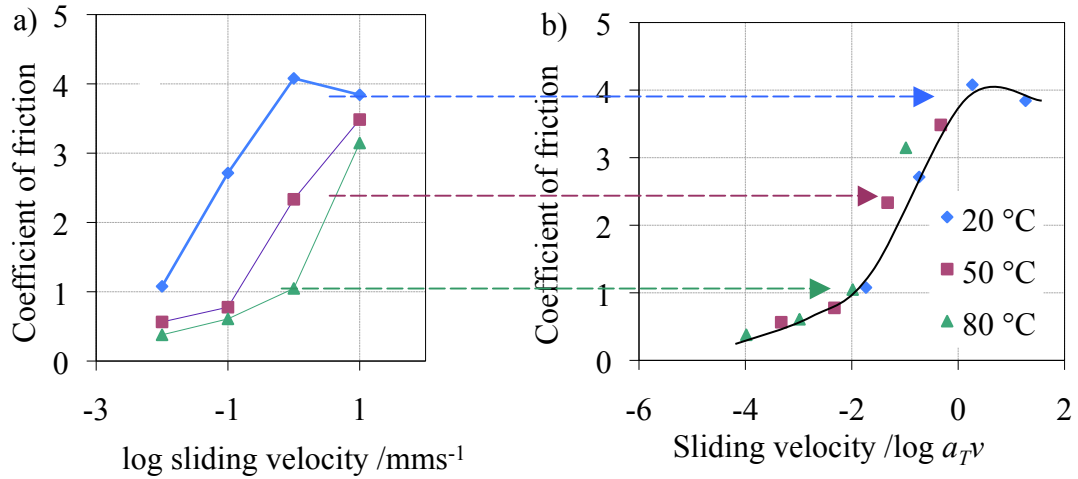
Figure 7.1: a) Friction vs. sliding velocity for rough SBR-0 for a polished slider *R*=96mm and F*N*=1N. The friction data can be shifted in to one master curve, shown in b) as a thick black line for the time-temperature superposition of the coefficient of friction at a reference temperature of 23°C.

The data in Figure 7.1 b) are redrawn in Figure 7.2 to compare both friction data sets for SBR-0 and SBR-50. SBR-0 exhibits higher friction, as a result of its lower modulus, allowing for a higher deformation and hence an increased hysteresis contribution lost through the internal bulk deformation of the rubber. Furthermore, the adhesional influence on friction is likely to increase with a decrease in modulus as micro-asperities on the rubber surface can deform easier and hence increase the real area of contact.
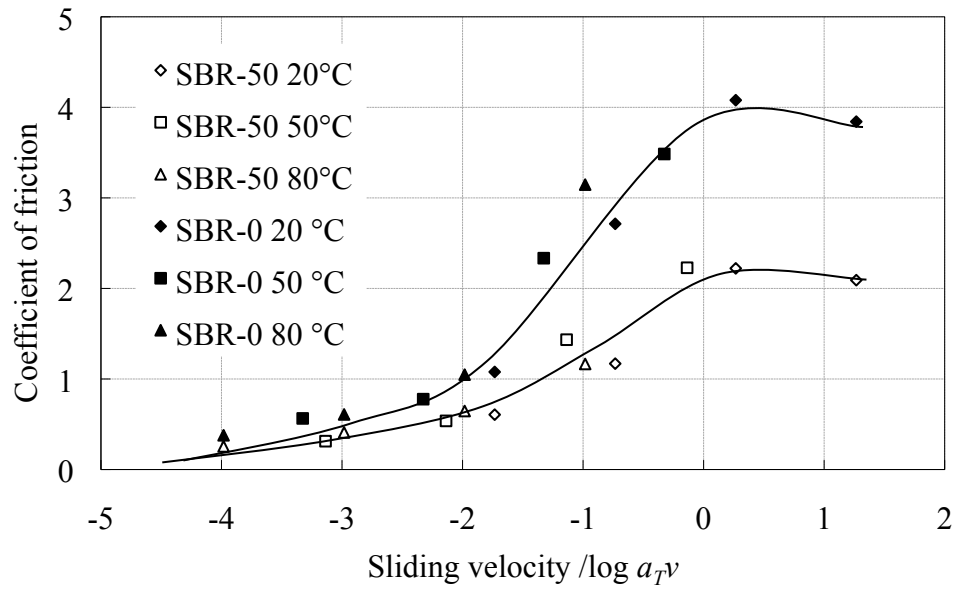
Figure 7.2: Comparison of the WLF time-temperature superposition for the rubbers SBR-0 and SBR-50. The coefficient of friction is shown versus sliding velocity under the same conditions as in Figure 7.1 b).

When Figure 7.2 for SBR is compared to Figure 7.3 for NR a similar trend can be observed for both materials, showing the large influence of the modulus on rubber friction.
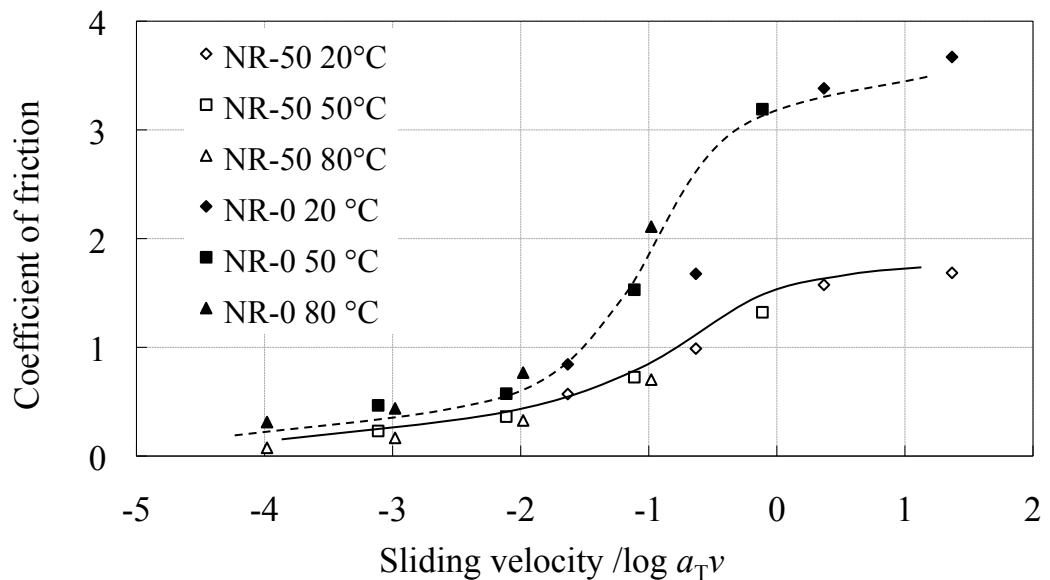
Figure 7.3: Comparison of the time-temperature superposition for the rubbers NR-0 and NRR-50. The coefficient of friction is shown versus sliding velocity under the same conditions as in Figure 7.1 b).

Grosch (1963) showed that his bell-shaped master curves, discussed in Section 2.5.4, exhibited a good correlation between the frequency of maximum friction of the master curve and the loss modulus maximum peak. The data presented in this work exhibit similar friction behaviour compared to the ones presented by Grosch (see Figure 2.27), where the maximum peak of the loss modulus is lower for SBR than for NR. This explains why the friction master curves for NR in Figure 7.3 are still rising at higher frequencies, whereas the master curves for SBR in Figure 7.2 show a decrease at the maximum sliding velocity tested. Supporting this, the comparative friction data presented by Grosch have a maximum for SBR at sliding velocity of around 10mm/s, while the maximum for NR is about two decades higher at 1000mm/s.

If the influence of the surface topography is investigated to examine and resolve the conflict between the data sets of Grosch (1963) and Barquins and Roberts (1986), then the question arises how the behaviour of an optically smooth surface as originally used by Barquins and Roberts has an effect on the behaviour shown in Figure 7.2 and Figure 7.3? For this reason a mirror-like smooth surface was prepared for SBR-50 and WLF time-temperature superposition was applied producing the graph shown in Figure 7.4.
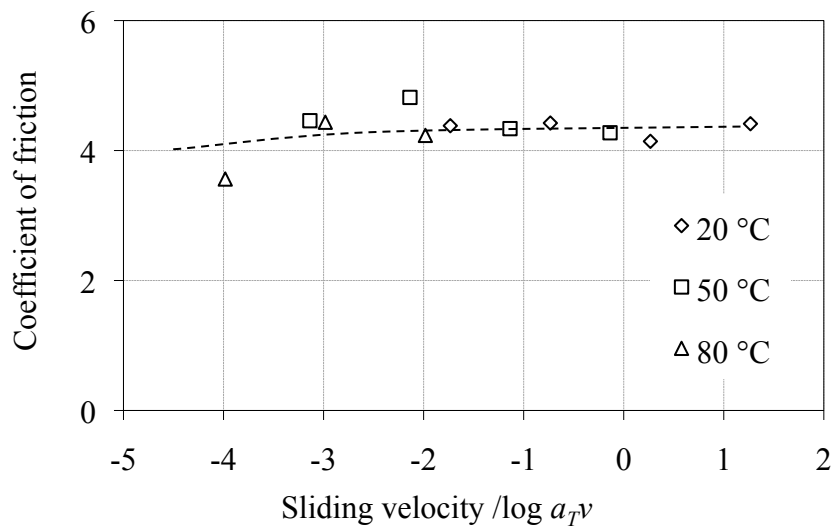
Figure 7.4: The WLF plot for an optically smooth SBR-50 and a polished hemisphere (*R*=96mm, *F~N~*=1N). No velocity dependence over the sliding velocity range measured is noted (Reference temperature 23°C).

Figure 7.4 shows almost no sliding velocity dependence over the entire sliding velocity range tested. In addition, the coefficient of friction is very high when compared to the maximum friction shown in Figure 7.2 for SBR-50. As the test parameters for the

smooth SBR-50 surface are the same as for the rough SBR-50 surface, the increased real area of contact between both optically smooth surfaces is likely to be one of the reasons for this change. Due to this increase in the number of adhesional bonds at the interface, the total frictional force increases. Another reason, as discussed in Section 2.5.4, is the importance of the characteristic length scale ζ of the micro roughness. According to Equation (2.52), larger asperities, as encountered for the rough rubber surface, excite the interface at lower frequencies, while smooth surfaces experience higher excitation frequencies. Therefore, when the loss modulus is considered, more energy is dissipated at a higher frequency and the friction is higher.

Beside the findings of Grosch (1963), Klüppel and Heinrich (2000) emphasise that also the geometric shape of the asperity plays an important role in rubber friction. In their study they showed that the worn asperities of an abraded road surface, exhibit different friction behaviour than asperities of a new road surface. Therefore, not only a certain length scale, determining the distance between asperities, but also the shape of each asperity is of great importance. The influence of different asperity geometries, idealised as rigid sliders, shown in Figure 3.30 is discussed in detail in Section 7.3.4.

7.3.2   *Frictional contribution from mechanical interlocking of microasperities*

To investigate the effects of surface roughness further, the friction behaviour of the rough rubber surface was examined using two rigid hemispherical steel indenters (R=6mm) with different surface properties. While the first indenter had a polished, smooth surface, the second indenter was prepared with the same surface roughness as the rough rubber surface (R_{max}=21μm). The differences in frictional behaviour are shown in Figure 7.5, where the coefficient of friction is plotted against sliding velocity for a rough SBR-50. It is shown that the rough slider exhibits a higher friction than the smooth surface, which is at first sight somewhat unexpected, as for a rough surface the contact area is smaller than that of a smooth surface and, hence, the adhesional contribution to friction decreases.
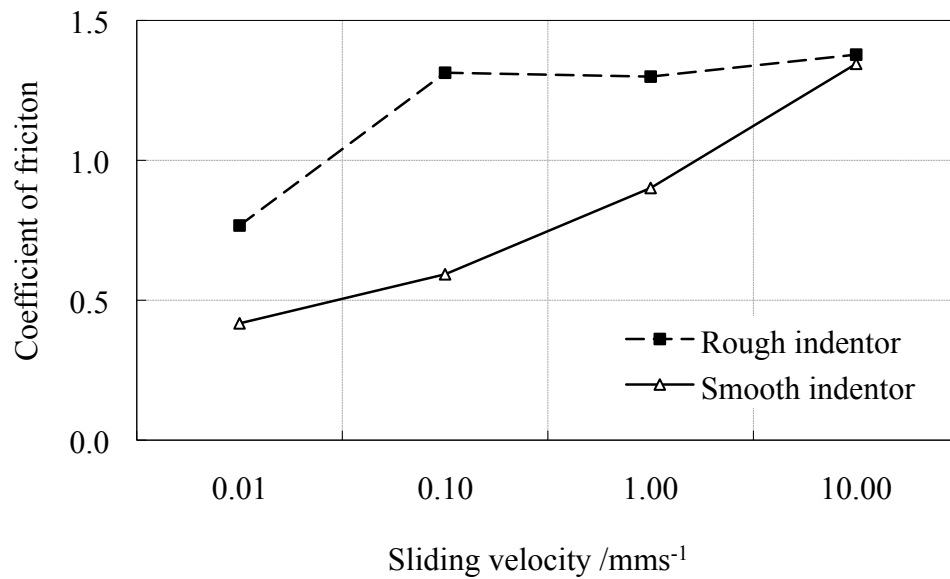
Figure 7.5: The friction for a rough SBR-50 differs with the surface finish of the rigid indenter. Two steel hemispheres (*R*=6mm) were tested, while one had a smooth, polished surface finish and the other had the same roughness as the rubber surface.

However, if the similarity of the surface finish of rough rubber and rough indenter are considered, an interlocking of the asperities of similar shape and size is likely to contribute to the frictional force, as is shown schematically in Figure 7.6.
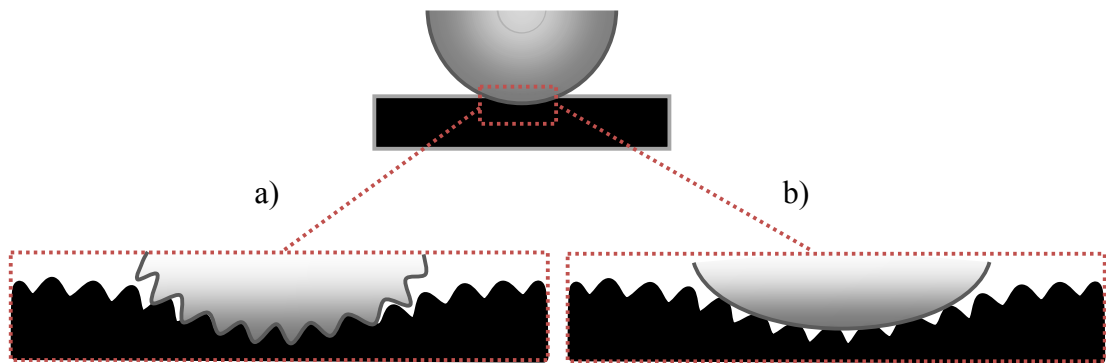
Figure 7.6: Schematic figure of a rigid hemispherical indenter on a rectangular rubber block. The shown magnifications of surface finishes of the rigid indenter are specified into two cases: In a) the same roughness as the rubber surface and in b) a smooth rigid surface of the slider is shown.

Hence, the rough slider exhibits a higher friction than the smooth surface, while the source of friction is thought to be only due to hysteresis and geometrical interlocking with only modest surface adhesion for the rough on rough surface combination. The

outcome of the experimental data set presented in Figure 7.5 shows another aspect of the different influences of surface preparation on the total frictional force.

7.3.3 Investigations of the velocity dependence of different indenter geometries and rubber topography

It is apparent that the surface finish of the rubber clearly changes the frictional behaviour as it was shown by the confirmation of the reported conflict between Grosch (1963) and Barquins and Roberts (1986) and the above described interlocking process of two different surface finishes for the rigid slider. The next aspect of this study examines how the geometry shape of a rigid indenter influences the frictional force output for rough and smooth rubber surface finishes. For this investigation two significantly different indenter shapes, a hemispherical steel indenter with a radius of R=240mm and a conical steel cone with an angle of 30° were chosen. By changing the normal load (5N and 15N), the influence of the real area of contact for both shapes was investigated.

The frictional investigation of the hemispherical indenter on SBR-0 for both, a rough and a smooth rubber surface is given in Figure 7.7. As shown earlier, it is confirmed that the smooth rubber surface shows little velocity dependence over several decades of sliding velocity, while with a rough rubber surface the expected velocity dependence is exhibited. At high friction coefficients measured for the smooth surface, it was likely that Schallamach waves were present, however, they could not be directly observed using the Plint friction tester. In addition, for the smooth surface a load dependence between 5N and 15N was seen, which was much smaller for the rough rubber surface. For both surfaces, rough and smooth, the apparent area of contact increases with normal load, however, only for the smooth surface was this change in contact area significant, probably reflecting a higher real area of contact than for the rough rubber surface.
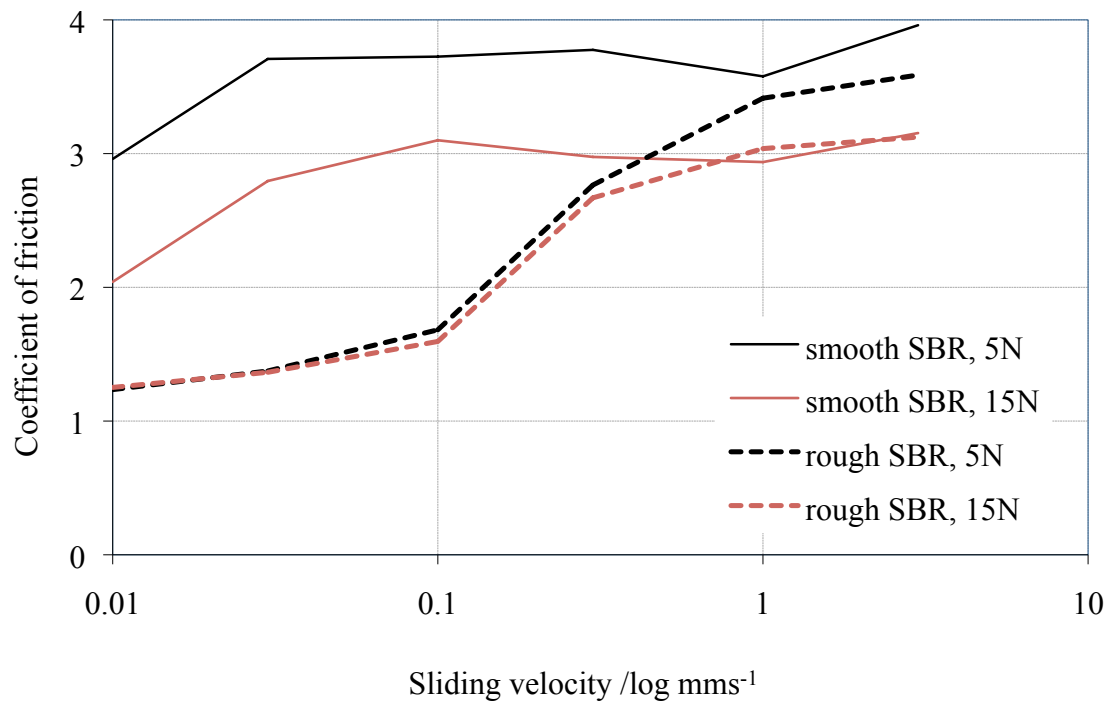
Figure 7.7: Coefficient of friction versus sliding velocity for a hemisphere of *R*=240mm on both, smooth (thick line) and rough (dashed line) SBR-0 at F_N=5N and 15N.

In contrast, if a sharp conical indenter was considered, no velocity dependence for both rubber surfaces, rough and smooth was exhibited, as is shown in Figure 7.8.
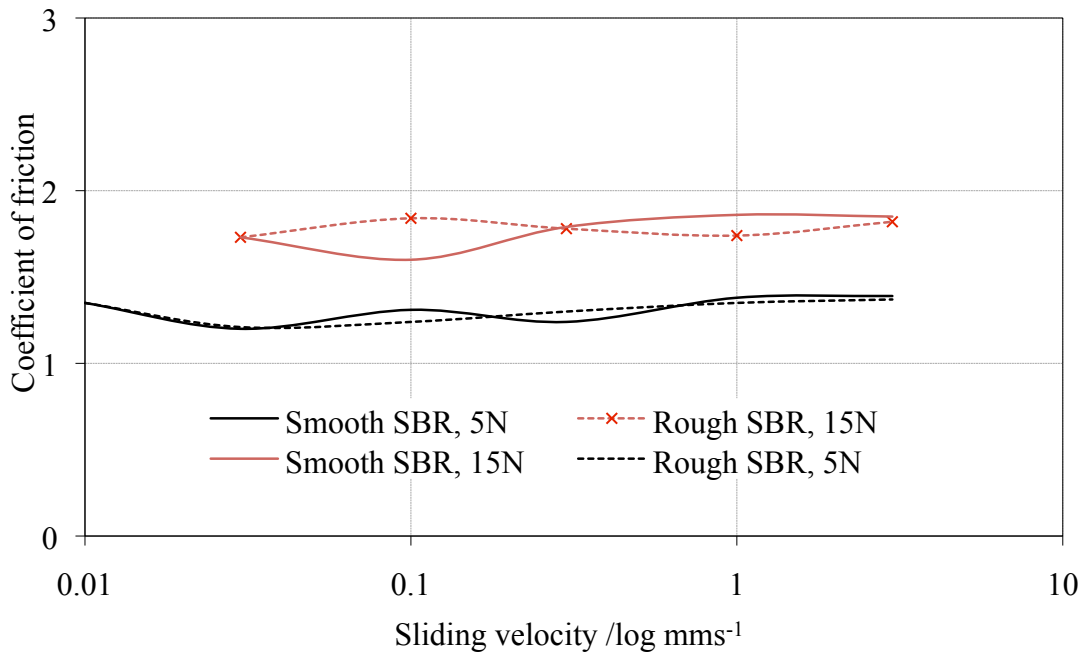
Figure 7.8: Coefficient of friction versus sliding velocity for a cone angle of 30° on both, smooth (thick line) and rough (dashed line) SBR-0 at F_N=5N and 15N.

From this it was seen that for very sharp asperities no relation to the real area of contact exists and, therefore, a relation to a characteristic length scale of the surface roughness is unlikely. Only a load dependence of the coefficient of friction was seen, reflecting the larger indentation of the sharp asperity into the soft rubber, which deformed a larger volume of rubber when sliding, creating a higher frictional force. From this investigation it becomes apparent, that different indenter geometries have a distinct influence on the frictional force output, and it is shown that for similar test conditions a distinct difference is noted for the two investigated indenter geometries. This effect of different indenter geometries is investigated in more detail in the Section 7.3.4 for a rough rubber surface in terms of the load dependence for a fixed sliding velocity.

7.3.4   *Friction dependence on interface geometry*

In the previous sections it was shown that the macro and microscopic topography of a friction interface is of great importance to its frictional behaviour in terms of velocity dependence. In this section several indenter geometries are investigated experimentally under varying normal loads in terms of their frictional contribution due to their specific geometry. It is shown that both, sharp and blunt asperities can exhibit high friction. While the high friction of very sharp asperities usually results from a high hysteresis contribution and fracture energy dissipation, blunt or smooth surfaces show a strong adhesional contribution. For the purpose of investigating this behaviour a broad range of cones, representing very sharp asperities with an angle of 10° to 100° and flatter cone asperities with an angle of up to 160° as well as hemispheres from R=6mm to R=240mm, were tested. The geometries for each slider are shown in Figure 3.30. The sliding velocity was kept constant at 0.1mm/s in order to keep the effects of frequency dependence as low as possible. A range of normal loads for each indenter geometry from 1N to 20N, on SBR-0 was tested in this investigation using the Plint friction tester.

The Plint friction tester is not set up to measure the vertical displacement of the indenter. From the amount of indentation into the rubber surface, however, a first comparison on the amount of deformation of the bulk rubber for the different indenter geometries can be made. While the indentation depth for hemispheres (Timoshenko and Goddier 1973) and conical indenters (Sneddon 1975) into semi infinite rubber blocks

can be calculated, however, in the case of a finite rubber block with a thickness of 5.5mm, these equations fail to predict the indentation behaviour reliably. Therefore, all indenter geometries were separately tested in indentation tests, as described in Section 4.3.4, and confirmed using FEA. While the hemispheres indent only a small amount into the rubber block, the indentation level of the cones increases rapidly with normal load, as is shown in Figure 7.9. In the analytical approach the square of the penetration depth is proportional to the normal load. So the measured data are plotted as indentation depth squared versus normal load.
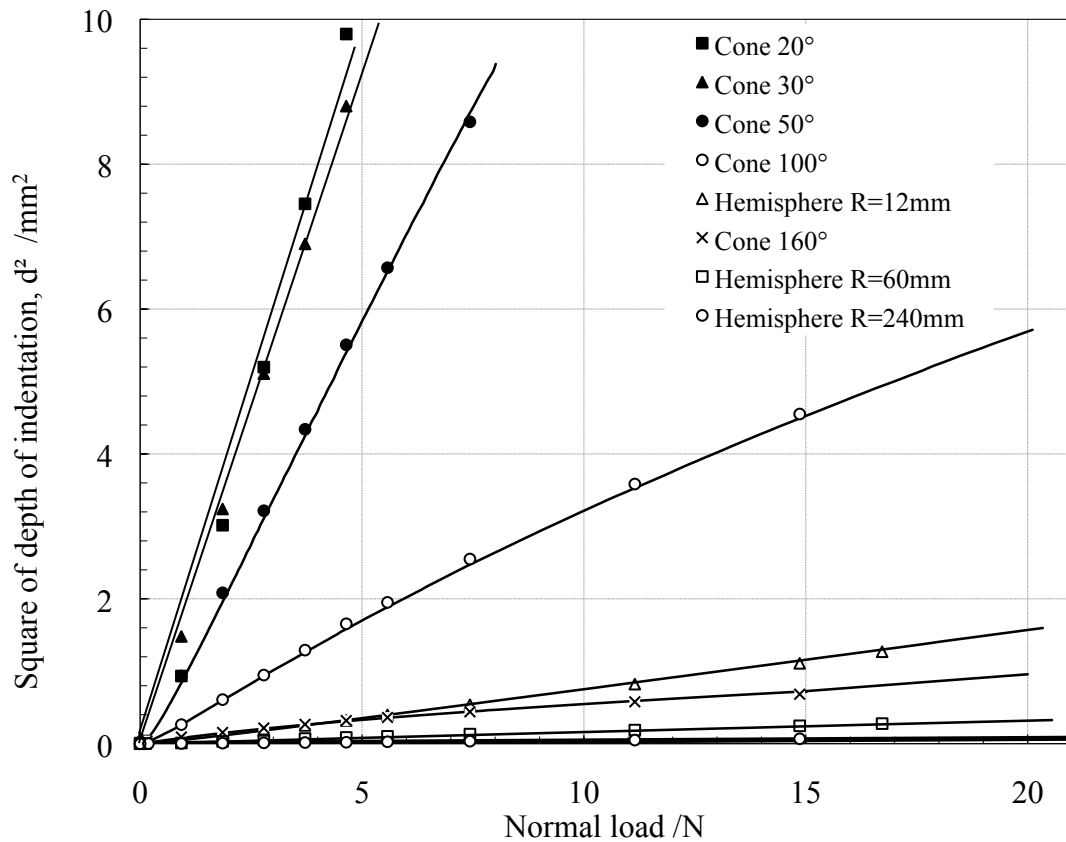
Figure 7.9: The indentation of cones and hemispheres at F_N=1 to 20N can be predicted well using FEA. The data points reflect experimental data, whereas thick lines show the corresponding FEA calculation.

Accordingly, if the friction coefficient for the cones was measured over the same range of normal loads, the frictional influence of the different cone angles is shown in Figure 7.10 (and later that of the different radii of hemispheres in Figure 7.13). For blunt cones, from a cone angle of 160° up to 50°, the coefficient of friction was almost independent of the normal load and no scratch patterns were observed within the test range. For sharper cones, from an angle of 50°, with an increase in cone sharpness a fracture

pattern on the surface was observed even with just a single pass and the friction increases with the indentation depth.
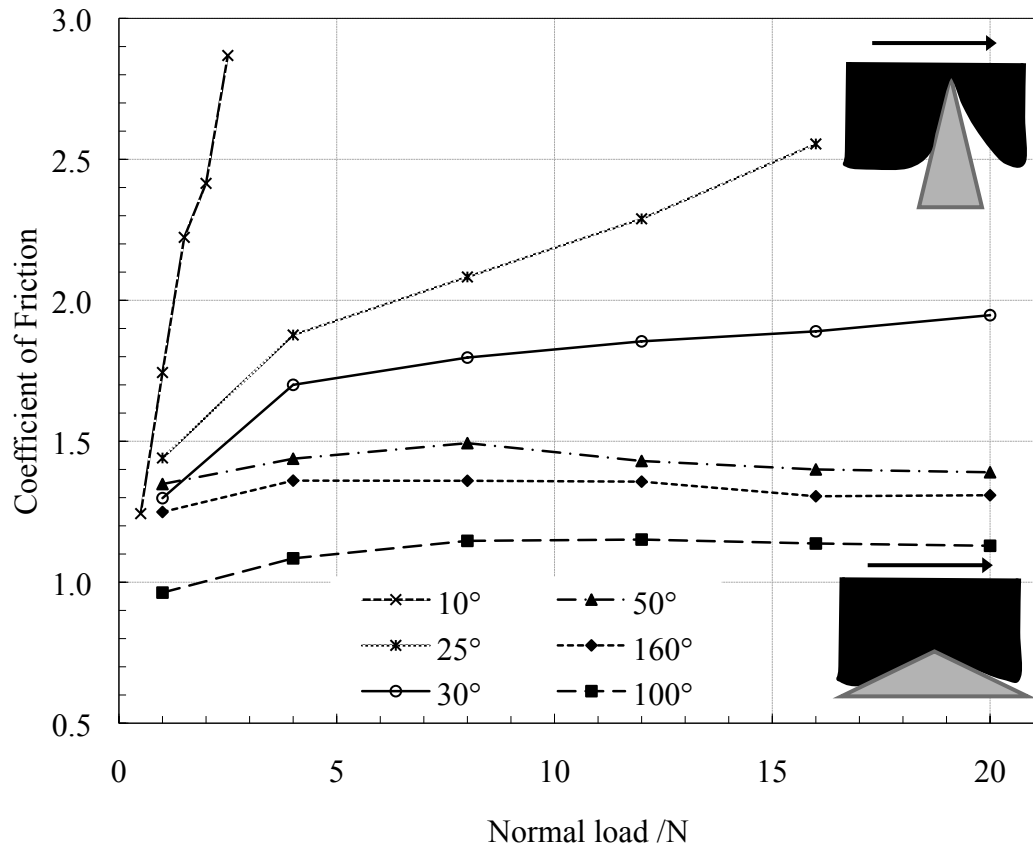
Figure 7.10: Coefficient of friction of conical indenters (α=10° to 160°) on rough SBR-0 at F_N=1 to 20N. The resulting frictional force increases with increasing cone sharpness. It is interesting to note that the cone with 160° shows higher friction than that of 100°.

With increasing cone sharpness the depth of indentation increases under similar normal loads, as shown in Figure 7.9, so a larger volume of rubber is deformed horizontally by a sliding indenter, increasing the energy losses due to deformation. For this reason the friction increases with cone angle in Figure 7.10. In addition to adhesion and hysteresis losses, the energy lost due to fracture of rubber contributes to the total frictional force, resulting in an increase of the coefficient of friction with normal load for the sharper cones (10° to 50°). According to Gent (2001) the stored energy due to large deformations while sliding can be the driving force for propagating cracks, and, as described by Fukahori et al. (2008), cracks propagate in abrasion processes if the local stresses are bigger than the tensile stresses. An example of fracture induced by a cone with an angle of 10° is shown in Figure 7.11.
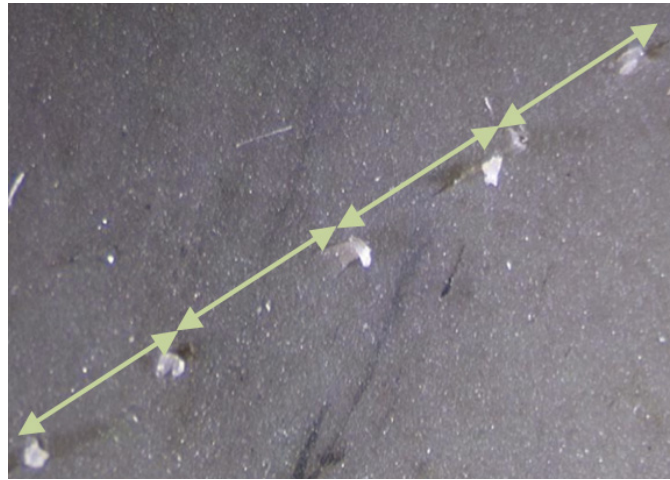
Figure 7.11: Fracture pattern induced by a conical indenter of 10° and a normal load of F_N=2N. The spacing between the induced crack patterns is dependent on the normal load and an arrow indicates the length between two subsequent cracks.

The cracks induced by the sharp asperities appear as a repetitive pattern on the rubber surface and a relationship between the spacing of these patterns and the normal load exists, as is shown in Figure 7.12. However, this relationship is only noted but not further investigated in this work, as extensive investigations on needle scratch experiments have been conducted previously by Schallamach (1952).
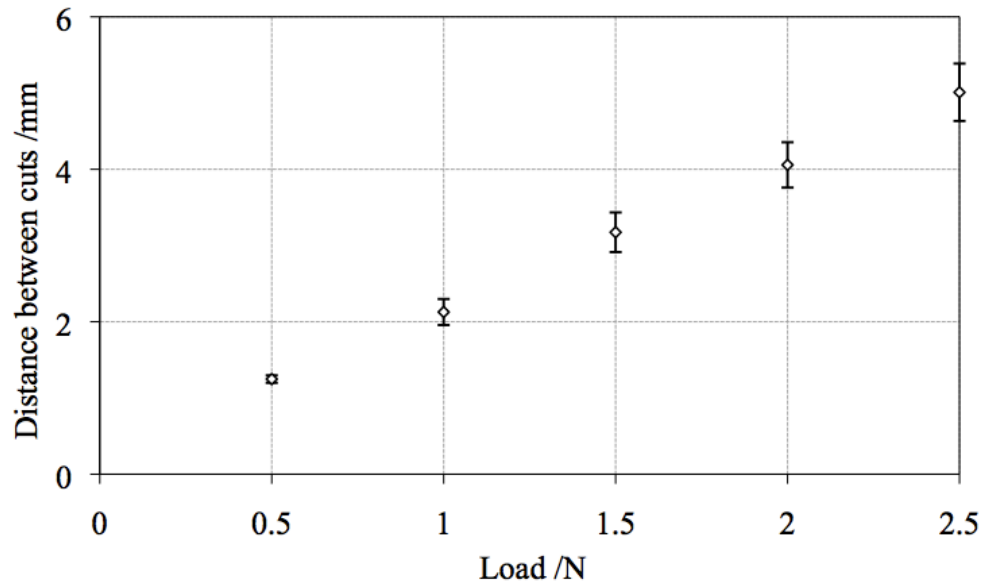
Figure 7.12: Relationship of the distance between two cracks on an SBR-0 surface for a conical indenter of 10° measured over a range of normal loads.

In the extreme case of needle-like cones (10°), the indentation can lead to penetration into the rubber, leading to an almost infinite coefficient of friction due to large horizontal deformation of rubber. Figure 7.10 shows that very sharp asperities exhibit the highest friction despite their very small area of contact. However, when the cone angle increases to for example 160°, the friction force is again seen to increase. While the maximum stresses at the tip of each cone increase with cone sharpness, for blunt cones the contact area increases, increasing the adhesional friction term. A flat surface with a cone angle of 180° would give in theory, a further increase in friction, as shear forces become greater for two flat surfaces. Nevertheless, a flat surface, can not be tested with the Plint friction tester, as edge effects become apparent and, therefore, an intimate contact between both surfaces can not be established. For this reason smooth hemispheres were used to represent blunt cones, or, for the hemisphere with a radius R=240mm to represent an almost flat contact.

Figure 7.13 shows the coefficient of friction for three hemispheres of different radii, emphasizing that with an increase in the radius of curvature the friction increases as the area of contact increases. In contrast to cones, the coefficient of friction decreases with load, confirming the general findings in literature (Thirion 1946; Schallamach 1969; Myant et al. 2009). No abrasion was noted for the hemispheres, as the pressure distribution underneath the slider was considerably less than for the cones.
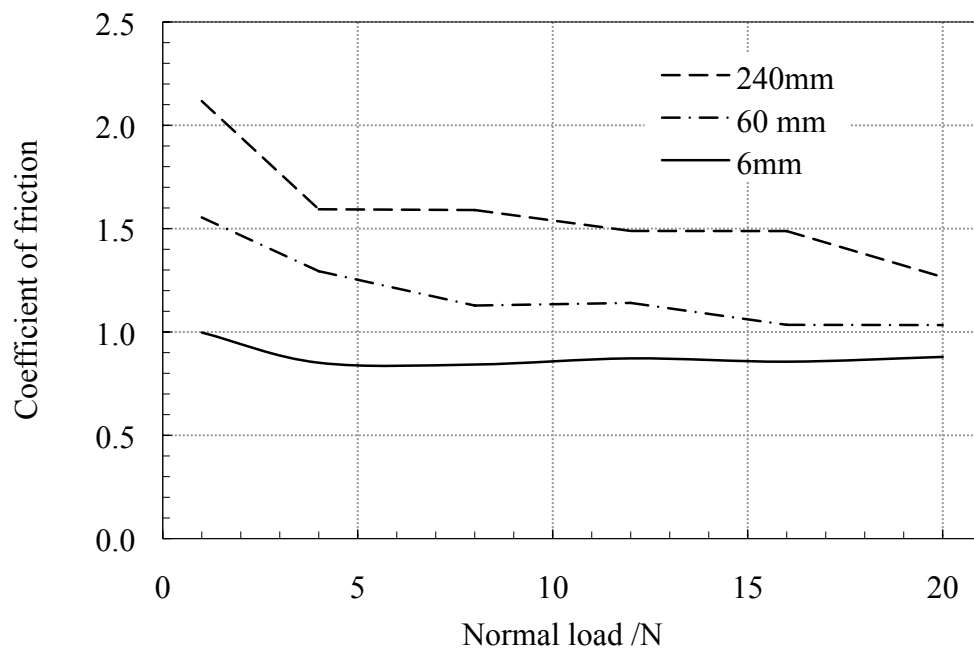
Figure 7.13: The coefficient of friction versus normal load for hemispherical indenters on rough SBR-0 at F_N=1 to 20N.

In order to relate the frictional results gained from the investigations of hemispheres with these gained from conical indenters a supposition is made: When a hemisphere is assumed to be a blunt or abraded cone, the amount of indentation *d* in relation to the radius of contact *a*, could be expressed as an angle *θ*, as shown schematically in Figure 7.14. This angle, if constant over a certain range of normal loads, might allow for a theoretical comparison of both indenter geometries.
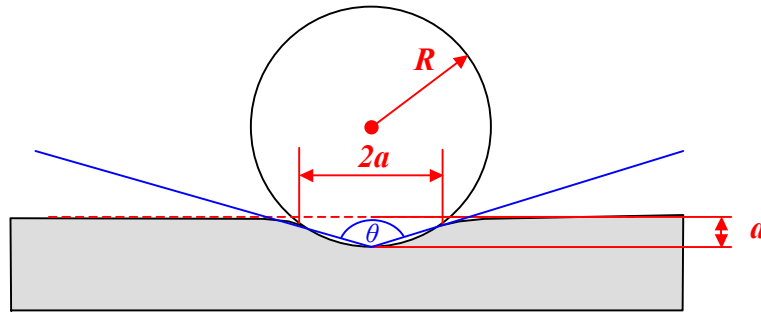
Figure 7.14: The interface of a hemisphere with radius *R* indenting into a soft rubber surface can be defined by the indentation depth *d* and the radius of contact *a*. If lines (blue) through the point of maximum indentation and the maximum radius of contact are drawn, an angle *θ* can be defined.

It is acknowledged that the supposition of describing the interface of a hemisphere with the help of an angle neglects the fact that for both geometries during sliding the contributions to the total friction are different, so that the assumption remains of theoretical nature only. FEA models have been employed to calculate the indentation depth *d* and the radius of contact *a*, similar to the models already used to calculate the results presented in Figure 7.9 for a finite block thickness of 5.5mm. The calculated cone angles from the modelled indentation depth and contact radii in relation to the normal load are given in Figure 7.15. It is shown that the radii of the hemispheres influence the calculated values for the cone angle, based on the theoretical supposition made. The related cone angle for the hemisphere of *R*=6mm decreases significantly with normal load as the indentation depth increases more than compared to the larger hemispheres (see also Figure 7.9). In contrast, the values calculated for the larger hemispheres, for example that of *R*=240mm, are almost constant. From this observation it is suggested that the larger hemisphere might reflect a flat geometry much better, as less dependence on the normal load (indentation depth) is given, so that an almost flat surface of around 177° for the hemisphere of *R*=240mm can be assumed.
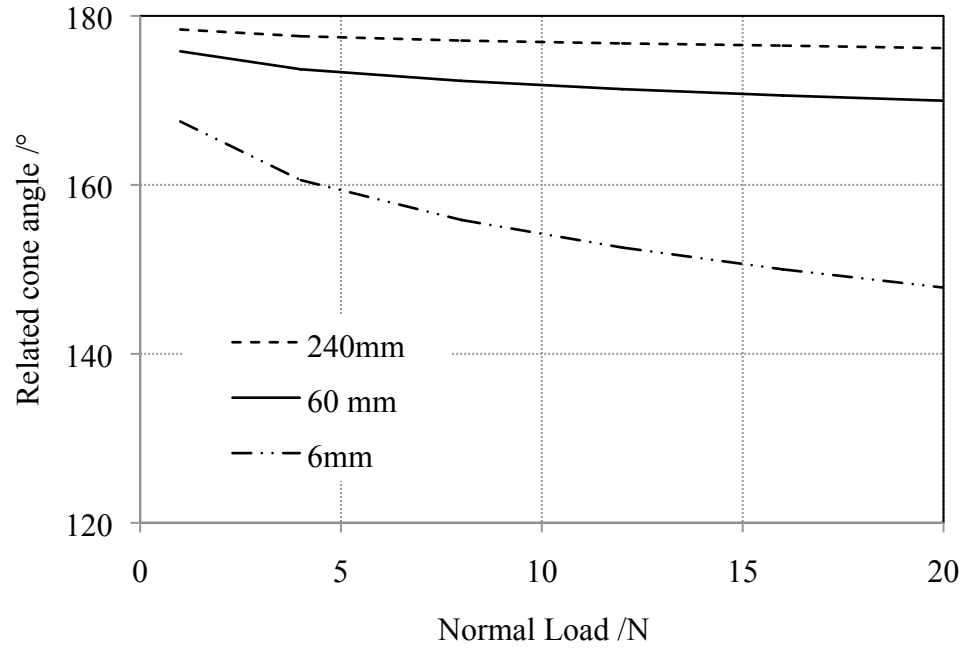
Figure 7.15: Converted indentation depth and contact radii for hemispheres as shown in Figure 7.21 for hemispheres from *R*=6mm, 60mm and 240mm.

In order to qualitatively express the findings made for both indenter profiles, this assumption may be allowed for, so that the results from Figure 7.10 and Figure 7.13 can be redrawn into Figure 7.16. The coefficients of friction for cones are given at a range of normal loads from 4N to 16N and the specific cone angle. The converted data for the hemispheres are given for all three hemisphere radii (*R*=6mm, 60mm, 240mm) in relation to the coefficient of friction.

From Figure 7.23 it becomes apparent that the coefficient of friction over the tested range of geometries shows maximum friction at both extremes, on the one side for very sharp (10°) and on the other side for blunt (180°) indenter profiles. The decrease of the coefficient of friction towards the middle of the graph represents the transition point, at which the deformation of the rubber bulk becomes less apparent and the area of contact increases the adhesional contribution to the total frictional force as the cones become flatter in geometry.
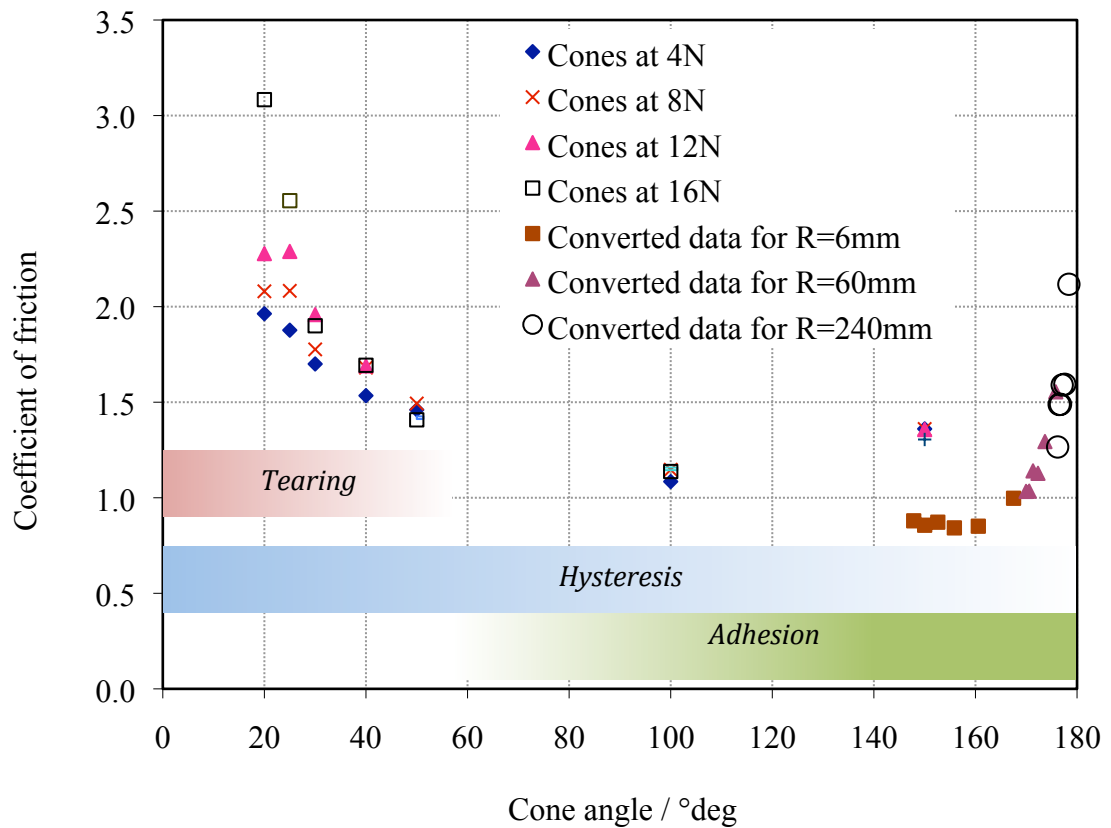
Figure 7.16: The results presented in Figure 7.10 for cones and Figure 7.13 for hemispheres are redrawn as the coefficient of friction versus cone angle. The hemispheres are assumed to represent abraded cones and can be, therefore, expressed as an angular geometry as well.

It is supposed that the frictional force output of very sharp asperities up to an angle of 30° is mostly dominated by large bulk rubber deformations with a combination of high-energy dissipation due to tearing. Up to an angle of 50°, the contribution from fracture energy dissipation decreases and is negligible for cones bigger than 50°. Similar values for the critical angle of a cone in terms of tearing behaviour have been presented in literature (Schallamach 1969). With increasing cone angle, the contribution from hysteresis energy dissipation decreases as the indentation depth also decreases and around an angle of 100°, the area of contact (adhesion) becomes the dominant contribution to the total frictional force. By assuming the spheres to be blunt or flat cones it is shown that all friction values for the hemispheres correlate into a master curve, which increases with increasing angle, as the contact area increases. As shown in Figure 7.15 larger hemispheres represent a flat surface more satisfactorily than small hemispheres, as an almost load independence is exhibited, so that the data presented in Figure 7.16 for the hemisphere of *R*=6mm might be reasonable to be excluded from the

interpretation of the presented data. From this analysis it is shown that if the high friction values at the extremes of 10° and 180° are considered, both sharp and blunt asperities exhibit a high coefficient of friction.

Effect of lubrication

For demonstration purposes the effect of soap lubrication, which lead to zero friction in Section 4.3.3, can be illustrated by using conical sliders. The cone geometry results in a higher hysteresis loss when compared to similar size hemispheres as a larger volume of rubber is deformed due to larger penetration of sharp cones into the rubber. Figure 7.17 shows the sliding friction results for a 60° and 120° cone on a SBR rubber block under dry and lubricated (soap water solution) conditions.
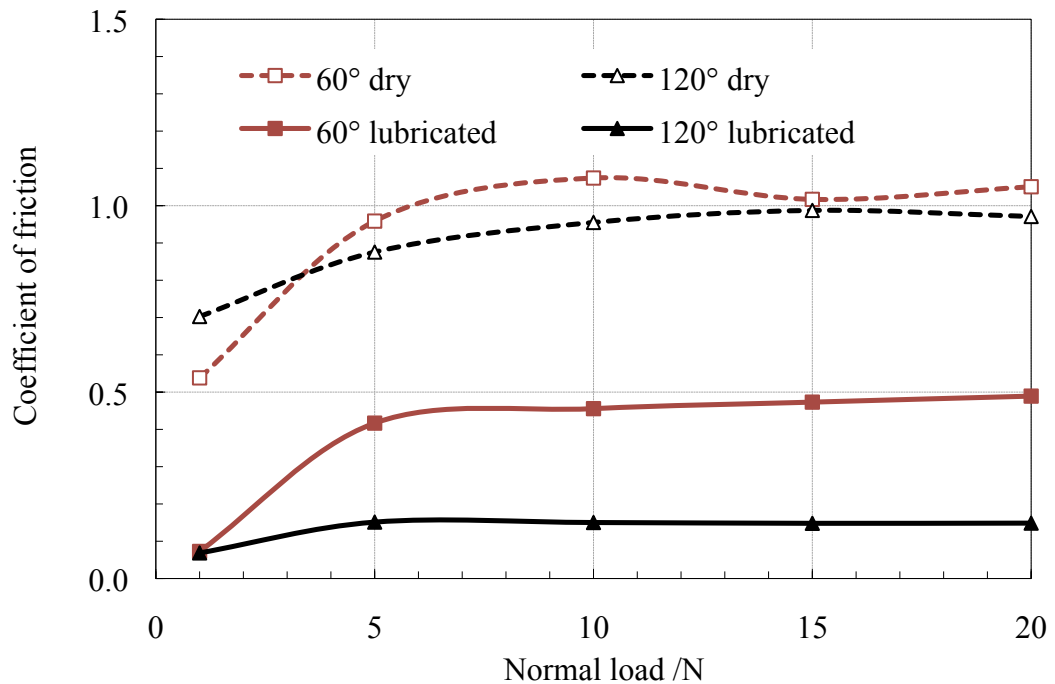
Figure 7.17: Lubrication reduces the coefficient of friction significantly for different cones of an angle of 60° and 120° on SBR-0 at a sliding velocity of 1mm/s.

It is interesting to note that the frictional behaviour shown in Figure 7.17 under dry conditions is similar for both cones, however, the lubricated contact shows a much greater reduction in friction for the 120° cone than for the 60° conical slider. This contrasting behaviour is a good example, for wet and dry breaking on different road surfaces with different asperity sharpness. While the sharp 60° cone deforms the rubber

extensively, the flatter 120° cone has a higher contact area and therefore loses contact more easily while deforming the rubber less.

7.4   *Conclusions*

Self-compounded NR and SBR rubber samples have been prepared with different surface finishes and analysed in terms of their frictional behaviour. The sliding velocity dependence was investigated for both, microscopically rough and smooth surfaces, and the conflict between the findings of Grosch (1963) and Barquins and Roberts (1986) was explained in terms of the rubber surface finish. It was shown that the surface topography is of paramount importance at a frictional interface and that subtle changes might result in large deviations from the expected frictional behaviour.

In addition, different macroscopic indenter geometries have been investigated under several normal loads. The resulting frictional force for a variety of conical indenters when sliding over a microscopically rough rubber surface was analysed and compared to hemispheres, which were assumed to represent almost flat indenter profiles. From this analysis a transition of the different influences (adhesion, hysteresis, wear and lubrication) affecting the total frictional force were examined. It was shown that the friction of sharp profiles is mostly dominated by hysteresis and fracture energy dissipation, while blunt surfaces or hemispherical surfaces are dominated by adhesional influences, and hence the real area of contact. A theoretical supposition was made to directly compare both, hemispherical and conical, slider geometries and it was shown that both sharp and blunt indenter profiles can exhibit very large coefficients of friction.

8   Conclusions and future work

The work presented in this study investigates the friction experienced by a soft rubber sliding against a rigid substrate on different length scales of interest, highlighting the differences between both macroscopically and microscopically rough and smooth interface geometries. Unlike most other solid materials, elastomers exhibit distinct, rate dependent frictional behaviour due to its viscoelastic nature, which is affected by different parameters such as surface topography, interface geometry, temperature or sliding velocity. In this work, several investigations have been undertaken, both experimentally and computationally in order to examine mechanisms in rubber friction, which are still under debate and not fully understood.

In the case of a dry friction interface without wear, the total friction is commonly described to result from both, adhesion and hysteresis contributions. While adhesion is an intermolecular process, whose contribution increases with increasing surface smoothness, the frictional contribution of hysteresis results from energy dissipation in the bulk rubber due to deformation, for example by surface asperities on a rough, solid substrate. In addition, it was proposed by Schallamach (1969) that a macroscopically wrapping of the rubber around a rigid slider, similar to a rope wrapping around a capstan, might also contribute to the total frictional force. Nevertheless, no experiments had been carried out to confirm this and this study remained only theoretical and based on two-dimensional considerations, because in 1969 no suitable techniques existed yet to analyse the stresses at the interface. This problem was investigated in this work by the deliberate alteration of the influences of adhesion and hysteresis so that a possible geometrical influence could be examined. It was shown experimentally and confirmed using a three-dimensional FEA approach for the first time that an additional, entirely geometrical factor also exists. This contribution considerably increases the measured resulting coefficient of friction and is anticipated to make a significant contribution to many every-day frictional sliding applications.

Future investigations might wish to apply this approach to a multi-asperity level that would be typical for a road surface for example. A first approach could investigate the geometric influence of a finite number of (similar) hemispheres, both in experiments and in the FEA, while further investigations might wish to alter the radii of hemispheres to apply the findings to a more typical surface with a roughness at several different length scales.

In rubber friction different rate dependent sliding mechanisms exist, providing relative displacement at the friction interface. This displacement mechanism is influenced by the microscopically surface topography of the friction interface. For a microscopically rough interface at very low sliding velocities a constant, smooth peeling and unpeeling process of the rubber surface provides relative displacement, which changes to stick-slip motion when the sliding velocity increases due to the viscoelastic nature of the rubber. However, in the special case of an microscopically smooth rubber sliding against an optical smooth rigid surface, instabilities on the rubber surface, known as Schallamach waves (Roberts 1988), provide for a relative displacement between the two surfaces over a broad range of sliding velocities. Despite broad experimental investigations on Schallamach waves, virtually no information on the modelling of these surface instabilities using FEA techniques is available in literature. A reason for this is that modelling of contact at an interface, subject to a large deformation, where high friction is present, is extremely challenging for the FEA software. To validate the approach for modelling a buckling phenomenon and prior to the investigation of Schallamach waves, a general surface buckling under compression was examined experimentally and modelled. A comparison with the instability theories of Biot (1965) and Gent and Cho (1999) confirmed the validity of the used FEA approach. By using a purely elastic explicit dynamics FEA approach, the build up and successive propagation of a buckling instability, similar in its nature to a Schallamach wave, was shown successfully for the first time. It was confirmed that for this model the wave of detachment provides the only relative displacement between the slider and the rubber. The progression velocity for the wave in the model was comparable to the shear wave velocity, which is much faster than is observed in experimental investigations.

In order to simplify the FEA model the interfacial energies were not introduced into the model as a first modelling approach. However, in future the introduction of a surface

energy term at the interface might provide a more realistic prediction of the wave progression velocity, as it was shown in the past that this is directly related to wave progression and the dissipated energy at the interface. It is suggested that to determine experimentally this surface energy, a test series on the rate dependence of the peel energy, using a similar interface geometry used to investigate Schallamach waves, should be considered.

In addition to the FEA calculations on Schallamach waves, an experimental investigation examined the relationship of Schallamach waves and stick-slip motion. Wu-Bavouzet et al. (2007) suggested that a transition zone exists, where Schallamach waves transform into stick-slip motion. This transition zone was further investigated in terms of the wave frequency and the wave progression velocity and two transitions, firstly, from smooth sliding to the formation of Schallamach waves and, secondly, from Schallamach waves into (heavy) stick-slip motion was described. Commonly it is reported that Schallamach waves are only present on optically smooth surfaces, however, this work emphasised that Schallamach waves also occur on rough surfaces, where slip waves have now been observed. These are similar in their nature to Schallamach waves, but travel about ten times faster, as friction on rough surfaces is less affected by the damping effects of adhesion. A detailed analysis of high-speed videos at 1000 frames per second, attached to this work, made an observation of these rough surface waves possible. Furthermore, an unresolved phenomenon was investigated, which was firstly mentioned by Barquins and Courtel (1975), in which a single Schallamach wave over the length of contact was shown to travel with a constant velocity up to a certain point after which the progression velocity of the wave increased significantly. It was shown in this work by experimental observations and with the aid of FEA that the compressive stress field governs the initial slow propagation of the wave, while the increase of progression velocity is dominated by the tensile stresses at the rear of the contact zone.

Future work on Schallamach waves might want to investigate the surface roughness dependence further in order to specify the relationship between Schallamach waves and stick-slip motion. For this investigation it might be interesting to investigate surfaces with different roughness values, while the surface might be chemically altered in order to maintain high friction. By this analysis the common belief that Schallamach waves

only occur on smooth surfaces could be further challenged, as usually only smooth surfaces can generate a friction force high enough at the interface to build up surface instabilities.

The sliding velocity dependence of rubber friction was investigated for different unfilled and filled NR and SBR model materials. Both rough and smooth surfaces were moulded onto the rubber in order to re-examine the conflict between the findings of Grosch (1963) and Barquins and Roberts (1986). From the findings in this work, it was confirmed that the surface topography is of paramount importance in determining the frictional force output and that by altering the surface topography conflicting findings can be described. In addition the applicability of the WLF time-temperature superposition was proven to work for the compounded model materials. Investigations on the influence of different macroscopic indenter geometries with both conical and hemispherical shape showed that the different components of the total friction force (adhesion, hysteresis and wear) correlate clearly to the geometry of a slider. While the friction of sharp profiles is mostly dominated by hysteresis and fracture energy dissipation, blunt surfaces or hemispherical surfaces are dominated by an adhesional term. This investigation on asperities from sharp to blunt showed that both types of profile can exhibit high friction.

To develop this investigation further in the future, modified cones with hemispherical tips might gain a further insight into the geometrical influences of both hemispheres and cones on rubber friction. It might be fruitful to examine these abraded cones further using FEA, as for cones with rounded tips less complications in the FEA arise than for sharp tips, where mesh penetration of the cone tip leads to large distortions in the mesh and a divergence in the solution.

The work presented investigated rubber friction in terms of macro and microasperities and its influence on the sliding mechanisms encountered through these differences in surface topographies. It was shown that the parameter of surface topography is of paramount importance of a frictional interface and alters the friction significantly as well as having a great impact on the displacement mechanisms at the interface such as Schallamach waves. However, it is interesting to consider also a geometry of in which shape and surface topography are both fixed and assumed to be constant in order to

investigate the ratio of adhesion to hysteresis impact on the total frictional force resulting from different translation mechanisms such as rolling, sliding or torsion. A preliminary study is described next and this is considered to be of interest for future work on rubber friction.

It is known that the dynamic contact between a rigid cylinder and a rubber surface can be dominated by different contributions from the adhesion and the deformation of the rubber and a relationship between these. To investigate this, three different modes, namely rolling, torsion and sliding are thought to be likely to each contribute to the total friction in a different way. Rolling is defined when a cylinder roles over the surface, which is believed to have a dominating hysteresis contribution term (Tabor 1960). The second is defined as torsion, where a cylinder is rotated in a fixed position relative to the fixed rubber surface, where the rubber after an initial deformation does not change its geometry and hence the adhesion term is the dominant contribution (Roberts and Thomas 1975). The third situation requires a locked cylinder to be slid without torsion or rolling over a rubber surface. In this case there is a contribution from both, adhesion and hysteresis. A separate examination of each setup helps to understand in how far the energy dissipation processes in friction, adhesion and hysteresis, are interacting and how the different states of frictional displacement, rolling, torsion and sliding are related. An initial equation to relate the forces is considered and is evaluated as:

$$F_{SLIDING} = F_{ROLLING} + F_{TORSION}. \tag{8.1}$$

Three different test setups are required and are shown schematically in Figure 8.1. All setups use geometrically identical contact situations of constant micro and macroscopic asperity sizes, where a rubber block contacts a steel cylinder (the outer race of a ball bearing, $R=7.5mm$) under a given normal load ranging from 1N to 10N. The resulting frictional forces $F_{ROLLING}$ and $F_{SLIDING}$, derived in Figure 8.1 a) and b), were both measured using the experimental setup shown in Figure 8.1 b). By displacing a rubber block relative to the rigid roller, which freely rotates for setup in Figure 8.1 a) and is fixed (highlighted in blue) for setup b) the arising frictional force can be measured. For the investigation on the torsional force $F_{TORSION}$, shown in c), a different experimental setup was designed, which is shown in Figure 8.2 a). Here a stiff string, connecting the axis of the cylinder to a screw-driven tensile test machine, rotates the cylinder, whilst the rubber remains in a constrained stationary position (highlighted in blue in Figure 8.1

c)). The force required to pull the string at a constant velocity is measured using the load cell of the screw-driven test machine. The sliding velocity at the point of contact of each system was kept constant at 10mm/s.
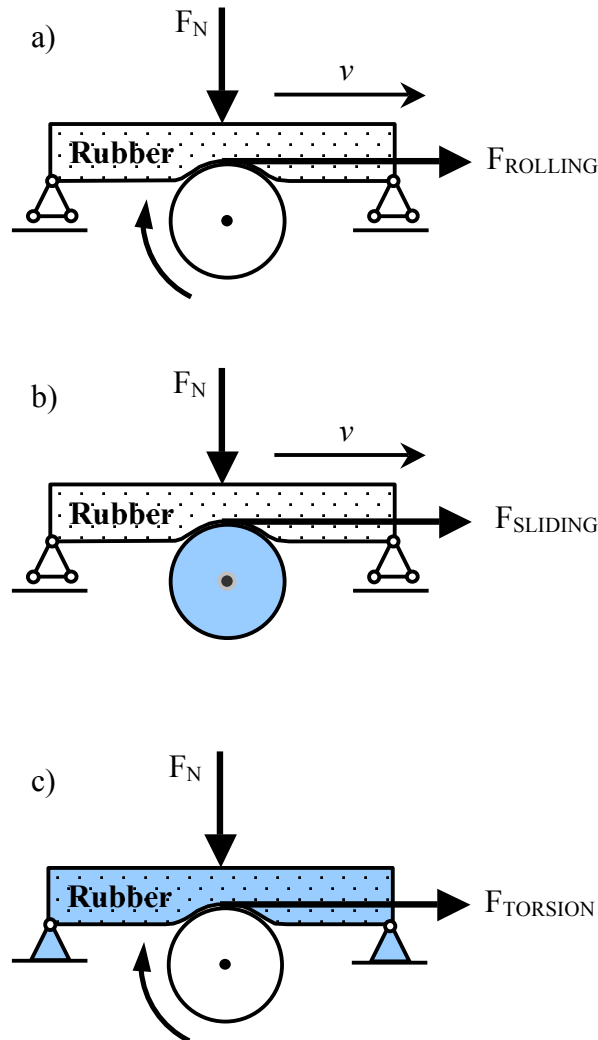
Figure 8.1: The constrained parts in the setups for rolling, sliding and torsion are highlighted in blue. a) Setup to investigate rolling: Cylinder rotates due to the relative displacement of the rubber block with velocity *v*, while in position b) sliding is measured as the cylinder is fixed and the rubber is displaced relative to the cylinder. Setup c) is used to investigate torsional forces, where a screw driven cylinder rotates on a fixed rubber block.
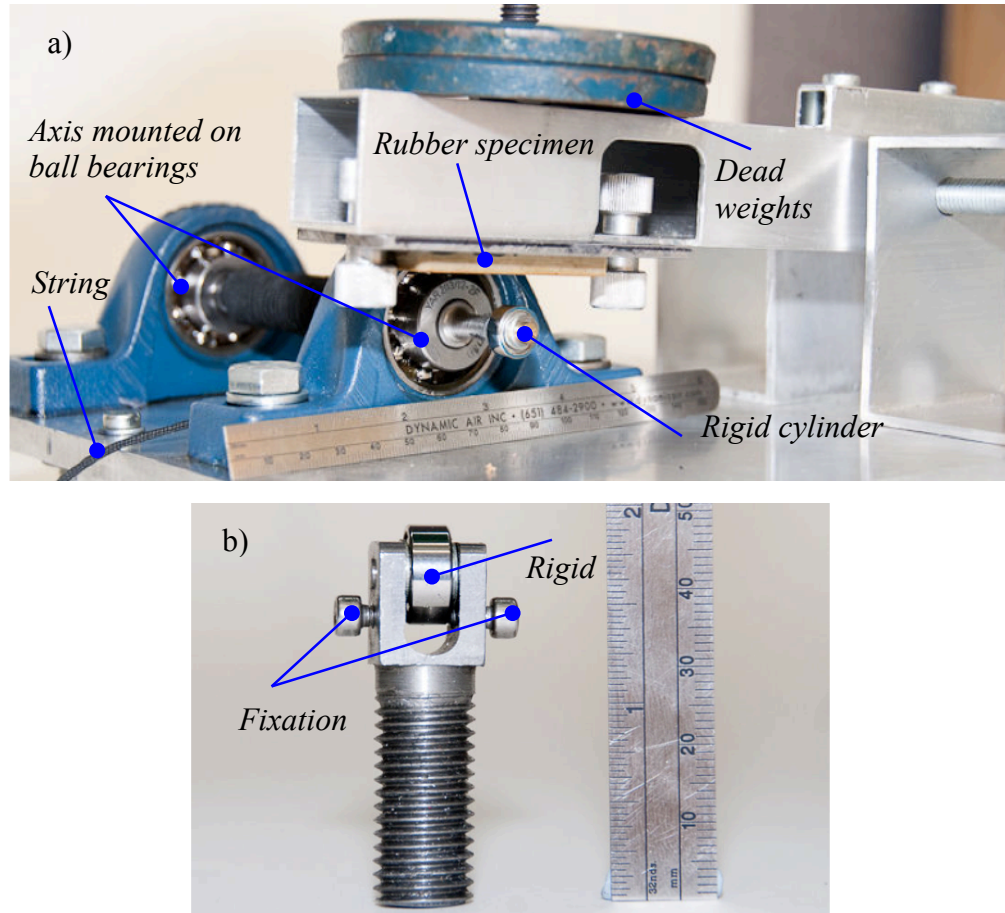
Figure 8.2: a) Setup to investigate torsion between a rubber and a rigid cylinder loaded by dead weights. b) Setup to investigate both rolling and sliding using either Plint or QMUL friction tester. The freely rotating cylinder can be fixed via a stud screw.

As the rolling friction is usually experienced to be very low a higher loss 3, 4-polyisoprene rubber (IR), with a T_g of -8°C was used. The frictional forces in the three measured states of friction rolling, sliding and torsion are shown in Figure 8.3. As expected the frictional sliding force $F_{SLIDING}$ is greater than the values for $F_{TORSION}$ and $F_{ROLLING}$, as both, adhesion and hysteresis contribute during sliding. However, the assumption made in Equation (8.1) that a simple summation of $F_{TORSION}$ and $F_{ROLLING}$ would express $F_{SLIDING}$ can not be met satisfactorily. Reasons for this could be the different amounts of deformation of rubber between sliding and torsion. Furthermore, as the rubber block conforms to the cylindrical indenter, wrapping of the rubber around the rigid slider contributes to sliding, as confirmed in Chapter 4, whereas no wrapping occurs for the rolling contact.
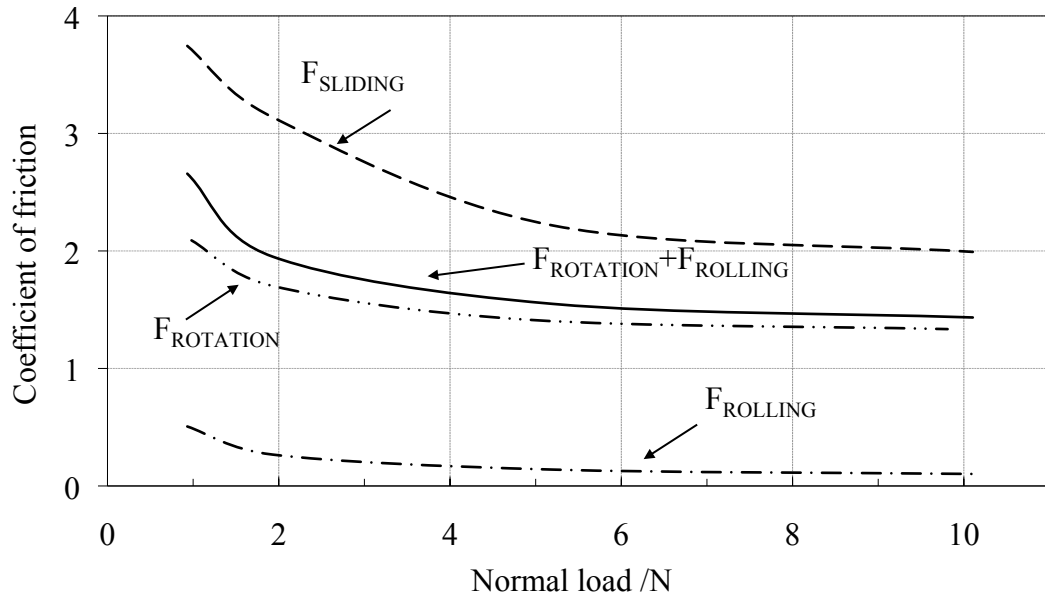
Figure 8.3. Three different states of rolling measured on IR rubber. The sum of frictional forces from torsion and rolling is shown as well, but is insufficient to explain the sliding force output.

From the results shown in Figure 8.3, it is acknowledged that more investigations need to be conducted on the given problem and this is suggested next.

Tabor (1960) found that in his experiments, steel spheres had an almost identical friction coefficient when either rolling on dry rubber or sliding on lubricated rubber. This finding shows that most of the rolling friction in his setup was due to the deformation of the bulk rubber, however, for very smooth surfaces the surface energy might have a significant influence, due to the peeling and unpeeling of the rolling contact, as it was shown by Roberts and Thomas (1975) on rolling experiments. Therefore, for the present investigation it is thought reasonable to further subdivide the given relationship of rolling, torsion and sliding into contributions for each from hysteresis, adhesion and geometric effects, by designing suitable test conditions. The use of a suitable lubricant could help to investigate the individual hysteresis influence by decreasing the adhesion on each of the three systems. In contrast, experiments carried out at an almost static sliding velocity might decrease the influence on hysteresis, as discussed in Chapter 4.

Preliminary tests on IR, which were not considered so far in the presented work, as they could only be tested for the rolling but not the torsion setup, investigated the possibility to increase rolling resistance by a decrease in test temperature. The T_g of the IR used is

around -8°C, which is significantly higher than conventional rubbers like NR or SBR with a T_g of -70°C or -55°C, respectively (Gent 2001). The peak of the loss modulus measured via DMA testing for the employed IR rubber is at -3°C. Therefore, a decrease in test temperature increases the energy lost due to deformation significantly in comparison to the energy dissipated at room temperature. The test temperature for the Plint friction tester can be decreased by using a Peltier device. The problems of ice and moisture built up on the rubber surface, as were described in Section 3.7.3, were avoided, as the temperature at the interface was only decreased by 10°C, so that the rolling force was tested at a room temperature of 22°C and a decreased temperature of 12°C. Figure 8.4 shows that this decrease of 10°C significantly increases the exhibited rolling force. It is shown that the loss modulus at 22°C has a value of 2.67MPa, while the loss modulus at 12°C is 15MPa.
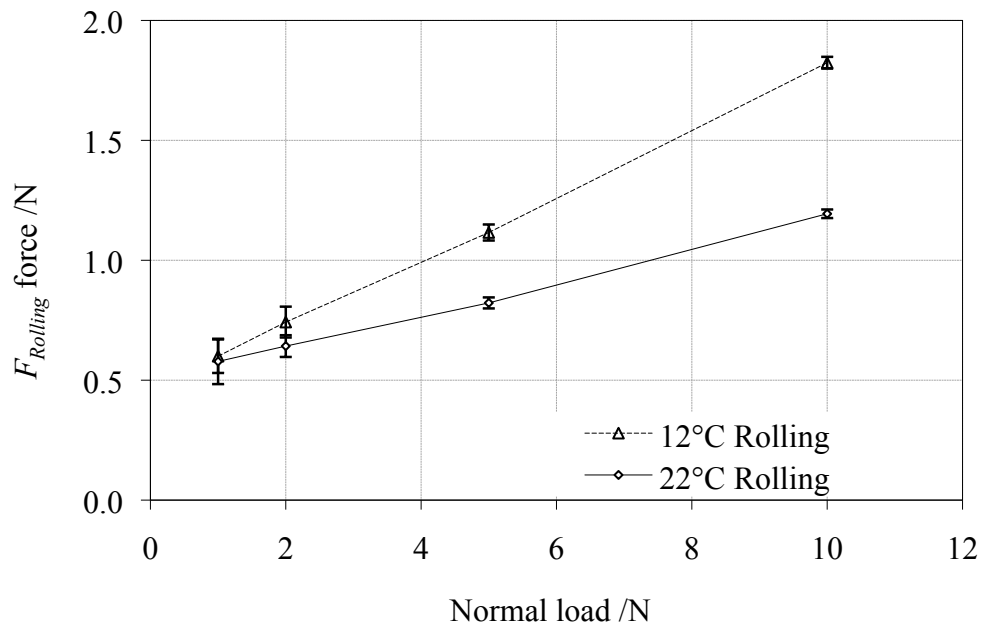
Figure 8.4: The temperature dependence of the resulting rolling force versus normal is shown.

From this test it is shown that decreasing the test temperature can increase the rolling force. However, the design of the torsion setup does not allow for friction testing other than at the ambient temperature. For this reason the examination on the effect of temperature could not be further pursued, however, a redesign of the torsion setup would allow for a more detailed investigation in the future. By this the application of a WLF time-temperature superposition becomes possible and would give further insight

as the analysis and comparison of each of the three resulting mastercurves for rolling, torsion and sliding would help to further understand the problem.

Summarising the outcome of this ongoing investigation on the contributions of adhesion and hysteresis to a frictional interface of fixed geometry and fixed surface topography the assumption that a simple summation of the frictional rolling and torsional forces can express the frictional sliding force is shown to be not entirely valid. However, tests using different ambient temperatures have yet shown again the dependence of (sliding and) rolling friction on viscoelastic properties, so that a more detailed analysis of the temperature and rate dependence might give better insights in future.

9   Appendix

9.1   List of Publications

Influence of interface geometry on rubber friction

P. Gabriel, A.G. Thomas, J.J.C. Busfield *

Department of Materials, Queen Mary, University of London, Mile End Road, London E1 4NS, UK

ARTICLE INFO

ABSTRACT

While the mechanics of rubber friction are still debated, it is widely accepted that there are two principal factors, adhesion and hysteresis, commonly considered to give rise to a frictional force during the sliding of a rigid surface on a flexible elastomer. The experiments described here, validated by finite element analysis (FEA), confirm an additional (third) geometric factor, which had been observed previously by Schallamach (1969) [14] and by Liang et al. (2009) [12], but which has not been fully investigated. Under certain conditions, it can increase the frictional force significantly above that expected from a consideration of the interfacial coefficient of friction alone. This contribution increases with the depth of penetration of the rigid surface into the elastomer and is therefore perhaps comparable to the frictional behaviour found when wrapping a rope around a capstan (Shames, 1980 [23]). This term is thought likely to make a significant contribution to most frictional sliding applications such as tyres on a road surface.

© 2009 Elsevier B.V. All rights reserved.

1. Introduction

Various friction theories have been developed on the different components of rubber friction [1–4]. Frequently, assuming a dry, smooth contact with reasonably low shear forces, the total frictional force (F_{TOTAL}) during sliding at an elastomer/rigid interface is considered to arise from the combination of two forces [5]:

$$F_{TOTAL} = F_{ADHESION} + F_{HYSTERESIS} \tag{1}$$

The adhesion term ($F_{ADHESION}$) is a surface effect resulting from the intermolecular interaction between two surfaces [6] and the hysteresis term ($F_{HYSTERESIS}$), sometimes referred to as the deformation contribution, results from the energy lost through the bulk deformation process of a certain volume of rubber [7]. It is worth emphasizing that both factors are not independent as shown by Schallamach [8] and Roberts [4]. Suitable modification, for example by lubricating the interface, can alter either of the two terms and can therefore change their ratio significantly. Fuller and Tabor [9] and Persson [10] have all stated that $F_{ADHESION}$ is negligible in a tyre/road contact, and the major contribution to friction is from the hysteresis term alone. However, in very smooth contact situations it is shown that adhesion has the main influence on rubber friction [6]. The question arises: is it possible to describe the complexity of rubber friction by just a single term? If not, then how might additional factors, such as an entirely geometric contribution to the frictional sliding force, contribute to the mechanics of rubber friction?

---

* Corresponding author. Tel.: +44 20 7882 8866.
  E-mail address: j.busfield@qmul.ac.uk (J.J.C. Busfield).

When a rigid hemisphere slides on top of a flat, elastic material, large (tensile) stresses are observed at the rear of the slider, whereas compressive stresses are built up in front [11]. The stresses can build up until failure, resulting in fracture/wear [12]. Huffington [13] and Roberts [4] showed that the frictional tangential stresses can be resolved into horizontal and vertical directions. Schallamach [14] refined these findings by investigating the frictional forces acting on the system and by measuring the uplift experienced by the slider. While Schallamach [14] referred to the capstan effect [23] in order to explain the general phenomena, no corroborating evidence for the effect has ever been presented. This paper, by using FEA to validate experiments, confirms how far the additional geometric wrapping might influence frictional force output for the first time.

2. Experimental background

Two basic configurations are required to investigate this geometric effect; one configuration in which a wrapping of rubber around an asperity is developed, and one in which a hemisphere is deformed into a flat configuration and no wrapping is possible. Both setups used throughout this work (both experimentally and in the FEA models), are shown in Figs. 1 and 2 respectively. Fig. 1 shows a rigid spherical slider indenting into and sliding along a rubber block where the rubber wraps around the indenter. This contrasts with Fig. 2 where a rubber sphere is deformed to conform to the flat shape of the rigid contact surface without wrapping. The first case can be considered similar to the behaviour of a smooth rubber tyre surface sliding over an individual asperity in a road surface. Throughout this work the test geometries shown in Figs. 1 and 2 will be denoted as configuration 1 and 2 respectively.

Publication in Wear (Gabriel et al. 2010a).

Mechanics of frictional sliding

at the elastomer/rigid surface interface

FEA investigation of rubber friction has identified a geometric factor that can increase frictional force above that expected from the interfacial friction coefficient

by P. Gabriel, A.G. Thomas and J.J.C. Busfield, department of materials, Queen Mary, University of London, UK

Understanding the general mechanics of rubber friction is of significant interest when trying to understand the interaction between a tire and the road. Extensive earlier work (Grosch 2007) shows that rubber friction is affected by many different parameters, which often interact with each other. These parameters include temperature and sliding velocity (Grosch 1963), normal load (Schallamach 1952), surface finish (Persson 1999), the elastic and viscoelastic properties of the elastomer (Ferry 1961; Grosch 1963), abrasion behavior (Liang *et al* 2008), and the contact area (Johnson *et al* 1971). Frequently total frictional force (F_{TOTAL}) during sliding at an elastomer/rigid interface is considered the summation of four forces, as in Equation 1:

$$F_{TOTAL} = F_{ADHESION} + F_{HYSTERESIS} + F_{VISCOUS} + F_{COHESION}$$

The adhesion force ($F_{ADHESION}$) represents the intermolecular process taking place on the surface of the rubber due to the surface energy interaction (Roberts and Thomas 1975). The hysteresis force ($F_{HYSTERESIS}$) represents the forces resulting from the viscoelastic irreversible energy dissipation of the rubber due to the deformation of the rubber. On rough surfaces, or in the presence of a lubricant, the hysteresis is assumed to make the greatest contribution to the rubber friction force and the influence of adhesion decreases.

By considering the viscous shear of the fluid between rubber and an opposing surface, an additional factor $F_{VISCOUS}$ contributes to a reduction in the friction force. In an extreme case, the rubber completely loses contact with the surface due to aquaplaning, and the frictional force is given by $F_{VISCOUS}$ alone. In the case of abrasion or wear of the rubber surface, a fourth cohesive factor ($F_{COHESION}$) is defined, due to the additional energy needed to abrade the rubber (Southern and Thomas 1978; Fukahori and Yamazaki 1995). Assuming a dry contact with reasonably low shear forces, the contributing processes to rubber friction can be considered to be $F_{ADHESION}$ and $F_{HYSTERESIS}$ alone. According to Persson (2001), the $F_{ADHESION}$ is negligible in a tire/road contact, and the contribution from hysteresis is the only term. So is it possible to describe the complexity of rubber friction by $F_{HYSTERESIS}$ alone? If not, how might additional factors, such as an entirely geometrical contribution to the frictional sliding force, contribute to the mechanics of rubber friction?

Different test setups are shown in Figures 1 and 2. Figure 1 shows a rigid slider indenting and sliding over a rubber block where the rubber wraps around the indentor. The depth of indentation and the diameter of the rigid slider are marked with 'd' and 'D', respectively. This contrasts with Figure 2, where a rubber sphere slides over a smooth rigid surface and the rubber sphere is deformed to conform to the flat shape of the rigid contact surface. The first case can be considered similar to the behavior of a smooth rubber tire surface sliding over an individual asperity in the road surface.

A finite element analysis (FEA) process is used to investigate the interactions at the elastomer/rigid surface interface. In this friction model, a slider, representing a single-surface asperity, slides over a flat rubber block. The expected behavior is shown experimentally in Figures 3 to 5. In Figure 3, a hemispherical slider comes into contact with a soft rubber surface. In Figure 4 the slider is loaded vertically with a normal load 'N', which results in the indentor penetrating into the rubber, producing a symmetrical stress field around the contact area. This pattern is highlighted by the reflection of the grid in the background in the mirror-like rubber surface. When the slider moves over the rubber surface, the stress field becomes
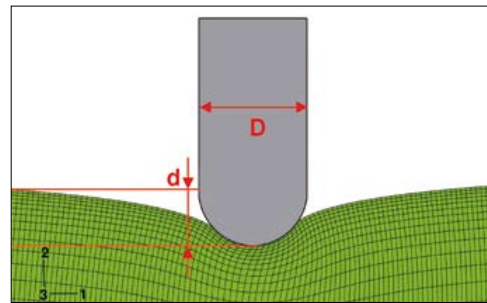
Figure 1: Experimental model of a semicircular wedge indenting into a rubber sheet
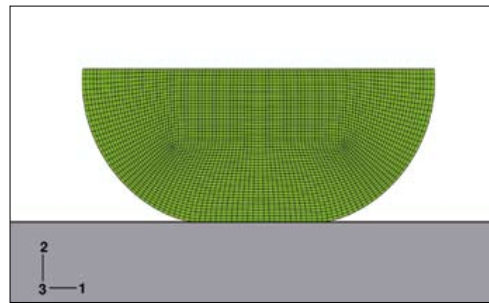
Figure 2: Experimental model of a rubber sphere indenting into a flat rigid surface

Published review of paper presented at Tire Technology International 2008, Cologne.

The mechanics of sliding friction between a rigid indenter and a rubber surface

P. Gabriel, Y. Fukahori, A.G. Thomas & J.J.C. Busfield*

Department of Materials, Queen Mary University of London, Mile End Road, LONDON, E1 4NS, UK

* Corresponding author: E-mail: j.busfield@qmul.ac.uk, Tel: +44 (0)20 7882 8866

ABSTRACT: The frictional behaviour of rubber is explored in this paper. Two principal factors, adhesion and hysteresis, are commonly considered to make the greatest contribution to rubber friction. Gabriel et al. (submitted) also highlighted the contribution from an additional geometric factor. The geometrical influence for a range of different indenters on rubber friction is investigated further here using finite element analysis. The frictional force resulting from the dynamic contact between a rigid cylinder and rubber can be considered in several ways: the first defined as rolling where the cylinder roles over the surface, which is believed to have a significant hysteresis term; the second where a cylinder is rotated in a fixed position relative to the sheet, where the geometry does not change and hence the adhesion term would be the dominant contribution. The third situation requires a locked cylinder to be dragged without rotation over a rubber surface. In this case there will be a contribution from adhesion and hysteresis. The detailed relationship between these terms is explored here for a rubber with a high glass transition temperature and hence large viscoelasticity at room temperature.

1 INTRODUCTION

Different contributions to rubber friction are investigated in this paper. The main sources for the frictional force arise when an elastomer is slid over a rigid surface are described as a combination of both an adhesional and a hysteresis term. The adhesional term is a surface effect resulting from the intermolecular interaction between two surfaces (Roberts & Thomas 1975). The hysteresis term, also sometimes known as the deformation contribution, results from the energy lost through the deformation process of a certain volume of rubber (Roberts 1992). Gabriel et al. (submitted) showed the geometry of the contacting surfaces can also make an additional contribution. Two cases were compared, in which a rubber was in sliding contact with a flat or hemispherical shaped surface. In the former case, the rubber stays in plane contact, whereas in the latter, the rubber conforms to the hemisphere, resulting in an increase in the frictional force. As shown in Figure 1 the contact area between a tyre and a road surface is governed by the geometry of the individual surface asperities. The arising frictional force is, therefore, influenced by the typical average shape and sharpness of individual asperities.
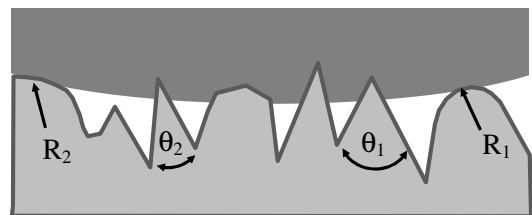
Figure 1. Schematic drawing of tyre and road contact. The different angles, θ, and radii, R, show the different idealised asperities.

Extending the investigations on geometric effects, the influence of different interface geometries (conical and hemispherical) on the resulting frictional force is investigated to examine how both very smooth, as well as extremely rough surfaces can have a high coefficient of friction. In addition, three different frictional contact situations have been monitored experimentally: The first case uses a cylinder that rolls over a flat rubber surface where the frictional force results predominantly from the hysteresis contribution alone (Moore & Geyer 1972). The second case arises when a cylinder rotates in a fixed position, so there is no change in the deformed

FEA MODELLING OF SCHALLAMACH WAVES

P. Gabriel, Y. Fukahori, A.G. Thomas & J.J.C. Busfield*
Department of Materials, Queen Mary University of London
Mile End Road, LONDON, E1 4NS, UK

* Corresponding author:
E-mail: j.busfield@qmul.ac.uk
Tel: +44 (0)20 7882 8866

ABSTRACT

The work described here uses an explicit dynamics finite element analysis (FEA) approach to model both the initiation and progression of waves of detachment for the first time. The term Schallamach waves is used to describe the 'waves of detachment' that sometimes arise during the frictional sliding of a smooth rubber surface against a smooth rigid surface. Extensive experimental investigations have been made since Schallamach first observed the waves in 1971, however no FEA modelling approach has been undertaken yet. The use of the finite element method allows for the detailed stress and strain analysis at the interface to be examined. The limitations of using a purely elastic solution in plane-strain are explored. To validate the explicit dynamics approach for modelling the Schallamach waves, another biaxial compressive buckling mode has also been modelled.

Keywords: Schallamach waves, waves of detachment, surface instabilities, rubber friction, Modelling.

1

How does rubber truly slide between Schallamach waves and stick-slip motion?

Y. Fukahori*, P. Gabriel and J.J.C. Busfield

Department of Materials, Queen Mary, University of London, Mile End Road, London, E1 4NS, UK

* Corresponding author: E-Mail: yoshi-fukahori@mrj.biglobe.ne.jp

Tel: +81 (0)42 666 0150

ABSTRACT

Schallamach waves have been investigated using new view of their dynamic behaviour. Two new insights were introduced to elucidate the mechanism of the initiation and propagation of the wave of detachment, firstly the surface interaction can produce a meniscus effect at the rubber surface and secondly the stick-slip motion can be seen to have a significant role during the sliding of rubber. The meniscus could perhaps be a source of the initiation of the wave of detachment at the leading edge and might have a role to play in the peeling of the rubber away from the trailing edge of the contact simultaneously. The characteristics in the propagation of the waves such as their frequency, their high progression velocity and the sliding velocity dependence all correlate with the periodic stick-slip motion. True finite sliding was observed to take place during a slip stage in the stick-slip motion whether waves of detachment appear or not on the contact area. Thus, the contribution of the waves to the frictional sliding of rubber is to decrease the contact area before true sliding and allow smoother sliding to occur during rubber friction.

1. INTRODUCTION

The understanding of rubber friction behaviour was significantly advanced in 1971 when the experimental results of Johnson et al. [1] and Schallamach [2] were both published. Johnson et al. [1] showed that the area of contact between a rigid sphere and a flat rubber surface was larger than the value estimated from the Hertzian contact theory. They proposed that the molecular attraction of van-der-Waals forces, acting between the sphere and the rubber surface, lead to an increase in the contact area. Schallamach [2] observed that when a rigid sphere slides on a rubber surface, true sliding (slipping) does not occur. Instead, folds are generated that are known as waves of detachment (and which have subsequently become known as Schallamach waves), which cross the contact zone on the rubber surface from the front to the rear end of the slider.

1

9.2   List of Conference papers

2008   Tire Technology Expo, Cologne, Germany, *The mechanics of frictional sliding at the elastomer / rigid interface*.

2008   174th Rubber Mini Expo, American Chemistry Society, Rubber Division, Lousiville, Kenntucky, USA, *Influence of interface geometry on rubber friction*

2009   Tire Technology Expo, Hamburg, Germany, *Frictional sliding of rubber*

2009   European Conference for Constitutive Models for Rubber VI, Dresden, Germany, Poster, *The mechanics of sliding friction between a rigid indenter and a rubber surface*

9.3   FEA input file used in chapter 4

```
*Heading
** Job name: INPUTFILE FOR WEAR PAPER Model name: 3D Slider 5mm mooney NR-0
** Generated by: Abaqus/CAE Version 6.8-2
*Preprint, echo=NO, model=NO, history=NO, contact=NO
**
** PARTS
**
*Part, name=Rubberblock
*End Part
**
*Part, name=Slider
*End Part
**
**
** ASSEMBLY
**
*Assembly, name=Assembly
**
*Instance, name=Part-2-1, part=Slider
*Node
[...]
*Element, type=R3D4
[...]
*Node
  1365,        0.,        8.,        0.
*Nset, nset=Part-2-1-RefPt_, internal
1365,
*Nset, nset=SliderSetRP
 1365,
*Elset, elset=_SliderSurface_SPOS, internal, generate
   1, 1362,    1
*Surface, type=ELEMENT, name=SliderSurface
_SliderSurface_SPOS, SPOS
*Elset, elset=Part-2-1, generate
   1, 1362,    1
*End Instance
**
*Instance, name=Rubberblock-1, part=Rubberblock
    -1.25,        0.,        -9.5
*Node
[...]
*Element, type=C3D8R
[...]
*Nset, nset="Rubber Surface"
[...]
*Elset, elset="Rubber Surface"
[...]
*Nset, nset=RubberBottom
[...]
*Elset, elset=RubberBottom
[...]
*Nset, nset=RubberSides
[...]
*Elset, elset=RubberSides
[...]
```

```
*Nset, nset=_PickedSet28, internal, generate
    1, 29315,    1
*Elset, elset=_PickedSet28, internal, generate
    1, 25600,    1
*Elset, elset=_RubberSurface_S2, internal
[...]
*Elset, elset=_RubberSurface_S4, internal, generate
 21005, 21750,    5
*Elset, elset=_RubberSurface_S5, internal
[...]
*Surface, type=ELEMENT, name=RubberSurface
_RubberSurface_S2, S2
_RubberSurface_S6, S6
_RubberSurface_S4, S4
_RubberSurface_S5, S5
*Elset, elset=_RubberSurfaceBottom_S4, internal
 [...]
*Elset, elset=_RubberSurfaceBottom_S1, internal
  [...]
*Elset, elset=_RubberSurfaceBottom_S2, internal
 [...]
*Elset, elset=_RubberSurfaceBottom_S6, internal
  [...]
*Surface, type=ELEMENT, name=RubberSurfaceBottom
_RubberSurfaceBottom_S4, S4
_RubberSurfaceBottom_S1, S1
_RubberSurfaceBottom_S2, S2
_RubberSurfaceBottom_S6, S6
*Elset, elset=_RubberSurfaceSides_S4, internal
 [...]
*Elset, elset=_RubberSurfaceSides_S5, internal
 [...]
*Elset, elset=_RubberSurfaceSides_S2, internal
 [...]
*Elset, elset=_RubberSurfaceSides_S6, internal
 [...]
*Surface, type=ELEMENT, name=RubberSurfaceSides
_RubberSurfaceSides_S4, S4
_RubberSurfaceSides_S5, S5
_RubberSurfaceSides_S2, S2
_RubberSurfaceSides_S6, S6
** Section: rubber
*Solid Section, elset=_PickedSet28, material=Rubber
1.,
*End Instance
**
*Nset, nset=side2, instance=Rubberblock-1
 [...]
*Elset, elset=side2, instance=Rubberblock-1
[...]
*Nset, nset=side, instance=Rubberblock-1
[...]
*Elset, elset=side, instance=Rubberblock-1
[...]
*Rigid Body, ref node=Part-2-1.Part-2-1-RefPt_, elset=Part-2-1.Part-2-1
*End Assembly
*Amplitude, name=Amp-1
     0.,      0.,    0.038,    1.9
*Amplitude, name=Amp-2
     0.,      0.,     0.07,     5.
```

```
**
** MATERIALS
**
*Material, name=Rubber
*Density
 1e-09,
*Hyperelastic, mooney-rivlin
 0.0717, 0.0713,    0.
**
** INTERACTION PROPERTIES
**
*Surface Interaction, name=IntProp-1
*Friction
** THE VALUE ENTERED HERE DETERMINES THE FRICTION AT THE INTERFACE
 0.22,
**
**-----------BOUNDARY CONDITIONS---------------------------------
**
** Name: RubberBottom Type: Displacement/Rotation
*Boundary
Rubberblock-1.RubberBottom, 1, 1
Rubberblock-1.RubberBottom, 2, 2
Rubberblock-1.RubberBottom, 3, 3
** Name: RubberSides1 Type: Displacement/Rotation
*Boundary
side, 1, 1
** Name: RubberSides2 Type: Displacement/Rotation
*Boundary
side2, 2, 2
** Name: Slider Type: Displacement/Rotation
*Boundary
Part-2-1.SliderSetRP, 1, 1
Part-2-1.SliderSetRP, 2, 2
Part-2-1.SliderSetRP, 3, 3
Part-2-1.SliderSetRP, 4, 4
Part-2-1.SliderSetRP, 5, 5
Part-2-1.SliderSetRP, 6, 6
**
** ---------- STEP: Step-1INDENTATION STEP-------------------------------------

**
**
*Step, name=Step-1
Indentation
*Dynamic, Explicit
, 0.04
*Bulk Viscosity
0.06, 1.2
**
** BOUNDARY CONDITIONS
**
** Name: Slider Type: Displacement/Rotation
*Boundary, amplitude=Amp-1
Part-2-1.SliderSetRP, 1, 1
Part-2-1.SliderSetRP, 2, 2, -1.
Part-2-1.SliderSetRP, 3, 3
Part-2-1.SliderSetRP, 4, 4
Part-2-1.SliderSetRP, 5, 5
Part-2-1.SliderSetRP, 6, 6
**
```

```
** INTERACTIONS
**
** Interaction: Int-1
*Contact Pair, interaction=IntProp-1, mechanical constraint=KINEMATIC, cpset=Int-1
Part-2-1.SliderSurface, Rubberblock-1.RubberSurface
**
** OUTPUT REQUESTS
**
*Restart, write, number interval=1, time marks=NO
**
** FIELD OUTPUT: F-Output-1
**
*Output, field, variable=PRESELECT
**
** HISTORY OUTPUT: H-Output-1
**
*Output, history
*Node Output, nset=Part-2-1.SliderSetRP
RF1, RF2, U1, U2
*End Step
** ----------------------------------------------------------------
**------------STEP: Step-2 RELATIVE DISPLACEMENT BETWEEN THE TWO BODIES---------
**
*Step, name=Step-2
*Dynamic, Explicit
, 0.07
*Bulk Viscosity
0.06, 1.2
**
** BOUNDARY CONDITIONS
**
** Name: Slider Type: Displacement/Rotation
*Boundary, amplitude=Amp-2
Part-2-1.SliderSetRP, 1, 1, 1.
Part-2-1.SliderSetRP, 2, 2
Part-2-1.SliderSetRP, 3, 3
Part-2-1.SliderSetRP, 4, 4
Part-2-1.SliderSetRP, 5, 5
Part-2-1.SliderSetRP, 6, 6
**
** OUTPUT REQUESTS
**
*Restart, write, number interval=1, time marks=NO
**
** FIELD OUTPUT: F-Output-1
**
*Output, field, variable=PRESELECT
**
** HISTORY OUTPUT: H-Output-1
**
*Output, history
*Node Output, nset=Part-2-1.SliderSetRP
RF1, RF2, U1, U2
*End Step
```

9.4 FEA input file used in chapter 5

```
*Heading
** Job name: Schallamach wave odel name: 20091106mod-07
** Generated by: Abaqus/CAE Version 6.8-2
*Preprint, echo=NO, model=NO, history=NO, contact=NO
**
** PARTS
**
*Part, name=RUBBER-1
*Node
[...]
*Element, type=CPE4R
*Element, type=
[...]
*Nset, nset=_PICKEDSET2, internal, generate
   1,  8151,    1
*Elset, elset=_PICKEDSET2, internal, generate
   1,  7904,    1
*Nset, nset=WHOLE, generate
   1,  8151,    1
*Elset, elset=WHOLE, generate
   1,  7904,    1
*Nset, nset="BOTTOM LINE"
[...]
*Elset, elset="BOTTOM LINE
[...]
*Nset, nset="RUBBER SIDES"
[...]
*Elset, elset="RUBBER SIDES"
[...]
*Elset, elset=CINSET
[...]
*Elset, elset=CINSET2
[...]
*Nset, nset="TOP SURFACE"
[...]
*Elset, elset="TOP SURFACE"
[...]
*Elset, elset="_RUBBER SURFACE_S2", internal, generate
[...]
*Elset, elset="_RUBBER SURFACE_S4", internal, generate
[...]
*Elset, elset="_RUBBER SURFACE_S2", internal, generate
[...]
*Elset, elset="_RUBBER SURFACE_S4", internal, generate
[...]
*Surface, type=ELEMENT, name="RUBBER SURFACE"
[...]
* Region: (Section-1-_PICKEDSET2:Picked)
*Elset, elset=_I1, internal
[...]
** Section: Section-1-_PICKEDSET2
*Solid Section, elset=_I1, material=RUBBER
12.,
** Section: Section-2-CINSET
*Solid Section, elset=CINSET, material=CINELEMENTS
12.,
```

** Section: Section-3-CINSET2
*Solid Section, elset=CINSET2, material=CINELEMENTS
12.,
*End Part
**
*Part, name=SLIDER-1
*Node
[...]
*Element, type=R2D2
[...]
*Nset, nset=SLIDER-1-RefPt_, internal
 93,
*Nset, nset=SLIDER-1-REFPT_, internal
 93,
*Nset, nset=REFPOINTANALYTICALSLIDER
 93,
*Elset, elset=SLIDER-1, generate
  1, 92, 1
*Elset, elset="_SURFACE ANALYTICAL SLIDER_SNEG", internal, generate
  1, 92, 1
*Elset, elset="_SURFACE ANALYTICAL SLIDER_SNEG", internal, generate
  1, 92, 1
*Surface, type=ELEMENT, name="SURFACE ANALYTICAL SLIDER"
"_SURFACE ANALYTICAL SLIDER_SNEG", SNEG
*End Part
**
** ASSEMBLY
**
*Assembly, name=Assembly
**
*Instance, name=RUBBER-1, part=RUBBER-1
*End Instance
**
*Instance, name=SLIDER-1, part=SLIDER-1
*End Instance
**
*Nset, nset=_PICKEDSET101, internal, instance=SLIDER-1
 93,
*Elset, elset=CIN, instance=RUBBER-1
[...]
*Nset, nset=_M7, internal, instance=RUBBER-1
[...]
** Constraint: RigidBody-1
*Rigid Body, ref node=SLIDER-1.SLIDER-1-REFPT_, elset=SLIDER-1.SLIDER-1
*End Assembly
*Amplitude, name=AMP-1
      0.,   0.,   0.0036,   0.181
*Amplitude, name=AMP-2
      0.,   0.,   0.08,   0.8
*Amplitude, name=AMP-3
      0.,   0.,   0.02,   0.2
**
** MATERIALS
**
*Material, name=CINELEMENTS
*Density
 1e-09,
*Elastic
 1.6, 0.495
*Material, name=RUBBER

*Density
 1e-09,
*Hyperelastic, mooney-rivlin, moduli=LONG TERM
 0.17,   0.1, 0.0740741
**
** INTERACTION PROPERTIES
**
*Surface Interaction, name=INTPROP-1
*Friction
4.,
*Contact Damping, definition=CRITICAL DAMPING FRACTION
0.3,
**
** BOUNDARY CONDITIONS
**
** Name: Disp-BC-1 Type: Displacement/Rotation
*Boundary
RUBBER-1."BOTTOM LINE", 1, 1
** Name: Disp-BC-2 Type: Displacement/Rotation
*Boundary
RUBBER-1."BOTTOM LINE", 2, 2
** Name: Disp-BC-3 Type: Displacement/Rotation
*Boundary
RUBBER-1."RUBBER SIDES", 1, 1
** Name: Disp-BC-4 Type: Displacement/Rotation
*Boundary
_PICKEDSET101, 1, 1
** Name: Disp-BC-5 Type: Displacement/Rotation
*Boundary
_PICKEDSET101, 2, 2
** Name: Disp-BC-6 Type: Displacement/Rotation
*Boundary
_PICKEDSET101, 6, 6
** --
** STEP: Step-1
**
*Step, name=Step-1
Indentation of the indentor
*Dynamic, Explicit
, 0.005
*Bulk Viscosity
0.06, 1.2
**
** BOUNDARY CONDITIONS
**
** Name: Disp-BC-1 Type: Displacement/Rotation
*Boundary, op=NEW
** Name: Disp-BC-2 Type: Displacement/Rotation
*Boundary, op=NEW
** Name: Disp-BC-3 Type: Displacement/Rotation
*Boundary, op=NEW
** Name: Disp-BC-4 Type: Displacement/Rotation
*Boundary, op=NEW
** Name: Disp-BC-5 Type: Displacement/Rotation
*Boundary, op=NEW
** Name: Disp-BC-6 Type: Displacement/Rotation
*Boundary, op=NEW
** Name: Disp-BC-7 Type: Displacement/Rotation
*Boundary, op=NEW
RUBBER-1."BOTTOM LINE", 2, 2

** Name: Disp-BC-8 Type: Displacement/Rotation
*Boundary, op=NEW
_M7, 1, 1
** Name: Disp-BC-9 Type: Displacement/Rotation
*Boundary, op=NEW
RUBBER-1."BOTTOM LINE", 1, 1
** Name: Disp-BC-10 Type: Displacement/Rotation
*Boundary, op=NEW, amplitude=AMP-1
_PICKEDSET101, 1, 1
** Name: Disp-BC-11 Type: Displacement/Rotation
*Boundary, op=NEW, amplitude=AMP-1
_PICKEDSET101, 2, 2, -1.
** Name: Disp-BC-12 Type: Displacement/Rotation
*Boundary, op=NEW, amplitude=AMP-1
_PICKEDSET101, 6, 6
**
** INTERACTIONS
**
** Interaction: CONTACT-1-1
*Contact Pair, interaction=INTPROP-1, mechanical constraint=PENALTY, cpset=CONTACT-1-1
RUBBER-1."RUBBER SURFACE", SLIDER-1."SURFACE ANALYTICAL SLIDER"
**
** OUTPUT REQUESTS
**
*Restart, write, number interval=1, time marks=NO
**
** FIELD OUTPUT: F-Output-1
**
*Output, field
*Element Output, directions=YES
ENER, LE, S
**
** FIELD OUTPUT: F-Output-2
**
*Node Output
RF, U
*Element Output, directions=YES
LE,
**
** HISTORY OUTPUT: H-Output-1
**
*Output, history
*Node Output, nset=SLIDER-1.REFPOINTANALYTICALSLIDER
RF1, RF2, U1, U2
*End Step
** --
** STEP: Step-2
**
*Step, name=Step-2
Movement
*Dynamic, Explicit
, 0.08
*Bulk Viscosity
0.06, 1.2
**
** BOUNDARY CONDITIONS
**
** Name: Disp-BC-7 Type: Displacement/Rotation
*Boundary, op=NEW
** Name: Disp-BC-8 Type: Displacement/Rotation

```
*Boundary, op=NEW
** Name: Disp-BC-9 Type: Displacement/Rotation
*Boundary, op=NEW
** Name: Disp-BC-10 Type: Displacement/Rotation
*Boundary, op=NEW
** Name: Disp-BC-11 Type: Displacement/Rotation
*Boundary, op=NEW
** Name: Disp-BC-12 Type: Displacement/Rotation
*Boundary, op=NEW
** Name: Disp-BC-13 Type: Displacement/Rotation
*Boundary, op=NEW
RUBBER-1."BOTTOM LINE", 2, 2
** Name: Disp-BC-14 Type: Displacement/Rotation
*Boundary, op=NEW
_M7, 1, 1
** Name: Disp-BC-15 Type: Displacement/Rotation
*Boundary, op=NEW
RUBBER-1."BOTTOM LINE", 1, 1
** Name: Disp-BC-16 Type: Displacement/Rotation
*Boundary, op=NEW, amplitude=AMP-2
_PICKEDSET101, 1, 1, 1.
** Name: Disp-BC-17 Type: Displacement/Rotation
*Boundary, op=NEW, amplitude=AMP-2
_PICKEDSET101, 2, 2
** Name: Disp-BC-18 Type: Displacement/Rotation
*Boundary, op=NEW, amplitude=AMP-2
_PICKEDSET101, 6, 6
**
** OUTPUT REQUESTS
**
*Restart, write, number interval=1, time marks=NO
**
** FIELD OUTPUT: F-Output-3
**
*Output, field, number interval=400
*Element Output, directions=YES
ENER, LE, S
**
** FIELD OUTPUT: F-Output-4
**
*Node Output
RF, U
*Element Output, directions=YES
LE,
**
** HISTORY OUTPUT: H-Output-2
**
*Output, history
*Node Output, nset=SLIDER-1.REFPOINTANALYTICALSLIDER
RF1, RF2
*End Step
** ----------------------------------------------------------------
** STEP: Step-3
**
*Step, name=Step-3
*Dynamic, Explicit
, 0.02
*Bulk Viscosity
0.06, 1.2
**
```

```
** BOUNDARY CONDITIONS
**
** Name: Disp-BC-13 Type: Displacement/Rotation
*Boundary, op=NEW
** Name: Disp-BC-14 Type: Displacement/Rotation
*Boundary, op=NEW
** Name: Disp-BC-15 Type: Displacement/Rotation
*Boundary, op=NEW
** Name: Disp-BC-16 Type: Displacement/Rotation
*Boundary, op=NEW
** Name: Disp-BC-17 Type: Displacement/Rotation
*Boundary, op=NEW
** Name: Disp-BC-18 Type: Displacement/Rotation
*Boundary, op=NEW
** Name: Disp-BC-19 Type: Displacement/Rotation
*Boundary, op=NEW
RUBBER-1."BOTTOM LINE", 2, 2
** Name: Disp-BC-20 Type: Displacement/Rotation
*Boundary, op=NEW
_M7, 1, 1
** Name: Disp-BC-21 Type: Displacement/Rotation
*Boundary, op=NEW
RUBBER-1."BOTTOM LINE", 1, 1
** Name: Disp-BC-22 Type: Displacement/Rotation
*Boundary, op=NEW, amplitude=AMP-3
_PICKEDSET101, 1, 1, 1.
** Name: Disp-BC-23 Type: Displacement/Rotation
*Boundary, op=NEW, amplitude=AMP-3
_PICKEDSET101, 2, 2
** Name: Disp-BC-24 Type: Displacement/Rotation
*Boundary, op=NEW, amplitude=AMP-3
_PICKEDSET101, 6, 6
**
** OUTPUT REQUESTS
**
*Restart, write, number interval=1, time marks=NO
**
** FIELD OUTPUT: F-Output-5
**
*Output, field, number interval=400
*Element Output, directions=YES
ENER, LE, S
**
** FIELD OUTPUT: F-Output-6
**
*Node Output
RF, U
*Element Output, directions=YES
LE,
**
** HISTORY OUTPUT: H-Output-3
**
*Output, history
*Node Output, nset=SLIDER-1.REFPOINTANALYTICALSLIDER
RF1, RF2
*End Step
```

9.5   DVD content

The DVD at the back of this thesis contains the data files listed below. The time given in the video frame is in the format **hh:mm:ss:ms** (with **hh**=hours, **mm**=minutes, **ss**=seconds and **ms**=milliseconds). The spacing between two marks on the ruler shown at the right hand side is 1mm.

1. Videos of Schallamach waves on smooth surface

    Filename: Smooth_NR3_1mms_0.6N.avi
    Filename: Smooth_NR3_10mms_1.3N.avi

2. Videos of slip-waves on rough surface.

    Filename: Rough_NR1_3mms_1.3N.avi
    Filename: Rough_NR1_10mms_1.3N.avi

10 References

Agulló, N. and Borrós, S. (2002). *Qualitative and quantitative determination of the polymer content in rubber formulations*, J. Therm. Anal. Calorim. **67**, 513-522.

Aklonis, J. J. and MacKnight, W. J. (1983). *Introduction to polymer viscoelasticity*, New York, John Wiley & Sons, Inc.

Amontons, G. (1699). *Mémoires de l'acadèmie royale*, Histoire de l'Académie Royale des Sciences avec les Mémoires de Mathématique et de Physique 206.

Arfken, G. B., Griffing, D. F., Kelly, D. C. and Priest, J. (1989). *University physics*, Orlando, Harcourt Brace Jovanovich.

Arnold, S. P., Roberts, A. D. and Taylor, A. D. (1987). *Rubber friction dependence on roughness and surface energy*, J. Nat. Rubber R. **2**, 1-14.

Ashraf, M. A., Sobhi-Najafabadi, B., Gol, O. and Sugumar, D. (2007). *Finite element analysis of a polymer-polymer sliding contact for Schallamach wave and wear*. 6th International Conference on Fracture and Damage Mechanics. Madeira, Trans Tech Publications Ltd**, 633-636.

ASTM (1999). *Standard test method for rubber properties - durometer hardness (ASTM D 2240-02b)*, West Conshohocken, ASTM International.

ASTM (2002). *Standard test methods for vulcanized rubber and thermoplastic elastomers - tension (ASTM D 412 – 98a)*, West Conshohocken, ASTM International.

ASTM (2004a). *Rubber products - chemical analysis*, West Conshohocken, ASTM International.

ASTM (2004b). *G143-03 Standard test method for measurement of web/roller friction characteristics*, West Conshohocken, ASTM International.

Axel (2006). *Testing brief - measuring rubber and plastic friction for analysis (company data sheet)*, Ann Arbor, Axel Products Inc.

Bachmann, T. (1998). *Wechselwirkung im Prozess der Reibung zwischen Reifen und Fahrbahn (Interaction in the process of friction between tyre and road surface)*, Düsseldorf, VDI Verlag.

Barquins, M. (1983). *Energy dissipation in Schallamach waves*, Wear **91**, 103-110.

Barquins, M. (1984). *On a new mechanism in rubber friction*, Wear **97**, 111-114.

Barquins, M. (1985). *Sliding friction of rubber and Schallamach waves - A review*, Mater. Sci. Eng. **73**, 45-63.

Barquins, M. (1992). *Adherence, friction and wear of rubber-like materials*, Wear **158**, 87-117.

Barquins, M. (1993). *Friction and wear of rubber-like materials*, Wear **160**, 1-11.

Barquins, M. and Courtel, R. (1975). *Rubber friction and the rheology of viscoelastic contact*, Wear **32**, 133-150.

Barquins, M., Koudine, A. A. and Vallet, D. (1996). *On the existence of Schallamach waves during surface friction in rubber-like material as a function of thickness*, Cr. Acad. Sci. II B **323**, 433-438.

Barquins, M. and Roberts, A. D. (1986). *Rubber friction variation with rate and temperature: some new observations*, J. Phys. D. Appl. Phys. **19**, 547-563.

Bateman, L. (1963). *Chemistry and physics of rubber-like substances*, London, Maclaren.

Baumard, T. (2009). *Degradation of tyres in a motor race*, Diploma thesis, co-supervision of Philip Gabriel, École centrale Nantes and Queen Mary, University of London.

Baumberger, T. and Caroli, C. (2006). *Solid friction from stick-slip down to pinning and aging*, Adv. Phys. **55**, 279-348.

Best, B., Meijers, P. and Savkoor, A. R. (1981). *The formation of Schallamach waves*, Wear **65**, 385-396.

Biot, M. A. (1965). *Mechanics of incremental deformations*, New York, Wiley.

Blaine, R., L. (2005). *The case for a generic definition of DSC*, TA Instruments, DMA Handbook.

Blau, P. J. (2001). *The significance and use of the friction coefficient*, Tribol. Int. **34**, 585-591.

Bowden, F. P. and Tabor, D. (1954). *Friction and lubrication of solids*, London, Oxford University Press.

Bowden, F. P. and Tabor, D. (1973). *Friction - An introduction to tribology*, London, Heinemann Educational Books Ltd.

Bradley, R. S. (1992). *The cohesive force between solids and the surface energy of solids*, Phil. Mag. **13**, 853-862.

Briggs, G. A. D. and Briscoe, B. (1975). *The dissipation of energy in the friction of rubber*, Wear **35**, 357-364.

Briggs, G. A. D. and Briscoe, B. (1979). *Surface roughness and the friction and adhesion of elastomers*, Wear **57**, 269-280.

Brydson, J. A. (1978). *Rubber chemistry*, Barking, Essex, Applied Science Publishers Ltd.

Brydson, J. A. (1988). *Rubber materials and their compounds*, New York, Elsevier Science Publishers Ltd.

BSI (1997). *BS3558-1, ISO 1382:1996 - Glossary of rubber terms part 1*, London, British Standard Institute.

Budinski, K. G. (2001). *Friction of plastic webs*, Tribol. Int. **34**, 625-633.

Busfield, J. J. C. (2000). *The prediction of the mechanical performance of elastomeric components using finite element analysis*, PhD Thesis, Queen Mary, University of London.

Busfield, J. J. C. (2010). *Rubber materials,* Lecture notes, Queen Mary, University of London.

Busfield, J. J. C., Davies, C. K. L. and Thomas, A. G. (1996). *Aspects of fracture in rubber components*, Progr. Rubber Plast. Tech. **12**, 191.

Busfield, J. J. C., Jha, V., Liang, H., Papadopolous, I. C. and Thomas, A. G. (2005). *Prediction of fatigue crack growth using finite element analysis techniques applied to three-dimensional elastomeric components*, Plast. Rubber Compos. **34**, 349-356.

Busfield, J. J. C. and Thomas, A. G. (1999). *Indentation tests on elastomer blocks*, Rubber Chem. Technol. **72**, 876-894.

Coveney, V. and Menger, C. (1999). *Initiation and development of wear of an elastomeric surface by a blade abrader*, Wear **233**, 702-711.

Denny, D. F. (1953). *The influence of load and surface roughness on the friction of rubber-like materials*, P Phys. Soc. **66**, 721-727.

Derjaguin, L. D., Muller, M. and Toporov, Y. P. (1975). *Effect of contact deformations on the adhesion of particles*, J. Coll. and Interface Sci. **67**, 378.

Désoyer, T. and Martins, J. A. C. (1998). *Surface instabilities in a Mooney-Rivlin body with frictional boundary conditions*, Int. J. Adhes. Adhes. **18**, 413-419.

Dick, J., S., (2001). *Rubber technology - compounding and testing for performance*, Munich, Carl Hanser Verlag.

Dowson, D. and Higginson, G. R. (1977). *Elasto-hydrodynamic lubrication*, Oxford, Pergamon Press.

Eichhorn, U. (1993). *Reibwert zwischen Reifen und Fahrbahn - Einflussgrößen und Erkennung (Friction coefficient between tyre and road surface - Parameters and Identification)*, Düsseldorf, VDI Verlag.

Euler, L. (1769). *Remarques sur l'effect du frottement dans l'eyuilibre*, Memoires de l'acaemie des sciences de Berlin **18**, 265-278.

Eytelwein, J. A. (1808). *Handbuch der Statik fester Körper, Band 2 (Hand book on the statics of rigid bodies, Book 2)*, Berlin, G.Reimer.

Fagan, M. J. (1992). *Finite element analysis - theory and practice*, Harlow, Longman Group.

Fenner, D. N. (1987). *Engineering stress analysis*, Chichester, John Wiley.

Fernández-Berridi, M. J., González, N., Mugica, A. and Bernicot, C. (2006). *Pyrolysis-FTIR and TGA techniques as tools in the characterization of blends of natural rubber and SBR,* Thermochim. Acta **444**, 65-70.

Ferry, J. D. (1961). *Viscoelastic properties of polymers*, New York, Wiley.

FisherScientific (2007). *Safety data sheet for analytical acetone*, Fisher Scientific, Loughborough.

Flexsys (2005). *Safety data sheet on Santoflex 6PPD (Product code 460921)*, Dublin, Flexsys.

Foreman, J. and Reed, K. (2005a). *Dynamic mechanical analyzers: How do they work?*, TA Instruments, DMA Handbook **TAA-229** 1-4.

Foreman, J., Sauerbrunn, S. R. and Marcozzi, C. L. (2005b). *Exploring the sensitivity of thermal analysis techniques of the glass transition, TA-082*, Crawley, TA Instruments.

Fukahori, Y., Gabriel, P. and Busfield, J. J. C. (2010). *How does rubber truly slide between Schallamach waves and stick-slip motion?*, (submitted to Wear)1-30.

Fukahori, Y., Liang, H. and Busfield, J. J. C. (2008). *Criteria for crack initiation during rubber abrasion*, Wear **265**, 387-395.

Fukahori, Y. and Yamazaki, H. (1994a). *Mechanism of rubber abrasion. Part 1: Abrasion pattern formation in natural rubber vulcanizite*, Wear **171**, 195-202.

Fukahori, Y. and Yamazaki, H. (1995). *Mechanism of rubber abrasion. Part 3: how is friction linked to fracture in rubber abrasion?*, Wear **188**, 19-26.

Fuller, K. N. G. and Tabor, D. (1975). *The effect of surface roughness on the adhesion of elastic solids*, P. Roy. Soc. Lon. A **345**, 327-342.

Gabriel, P., Fukahori, Y., Thomas, A. G. and Busfield, J. J. C. (2009). *The mechanics of sliding friction between a rigid indenter and a rubber surface*. Proc. VI ECCMR. Dresden, 305.

Gabriel, P., Fukahori, Y., Thomas, A. G. and Busfield, J. J. C. (2010b). *FEA modelling of Schallamach waves*, Rubber Chem. Technol., (accepted for publication).

Gabriel, P., Thomas, A. G. and Busfield, J. J. C. (2010a). *Influence of interface geometry on rubber friction*, Wear **268**, 747-745.

Gent, A., N. and Cho, I. S. (1999). *Surface instabilities in compressed or bent rubber blocks*, Rubber Chem. Technol. **72**, 253-262.

Gent, A., N., (2001). *Engineering with rubber*, Munich, Carl Hanser Verlag.

Gent, A. N. (2005). *Elastic instabilities in rubber*, Int. J. Nonlinear Mech. **40**, 165-175.

Gough, J. (2003). *Operation manual of Plint rubber friction machine*, Hertford, TARRC.

Gough, J., Greorgy, I. H. and Muhr, A. H. (1999). *Determination of constitutive equations for vulcanized rubber* in: Finite element analysis of elastomers, Professional Engineering Publishing Ltd., London, 5-26.

Gough, J., Muhr, A. H. and Kwong, M. (2001). *Measurement and modelling of friction of rubber*. Proc. II ECCMR. D. Besdo, R. H. Schuster and J. Ihlemann. Hannover, A a Balkema Publishers**:** 165-171.

Green, A. E. and Zerna, W. (1968). *Theoretical elasticity*, Oxford, Oxford University Press.

Greenwood, J. A. and Tabor, D. (1958). *The Friction of hard sliders on lubricated rubber: The importance of deformation losses*, P. Phys. Soc. **71**, 989.

Greenwood, J. A. and Williamson, J. B. P. (1966). *Contact of nominally flat surfaces*, P. Roy. Soc. Lon. A **295**, 300-319.

Grönqvist, R., Hirvonen, M. and Tohv, A. (1999). *Evaluation of three portable floor slipperiness testers*, Int. J. Ind. Ergonom. **25**, 85-95.

Grosch, K. A. (1963). *The relation between the friction and viscoelastic properties of rubber* P. Roy. Soc. Lon. A **274**, 21-39.

Grosch, K. A. (1996). *The rolling resistance, wear and traction properties of tread compounds*, Rubber Chem. Technol. **96**, 496-567.

Grosch, K. A. (2007). *Rubber friction and its relation to tire traction*, Rubber Chem. Technol. **80**, 379-411.

Grosch, K. A. and Schallamach, A. (1965). *Relation between abrasion and strength of rubber*, Trans IRI **41**, 80.

Haines, P. J. (1995). *Thermal methods of analysis* London, Blackie academic and professional.
Harewood, F. J. and McHugh, P. E. (2007). *Comparison of the implicit and explicit finite element method using crystal plasticity*, Comp. Mater. Sci. **39**, 481-494.

Heideman, G., Datta, R. N., Noordermeer, J. W. M. and van Baarle, B. (2005). *Influence of zinc oxide during different stages of sulfur vulcanization. Elucidated by model compound studies.*, J. Appl. Polym. Sci. **95**, 1388-1404.

Hertz, H. (1896). *Miscellaneuos papers*, Macmillan, London146.

Hobson, T. (2005). *Poster of roughness factors*, Leicster, Taylor-Hobson.

Hoffmann, W. (1996). *Rubber technology handbook*, Munich, Hanser&Gardner.

Hong, W., Zhao, X. and Suo, Z. (2009). *Formation of creases on the surfaces of elastomers and gels*, Appl. Phys. Lett. **95**, 111901.

Hosler, D., Burkett, S. L. and Tarkanian, M. J. (1999). *Prehistoric polymers: Rubber processing in ancient Mesoamerica*, Science **284**, 1988-1990.

Huffington, J. D. (1961). *Internal friction in fibre assemblies*, Brit. J. of Appl. Phys. **12**, 99-102.

Hutchings, R. (1992). *Physics*, Walton-on-Thames, Thomas Nelson and Sons Ltd.

ISO (1992). *Rubber: Determination of solvent extract*, Geneva, Switzerland, International Organization for Standardization.

Jha, V. (2009). *Electrically conductive elastomers*, PhD Thesis, Queen Mary, University of London, 64.

Johnson, K. L. (1985). *Contact mechanics*, Cambridge, Cambridge University Press.

Johnson, K. L., Kendall, K. and Roberts, A. D. (1971). *Surface energy and the contact of elastic solids*, P. Roy. Soc. Lon. A **324**, 301-313.

Kim, J., Kang, Y. H., Choi, H. H., Hwang, S. M. and Kang, B. S. (2002). *Comparison of implicit and explicit finite-element methods for the hydroforming process of an automobile lower arm*, Int. J. Adv. Manuf. Tech. **20**, 407-423.

Klüppel, M. and Fritzsche, J. (2009). *Viscoelastic properties of filler reinforced elastomers*. Proc. VI ECCMR. Dresden, 111.

Klüppel, M. and Heinrich, G. (2000). *Rubber friction on self-affine toad tracks*, Rubber Chem. Technol. **73**, 578-606.

Klüppel, M. and Heinrich, G. (2008). *Rubber friction, tread deformation and tire traction*, Wear **265**, 1052–1060.

Koudine, A. A. and Barquins, M. (1997). *On the influence of rubber thickness on the existence of Schallamach waves*, Int. J. Adhes. Adhes. **17**, 107-110.

Koudine, A. A., Lambert, M. and Barquins, M. (1997). *Some new experimental results on the Schallamach waves propagation by space-time analysis*, Int. J. Adhes. Adhes. **17**, 359-363.

Kuhn, W. (1936). *Beziehungen zwischen Molekuelgroesse, statisticher Molekülgestalt und elastischen Eigenschaften hochpolymerer Stoffe*, Kolloid Z. **76**, 258.

Kumar, P. (2007). *Investigating the recycled rubber granulate-virgin rubber interface*, PhD Thesis, Queen Mary, University of London.

Kumar, P., Fukahori, Y., Thomas, A. G. and Busfield, J. J. C. (2007). *Volume changes under strain resulting from the incorporation of rubber granulates into a rubber matrix*, J. Polym. Sci. Pol. Phys. **45**, 3169 - 3180.

Kummer, H. W. (1966). *Unified theory of rubber and tire friction, engineering research bulletin B-94*, The Pennsylvania State University, University College.

Kunz, J. and Studer, M. (2006). *Determining the modulus of elasticity in compression via the Shore A hardness*, Kunststoffe Int., **6**.

Kutz, M. (1998). *Mechanical engineer's handbook*, New York, John Wiley & Sons.

Lazeration, J. J. (1987). *Determination of the coefficient of friction of rubber at realistic tire contact pressures*, Rubber Chem. Technol. **60**, 966-974.

Le Gal, A. (2007). *Investigation and modelling of rubber stationary friction on rough surfaces*, PhD Thesis, Gottfried Wilhelm Leibniz University of Hanover.

Le Gal, A., Yang, X. and Klüppel, M. (2005). *Evaluation of sliding friction and contact mechanics of elastomers based on dynamic-mechanical analysis*, J. Chem. Phys. **123**, 014704.

Liang, H. (2007). *Investigating the mechanism of elastomer abrasion*, PhD Thesis, Queen Mary, University of London.

Liang, H., Fukahori, Y., Thomas, A. G. and Busfield, J. J. C. (2009). *Rubber abrasion at steady state*, Wear **266**, 288-296.

Lin, Y.-J. and Hwang, S.-J. (2004). *Temperature prediction of rolling tires by computer simulation*, Math. Comput. Simulat. **67**, 235-249.

Lindner, M. (2005). *Experimentelle und theoretische Untersuchungen zur Gummireibung an Profilklötzen und Dichtungen*, PhD thesis, University of Hannover, Faculty of machine construction.

Loadman, M. J. R. (1998). *Analysis of rubber and rubber-like polymers*, AH Dordrecht, Kluwer Academic Publishers.
Machado, G., Chagnon, G. and Favier, D. (2009). *Experimental observation of induced anisotropy of th Mullins effect in particle-reinforced silicone rubber*. Proc. VI ECCMR. Dresden, CRC Press.

Maegawa, S. and Nakano, K. (2008). *Occurrence of stick-slip and Schallamach waves in sliding between hard and soft surfaces*. 2nd international conference on advanced tribology, Singapore.

McNaught, A. D. and Wilkinson, A. (1997). *Compendium of chemical terminology - The gold book*, Oxford, Blackwell Science Ltd.

Meyer, E., Overney, R. M., Dransfeld, K. and Gyalog, T. (1998). *Nanoscience – Friction and rheology on the nanometre scale*, Singapore, World Scientific Publishing Co. Pte. Ltd.

Mooney, M. (1940). *A theory of large elastic deformation*, J. Appl. Phys. **11**, 582.

Moore, D. F. (1972). *The friction and lubrication of elastomers*, Oxford, Pergamon Press.

Mori, K., Kanea, S., Kanae, K., Hirahara, H., Oishi, Y. and Iwabuchi, A. (1994). *Influence on friction force of adhesion force between vulcanizates an sliders* Rubber Chem. Technol. **67**, 797-805.

Morton, M. (1987). *Rubber technology*, New York, Van Nostrand Reinhold Company Inc.

Mullins, L. (1969). *Softening of rubber by deformation*, Rubber Chem. Technol. **42**, 339.

Myant, C., Spikes, H. A. and Stokes, J. R. (2009). *Influence of load and elastic properties on the rolling and sliding friction of lubricated compliant contacts*, Tribology International doi: 10.1016/j.triboint.2009.04.034, 1-9.

Ohm, R. F. (1990). *The Vanderbilt rubber handbook*, Norwalk, R. T. Vanderbilt Company Inc.

Palasantzas, G. (2005). *Comparison of hysteretic and adhesive coefficient of friction for rubbers sliding onto self-affine rough surfaces*, J. Appl. Phys. **97**.

Pan, X.-D. (2007). *Wet sliding friction of elastomer compounds on a rough surface under varied lubrication conditions*, Wear **262**, 707-717.

Persson, B. N. J. (1998). *On the theory of rubber friction*, Surf. Sci. **401**, 445-454.

Persson, B. N. J. (1999). *Sliding friction*, Surf. Sci. Rep. **33**, 83-119.

Persson, B. N. J. (2001a). *Elastic instabilities at a sliding interface*, Phys. Rev. B **63**, 104101.

Persson, B. N. J. (2001b). *Theory of rubber friction and contact mechanics*, J. Chem. Phys. **118**, 3840-3861.

Persson, B. N. J. (2001c). *Elastoplastic contact between randomly rough surfaces*, Phys. Rev. Lett. **87**.

Persson, B. N. J. (2006). *Rubber friction: role of the flash temperature*, J. Phys. Condens. Mat. **18**, 7789-7823.

Persson, B. N. J. and Volokitin, A. I. (2006). *Rubber friction on smooth surfaces*, Eur. Phys. J. E **21**, 69-80.

Pinnington, P. J. (2009). *Rubber friction on rough and smooth surfaces*, Wear **267**, 1653–1664.

Plint-Manual (1997). *Plint friction tester manual*, Newbury, Phoenix Tribology Ltd.

Qui, C. (2007). *Investigations on parameters affecting rubber friction - using a formula one tyre compound*, Master Thesis - Queen Mary, University of London.

Rajan, V. V., Dierkes, W. K., Joseph, R. and Noordermeer, J. W. M. (2006). *Recycling of NR based cured latex material reclaimed with 2,2 '-dibenzamidodiphenyldisulphide in a truck tire tread compound*, J. Appl. Polym. Sci. **102**, 4194-4206.

Rajan, V. V., Dierkes, W. K., Joseph, R. and Noordermeer, J. W. M. (2007). *Effect of diphenyldisulfides with different substituents on the reclamation of NR based latex products*, J. Appl. Polym. Sci. **104**, 3562-3580.

Rand, C. J. and Crosby, A. J. (2006). *Insight into the periodicy of Schallamach waves in soft material friction*, Appl. phys. lett. **89**, 261907.

Rand, C. J. and Crosby, A. J. (2007). *Friction of soft elastomeric surfaces with a defect*, Appl. phys. lett. **91**, 261909.

Ratsimba, C. H. H. (2000). *Fatigue crack growth of carbon black reinforced elastomers*, PhD Thesis, Queen Mary, University of London.

Reuvekamp, L. A. E. M., van Swaaij, P. J. V. and Noordermeer, J. W. M. (2009). *Silica reinforced tire tread compounds influence of functional groups of silane coupling agents on dynamic and mechanical properties*, Kautsch. Gummi Kunstst. **62**, 35-43.

Rivlin, R. S. (1948). *Large elastic deformations of isotropic materials I. Fundamental concepts*, Philos. T. R. Soc. A **240**, 459-470.

Rivlin, R. S. (1956). *Large elastic deformations*, New York, Academic Press, 351.

Road Research Laboratory, R. (1960). *Instructions for using the portable skid-resistance tester*, Berkshire, Road Research Laboratory.

Roberts, A. D. (1971). *Direct measurement of electrical double-layer forces between solid surfaces,* J. Colloid Interf. Sci. **41**, 23-34.

Roberts, A. D. (1974). *Lubrication studies of smooth rubber contacts from: The physics of tire traction, theory and experiment*, Warren, General Motors Corporation Research Laboratories.

Roberts, A. D. (1979). *Looking at rubber adhesion*, Rubber Chem. Technol. **52**, 23.

Roberts, A. D. (1981a). *Adhesion and friction of elastomers*, Rubber Chem. Technol. **54**, 944-962.

Roberts, A. D. (1988). *Natural rubber science and technology*, Oxford, Oxford University Press.

Roberts, A. D. (1992). *A guide to estimating the friction of rubber*, Rubber Chem. Technol. **65**, 673-686.

Roberts, A. D. (1994). *New rubber friction testing machine*, Rubber World **209**.

Roberts, A. D. and Jackson, S. A. (1975). *Sliding friction of rubber*, Nature **257**, 118-120.

Roberts, A. D. and Richardson, J. C. (1981). *Interface study of rubber-ice friction*, Wear **67**, 55-69.

Roberts, A. D. and Thomas, A. G. (1975). *The adhesion and friction of smooth surfaces*, Wear **33**, 46-64.

Roberts, A. D. and Thomas, A. G. (1977). *Static friction of smooth clean vulcanized rubber*, Rubber Chem. Technol. **50**, 266-271.

Schallamach, A. (1952). *The load dependence of rubber friction*, Proc. Roy. Soc. Lon. B **65**, 657-661.

Schallamach, A. (1958). *Friction and abrasion of rubber*, Wear **1**, 384-417.

Schallamach, A. (1963). *Abrasion pattern on rubber*, Rubber Chem. Technol. **63**, 320-327.

Schallamach, A. (1969). *Friction and frictional rise of wedge sliders on rubber*, Wear **13**, 13-25.

Schallamach, A. (1971). *How does rubber slide?*, Wear **17**, 301.

Scherbakov, M. and Goodyear, T. R. (2004). *The sensitivity of frictional characterization of elastomers and elastomeric composites*, Rubber World Sept**.**, 42-47.

Scherbakov, M. and Gurvich, M., R. (2003). *An approach of frictional characterization for elastomers and elastomeric composites*, J. Elastom. Plast. **35**, 335.

Schramm, E. J. (2002). *Reibung von Elastomeren auf rauen Oberflächen und Beschreibung von Nassbremseigenschaften von PKW-Reifen*, Phd thesis, University of Regensburg, Faculty of Physics.

Seidelt, S., Müller-Hagedom, M. and Bockhorn, H. (2006). *Description of tire pyrolysis by thermal degradation behaviour of main components*, J. Anal. Appl. Pyrol. **75**, 11-18.

Sezna, J. A. (1991). *Correlation of results from curemeters of different designs*. 139th Technical Meeting of the Rubber Division, ACS. Toronto.

Sezna, J. A. and del Vecchio, R. J. (2003). *Fundamentals of rubber technology (Chapter 6)*, Akron, Rubber Division, American Chemical Society.

Shaw, M. T. and MacKnight, W. J. (2005). *Introduction to polymer viscoelasticity*, Hoboken, John Wiley & Sons, Inc.

Sherma, J. (1991). *Handbook of thin-layer chromatography*, New York, Marcel Dekker Inc.

Shigley, J. E. and Mischke, C. R. (1989). *Mechanical engineering design*, New York, McGraw-Hill Book Co.

Shulman, V. L. (2004). *Tyre recycling*, RAPRA review reports **7**.

Sills, S., Vorvolakos, K., Chaudhury, M. K. and Overney, R. M. (2007). *Molecular origins of elastomeric friction / Nanotribology: Friction and wear on the atomic scale*, New York, Springer Verlag.

Simulia (2009). *Abaqus user's manual, v. 6.8.2*, Providence, Simulia.

Sircar, A. K. (1997). *Thermal characterization of polymeric materials*, Academic Press.

Smith, R. H. (2008). *Analyzing friction in the design of rubber products and their paired surfaces*, Boca Raton, Fla. ; London, CRC.

Sneddon, I. (1975). *Applications of integral transforms in the theory of elasticity*, New York, Springer-Verlag.

Southern, E. and Thomas, A. G. (1965). *Effect of constraints on the equilibrium swelling of rubber vulcanizates*, J. Polym. Sci. Chem. **3**, 641-646.

Southern, E. and Thomas, A. G. (1972). *Impact of rigid spheres on rubber*, J. Appl. Polym. Sci. **16**, 1641.

Southern, E. and Thomas, A. G. (1978). *Studies of rubber abrasion*, Plast. Rub. Mat. Appl. **3**, 133-138.

Sperling, L. H. (2001). *Introduction to physical polymer science*, Bethlehem, Pennsylvania, John Wiley & Sons, Inc.

Stanley, W. F. (1994). *Portable skid resistance tester - instructions for use*, London, Stanley Ltd.

Sun, J. S., Lee, K. H. and Lee, H. P. (2000). *Comparison of implicit and explicit finite element methods for dynamic problems*, J. Matter. Process. Tech. **105**, 110-118.

TA-Instruments (2005a). *Thermal Solutions, Effect of frequency on the modulus and glass transition temperature of PET*, TA Instruments, DMA Handbook.

TA-Instruments (2005b). *Thermal applications note – Enhanced DSC glass transition*, TA Instruments, DMA handbook.

Tabor, D. (1960). *Hysteresis losses in the friction of lubricated rubber*, Rubber Chem. Technol. **33**, 142-150.

Tabor, D. and Fuller, K. N. G. (1965). *The effect of surface roughness on the adhesion of elastic solids*, Proc. Roy. Soc. Lon. A **345**, 327-342.

Tanner, R. I. (2000). *Engineering rheology*, Oxford, Oxford University Press.

Tatara, Y. (1993). *Large deformations of a rubber sphere under diametral compression*, Jpn. Soc. Mech. Eng. Int. J. **36**, 190-196.

Thirion, P. (1946). *The coefficient of adhesion of rubber*, Rubber Chem. Technol. **21**, 505-515.

Thomas, L. C. (2005). *Modulated DSC® paper #5 measurement of glass transitions and enthalpic recovery*, TA Instruments, User Manual for DMA.

Timoshenko, S. P. and Goddier, J. N. (1973). *Mathematical theory of elasticity*, New York, McGraw-Hill.

Treloar, L. R. G. (1975). *The physics of rubber elasticity*, Oxford, Clarendon Press.

Turi, E. A. (1997). *Thermal characterization of polymeric materials*, New York, Academic Press.

Uchiyama, Y., Wada, N., Iwai, T., Ueda, S. and Sado, S. (2005). *Friction of short fiber reinforced rubber on wet surfaces*, J. Appl. Polym. Sci. **95**, 82-89.

Verbruggen, M. A. L., van der Does, L., Noordermeer, J. W. M., van Duin, M. and Manuel, H. J. (1999). *Mechanisms involved in the recycling of NR and EPDM*, Rubber Chem. Technol. **72**, 731-740.

Wallace Ltd. (1997). *Manual for hardness tester H17A OP1 Issue 2*, Kingston, Wallace.

Waters, N. E. (1965). *The indentation of thin rubber sheets by spherical indenters*, Brit. J. of Appl. Phys. **16**, 557-563.

White, J. R. and De, S. K. (2001). *Rubber technologist's handbook*, Shawbury, Rapra Technology Ltd.

Williams, M. L., Landel, R. F. and Ferry, J. D. (1955). *The temperature dependence of relaxation mechanisms in amorphous polymers and other glass-forming liquids*, J. Am. Chem. Soc. **77**, 3701-3707.

Wu-Bavouzet, F., Clain-Burckbuchler, J., Buguin, A., De Gennes, P. G. and Brochard-Wyart, F. (2007). *Stick-slip: Wet versus dry*, J. Adhesion **83**, 761-784.